Studies of Erosion in Gas-Solid Flows by Using Experimental and Numerical Techniques

Dissertation

zur Erlangung des akademischen Grades

Doktoringenieur

(Dr.-Ing.)

von **M.Sc. Guilherme Antônio Novelletto Ricardo**

geboren am 16.07.1988, in Rodeio – SC (Brasilien)

genehmigt durch die Fakultät für Verfahrens- und Systemtechnik

der Otto-von-Guericke-Universität Magdeburg

Promotionskommission: Prof. Dr.-Ing. Berend van Wachem (Vorsitz)

Prof. Dr.-Ing. habil. Martin Sommerfeld (Gutachter)

Prof. Dr. Henry França Meier (Gutachter)

Prof. Dr.-Ing. habil. Dr. h.c. Stefan Heinrich (Gutachter)

eingereicht am: 31.01.2020

Promotionskolloquium am: 30.04.2020

Schriftliche Erklärung

Ich erkläre hiermit, dass ich die vorliegende Arbeit ohne unzulässige Hilfe Dritter und ohne Benutzung anderer als der angegebenen Hilfsmittel angefertigt habe. Die aus fremden Quellen direkt oder indirekt übernommenen Gedanken sind als solche kenntlich gemacht.

Insbesondere habe ich nicht die Hilfe einer kommerziellen Promotionsberatung in Anspruch genommen. Dritte haben von mir weder unmittelbar noch mittelbar geldwerte Leistungen für Arbeiten erhalten, die im Zusammenhang mit dem Inhalt der vorgelegten Dissertation stehen.

Die Arbeit wurde bisher weder im Inland noch im Ausland in gleicher oder ähnlicher Form als Dissertation eingereicht und ist als Ganzes auch noch nicht veröffentlicht.

Declaration

I hereby declare that I prepared the work submitted without inadmissible assistance and without the use of any aids other than those indicated. Facts or ideas taken from other sources, either directly or indirectly have been marked as such.

In particular, I did not use the services of a commercial graduation consultation. Further I have not made payments to third parties either directly or indirectly for any work connected with the contents of the submitted dissertation.

The work has not been submitted as a dissertation either in Germany or abroad in the same or similar form and has also not been published as a whole.

26.05.2020, Halle (Saale)

To my family and friends

"Carry on, you will always remember

Carry on, nothing equals the splendour"

(Kansas)

Preface

This document addresses the research work that I have performed from June 2015 to May 2020 at the multiphase flow working group of the Faculty of Process- and Systems-Engineering (IVT) of the Otto-von-Guericke-Universität Magdeburg. This work concerns studies of solid particle erosion in gas-solid flows by means of experimental and numerical techniques and therefore comprises both numerical simulations and experiments.

The first experimental analysis investigates the influence of solid particle erosion on the surface roughness of different ductile materials in an impingement jet facility, in which the impact of erosion time, inclination angle and particle shape is evaluated. The second experimental study aims to acquire erosion data on bends together with obtaining particle velocity distributions prior to the bends, considering different particle mass loadings and particle shape. The data obtained in this experimental study also serve as additional information for validating numerical methods.

From a numerical point of view, the influence of parameters such as phase interaction, surface roughness and particle mass loading on predictions of gas-solid flow in pneumatic conveying systems involving solid particle erosion is deeply examined. To achieve this goal, the coupled Euler-Lagrange approach is utilized through the free and open-source CFD code OpenFOAM® 4.1, in which its standard Lagrangian libraries are extended to account for all essential models for predicting the behaviour of gas-solid flows and estimating solid particle erosion.

Zusammenfassung

Die vorliegende Arbeit umfasst sowohl Experimente als auch numerische Simulationen. Eine experimentelle Analyse der Änderungen der Oberflächenrauheit von duktilen Materialien aufgrund von Feststoffpartikelerosion wird in einer Aufprallstrahlanlage unter Berücksichtigung von Erosionszeiten von 2,5, 5 und 10 Stunden und Neigungswinkeln von 10°, 20°, 30° und 40° durchgeführt. Die Luft- und Partikelgeschwindigkeit am Ausgang des Strahls waren ungefähr 26 m/s für die Luft und 9,5 m/s für die Partikel. Proben aus Aluminium 5754, Kupfer und Messing (70%Cu-30%Zn) wurden einer Erosion durch Quarzsand- und kugelförmige Glasperlenpartikeln mit einem anzahlgemittelten Durchmesser von 235,4 µm bzw. 211,5 µm unterzogen. Luftgeschwindigkeitsmessungen wurden am Ausgang des Aufprallstrahls unter Verwendung eines Einkomponenten-Laser-Doppler-Anemometers (LDA) durchgeführt. Messungen der Partikelbewegung wurden mit einer kombinierten Methode der Schattenbildgebung und der *Particle Image Velocimetry* (PIV) realisiert. Zweidimensionale Rauheitsprofile wurden durch optisches Scannen der Oberfläche jeder Probe nach der Erosion erfasst und mit dem Anfangszustand der Oberfläche verglichen. Die Veränderungen der Materialoberfläche wurden in der Region mit der stärksten Erosion anhand von drei Rauheitsparametern bewertet: R_a (arithmetische Durchschnittshöhe), RS_m (durchschnittlicher Abstand an der Mittellinie) und $\Delta\gamma$ (Standardabweichung der Rauhigkeitswinkelverteilung). Geschwindigkeitsmessungen des Strahlstroms zeigten den Einfluss des Neigungswinkels auf die Partikelbewegung. Die optischen Messungen lieferten den Einfluss von Feststoffpartikelerosion, Neigungswinkel und Partikelform auf die Oberflächenrauheit der untersuchten Materialien. Darüber hinaus ermöglichten die experimentellen Daten die Entwicklung einer einfachen Korrelation, um die Abhängigkeit des Rauhigkeitswinkel $\Delta\gamma$ von der Feststoffpartikelerosion und dem Neigungswinkel für jedes analysierte Material abzuschätzen. Weiterhin wurde eine detaillierte experimentelle und

numerische Untersuchung der Erosion durch Partikeltransport in einem pneumatischen Fördersystem durchgeführt. Erosions- und Partikelgeschwindigkeitsverteilungen wurden experimentell in einem pneumatischen Fördersystem erhalten, das aus einem horizontalen Rohr, einem 90°-Bogen, einem vertikalen Rohr und einem zweiten 90°-Bogen bestand. Krümmer aus Aluminium 6060-T66 wurden durch Quarzsand- und kugelförmige Glasperlenpartikeln mit einem mittleren Durchmesser von 234,6 µm bzw. 211,5 µm einer Erosion ausgesetzt. Die Erosionstiefe wurde an mehreren Stellen auf der Außenfläche beider Krümmer durch Anwendung einer nicht-invasiven Ultraschalltechnologie (UT) bewertet, aus der schließlich dreidimensionale Erosionskarten erhalten wurden. Die Geschwindigkeitsverteilungen des Fluides und der dispergierten Phase wurden vor jeder der Krümmer unter Verwendung eines Einkomponenten-Laser-Doppler-Anemometers und der Laserlichtschnitt in Kombination mit dem *Particle Image Velocimetry* gemessen. Es wurden Versuche mit einer Fördergeschwindigkeit von etwa 37,9 m/s für zwei unterschiedliche Partikelmassenbeladungen durchgeführt, d.h. η = 0,3 and 1,0 kg Partikel/kg Luft. Die experimentellen Ergebnisse zeigen nicht nur die unterschiedlichen Eigenschaften der Erosionskarten, die mit unterschiedlichen Partikelmassenbeladungen und Partikeltypen erhalten wurden, sondern auch das Auftreten des Abschirmeffekts mit zunehmender Partikelmassenbeladung. Mit den durchgeführten experimentellen Studien werden auch nützliche Informationen für die Validierung numerischer Methoden und Erosionsmodellen bereitgestellt. Überdies wurde das gekoppelte Euler-Lagrange Verfahren in Kombination mit dem Standard-k-ε-Turbulenz-Modell angewendet, um die zuvor beschriebene Gas-Feststoff-Strömung vorherzusagen und die Erosion abzuschätzen. Alle numerischen Simulationen wurden mit dem Open-Source-Code OpenFOAM® 4.1 durchgeführt. Die Standard-Lagrange-Bibliotheken von OpenFOAM® 4.1 wurden jedoch erweitert, um alle notwendigen Modelle zu berücksichtigen. Partikel werden sowohl unter Berücksichtigung der Translations- als auch der Rotationsbewegung verfolgt und alle relevanten Kräfte, die auf die Partikel wirken, wie Schwerkraft/Auftrieb, Widerstand und Auftrieb aufgrund von Scherung und Partikelrotation, werden berücksichtigt. Die turbulente Dispersion der Partikel wird stochastisch durch ein Einschritt-Langevin-Modell beschrieben und der Einfluss der Oberflächenrauheit auf die Partikel-Wand-Kollision wird stochastisch in Form einer Rauheitswinkelverteilung berücksichtigt. Die Partikel-Partikel-Interaktion, nämlich die 4-Wege-Kopplung, wird unter Berücksichtigung eines stochastischen Ansatzes berechnet, bei dem in jedem Lagrange-Zeitschritt ein fiktiver Kollisionspartner auf der Grundlage der lokalen Eigenschaften der

realen Teilchen erzeugt wird (Eigenschaften in jeder numerischen Zelle). Vier in der Literatur verfügbare Erosionsmodelle werden implementiert und zusätzlich durch experimentelle Daten von Mazumder et al.[1] and Solnordal et al.[2] validiert. Außerdem wird eine numerische Validierung eines Gas-Feststoff-Strömung durchgeführt, wie von Huber[3] and Huber and Sommerfeld[4,5] beschrieben, wobei eine gute Übereinstimmung zwischen Berechnungen und Messungen erzielt wurde. Schließlich werden Vorhersagen der Erosionstiefe und der Geschwindigkeitsverteilung mit den erhaltenen experimentellen Daten verglichen. Darüber hinaus wird der Einfluss des Kopplungsgrades und der Oberflächenrauheit auf die Ergebnisse numerisch detailliert analysiert. Der Einfluss der Änderungen auf die Oberflächenrauheit aufgrund der Erosion auf die Partikelbewegung innerhalb des Systems und auf die Erosion selbst wird ebenfalls numerisch aufgezeigt. Die numerischen Ergebnisse verdeutlichen die Fähigkeit des gekoppelten Euler-Lagrange Verfahrens zur Vorhersage von Gas-Feststoff-Strömungen und zeigen, wie wichtig es ist, sowohl Partikelkollisionen als auch Partikel-Wand-Interaktion zu berücksichtigen. Obwohl einige Abweichungen festgestellt wurden, stimmen die meisten numerischen Ergebnisse mit den experimentellen Daten der pneumatischen Fördereinrichtung ziemlich gut überein.

Abstract

The current work is comprised of both experiments and numerical simulations. An experimental analysis of the changes in the surface roughness of ductile materials exposed to solid particle erosion is performed in an impingement jet facility considering erosion times of 2.5, 5 and 10 hours and inclination angles of 10°, 20°, 30° and 40°. Air and particle velocity at the exit of the jet were approximately 26 m/s and 9.5 m/s, respectively. Aluminium 5754, copper and brass (70%Cu-30%Zn) samples were subjected to erosion by quartz sand and spherical glass beads particles with a number mean diameter of 235.4 µm and 211.5 µm, respectively. Air velocity measurements were performed at the exit of the impingement jet by using a one-component laser Doppler anemometer (LDA). Measurements of particle motion were acquired by applying a combined method of shadow imaging and particle image velocimetry (PIV). Two-dimensional roughness profiles were acquired by optically scanning the surface of each sample after erosion and compared with the initial state of the surface. Changes in the material surface were assessed in the region with most pronounced erosion in terms of three roughness parameters: R_a (arithmetic average height), RS_m (mean spacing at the mean line) and $\Delta\gamma$ (standard deviation of the roughness angle). Velocity measurements of the jet flow demonstrated the influence of the inclination angle on particle motion. The optical measurements showed the influence of solid particle erosion, inclination angle and particle shape on the surface roughness of the analysed materials. Moreover, the experimental data allowed for the development of a simple correlation to estimate the dependence of the roughness angle $\Delta\gamma$ on solid particle erosion and inclination angle for each material analysed. In addition, a detailed experimental and numerical analysis of erosion due to particle transport in a pneumatic conveying system was performed. Erosion and particle velocity distributions were obtained experimentally in a pneumatic conveying system composed of a horizontal pipe, a 90° bend, a vertical pipe and a second 90° bend. Aluminium 6060-T66 bends were exposed

to erosion by quartz sand and spherical glass beads particles with a number mean diameter of 234.6 µm and 211.5 µm, respectively. Erosion depth was assessed at several locations on the outer surface of both bends by applying a non-invasive Ultrasonic Technology (UT), from which three-dimensional erosion maps were finally obtained. Fluid and dispersed phase velocity distributions were measured prior to each one of the bends by applying a one-component laser Doppler anemometer and the laser-light sheet technique combined with particle image velocimetry. Experiments were carried out with a conveying velocity of about 37.9 m/s for two different particle mass loadings, i.e. η = 0.3 and 1.0 kg particles/kg air. The experimental results not only show the distinct characteristics between the erosion maps obtained with different particle mass loadings and different particle types, but also show the emergence of the shielding effect with increasing particle mass loading. Also, with the conducted experimental studies useful information is provided for validating numerical methods and erosion models. Moreover, the coupled Euler-Lagrange approach in combination with the standard k-ε turbulence model was applied for predicting the previously described gas-solid flow and estimating erosion. All numerical simulations were performed using the free and open-source code OpenFOAM[®] 4.1. However, the standard Lagrangian libraries from OpenFOAM[®] 4.1 were extended to account for all necessary models. Particles are tracked considering both translational and rotational motion and all relevant forces acting on the particles, such as gravity/buoyance, drag and transverse lift due to shear and particle rotation, are accounted for. Particle dispersion due to turbulence is predicted stochastically by means of a single step Langevin equation and the influence of surface roughness on particle-wall interaction is accounted for stochastically in terms of a roughness angle distribution. Particle-particle interaction, namely 4-way coupling, is computed by considering a stochastic approach, in which a fictitious collision partner is generated each Lagrangian time step based on the local properties of real particles (properties in every numeric cell). Four erosion models available in the literature are implemented and validated through experimental data provided by Mazumder et al.[1] and Solnordal et al.[2]. Furthermore, a numerical validation of a gas-solid flow as described by Huber[3] and Huber and Sommerfeld[4,5] is also performed, in which a good agreement between calculations and measurements was obtained. Lastly, predictions of erosion depth and velocity distribution are compared with the obtained experimental data. Moreover, the influence of the degree of coupling and surface roughness on the results are analysed numerically in detail. The impact of the changes on surface roughness due to erosion on particle motion within the system and erosion itself is numerically demonstrated as well.

The numerical results highlight the ability of the coupled Euler-Lagrange approach in predicting gas-solid flows and reveal the importance of considering both inter-particle collisions and particle-wall interactions accounting for surface roughness. Although some discrepancies have been obtained, most of the numerical results are in reasonably good agreement with the experimental data acquired in the pneumatic conveying facility.

Contents

Nomenclature

Latin Symbols

a	Model parameter [-] in Equation (VI-1) and (V-58)
A, B, X, W, Y, Z	Model parameters [-]
A_p	Cross-section area of a sphere [m^2]
A_S	Surface element area [m^2]
b_1, b_2, c_1, c_2	Model parameters [-]
BH	Brinell Hardness [HB]
C	Empirical constant [-]
C_D	Drag coefficient [-]
$C\mu, c_{\varepsilon 1}, c_{\varepsilon 2}$	k-ε model constants
C_L	Constant for the calculation of the Eulerian length scale [-]
C_{lr}	Slip-rotation lift force coefficient [-]
C_{ls}	Slip-shear lift force coefficient [-]
c_p	Particle concentration [kg/m^3]
C_R	Rotational coefficient [-]
C_T	Constant for the calculation of the integral time scale of turbulence [-]
d_p, D_p	Particle diameter [m]
e	Normal restitution coefficient [-]
$E(\alpha)$	Dependence of erosion on particle impact angle [mm^3/kg]
E_{90}	Erosion damage at normal impact angle [mm^3/kg]
E_C	Cutting wear [m^3]
E_D	Deformation wear [m^3]
E_S	Total erosion ratio at each surface element area [m^3/kg]
E_i	Erosion caused by particle i [m^3/kg]
E_{PR}	Penetration ratio [m/kg]
f_c	Collision frequency [1/s]

$\vec{F}_D$	Drag force [(kg m)/s^2]
$\vec{F}_g$	Gravity force [(kg m)/s^2]
$\vec{F}_{lr}$	Slip-rotational lift force [(kg m)/s^2]
$\vec{F}_{ls}$	Slip-shear lift force [(kg m)/s^2]
$\vec{F}_P$	Buoyancy force [(kg m)/s^2]
F_s	Particle shape coefficient [-]
$F(\alpha), f(\alpha), (\alpha)$	Function of the impact angle [-]
$f(\Delta r)$	Longitudinal two-point correlation function [-]
$\vec{g}$	Gravitational acceleration [m/s^2]
$g(\Delta r)$	Transverse two-point correlation function [-]
H_p	Particle hardness [GPa]
H_t	Target material hardness [GPa]
Hv	Vickers hardness [GPa]
I_p	Moment of inertia for a sphere [kg m^2]
$\vec{J}$	Impulsive force vector [(kg m)/s]
J_x, J_y, J_z	Impulsive force components [(kg m)/s]
k	Turbulent kinetic energy [m^2/s^2]
K	Particle property factor [-] in Equation (V-79); Ratio of normal to tangential force [-] in Equation (V-81); Cut-off velocity [m/s] in Equation (V-86); Scaling parameter [-] in Equation (V-87)
k_1, k_2, k_3	Model parameter [-]
L	Distance of particle centres [m] in Equation (II-8); Lateral displacement [m] in Equation (V-56)
L_a	Non-dimensional lateral displacement [-]
L_E	Eulerian length scale [m]
m_p	Particle mass [kg]
$\dot{m}_f$	Fluid phase total mass flux [kg/s]
$\dot{m}_p$	Dispersed phase total mass flux [kg/s]
m_T	Total injected mass of erodent
M	Total mass of particles [kg]
$\vec{n}$	Unit vector [-]
N_i	Number of all particles in the size fraction i [-]
n_p	Particle concentration based on the number of particles [p/m^3]
n	Velocity exponent [-] in Equation (II-9) and (V-87);

	Diameter exponent [-] in Equation (II-10);
	Empirical parameter [-] in Equation (II-11) and (V-82)
n_1, n_2	Model parameters [-]
p	Model parameter [-] in Equation (V-80);
	Flow stress of the material surface [GPa] in Equation (V-81)
P	Mean pressure [Pa]
P_{coll}	Inter-particle collision probability [-]
P_{eff}	Effective roughness angle distribution function [°]
q_1, q_2	Model parameters [-]
r	Model parameter [-]
R_a	Arithmetic average height [µm]
$R_E(\Delta r)$	Eulerian correlation function [-]
Re_p	Particle Reynolds number [-]
Re_R	Reynolds number of particle rotation [-]
$R_L(\Delta t_L)$	Lagrangian correlation function [-]
RN	Uniform random number in the range [0,1] [-]
Re_s	Particle Reynolds number of the shear flow [-]
R_p	Particle radius [m]
RS_m	Mean spacing at the mean line [µm]
RS_i	Spacing between peaks [µm]
$R(St)$	Correlation function which depends on Stokes number [-]
S_ϕ	Source terms of the fluid phase
$S_{\phi p}$	Source terms due to phase interaction
St	Stokes number [-]
St_{Rel}	Relative Stokes number [-]
$\overline{S_{U,p}}$	Momentum source term [kg/(m^2 s^2)]
s_1, s_2	Model parameters [-]
t	Time [s]
τ_{coll}	Average time between inter-particle collision [s]
t_{cv}	Time required for a particle to cross a control volume [s]
Δt_E	Eulerian time step [s]
T_i	Torque acting on the rotating particle [N m]
t_L	Lagrangian time step [s]
T_L	Lagrangian integral time scale of turbulence [s]
U_f	Fluid bulk velocity [m/s]
u_p	Particle velocity [m/s]

u'_p	Particle velocity fluctuation [m/s]
$\bar{u}_{p,i}$	Local mean particle velocity [m/s]
u_{R1}	Velocity of the particle surface in relation to the contact point [m/s]
u_R, u_{Ry}, u_{Rz}	Relative velocity components of the particle in relation to the contact point [m/s]
V	Volume [m^3]
V_{cv}, V_c	Cell volume [m^3]
V_p	Particle volume [m^3] in Equation (II-1); Particle impact velocity [m/s] in Equation (V-82)
v_p, u_P, w_P	Particle linear velocity components (x, y, z) [m/s]
XX, ZZ	Random numbers in the range [0,1]
x_p	Coordinates of particle position [m]
Y_c	Radial distance of the boundary particle trajectory [m]
y_i	Height [µm]

Greek Symbols

$\alpha, \alpha_1, \alpha_0$	Particle impact angle [°]
$\sigma_\varepsilon, \sigma_k$	k-ε model constants
α_f	Fluid volume fraction [-]
α_p	Particle volume fraction [-]
β	Model parameter [-]
η	Particle mass loading [-]
η_p	Impact efficiency [-]
ρ_p	Particle density [kg/m^3]
ρ_f	Fluid density [kg/m^3]
π	Pi [-]
ϕ	Represents a transport variable in Equation (V-1); Particle sphericity in Equation (V-13); Inter-particle collision angle in Equation (V-57)
ϕ_C	Cutting coefficient [(N m)/m^3]
Γ	Effective transport tensor
ε	Turbulent dissipation rate [m^2/s^3]
ε_C	Deformation coefficient [(N m)/m^3]

ϵ_x, ϵ_z	Factors which indicate the proportion and direction of the motion of the particle surface with respect to the wall [-]
μ_f	Dynamic fluid viscosity [kg/(s m)]
μ_d	Dynamic friction coefficient [-]
μ_s, μ_0	Static friction coefficient [-]
μ_T	Turbulent viscosity [kg/(s m)]
ψ	Ratio of the depth of contact to the depth of cut [-]
γ	Roughness angle [°]
$\Delta\gamma_0$	Initial standard deviation of the roughness angle [°]
$\Delta\gamma$	Standard deviation of the roughness angle [°]
$\vec{\tau}$	Fluid shear stress [N/m^2]
τ_p	Particle response time [s]
δ_{ik}	Kronecker-delta [-]
$\vec{\omega}_f$	Fluid vorticity [rad/s]
$\vec{\omega}_p$	Particle angular velocity [rad/s]
$\omega_P^x, \omega_P^y\ \omega_P^z$	Particle angular velocity components [rad/s]
$\vec{\Omega}$	Relative rotation [rad/s]
ξ	Gaussian random number
σ_e	Standard deviation of the normal restitutio coefficient [-]
σ_F	Rms value of the fluid velocity fluctuation [m/s]
σ_p	Local rms-value of the particle velocity fluctuation [m/s]
Δr	Spatial distance between the virtual fluid element and the Lagrangian particle during the time step [m]

List of Figures

List of Tables

Chapter I

Introduction

1.1. Background and Thesis Overview

Particle transport in industry is commonly accomplished through pneumatic conveying systems. Such systems are found in numerous industrial areas such as chemical, pharmaceutical, food, mining, paint production, agriculture, metal refining and energy production. The application of this technique for the transport of solids is advantageous because it usually requires low maintenance and offers high flexibility and safety, besides being considered a cleaner technique compared to mechanical transport techniques. However, this method has disadvantages such as low energy efficiency and it usually requires larger dust collection systems and some materials are difficult to transport.

In addition to these disadvantages, erosion associated with numerous particle impacts on pipe walls, especially bends, is a major industrial problem. This degradation process, simply referred to herein as erosion or solid particle erosion, is also present in industrial processes and equipment such as cyclone separators, fluidized beds, valves, coal and hydraulic turbines and in the catalytic cracking of oil. Erosion causes industries not only to spend a lot of money on

maintaining or replacing damaged equipment, but also to lose profits due to sudden stops in the manufacturing process. Moreover, environmental health and safety may be threatened due to the possibility of leaking hazardous chemicals or powders through damaged equipment and pipes. Alternatively, erosion is a beneficial phenomenon in other processes, e.g. sandblasting, abrasive deburring and surface roughening.

The extent of erosion damage to materials depends on several parameters including properties of the target material and erosive particles, particle impact characteristics and operating conditions. Therefore, it is of great importance for engineers to appropriately understand the influence of these parameters on erosion to properly design industrial processes which may involve severe erosion. In addition, it is essential that industries and the scientific community develop strategies for estimating erosion rates in industrial processes to predict potential failures and the lifetime of pipelines and equipment to avoid environmental problems and to ensure the safety of their employees.

Since 1960, solid particle erosion has been thoroughly analysed experimentally, leading to the development of several models to estimate erosion considering various parameters. The development of these models is based on material removal mechanisms, which mainly depend on particle impact angle, particle shape and the type of target material (ductile or brittle). Although several models are available, the applicability of these models is generally restricted to specific operating conditions and certain combinations of target material and erodent particle, which often leads to inaccurate erosion rate predictions. Hence, the high variety of models often requires engineers and researchers to perform extensive testing and comparisons with experimental data to determine which model best suits the process under analysis. Consequently, experimental techniques represent an indispensable tool in developing models and methods for estimating and preventing solid particle erosion. Nevertheless, experimentally estimating erosion rate in industrial processes and equipment can be a complex task due to the geometric complexity of industrial equipment.

In recent decades, with the rapid technological advance in computational power, coupled with the improvement of numerical techniques and the development of more accurate mathematical models to represent physical phenomena, the use of computational fluid dynamic (CFD) techniques has been expanding rapidly. The advantages of numerical computation

compared to experimental investigations lie in the fast and cost-effective performance of numerical parameter studies, so that the effect of the various parameters on the considered process can be systematically investigated. These advances are the reason why numerical computing methods are increasingly used for the design and optimization of practical and industrial processes.

In this context, a powerful tool which enables accurate simulation of dispersed two-phase flows in pneumatic conveying systems and complex equipment and geometries is the application of the coupled Euler-Lagrange approach (point-particle). It allows to accurately predict the dispersed phase motion by tracking each individual particle through the flow field considering particle-wall and particle-particle interactions, among other elementary phenomena. Therefore, Lagrangian tracking provides insight into the impact velocity and angle of each particle which allows for the estimation of erosion rates when combined with a robust erosion model and the correct physical properties of the target material and erodent particle. Furthermore, CFD erosion assessment has the advantage that different parameters influencing erosion can be analysed separately.

The motivation for this PhD project is to obtain a systematic understanding towards numerical and experimental predictions of solid particle erosion in gas-solid flows, focusing on pneumatic conveying systems, which involves applying a combination of experimental and numerical techniques. Experimental techniques include the use of ultrasonic technology to perform erosion studies on bends, the application of an optical method to assess surface roughness of materials exposed to erosion, and the use of methods for determining continuous and dispersed phase velocities. Numerical techniques consist of predicting erosion rates and dispersed two-phase flow behaviour in pneumatic conveying systems based on the application of the coupled Euler-Lagrange approach, and encompassing the implementation of erosion models and elementary phenomena with subsequent validation of the results obtained by comparing them with experimental data.

1.2. Objective and Scope of the Thesis

The central objective of this PhD project is to perform experimental and numerical studies on solid particle erosion in gas-solid flows in order to provide a better understanding of the erosion phenomenon and to quantify the surface roughness variation. This is achieved by conducting a series of integrated steps as described in the following scope of research:

- to perform solid particle erosion studies in an impingement jet facility to evaluate the influence of particle impact angle, particle shape and erosion time on surface roughness of different materials;

- to develop an empirical correlation to express the relationship between surface roughness variation, particle impact angle and particle shape, and clarify the impact of those parameters on surface roughness;

- to design a pneumatic conveying system to obtain erosion profiles and maps on geometrically distinct bends and to measure continuous and dispersed phase velocity profiles prior to the bends, considering different particle mass loading and particle shape;

- to extend a transient, three dimensional CFD solver based on the coupled Euler-Lagrange approach to account for:

    1) all relevant forces acting on the particles,

    2) the turbulent dispersion of particles via a single Langevin equation,

    3) particle-wall interactions with rough surfaces,

    4) a stochastic modelling approach for particle-particle interactions.

- to validate the capability of the extended CFD solver to predict gas-solid flows in pneumatic conveying systems using available experimental data.

- to implement and validate available solid particle erosion models by comparing

numerical predictions with experimental data obtained in the designed pneumatic conveying system, as well as with experimental data available in the literature.

- to numerically analyse the influence of coupling degree (one-, two- and four-way coupling), parameters related to particle-wall interaction, particle mass loading and particle shape on solid particle erosion predictions and dispersed phase flow behaviour.

- to numerically investigate the effects of surface roughness variation due to solid particle erosion on numerical prediction of erosion and dispersed phase flow behaviour.

All numerical calculations and implementation of additional models, as previously described, were performed by using the free and open-source CFD code OpenFOAM® 4.1. OpenFOAM has the advantage of allowing the user to modify and include new models into its source code as needed, making OpenFOAM the most suitable CFD code for the development of this PhD project. Additionally, OpenFOAM is widespread in the scientific and academic fields, with growing use in industry and its basic libraries are continuously improved and extended by its developers.

1.3. Thesis Structure

For better readability, this thesis in divided into nine chapters as follows:

- Chapter I – This chapter provides a background to the subject area and details the objective and scope of the research. The organisation of the thesis is presented in this chapter as well;

- Chapter II – This chapter is divided into two main sections, which cover the theoretical foundation of dispersed two-phase flows and solid particle erosion. The first section enlightens important definitions used to characterize dispersed two-phase flows and presents related experimental and numerical work. The second section explains the fundamentals of solid particle erosion, which includes a description of most relevant parameters influencing erosion, existing erosion mechanisms and ripple formation on ductile materials, and a summary of numerical studies involving solid particle erosion;

- Chapter III – The experimental methodology and techniques applied to evaluate the influence of particle impact angle, particle shape and erosion time on surface roughness of different ductile materials are introduced in this chapter. The experimental facility and the properties of the particles and materials used in the current work is also detailed. Moreover, the measurement and assessment of surface roughness as well as the techniques applied to measure the continuous and dispersed phase velocities are described.

- Chapter IV – This chapter presents the methodology and experimental techniques used to acquire erosion profiles and maps on bends and to measure the continuous and dispersed phase velocities prior to the bends. The pneumatic conveying system and particle properties used are initially introduced. Then, the non-intrusive ultrasonic technology applied to perform erosion measurements is explained. Finally, the laser-doppler anemometry and laser-light sheet techniques are presented.

- Chapter V – This chapter is devoted to summarizing the numerical approach adopted in the present work, which is based on the transient, three-dimensional and coupled Euler-Lagrange approach. The governing equations which describe the continuous and dispersed phase flow behaviour are presented together with a brief description of all relevant forces acting on the particles. Then, the coupling between the continuous and dispersed phase and a turbulent dispersion model are introduced. Next, a stochastic approach to account for particle-wall interaction with rough surfaces and particle-particle interaction is presented in detail. Finally, all the erosion models used in this work are detailed.

- Chapter VI – Experimental data relating the influence of particle impact angle, particle shape and erosion time on surface roughness of the considered materials are presented and discussed in this chapter. Furthermore, an empirical correlation which expresses the surface roughness dependence on these parameters is developed for each material. Continuous and dispersed phase velocity profiles are presented and discussed as well.

- Chapter VII – A numerical validation based on experimental data available in the literature for a pneumatic conveying system is demonstrated in this chapter. The

numerical setup as well as the comparison between numerical and experimental results are presented. Additionally, five erosion models are validated with two additional cases available in the literature.

- Chapter VIII – This chapter covers the experimental results obtained in the pneumatic conveying system which are then compared with the numerical calculations performed. In addition to the numerical setup, a grid independence test is also presented. Besides the validation of the single-phase flow calculations, simulations of dispersed phase and erosion predictions are compared with experimental data regarding the influence of coupling degree, particle-wall interaction parameters, particle mass loading and particle shape.

- Chapter IX – Conclusions and suggestions for future work are presented in this chapter.

Chapter II

Literature Review

This chapter details the fundamentals needed for a better understanding of dispersed two-phase flows and solid particle erosion. Initially, important properties of dispersed two-phase flows as well as an overview of numerical and experimental studies related to gas-solid flows in pneumatic conveying systems are presented. In the following, the erosion phenomenon is described including the influence of parameters on erosion, erosion mechanisms and ripple formation, and numerical studies involving solid particle erosion. It should be noted that erosion models are presented in Chapter V, Section 5.9.

2.1. Dispersed Two-Phase Flow

Dispersed two-phase flows are encountered in several technical and industrial processes, as for example in production and transportation of solid particles, chemical engineering and biotechnology. In this kind of flow, one of the phases is present in the form particles, droplets or bubbles dispersed in a continuous carrier phase which may be gas or liquid, as illustrated in Figure II-1 (a). In addition, separated flows (i.e. stratified flows, slug flows, or film flows) are typical in industrial practice as well. Such flows are visualized in

Figure II-1 (b). For instance, stratified and slug flows are encountered in conveying pipes for crude oil, and, moreover, the observed flow regime depends on the spatial orientation of the pipeline. Relevant interfacial transport mechanisms are different for these distinct type of multiphase flows and, consequently, different numerical approach have to be applied[6].
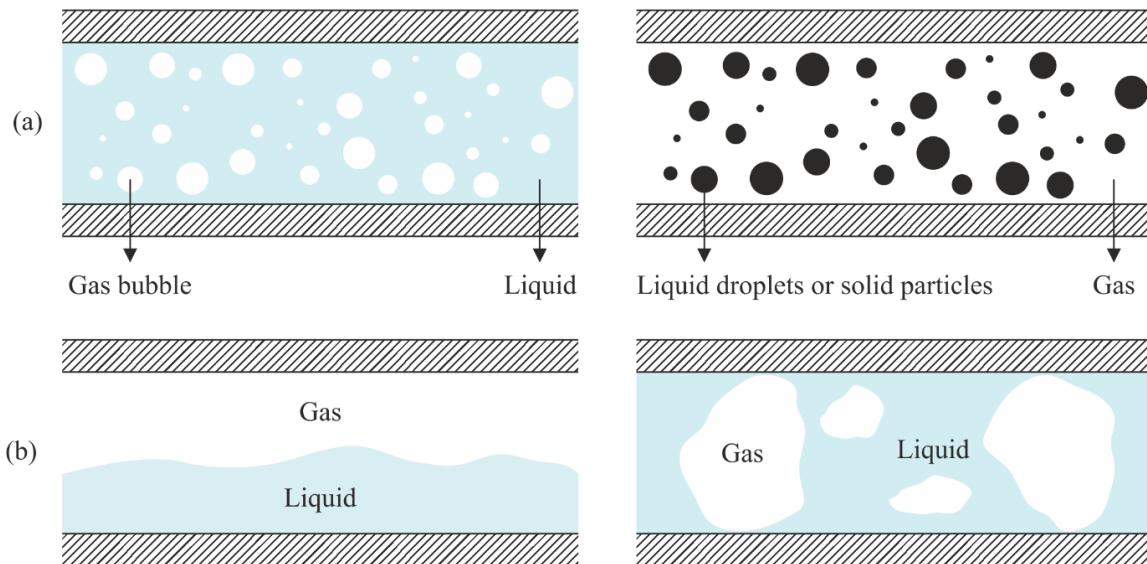
Figure II-1. Different regimes of two-phase flows: (a) dispersed two-phase flow and (b) separated two-phase flow. Source: adapted from Sommerfeld et al[6].

Dispersed two-phase flows may be classified with respect to different phases involved and Table II-1 summarizes some of the most import industrial processes where dispersed two-phase flows are present.

Table II-1. Overview of important industrial and technical applications of two-phase flows (Sommerfeld et al.[6]).

Continuous Phase	Dispersed Phase	Application
Gas	Solid	Pneumatic conveying, particle separation in cyclones and filters, fluidised beds
Liquid	Solid	Hydraulic conveying, liquid-solid separation, particle dispersion in stirred vessels
Gas	Droplet	Spray drying, spray cooling, spray painting, spray scrubbers
Liquid	Gas	Bubble columns, flotation

Several properties may be defined to characterize dispersed two-phase flows and the most relevant as regards to this work are briefly summarized below according to Sommerfeld

et al[6] and Crowe et al.[7]. Fluid and dispersed phase interaction mechanisms depend on the volume fraction of particles α_p within a control volume V, which is defined as:

$$\alpha_p = \sum_i N_i V_{p,i}/V \tag{II-1}$$

where N_i is number of all particles in the size fraction i having a particle volume $V_{p,i} = \pi d_{p,i}^3/6$. The sum of the volume fractions of all phase is equal to one whether more phases are involved and therefore, in the case of a two-phase flow, the volume fraction of the fluid phase α_f is specified as:

$$\alpha_p + \alpha_f = 1 \tag{II-2}$$

$$\alpha_f = \left(1 - \sum_i \alpha_{p,i}\right) \tag{II-3}$$

Additionally, the bulk density or concentration of the dispersed and fluid phase are given by:

$$\rho_p = c_p = \alpha_p \rho_p \tag{II-4}$$

$$\rho_f = (1 - \alpha_p)\rho_f \tag{II-5}$$

with ρ_p and ρ_f being the density of the dispersed and fluid phase, respectively. Particle concentration n_p may also by expressed as the number of particles N_p per unit volume:

$$n_p = \frac{N_p}{V} \tag{II-6}$$

The term particle mass loading η is often used to describe gas-solid flows and is defined as the total mass flux of the dispersed phase to that of the fluid:

$$\eta = \frac{\alpha_p \rho_p u_p}{(1 - \alpha_p)\rho_f U_f} = \frac{\dot{m}_p}{\dot{m}_f} \tag{II-7}$$

where $\dot{m}_p$ and $\dot{m}_f$ are respectively the total mass flux of the dispersed and fluid phase. u_p and U_f are bulk velocities of dispersed and fluid phase, respectively. The mass flux is a vector quantity and can also be defined as a local property. Also, an overall mass loading of the system may be defined as the total mass flow rate of the dispersed phase flow to the total mass flow rate of the continuous phase.

Another important parameter is the inter-particle spacing which represents the average distance between particles in two-phase flow systems. The inter-particle spacing is related to the volume fraction of the dispersed phase and may be estimated in the case of a regular, cubic arrangement of particles as follows:

$$\frac{L}{d_p} = \left(\frac{\pi}{6\alpha_p}\right)^{1/3} \tag{II-8}$$

where L is the distance of the centres of particles. For instance, the inter-particle spacing is 1.74 diameters for a volume fraction of the dispersed phase of 10%, which means that particles are too close to each other to be treated as isolated and therefore, fluid dynamic interactions become of importance (Sommerfeld et al.[6]).

Dispersed two-phase flows may be classified in terms of the importance of interaction mechanisms between fluid and dispersed phases, as provided by Elghobashi[8] and presented in Figure II-2 according to Sommerfeld et al.[6]. Depending on the volume fraction and inter-particle spacing, dispersed two-phase flows are generally characterized as dilute or dense flows, in which different interaction phenomena become meaningful. A two-phase system is commonly regarded as dense for volume fractions higher than $\alpha_p = 10^{-3}$ or an inter-particle spacing smaller than $L/d_p \approx 8$. In the first regime, defined by $\alpha_p < 10^{-6}$ and $L/d_p > 80$, the influence of the dispersed phase on the fluid phase may be neglected, which is referred to one-way coupling. In the second regime, i.e. $10^{-6} < \alpha_p < 10^{-3}$ and $8 < L/d_p < 80$, momentum transfer from the dispersed to the fluid phase is large enough to alter the flow characteristics and need to be accounted for. This interaction mechanism is named as two-way coupling. The third regime is characterized by high volume fractions and low inter-particle spacing ($\alpha_p >$

10^{-3} and $L/d_p < 8$) and therefore, particle-particle interaction becomes of importance, thus the term four-way coupling.

Inter-Particle Spacing L/d_p

| 100 | 10 | 1 |

| One-way Coupling $L/d_p > 80$ | Two-way Coupling $L/d_p > 8$ | Four-way Coupling $L/d_p < 8$ |

Dilute Dispersed Two-Phase Flows

Dense Dispersed Two-Phase Flows

| 1E-8 | 1E-7 | 1E-6 | 1E-5 | 1E-4 | 1E-3 | 1E-2 | 1E-1 | 1 |
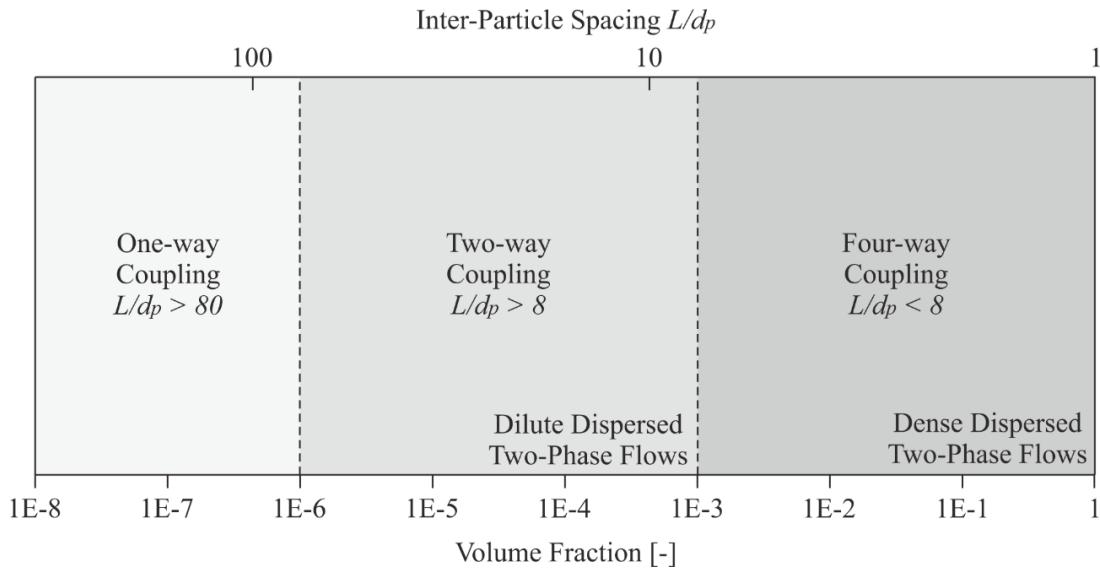
Volume Fraction [-]

Figure II-2. Regimes of dispersed two-phase flows as a function of particle volume fraction. Source: adapted from Sommerfeld et al.[6] and Elghobashi[8].

Studies of Pneumatic Conveying Systems

This section provides a brief summary of some numerical simulations based on the Euler-Lagrange approach and experimental research related to pneumatic conveying systems. Sommerfeld[9] numerically demonstrated an improvement in numerical simulations of turbulent gas-solid flows by including lift forces due to shear flows and particle rotation. Also, the analysis showed that considering an irregular bouncing model which accounts for wall roughness and asphericities in the particle shape results in a better agreement between numerical and experimental data with respect to the fluctuating velocity of particles.

Huber and Sommerfeld[5] performed numerical simulations based on the fully coupled Euler-Lagrange approach in connection with the standard k-ε epsilon turbulence model and all relevant forces such as drag, gravity/buoyancy and transverse lift due to shear and particle rotation were considered. Particle-wall and particle-particle interaction were modelled via a stochastic approach and the influence of wall roughness on wall collision was accounted for. The effects of wall roughness, inter-particle collisions and turbulence were analysed for a

dispersed gas-solid flow in different pipe configuration. Validation was performed by comparison with experimental data and a good agreement was obtained. It was demonstrated that wall roughness reduces the effect of gravitational settling and results in a considerable increase in the pressure drop in a horizontal pipe. In addition, as a result from wall roughness effects, a secondary gas flow was developed in the pipe cross-section. Moreover, it was found that even for relatively low particle mass loading, inter-particle collisions should be considered for a proper prediction of particle mass flux profiles. Finally, regions of high particle concentration are dispersed due to inter-particle collisions and therefore, gravitational settling is reduced.

A meticulous experimental analysis was conducted by Kussin and Sommerfeld[10] in a particle-laden horizontal channel flow with different wall roughness. Phase-Doppler anemometry was applied for simultaneous determination of air and particle velocity and the influence of several parameters were considered, such as conveying velocity, particle size and particle mass loading. The work revealed several aspects regarding channel flows. The average particle velocity was reduced with increasing particle size. An enhancement in the transverse dispersion of the particles across the channel and in wall collision frequency was observed when rough walls were considered. Additionally, the rms components of the particle velocity in the stream-wise and transverse directions were increased due to wall roughness. A damping was observed in both fluctuating velocity components with increasing particle mass loading as a result from the dissipation energy associated with the increase in inter-particle collision frequency. Furthermore, the transverse dispersion of the particles in the channel was improved because of inter-particle collisions, which resulted in a more uniform particle concentration distribution and in a reduced gravitational settling. Additionally, gravitational settling was found to be more effective for the case with low wall roughness, low particle mass loading and small conveying velocity.

Laín et al.[11] carried out detailed experiments in a particle-laden horizontal channel flow with particles with different size and particle mass loading by using phase-Doppler anemometry. Experimental data was used for the validation of the numerical approach applied, which is based on the fully coupled Euler-Lagrange approach. Turbulence was modelled by the Reynolds-stress model and the dispersed phase was computed considering all relevant

effects, such as turbulent dispersion, transverse lift forces, wall collisions with rough walls, and inter-particle collisions. The mean and fluctuating velocity components of the particles were compared to experimental results and a reasonably good agreement was achieved. The effects of wall roughness and inter-particle collisions were found to be of great importance in predicting particle phase properties. Also, inter-particle collisions redistribute the fluctuating velocity component of particles and contribute to an enhancement in the turbulent kinetic energy of the continuous phase.

Sommerfeld and Kussin[12] experimentally analysed the influence of particle size, mass loading, and wall roughness on particle velocity and concentration profile in a horizontal channel flow for a given conveying velocity. In addition, pressure loss measurements along the channel were performed. Measurements confirmed that a more uniform distribution of particles across the channel is obtained with increasing wall roughness and particle size as a result from the so-called shadow effect, in which momentum is transferred from the tangential to the normal particle velocity component. Moreover, changes in the particle concentration profile due to wall roughness effect are reduced with increasing particle size. Particle velocity distributions were found to be broadened with increasing wall roughness, which implies in a significant enhancement of the transverse particle velocity fluctuation yielding an increase in the wall collision frequency as a consequence of the reduction in the wall collision mean free path. Consequently, higher roughness results in larger slip velocity and higher pressure loss by the particles. Additional pressure loss is also observed with increasing particle mass loading and particle size. Finally, slip velocity and particle velocity fluctuation increased with particle size.

Laín and Sommerfeld[13] presented a comparison of numerical simulations of a dilute gas-solid flow in a 6 m long horizontal channel with experimental data. Calculations were performed based on the Euler-Lagrange approach using a Reynolds Stress turbulence model for the gas phase and accounting for two-way coupling. Particle-wall and particle-particle interaction were considered as well. It was shown that the additional pressure loss by the particles increases with particle size, particle mass loading and wall roughness, mostly as a result from increased particle-wall collision frequency. These trends were also observed in experiments. In addition, dispersed phase calculations for the particle velocity fluctuations

reasonably captured the behaviour observed experimentally for low, intermediate and high wall roughness. Finally, a good agreement was also obtained with the experiments for the predicted mean gas and particle velocities.

Numerical calculations were carried out by Laín and Sommerfeld[14] and compared with experimental data to investigate the development of a dilute phase flow in a 6 m horizontal channel and horizontal circular pipe with the same hydraulic diameter. The fully coupled Euler-Lagrange approach was applied in combination with the k-ε and Reynolds Stress turbulence models for the gas phase. Particles were tracked accounting for all relevant forces including drag, gravity/buoyancy, slip-shear and slip-rotational lift. Elementary phenomena such as turbulence effects on particle motion, particle-wall interactions with rough walls and inter-particle collisions were incorporated in the modelling approach. The so-called focusing effect was observed in the horizontal pipe with higher wall roughness, whereby particles are bounced back towards the core of pipe cross-section after colliding with its curved wall. The focusing effect was found to be more effective when inter-particle collisions are neglected, as the effect of particle dispersion is larger due to inter-particle collisions. Larger particle dispersion results in an increase in the wall collision frequency and consequently, in higher momentum loss, which increases the pressure loss by the particles. The pressure drop for the case with higher wall roughness was found to be remarkably higher in the pipe than in the channel. The focusing effect causes also a secondary flow in pipes to appear as result of the momentum transfer to the gas phase, which consists of two circulation regions in the case with low roughness, i.e. particle are mainly bouncing with the lower section of the pipe. Particle dispersion is higher for higher wall roughness and the focusing effect also occurs from the upper pipe wall producing four counter-rotating circulation zones. Although the intensity of the secondary flow observed is rather weak, instabilities may be expected in transient calculations. Finally, comparison between both turbulence models showed similar results.

Sommerfeld and Laín[15] applied the steady state, fully coupled Euler-Lagrange approach in connection with the standard k-ε model to evaluate parameters influencing dilute-phase pneumatic conveying in pipe systems. The dispersed phase was rigorously modelled by including all relevant fluid dynamic forces (i.e. drag, gravity/buoyancy, slip–shear lift force and slip–rotational lift force), particle-wall collisions with rough walls and inter-particle

collisions. The system was composed of a 5 m horizontal pipe, a 90° bend and a 5 m vertical pipe with a diameter of 150 mm. It was found that particle-wall and particle-particle interactions have major influence on the development of two-phase flow structure in pipe systems, especially with respect to particle concentration distribution. Also, the transport of particle through horizontal pipes is mainly governed by gravitational settling and turbulence, which means that very small particles may be well dispersed over the pipe-cross section while large particles are dispersed due to wall collisions as a result of their inertia. Additionally, it was demonstrated that due to inter-particle collisions, particles tend to be trapped within a dust rope which is formed in the bend due to centrifugal effects. This dust rope is completely disintegrated in the vertical pipe for large particles mainly due to their inertia and wall collisions. Finally, the pressure drop by the particles increases with increasing particle size.

2.2. The Erosion Phenomenon

According to Bitter[16], solid particle erosion is referred to as the wear resulting from the impact of free-moving particles on a solid, a process which causes the solid material to deform, fracture or be removed completely. The term solid particle erosion, or simply erosion, will be freely used throughout the document. Additionally, it should be noted that erosion data is reported differently depending on the investigators. Erosion rate is usually expressed as mass, volume or thickness loss of material per unit of time, such as kg/hr, mm^3/hr or mm/yr. Erosion ratio is generally referred to mass, volume or thickness loss of material per mass of impacting particle, e.g. kg/kg, mm^3/kg or mm/kg. The term penetration ratio is commonly used as well to express thickness loss per mass of impacting particle. Absolute or total erosion/penetration is defined only as the total mass, volume or thickness loss of material. More details about predictive equations are given in Section 5.9 as well.

The Influence of Parameters on Erosion

Solid particle erosion is a complex phenomenon as it depends on numerous parameters which are generally classified into erodent particle properties, target material properties and fluid properties. Due to the dependence of erosion on such parameters, erosion modelling and

prediction in gas-solid, liquid-solid or gas-liquid-solid flows is very challenging. Therefore, great effort has been put by investigators over the past decades to understand erosion mechanisms and which parameters influence erosion the most. The list of parameters influencing erosion and considered in erosion modelling is quite long and a review of all those parameters is not attempted here. For instance, Meng and Ludema[17] provided a detailed review of erosion models up to 1995 and Parsi et al.[18] up to 2014. The former highlighted 33 physical parameters used in erosion models while the latter 35. Also, Lyczkowski and Bouillard[19] provided similar review but focusing on erosion modelling in fluidized-bed systems. Thus, the most important parameters affecting solid particle erosion are briefly described in the following.

Particle Impact Velocity

It is well known that particle impact velocity strongly influences erosion. Finnie[20] proposed that mass loss by solid particle impacts is proportional to the particle impact velocity and follows a power law relationship:

$$mass\ loss \propto \vec{u}_p^n \tag{II-9}$$

Finnie suggested a theoretical velocity exponent of $n = 2$ by obtaining good agreement between experiments on several metals and his model. Additionally, several authors achieved good erosion predictions by using a velocity exponent of 2 (Bitter[16,21], Neilson and Gilchrist[22], Hutchings[23], Tilly[24], and Sundararajan[25]). Although a value of 2 for the velocity exponent is well accepted and generally produces good erosion predictions, investigators have reported different values as well. For instance, Sheldon and Finnie[26] analysed erosion on brittle materials at normal impact angle and reported velocity exponents of 3.2, 2.72 and 2.66 depending on the eroded material. Sundararajan and Shewmon[27] predicted a velocity exponent of 2.5. by eroding metals with particles at normal incidence angle. A value of 2.4 was derived by Wiederhorn and Hockey[28] based on their analysis of the influence of material parameters on brittle erosion. Additionally, according to Sheldon and Kanhere[29], the velocity exponent is typically between 2 and 3 for metallic materials. The deviation from the theoretical value of 2 is due to the influence of other impact conditions and material properties on solid particle

erosion. For example, Oka et al.[30,31] and Oka and Yoshida[32] derived such velocity exponent as a function of eroded material hardness. Nonetheless, the velocity exponent was found to be independent of both target material properties and erosion mechanism by Lindsley and Marder[33], yet is highly dependent on test conditions, including particle properties and erosion test apparatus as well. In their work, a value of 2.9 was obtained.

Particle Impact Angle

The relative angle at which particles impact the surface of the target material is an essential parameter in modelling solid particle erosion and describes the nature of erosion mechanisms as well. However, erosion mechanisms are also coupled with the type of material considered. As stated by Bitter[16,21] in relation to ductile materials, cutting wear is predominant at shallow impact angles while deformation wear is dominant at high impact angles. Therefore, ductile materials generally suffer from high erosion rates at shallow impact angles ranging from 20° to 40° whilst low erosion rate is observed at normal incidence angle. In contrast, brittle materials experience maximum erosion rate at impact angles close to 90°. The dependence of erosion on particle impact angle for ductile and brittle materials is illustrated in Figure II-3 according to Humphrey[34].
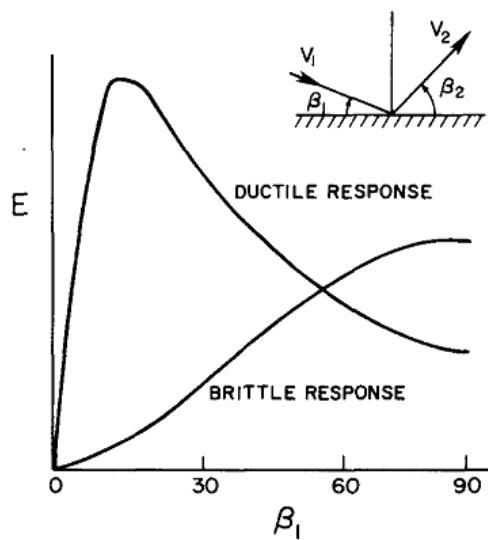
Figure II-3. Typical influence of particle impact angle β_1 on solid particle erosion E for ductile and brittle materials. Source: Humphrey[34].

Particle Size

The effect of particle size on erosion predictions is additionally a vital parameter as large particles travelling with the same velocity as small particles possess higher kinetic energy, which may result in higher erosion rate upon impacting with the material surface. According to Finnie[35,36] and the experimental data from Tilly and Sage[37], erosion rate is found to be nearly independent of particle size for particles larger than approximately 100 µm. In contrast, erosion rate is reduced as particle size is decreased bellow this size. A schematic relationship between erosion rate and particle size is shown in Figure II-4 as presented by Dundar and Inal[38], in which d_c represents a critical particle size above which erosion rate stabilizes. Nevertheless, the critical particle size generally assumes a different value depending on the investigator. Lynn et al.[39] performed slurry erosion tests for wide range of particle size, i.e. between 20 and 500 µm. It was demonstrated that the reduction of erosion rate with decreasing particle size for suspensions of constant solid loading reflects the reduction in the collision efficiency, i.e. number of particles impacting the surface, as well as in the particle impact velocity.
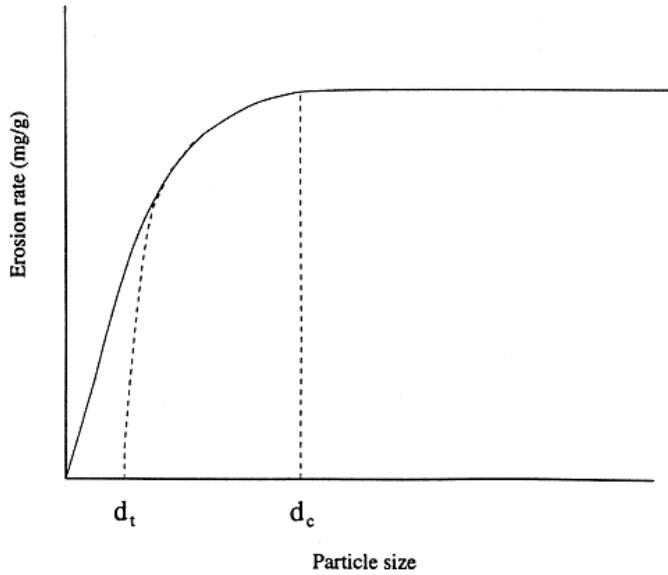
Figure II-4. Relationship between erosion rate and particle size. Source: Dundar and Inal[38].

According to the experimental work from Desale et al.[40], which analysed the effect of particle size of silica sand in the range of 37.5 to 655 µm on erosion rate of aluminium 6063,

erosion rate increases when increasing particle size at a constant particle concentration (wt%), although the number of impacts and particles is reduced and the kinetic energy is increased. Additionally, Desale et al.[40] and other researchers proposed that the relationship between erosion rate and particle size follows a power law function in the form as presented below:

$$erosion\ rate \propto D_p^n \qquad\qquad\qquad (II\text{-}10)$$

where the exponent n may vary in the range of 0.3 and 2.0 according to material properties, test conditions, size distribution and particle size (Desale et al.[40]).

Nevertheless, several researchers obtained a linear relationship between erosion rate and particle size (Elkholy[41], Clark[42], Gandhi and Borse[43]). Furthermore, several other parameters such as target material properties, particle size distribution, particle impact velocity, inter-particle collisions, experimental conditions, and fluid properties have shown influence on the relationship between erosion rate and particle size (Parsi et al.[18]).

Particle Shape

As will be discussed in the Section *Erosion Mechanisms*, different erosion mechanisms are observed according to particle shape. The ploughing and deformation mechanisms are most effective with spherical particles, while cutting is the dominant mechanism with angular particles. Levy and Chik[44] carried out erosion tests on AISI 1020 carbon steel at a velocity of 80 m/s at impact angles of 30° and 90° using angular and spherical particles. Results showed that erosion by angular particles were four times larger than by spherical particles. Liebhard and Levy[45] analysed experimentally the influence of several particle parameters including shape, mass, size, impact velocity and feed rate on erosion of 1018 steel using spherical glass beads and angular SiC. The erosion results demonstrated an increase of an order of magnitude in erosion with angular particles compared to spherical particles.

Besides, it is observed that the angle of maximum erosion changes due to particle shape. For instance, Roy et al.[46] explored the effect of particle shape on erosion of Cu, Cu-5.3Al and Cu-20Zn at two different particle impact velocities and impingement angles of 30° and 90°. Cu and its alloys presented ductile response when angular particles were used, i.e.

maximum erosion at oblique angles. Alternatively, a brittle response characterized by maximum erosion at normal impact angle was observed when spherical particles were employed.

Particle Concentration

The concentration of abrasive particles in a fluid stream is also an important parameter which affects the amount of material removal during solid particle erosion. It is naturally expected that by increasing the concentration of abrasive particles, erosion ratio (mass of material removed from the surface per unit mass of particles impacting the wall) increases accordingly as a larger number of particles impact on the target surface. Nevertheless, several investigators have shown that this is not entirely true. It should be noted that even though erosion ratio may decrease with increasing particle concentration, the absolute erosion increases.

Uuemŏis and Kleis[47] reported a decrease in the erosion ratio of metals, alloys and ceramics with increasing particle concentration. Additionally, the authors concluded that the effect of particle concentration on erosion ratio depends on particle velocity, angle, strength and size. Concentration effects were reported as larger for higher particle impact velocity and angle. Also, erosion by quartz sand particles led to a higher increase in the concentration effects than by cast iron particles. Additionally, changes in the erosion ratio due to the increase in the particle concentration was bigger whether small particles were considered. They suggested that when increasing particle flux, particle-particle collisions act as a shield which protects the material surface from particles travelling towards the surface.

By analysing inter-particle collisions in a sand-blast test rig using high-speed photography considering glass spheres as erodent particles, Andrews and Horsfield[48] demonstrated that particle-particle interactions introduces randomness into particle velocity and final impact angle when striking the target. Therefore, the reduction in erosion ratio for high particle concentration is a result of changes in the particle impact velocity and angle due to collisions and is not attributed to collisions reducing the number of particles colliding with the target.

Anand et al.[49] experimentally analysed the influence of erodent particle flux on erosion ratio for a range of different erosion conditions, in which erosion decreased significantly with increasing particle flux. Their research also sustained the fact that by increasing particle flux results in a shielding effect of the target surface by rebounding particles from the target surface. Turenne et al.[50] investigated the effects of sand concentration on erosion ratio by performing slurry erosion tests and concluded that erosion decreases following a power law of the sand volume fraction with an exponent of about one-third.

Moreover, the effect of particle concentration on erosion ratio of mild steel bends was examined by Deng et al.[51] in a pneumatic conveying system. It was reported a substantial reduction in the erosion ratio for high particle concentrations, which rises from the shielding effect resulting from particle-particle interaction. Their work additionally showed that the reduction in the erosion ratio due to high particle concentration has a stronger relationship in conveying systems than in erosion testers.

Conclusively, inter-particle collisions play a significant role in predicting erosion in pneumatic conveying systems, for instance, especially whether high particle concentration is considered. Therefore, in the scope of this thesis, a stochastic particle-particle interaction model is introduced in Chapter V, Section 5.6 to account for such particle concentration effect.

Material and Particle Properties

The hardness of the erodent particle impacts significantly on erosive process. Besides showing the effect of particle shape on erosion, Levy and Chik[44] analysed the effect of particle hardness by using different particle materials. Softer materials such as calcite (115 HV) and apatite (300 HV) presented very low erosion rates, which increased with particle hardness up to 700 HV. Above this value, a constant erosion rate was observed for 1018 steel. Therefore, SiO_2 (700 HV) is almost as erosive as SiC (3000 HV) even though its hardness is about four times lower. They concluded that softer particles shatter into smaller pieces upon impact and those small fragments hit the target surface with lower kinetic energy and mass, yielding low erosion rates. Additionally, the small pieces may adhere to the target surface and protect it from erosion. On the other hand, harder particles produce more erosion as particle shattering

is less effective. A relationship between erosion rate and ratio of target to particle hardness was proposed by Wada and Watanabe[52] as follows:

$$erosion\,rate \propto \left(\frac{H_t}{H_p}\right)^n \tag{II-11}$$

where n is an empirical exponent, H_t and H_p are the target and particle hardness. Parsi et al.[18] states that the density of the particle is also an important factor which influences erosion. Higher erosion rates result from denser particles due to their greater kinetic energy which generates more impact force during collisions.

The magnitude of erosion is highly dependent on target material hardness. Generally, erosion is inversely proportional to hardness of ductile materials (Finnie[35,36]). Nevertheless, Levy and Hickey[53] observed an opposite behaviour in some alloys and steels, where higher erosion rates were obtained for higher hardness. Additionally, Parsi et al.[18] suggests that target material toughness may be a better indicator of erosion performance than hardness.

Erosion Mechanisms

A brief description of existing solid particle erosion mechanisms is given in this section to clarify possible effects of erosion on surface roughness of ductile materials. As each wear mechanism has its own contribution to erosion, and each of these mechanisms could occur simultaneously, it is reasonable to assume that surface roughness formation or destruction depends on these mechanisms as well. The complexity of solid particle erosion relies on its dependence on the interaction between several parameters such as properties of the abrasive particle (density, mechanical properties and shape) and eroded material (mechanical properties) as well as impact conditions (incident angle and velocity). By impacting on a surface, particles suffer from total or partial loss of kinetic energy which could result in material removal.

Initially introduced by Finnie[20] in 1960, erosion occurs due to two main mechanisms, defined as cutting and deformation wear. Accordingly, erosion of ductile materials is associated with particles impacting onto the material surface with enough kinetic energy to

cause plastic deformation, in which fragments of the surface are removed by the displacement or cutting action of the abrasive particle. Alternatively, fragments are removed from the surface of brittle materials by intersection of subsurface crack formation, which originates and propagates from the impact location of the particle. Finnie[20] idealized the cutting mechanism occurring at low incidence angles as presented in Figure II-5, in which only the leading face of the particle contacts the surface. In Figure II-5, l is the depth of contact, y_t is the depth of cut and x_t is the length of cut. Finnie[20] was successful in predicting erosion at shallow impact angles but failed to predict at normal impact angles, as only the cutting mechanism was accounted for in his work.
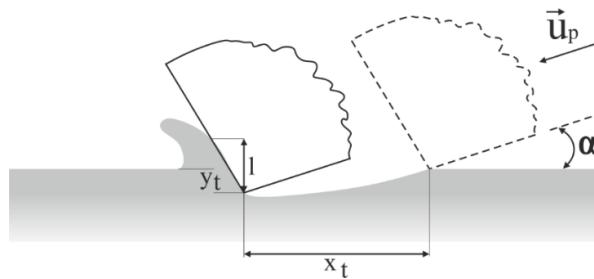
Figure II-5. Schematic representation of an abrasive particle colliding with a surface and removing material. Source: adapted from Finnie[20].

Bitter[16,21] states that erosion of metals rises from cutting and repeated deformation wear and that both mechanisms occur simultaneously, therefore extending the work of Finnie[20]. Due to repeated particle impacts, the surface of the material is shattered into small fragments if the elastic limit of the material is exceeded. This behaviour is mainly observed at higher impact angles. If, on the other hand, particles impact on a surface with shallow angles, the surface is exposed to shear stress, which removes small pieces of the surface if the shear strength of the material is exceeded. Unlike Finnie, his model was successful in predicting erosion at normal impact angles.

Hutchings et al.[54] proposed that erosion of ductile metals at small impact angle happens due to three main mechanisms depending on particle shape and orientation: cutting deformation, ploughing deformation by angular particle and ploughing deformation by spherical particle. These three mechanisms are illustrated in Figure II-6. In their perspective, cutting wear occurs during a collision between a flat-ended cylindrical particle and the material surface at an oblique angle, producing a displaced lip above the material surface. In this case,

the angle between the leading face of the particle and the target surface is large (Figure II-6 (a)). However, detachment of the formed lip depends upon mechanical properties of target material. It was observed by the same authors that the form of a crater left on the material surface by the impact of angular and spherical particles is considerably similar over a wide size range. For these types of particle, the angle between the leading face and the target surface is considerably smaller, which leads to ploughing rather than cutting deformation (Figure II-6 (b) and (c)). In this kind of wear, material is displaced to the front of the particle leading face forming a lip at the end of the crater. Also, material may be displaced to both sides of particle during impact. Additionally, the authors demonstrated that at impact angles bellow 30°, lip detachment could occur, and that at an impact angle of 40°, a large lip was formed which was not detached during the impact and was folded over the underlying metal instead. Nevertheless, consecutive particle impacts could remove formed lips and new ones could be formed as well. Later, Hutchings[23] proposed that erosion of metals at normal angle of incidence is associated with the formation and subsequent removal of platelets of metal lying parallel to the surface, referred to as platelet mechanism. This mechanism is supposed to be the main mechanism of material removal by spherical particles and have significant influence on erosion by angular particles. The experimental research conducted by Levy[55] not only confirmed the existence and importance of the platelet mechanism on erosion of ductile materials at normal impact angle but also showed that this mechanism is characteristic of erosion at oblique angles.
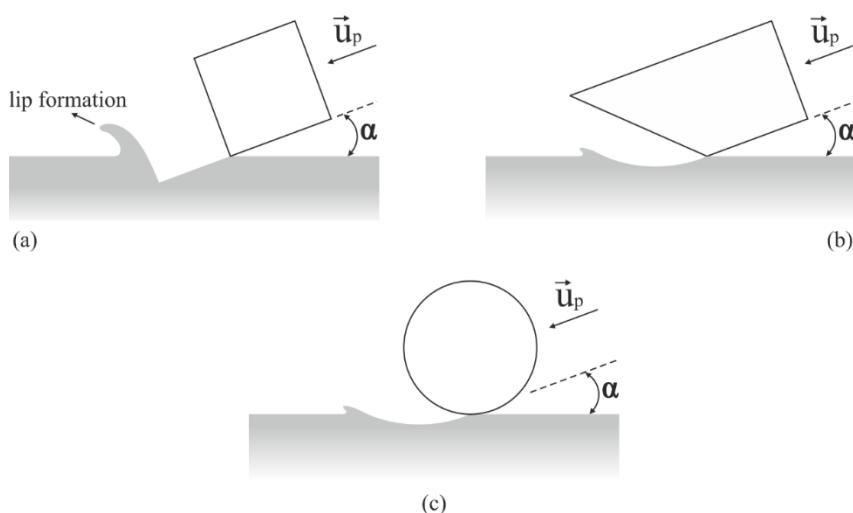
Figure II-6. Schematic representation of: (a) cutting deformation, (b) ploughing deformation with angular particle and (c) ploughing deformation with spherical particle. Source: adapted from Hutchings et al.[54].

Exploring erosion mechanisms further on, Islam and Farhat[56] distinguished between different mechanisms based on particle impact angle and velocity by subjecting API X42 steel to erosion under high abrasive feed rate.
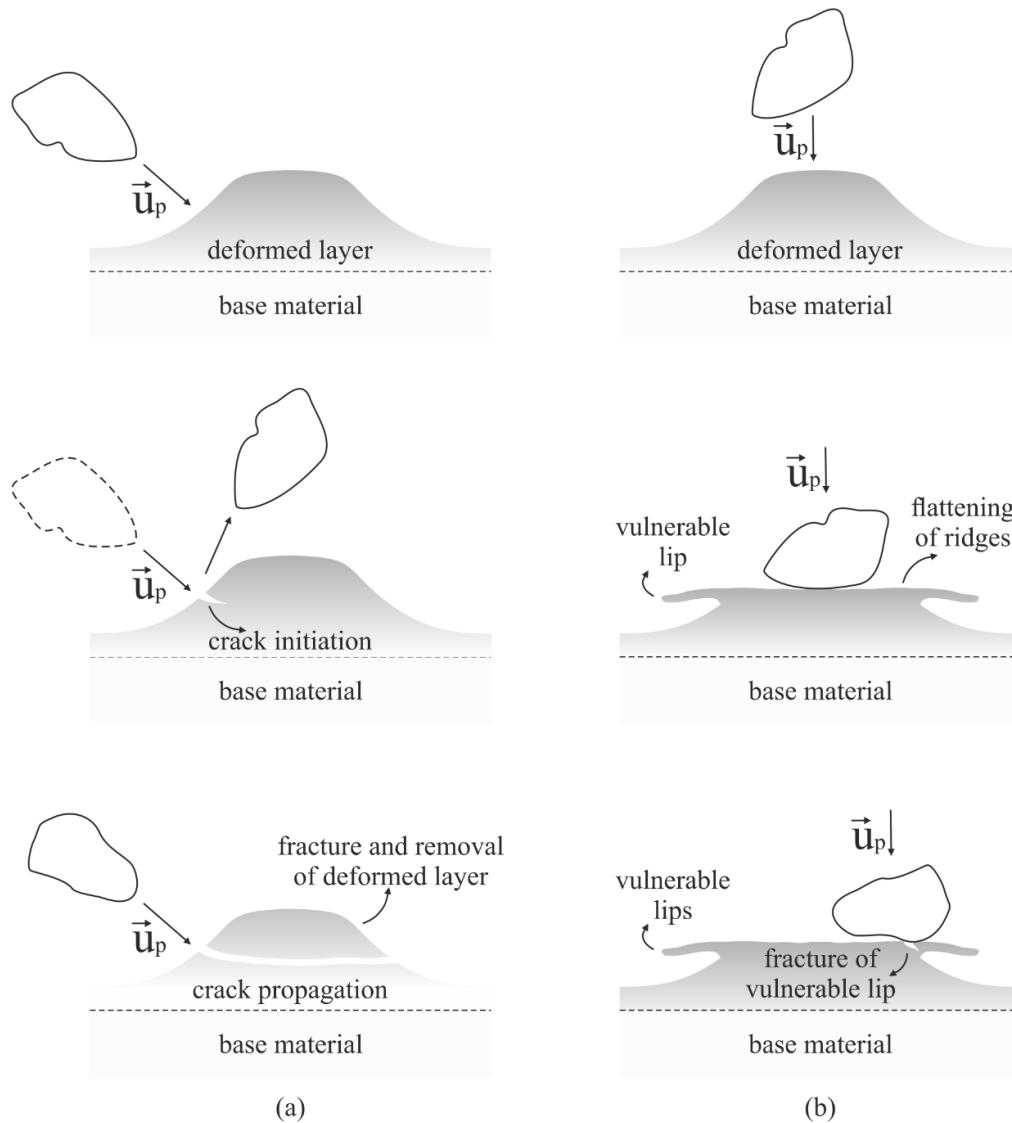
Figure II-7. Schematic representation of the stages of material removal at (a) low particle impact angle and high particle impact velocity, and at (b) 90° impact angle at low and high particle impact velocity. Source: adapted from Islam and Farhat[56].

It was demonstrated that ploughing is the dominant wear mechanism when the target material is eroded by impacting particles at low impact angle and velocity. Characteristic of this mechanism is the formation of front and lateral ridges by the squeezed metal during the sliding of the particle on the material surface. As pointed out by the authors, multiple particle

impacts flatten initially formed ridges, which could, consequently, be fractured and removed from the material surface. Under the condition of small incidence angles and high impact velocity wear by cutting was mainly observed (Figure II-8 (a)). Additionally, at evolved stages of erosion, the ridges around the crater could be removed by brittle fracture due to repeated particle impact and work-hardening of the surface (Figure II-7 (a)).
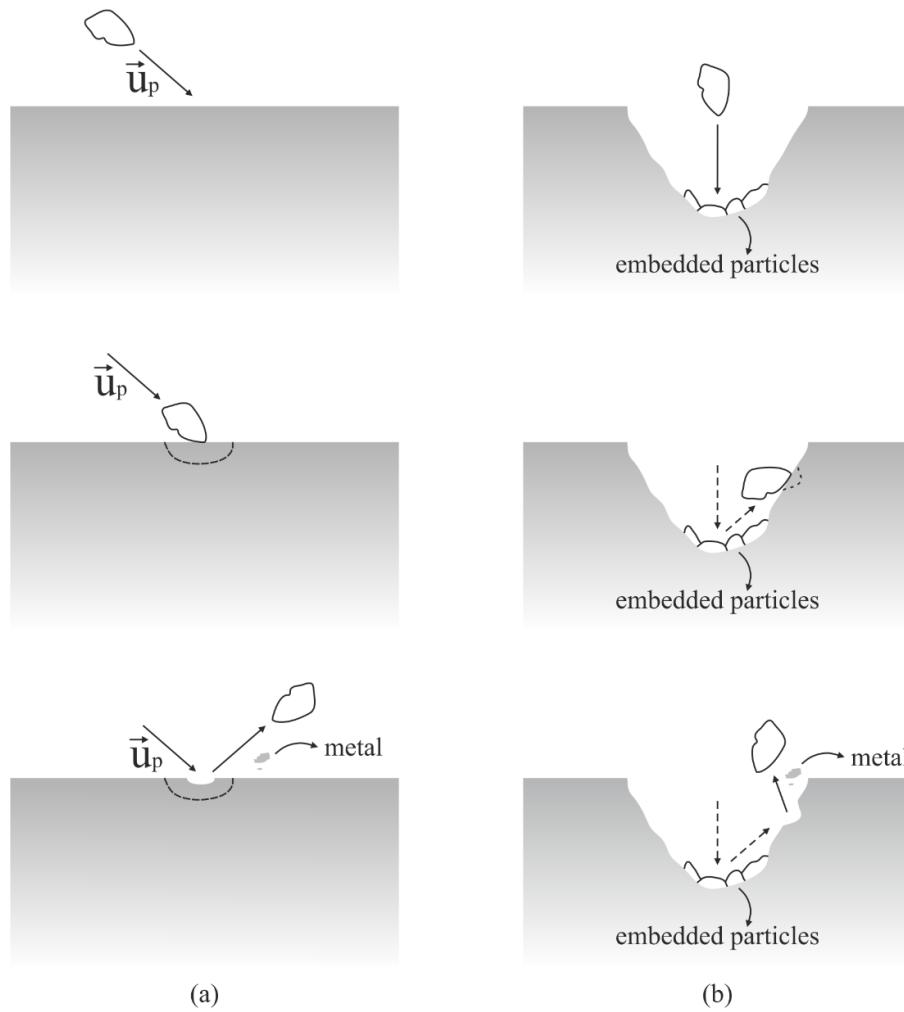
Figure II-8. Schematic representation of cutting wear at high particle impact velocity: (a) low particle impact angle (b) and secondary cutting wear occurs at high particle impact angle. Source: adapted from Islam and Farhat[56].

In contrast, plastic deformation followed by flattening and fracture of the ridges are the main wear mechanisms under high impact angle and low to moderate impact velocity. Under these conditions, metal is pushed out from the crater created after particle impact forming ridges around the crater, which could be then removed due to plastic deformation and flattening

of the ridges (Figure II-7 (b)). At high impact angle and velocity, particles are likely to deeply penetrate the metal matrix and to become embedded in the formed crater. Embedded particles suffer from repeated impact from other incoming particles and may be shattered into small pieces leaving exposed lips, which could be removed by plastic deformation followed by fracture. Similarly, secondary metal cutting was observed as well. Secondary metal cutting occurs when an incoming particle is deflected by an embedded particle and cuts the metal in its surroundings (Figure II-8 (b)).

As one can see, over the past decades several solid particle erosion mechanisms were observed and proposed. Even though many researchers attempted to isolate and determine the contribution of each wear mechanism to erosion, wear mechanisms could occur simultaneously or even just one could predominate.

The Mechanism of Ripple Formation on Ductile Materials

The development of regularly spaced ripples on surfaces exposed to solid particle erosion is very often observed, as shown in Figure II-9. A brief overview of the existing literature concerning ripple formation on material surfaces due to solid particle erosion is presented in the following, mostly focusing on ductile materials. Additionally, existing research regarding the effect of solid particle erosion and parameters on surface roughness of materials is introduced. To the author's knowledge, there is a lack of literature dealing with those aspect of solid particle erosion.

A ripple formation mechanism due to erosion was firstly suggested by Finnie and Kabil[57] in 1965. The authors stated that ripples do not form immediately when the target surface is eroded but rather a gradual transition from an initial condition to well-defined ripples is detected. During the initial period the surface appears to have a random roughness and a Gaussian distribution of surface amplitude might be expected. According to the authors, the key features of the ripple formation mechanism are: (1) ripples move downstream but at a decreasing rate as particle impact angle increases; (2) the growth of ripples is more rapid on soft materials and at high particle impact velocities; (3) ripples should not appear if particle impact angle is large enough and should be bigger for small incident angles; (4) ripples should

steepen on the downstream side at particle impact angles slightly greater than that for which erosion is a maximum; (5) ripple wavelength is expected to grow with increasing erosion; (6) ripple wavelength should be approximately a multiple of the length of cut produced by a single particle.
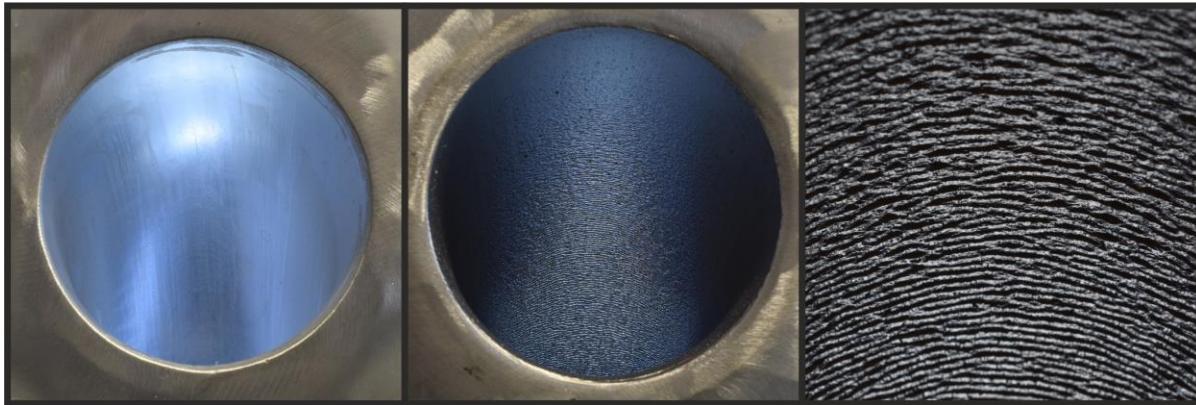
Figure II-9. Ripple pattern formed when a 90° aluminium 6060 bend is eroded by spherical glass beads (images on the middle and left side, left side illustrates a fresh bend). The flow comes from the bottom and exits perpendicular to the plane of the image. Source: author.

Carter et al.[58] observed ripple formation on the surface of copper due to solid particle erosion. The authors suggested that formation of well-defined ripples is fundamentally related to the morphology of individual impact craters, plastic flow, and mechanical interference of neighbouring moving ridges. Individual particle impacts produce craters which are transformed by plastic flow processes due to subsequent particle impacts into a collection of random depressions and ridges. Random depressions and ridges continue to flow until the mechanical interference between neighbouring moving ridges results in well-defined ripples. Also, the size of the ripples is of similar value to that of the impacting particles. Additionally, it was revealed that the wavelength of the ripples increases rapidly with erosion time but reaches an equilibrium state for all considered particle incidence angles. The amplitude of the ripples presented similar behaviour, i.e. increased to equilibrium values with increasing erosion. Moreover, the mean wavelength was about three times higher than the mean particle size (30 µm) whilst the amplitude was three times smaller for all impact angles analysed.

Griffin and Macmillan[59] analysed ripple formation on lead eroded at 3.5 m/s with 600 µm WC-8wt%Co particles by performing surface profilometry measurements together with

optical and scanning electron microscopy. The authors evaluated the effects of the impact angle on the ripple geometry and showed that the transition from transversely ripple topography to hill-and-valley topography is not related to the gradual destruction of transverse ripple pattern as particle incidence angle increases. The surface topography after erosion was characterized by ripples with transverse orientation with decreasing wavelength and amplitude at higher impact angles in the range of 15° to 45°. At an impact angle of 60°, a ripple pattern with longitudinal orientation of about the same size in wavelength and amplitude of those at 45° was observed. By increasing the impact angle even further, the ripple pattern with longitudinal orientation breaks up forming topographies characterized by hills and valleys with partially longitudinal orientation at 75° and isotropic at 90°. The authors also concluded that ripples may run parallel to the tangential component of the particle impact velocity.

Ballout et al.[60] studied ripple formation on the surface of pure aluminium during solid particle erosion in an air-blast system using sharp alumina (mean diameter of 406 µm) and spherical glass beads (mean diameter of 375 µm) as erodent particles. The main objective of the work was to provide experimental investigation of the effect of the erodent particle tangential velocity on ripple formation. Results confirmed that the tangential component of the particle impact velocity is mainly responsible for the formation of ripples on the surface of materials.

Talia et al.[61] investigated the effect of erodent particle shape, angle of impact and abrasive particle mixture on the formation of ripples on pure Al and Al-12Si surfaces. Erodent particles were angular Al_2O_3 and spherical glass beads with mean particle size of 406 µm and 400 µm, respectively. Impact angles of 20°, 30°, 60° and 90° were analysed considering impact velocities of 70 m/s for Al_2O_3 and 60 m/s for spherical glass beads. The feed rate was held in the range of 0.008 g/s to 0.012 g/s. Relevant conclusions drawn by the authors in terms of ripple formation are: (1) ripple formation is not necessarily a result from material removal and particle shape is an important parameter in determining whether ripple formation will occur and to which extent; (2) ripples are more pronounced at low particle impact angles and diminish at higher angles due to the relative importance of the normal and tangential components of the particle impact velocity; (3) no ripple formation was observed on the surface of Al-12Si eroded by sharp Al_2O_3 particles but ripples were formed on the surface of

Al-12Si when spherical glass beads were considered; (4) ripples were formed on the surface of pure aluminium even when no mass loss was detected, which suggests that ripples are formed by refold layers of displaced and poorly attached material; (5) the effectiveness of Al_2O_3 in removing material from Al-12Si is increased as the fraction of spherical glass beads in the erosive mixture is increased due to the combination of the displacement (ploughing) mechanism of spherical particles and the removal (cutting) mechanism of angular particles.

Fang et al.[62] conducted an experimental work to analyse the phenomenon of micro-ripple formation and removal mechanism in ceramic materials by solid-liquid slurry erosion. Micro-ripple patterns were observed on the surface of alumina, sialon and PSZ zirconia at low impact angle. The formation and ripple size were strongly influenced by slurry erosion conditions, such as flow velocity, impact angle, diameter, shape and hardness of particles, and mechanical properties of the eroded ceramics. Also, there is an incubation period before the start of ripple formation. The authors achieved a better understanding of the formation of micro-ripples on the surface of hard, brittle materials and based on experimental facts, both fracture and ploughing mechanism were found to occur.

Avcu et al.[63] investigated the effects of particle impact velocity and angle on surface roughness, erosion rate, and surface morphology of a titanium alloy (Ti6Al4V) exposed to solid particle erosion. Erosion tests were carried out under various impact angles (15°, 30°, 45°, 60°, 75° and 90°) and impact velocities (33 m/s, 50 m/s and 75 m/s) by using 120 mesh (90-125 µm) garnet erodent particles. The authors proved that the surfaces roughness of the titanium alloy was dramatically affected by both particle impingement angle and velocity. By using an optical profiler, surface roughness values, surface roughness maps and 3D surface roughness morphology were assessed. Results showed that surface roughness increases with the augmentation in particle impingement angle and velocity.

Kazarinov et al.[64] performed physical experiments to identify the influence of impact velocity (40 m/s, 80 m/s, 160 m/s and 200 m/s) on surface roughness of ultrafine- and coarse-grained aluminium 1235 (99.3% Al) eroded by 100 µm corundum particles in a wind tunnel. The authors showed that the change in the surface roughness increases with increasing in particle impact velocity. Additionally, the change in the surface roughness with particle impact velocity was significantly bigger for the coarse-grained alloy compared to the ultrafine-grained

counterpart. However, the authors did not mention whether the occurrence of well-defined ripples was observed. Similar research was performed by Atroshenko et al.[65], who analysed the behaviour of a grade 5 titanium alloy under conditions of high-speed erosion by two abrasive powders with 109 and 230 µm mean particle size. The surface roughness was found to increase with the increase in particle impact velocity. Evstifeev et al.[66] reached the same relationship between surface roughness and particle impact velocity by exposing EI-961 steel to solid particle erosion considering particle sizes of 25 µm, 109 µm and 230 µm. Moreover, the change in the surface roughness is found to increase for larger particles under similar impact conditions.

Abedini and Ghasemi[67] evaluated the effect of jet velocity (3 m/s, 6 m/s and 9 m/s), sand concentration and impact angles between 20° and 90° on the surface roughness of an Al-brass alloy after erosion and erosion-corrosion tests in a slurry impingement rig. The slurry consisted of distilled water, 35 g/l NaCl and 0-90 g/l SiO2 particles with average size of 250-500 µm. Eroded surfaces were characterized using 2D and 3D surface profilometry and scanning electron microscopy. It was found that increasing the jet velocity the average surface roughness, expressed in terms of the parameter R_a[1], increased and the change in the surface roughness with respect to the impact angle and sand concentration was also higher at higher jet velocities. Additionally, the formation of well-defined ripples on the eroded surfaces at a jet velocity of 9 m/s was the main reason for higher surface roughness at oblique angles as compared to normal angle, at which no ripple was observed. Well-defined ripples were observed at this velocity for impact angles of 20°, 40° and 50°. Therefore, the surface roughness increased up to 40° followed by a decrease up to 90°. According to the authors, ripples could be formed on the eroded surface of Al-brass alloy in the following conditions: under pure erosion tests, high jet velocity of 9 m/s, oblique angles and high sand concentrations.

---

[1] Surface roughness parameters are detailed in Chapter III, Section 3.2.

Numerical Studies of Solid Particle Erosion

Computational fluid dynamic (CFD) is a powerful methodology widely used to predict erosion in industrial processes and equipment. The referred methodology is based on the Euler-Lagrange approach, which consists of solving the flow field, tracking of particle trajectories and applying predictive erosion equations (Zhang et al.[68]). The solution of the flow field requires solving the time-averaged Navier-Stokes equations, which provide numerical data on pressure, velocity and turbulent kinetic energy fields. The averaging procedure produces unknown variables, namely Reynolds stresses, which require extra modelling provided by turbulence models. After, particles are tracked throughout the flow field by solving the equation of motion, which includes all relevant forces acting on the particles. Finally, erosion is computed via predictive equations based on the information of particle impact velocity and angle. More detailed information related to the Euler-Lagrange approach is given in Chapter V. The Euler-Euler approach may be applied to predict solid particle erosion in multiphase flows as well. Nevertheless, according to Parsi et al.[18] and Lee et al.[69], the Eulerian method for particles only provides a mean value for the particle motion in each control volume, which causes inaccurate prediction of particle impact velocity and angle and consequently, of erosion. Therefore, in following a brief literature overview regarding numerical prediction of solid particle erosion based on the Euler-Lagrange approach is presented.

Fan et al.[70] investigated numerically and experimentally a new method for protecting bends from erosion in gas-solid flows. The method consists of adding ribs to the outer wall of the inside of the bend and the authors experimentally demonstrated that the average erosion of ribbed bends was 33.5% of that of smooth bends. Based on the coupled Euler-Lagrange approach (standard k-ε turbulence model), it was found that by adding ribs, particle impact velocity tends to be in the range of 0 to 10 m/s compared to those velocities obtained for a smooth bend, which is in the range of 30 to 40 m/s. In addition, particle impact angle was reduced from the range of 20° to 30° for a smooth bend to the range of 0° to 10° for the ribbed bend. Also, the authors obtained good agreement between numerical and experimental data.

Erosion pattern on an elbow and a plugged tee was numerically analysed by Chen et al.[71], which additionally performed experimental erosion tests in both elbow and plugged tee

to validate their numerical results. Simulations were based on the Euler-Lagrange approach and the Differential Reynolds Stress turbulence model was used and only one-way coupling was considered. The correlations from Ahlert[72] and McLaury[73] were applied together with empirical correlations for the restitution coefficient (Grant and Tabakoff[74], Forder et al.[75] and Sommerfeld[76]). In conclusion, comparison between numerical and experimental data confirmed that a stochastic rebound model is required in numerical calculations to estimate erosion rate and pattern in plugged tee.

Zhang et al.[68] performed LDV (Laser Doppler Velocimetry) and erosion experiments using sand particles carried in streams of air and water flow impacting target specimens. The LDV technique was used to obtain the fluid velocity field and to measure particle velocities in a direct impact test section (i.e. flow through a nozzle perpendicular to the target surface), in which the experimental data was used to validate numerical results. Additional to weight loss measurements, the authors applied high sensitivity electrical-resistance probes to measured erosion rates. The fluid field was simulated using the second order Reynolds stress turbulent model and the effect of inter-particle collisions and the influence of particles on carrier phase were neglected. Several erosion models available in the literature were tested including the models from Finnie and McFadden[77], Bitter[16,21], Ahlert[72], and Oka et al.[31] and Oka and Yoshida[32]. According to the authors, the correlations from Ahlert and Oka not only predicted similar erosion rates but also presented very good agreement with the experimental data. Moreover, the authors achieved a good agreement between LDV data and CFD calculations for both fluid and particle velocities.

Mazumder[78] numerically evaluated the erosion caused by particle impacts in a dilute gas-solid flow through a U-bend, in which the effect of liquid and gas velocities on erosion were investigated for sand size varying from 50 µm to 300 µm. Fluid velocities of 15 m/s, 30.48 m/s and 45 m/s were considered in the investigation. The Euler-Lagrange approach together with the Realizable k-ε turbulence model and with the erosion equation presented by Edwards[79] were applied. Although no experimental validation was performed due to lack of experimental data, the numerical results, according to the author, provides insightful information on the relative magnitude and location of erosion in U-bend geometry.

Njobuenwu and Fairweather[80] used a CFD model coupled to a Lagrangian particle tracking method and several erosion models (Grant and Tabakoff[81], Menguturk and Sverdrup[82], Ahlert[72] and McLaury[73], Oka et al.[31] and Oka and Yoshida[32], Huang et al.[83]) to estimate erosion rate in four different 90° square cross-section bends for dilute particle-laden flow. Turbulence in the fluid phase was modelled through the standard k-ε model and forces such as drag, buoyancy, gravity and shear lift forces were included. They accounted for the effect of the fluid turbulence on the particle motion using the random Fourier series method. In addition, empirical restitution coefficients as a function of particle impact angle (Jun and Tabakoff[84]) and the stochastic effect of wall roughness (Sommerfeld and Huber[85]) were considered by the authors. The five models were compared to experimental data on erosion by alumina particles in long-radius 90° bend flows and predictions followed the same trend for all five models. However, differences in erosion magnitude were observed. Nevertheless, the authors concluded that the models performed well within experimental uncertainty.

Wong et al.[86] analysed, both experimentally and computationally, solid particle erosion caused by air-sand suspensions in an aluminium pipe annular cavity. The test section consisted of a 4" erosion rig and sand at a nominal feed rate of 30g/s was transported with ambient air considering a bulk flow velocity of 80 m/s. The experimental studies combined a multi-layer paint erosion technique and actual material loss measurements and considered sand with mean diameters of 198 µm and 38 µm. The authors applied the Euler-Lagrange approach in combination with the standard k-ε turbulence model and an erosion model based on that proposed by Chen et al.[71] was employed. Conclusively, erosion prediction on surfaces which experience secondary or higher order impacts is less accurate compared to surfaces on which direct impact are observed. Also, predictions within ±30% of the experimental values were reported for 198 µm sand particles, while 38 µm sand particle were over predicted by up to 100%.

Pereira et al.[87] evaluated numerically the performance of four erosion models in predicting erosion on a 90° bend by comparing the numerical results with the experimental data provided by Mazumder et al.[1]. The correlations proposed by Ahlert[72], Neilson and Gilchrist[22], Oka et al.[31] and Oka and Yoshida[32], and Zhang et al.[68] were applied. The influence of empirical models for the coefficients of restitution (Grant and Tabakoff[74] and Forder et al.[75])

and friction (Sommerfeld and Huber[85]) and surface roughness, as well as the effect of numerical parameters such as the number of computational particles were analyzed. Calculations were performed by applying the uncoupled Euler-Lagrange approach with the standard k-ε turbulence model. In conclusion, numerical results showed considerably differences among the correlations used, in which the Oka model together with the correlation of Grant and Tabakoff predicted erosion ratio more accurately. Additionally, the effect of the friction coefficient on the results was found to be not relevant and the surface roughness affected erosion, reducing its magnitude.

Kim et al.[88] evaluated the effect of the standard k-ε and shear stress transport (SST) turbulence models on erosion predictions based on the Finnie[20] erosion model. Simulations were conducted by using the Euler-Lagrange approach. The analysis was performed on sand-air jet system impacting on the target surface at a normal incidence angle. Sand mean size and velocity were 50 µm and 30 m/s, respectively, and the air flow rate was 8 l/min. Target material was WC brazed coating surface with and without boron element. The authors concluded that the SST model is closer to the experimental result than k–ε model because it accounts for the transport of the turbulent shear stress. Additionally, erosion rate is increased due to the increase in the hardness when the boron element is added in the WC brazed coating surface.

Solnordal et al.[2] performed an experimental and numerical analysis of bend erosion caused by sand in a pneumatic conveying system. They provided a detailed surface map of erosion depth in a 90° elbow ($R_{elbow} = 1.5D_{pipe}$) by conveying 200 kg and 300 kg of sand with a mean diameter of 184 µm with air at 80 m/s. The authors additionally carried out numerical simulations based on the Euler-Lagrange approach in connection with Shear Stress Transport (SST) turbulence model. Moreover, inter-particle collisions, particle rotation and particle-wall interaction were considered. The same erosion model as Wong et al.[86] was utilized. They showed that assuming smooth walls during particle-wall collisions leads to inaccurate prediction of maximum erosion and erosion scar. Additionally, it was reported that erosion depth and distribution may be accurately predicted by adopting a suitable rough wall collision model. However, it was suggested that erosion pattern may be additionally influenced by particle shape, surface profile development and changes in the surface roughness as well.

Duarte et al. [89] investigated the influence of sand concentration on the erosion of an 90° elbow considering different degrees of phase coupling, i.e. one-, two- and four-way coupling. The Oka et al.[31] and Oka and Yoshida[32] erosion model in combination with the standard k-ε turbulence model and the correlation for the restitution coefficient from Grant and Tabakoff[74] were applied. Additionally, particle-particle interaction was accounted for stochastically as described by Sommerfeld[90]. Numerical validation was performed with experimental data from Mazumder et al.[1]. In summary, the authors concluded that the effect of inter-particle collisions on erosion ratio may not be neglected even at low to moderate mass loadings. In addition, by increasing particle mass loading the maximum erosion ratio is diminished, effect which results from the shielding (or cushioning) effect. Similar numerical work was performed by Duarte et al.[91], which computed erosion in a 90° elbow by applying the Euler-Lagrange approach considering all relevant elementary processes, such as drag and lift forces, particle rotation, inter-particle collisions, particle-wall interaction and degree of coupling between the continuous and dispersed phases. Numerical predictions were validated with the experimental data from Solnordal et al.[2]. It was demonstrated that increasing surface roughness reduces erosion depth and that the particle impact angle was not affected by coefficients of friction (static and dynamic) but by the degree of surface roughness. Also, four-way coupling was found to be essential in predicting erosion depth accurately at higher particle mass loadings due to the associated shielding effect.

Laín and Sommerfeld[92] carried out extremely detailed numerical predictions of particle erosion of pipe bends by applying the Euler-Lagrange approach in combination with the standard k-ε turbulence model and full two-way coupling, i.e. influence of particles on turbulent properties via source terms. Particles were tracked considering particle translation and rotational motion and all relevant forces such as drag, gravity/buoyancy and transverse lift due to shear and particle rotation were accounted for. Furthermore, turbulent dispersion of particles, particle collisions with rough surfaces and inter-particle collisions were modelled stochastically. Erosion analysis was performed for two and four-way coupling considering mono-sized spherical glass beads as well as a size distribution of particles with the same number mean diameter, i.e. 40 µm. Particle mass loadings in the range of 0.3 to 1.0 were analysed as well. By employing the erosion model from Oka et al.[31] and Oka and Yoshida[32], erosion predictions were compared to the experimental data provided by Mazumder et al.[1].

Moreover, a 150 mm pipe system with 5 m horizontal pipe, pipe bend and 5 m vertical pipe with a bulk velocity of 27 m/s was considered for further analysis. It was found that particle-particle interactions reduce erosion depth although wall collision frequency is enhanced and in addition, considering a particle size distribution with the same number mean diameter as mono-sized particles yields much higher erosion depth. Finally, for higher particle mass loadings, bend erosion is reduced due to modifications of particle impact velocity and angle, although wall collision frequency is enhanced.

Duarte et al.[93] investigated numerically a dilute gas-solid flow and the relative erosion in three different pipe fitting designs, namely a standard elbow, plugged tee and vortex-chamber elbow. The fluid phase was computed in the Eulerian framework considering the Reynolds stress turbulence model (RSM) while particles were tracked in the Lagrangian framework account for particle linear and rotational motion. Inter-particle collisions and relevant forces such as drag, shear-induced lift, rotation-induced lift, and weight forces were considered. Energy loss during particle-wall interaction was evaluated according to the rebound model from Grant and Tabakoff[74] and the predictive equation from Oka et al.[31] and Oka and Yoshida[32] was applied. Good agreement was achieved by comparing numerical results obtained for the plugged tee to experimental data available in the literature. It was found that each of the pipe fitting designs has its own mechanism of erosion reduction which depends on the particle mass loading considered in the flow.

The literature presented is only a fraction of research on numerical studies of solid particle erosion. Nevertheless, the ability of CFD-based erosion modelling in predicting solid particle erosion in gas-solid or liquid-solid flows in complex geometries and equipment is clear. Therefore, the Euler-Lagrange approach is selected to perform the numerical calculations presented in the current work. Additionally, several erosion models have been proposed and tested by several investigators, however, each of these models may be more accurate in certain geometries or under specific flow conditions. Also, erosion models are usually developed for specific combinations of erodent and target material and may estimate erosion rates inaccurately when applied to different combinations.

Chapter III

Surface Roughness Variation due to Solid Particle Erosion

This chapter is devoted to present the experimental methods applied to analyze the effects of solid particle erosion on surface roughness of materials. A description of the experimental facility is initially introduced, including the materials and particle type which were considered in the analysis. Then, the technique used to characterize the surfaces of the eroded materials is presented together with the parameters considered to describe surface roughness. Finally, the experimental techniques employed to measure fluid and dispersed phase velocities is described.

3.1. Impingement Jet Facility

Reliable data on solid particle erosion and surface roughness were obtained in an impingement jet facility as illustrated in Figure III-1. The facility consists of a closed, recirculating system in which particles impact on the surface of the sample during the

considered experimental time. The jet (a) and sample were inserted within a chamber (b) and the movement of air and particles was achieved by a blower. A cyclone (c) was located after the chamber to separate the particles from the air stream, which were collected into the particle collector chamber (d). The feeding of particles into the system was accomplished by a Venturi (e) and controlled by a valve, which was located between the Venturi and the particle collector chamber. A filter was positioned between the cyclone exit and the blower to ensure maximum particle separation. The volumetric flow of air, which was controlled by a flowmeter and kept constant, was 14.4 m³/h, yielding a mean air velocity U_0 of about 26 m/s at the exit of the jet. The sample holder could be easily adjusted to a range of impingement angles from 5 to 90° and the nozzle diameter was 14 mm. Two rectangular glass windows were located on each side of the chamber to allow optical access. Relevant dimensions of the chamber are presented in Figure III-2.
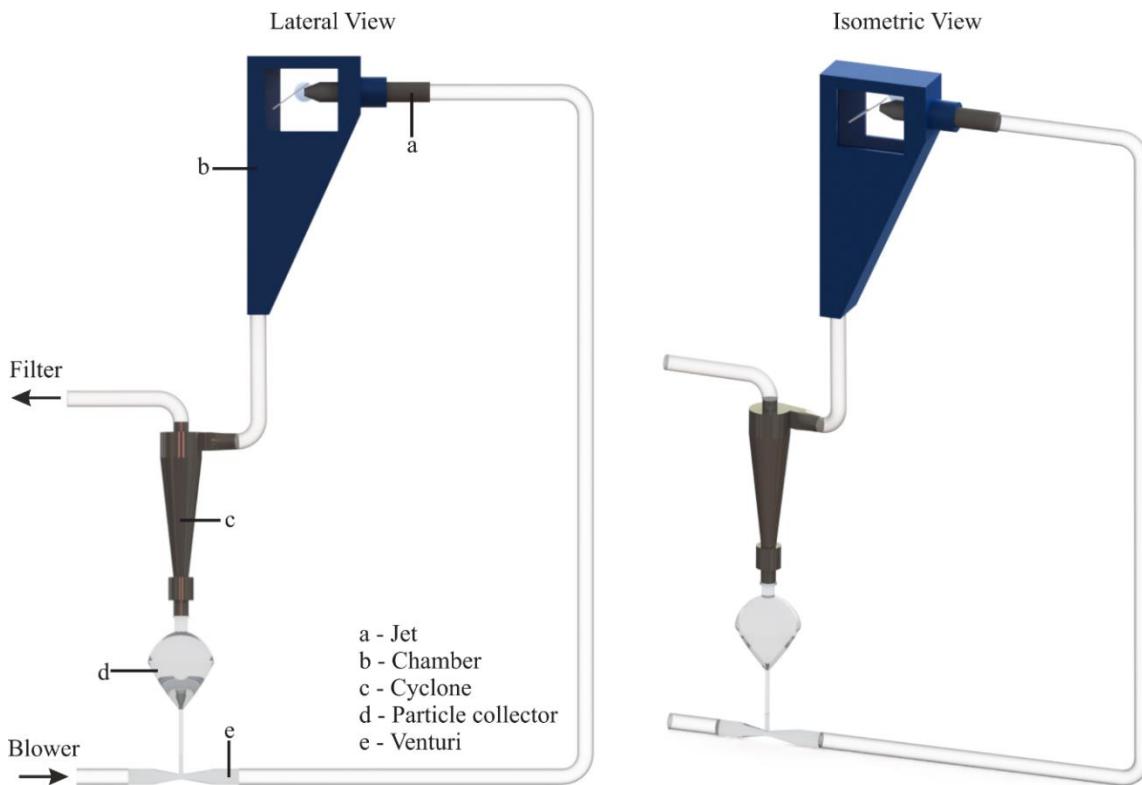
Figure III-1. Drawing of the impingement jet facility.

Solid particle erosion and surface roughness were analysed on rectangular plates with dimensions of 85 x 30 x 3 mm for 3 different erosion times: 2.5, 5 and 10 hours. An erosion time of 20 hours was also considered for a specific case considering quartz sand particles and

an inclination angle of 30°. The influence of the impingement angle on the surface roughness was investigated at impingement angles of 10, 20, 30 and 40°. Total erosion was quantified by measuring the initial and final weight of the sample after the considered experimental time. An error of about 4.8% was estimated in the obtained mass loss.
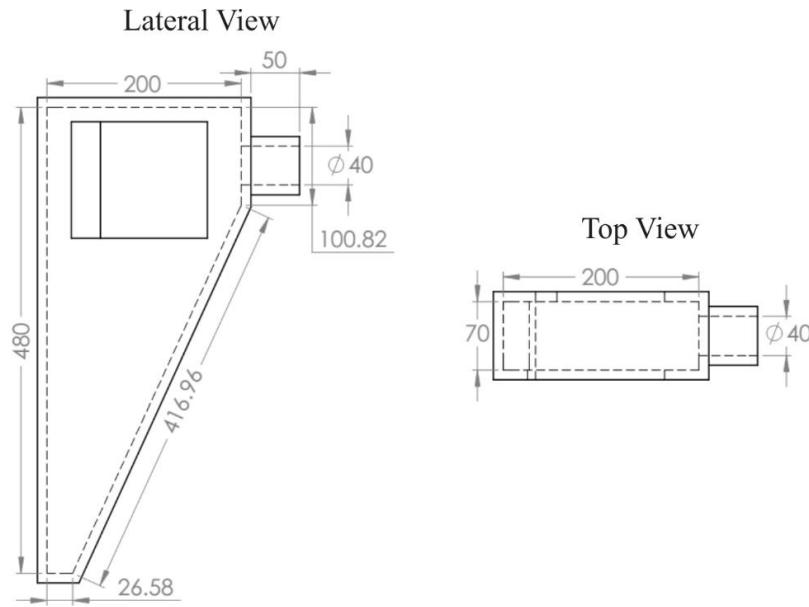
Figure III-2. Geometrical characteristics of the chamber. Units in millimetre. Wall thickness of 1 mm.

The effect of particle shape on both erosion and surface roughness was analysed by considering quartz sand and spherical glass beads particles with a number mean diameter of 235.4 µm and 211.5 µm, respectively. Figure III-3 shows the particle size distribution functions of both types of particle used, measured by a laser diffraction particle size analyser. The mass flow rate of quartz sand and spherical glass beads particles was about 1.28 g/s and 1.38 g/s, respectively. The associated error with the mass flow rate of particles is circa 4.1% for quartz sand and 4.2% for spherical glass beads. Aluminium 5754, copper and brass (70%Cu-30%Zn) were analysed. Table III-1 summarizes the relevant material and particle properties.
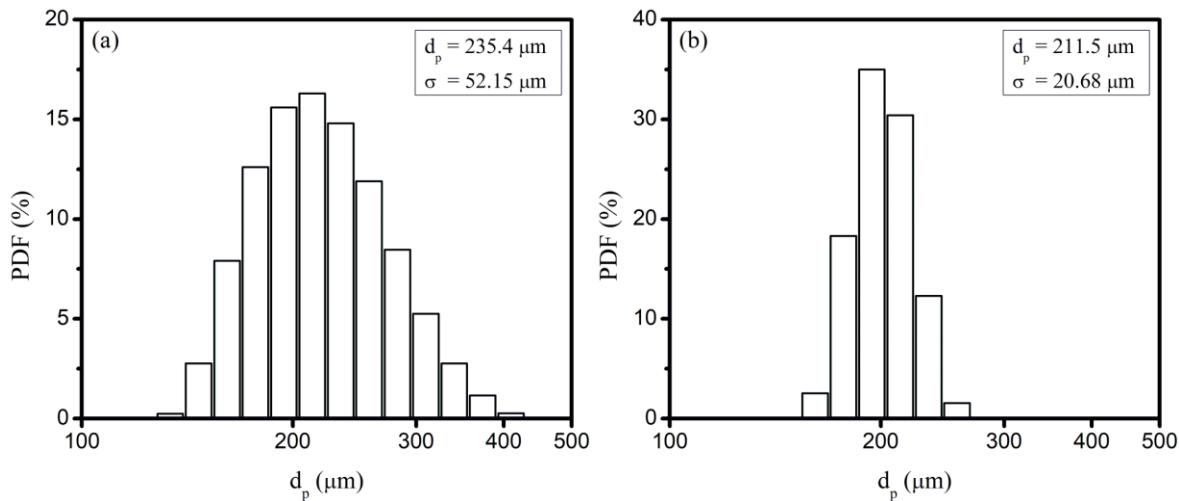
Figure III-3. Measured number-based particle size distribution: (a) quartz sand and (b) spherical glass beads particles.

Table III-1. Relevant material and particle properties.

Property	Aluminium 5754	Copper	Brass 70/30	Quartz Sand	Glass Beads
Density, ρ [kg/m^3]	2700	8960	8530	2650	2500
Vickers Hardness[a], Hv [GPa]	0.74	0.9	1.2	-	-
Particle diameter, d_p [µm]	-	-	-	235.4	211.5

[a] Measured by TRIBOTRON AG by means of a standard Vickers Hardness test using a load of 1.0 kgf.

In order to evaluate the changes on the surface roughness of materials exposed to solid particle erosion over long periods of time, the particles were reutilized. Therefore, it is important to quantify possible particle degradation during the experimental time. Hence, preliminary tests were performed with both types of particle during different experimental times and particle degradation was characterized based on changes on particle size distribution. Figure III-4 (a) compares particle size distributions between fresh and reused quartz sand particles for 2.5 hours while Figure III-4 (b) compares fresh and reutilized spherical glass beads particles for 2.5 and 5 hours. After reusing quartz sand particles for 2.5 hours a decrease of about 4.2% was observed in its mean number diameter, even though impact velocity was considerably low. The reduction is attributed to the repetitive particle collisions with the sample allied to the non-sphericity thereof. Quartz sand particles have sharp edges that could break during impact, releasing small fragments into the system, as can be seen in the

microscopic view shown in Figure III-5 (b). In contrast, spherical glass beads particles showed insignificant degradation after being reused for 2.5 and 5 hours, as can be seen in Figure III-4 (b) and in the microscopic view presented in Figure III-5 (d). Based on the preliminary tests performed, the amount of quartz sand and spherical glass beads particles was changed every 2.5 and 5 hours, respectively, in order to avoid strong particle degradation.
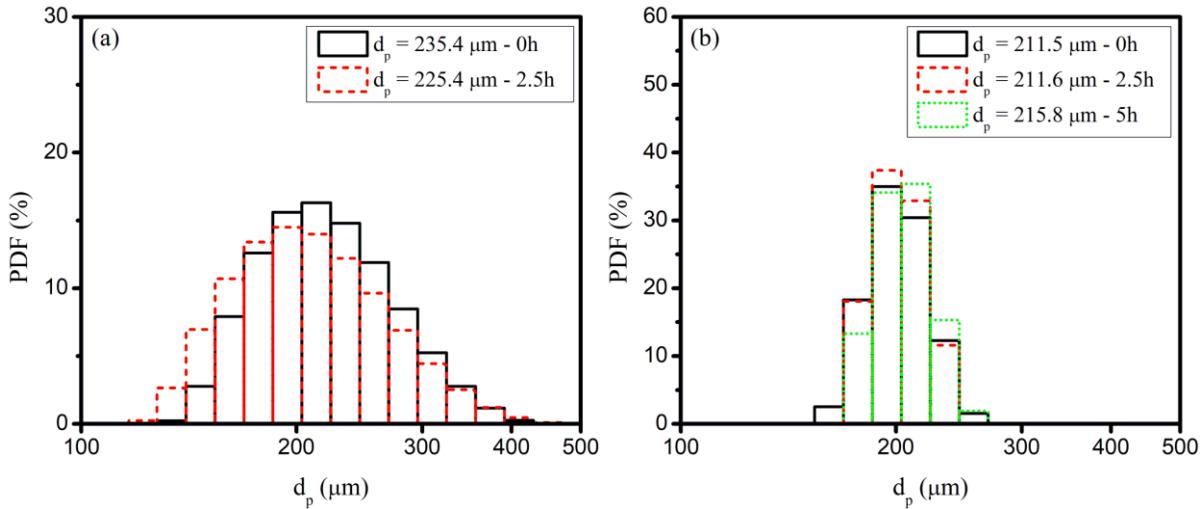
Figure III-4. Measured number-based particle size distribution for different experimental times: (a) quartz sand and (b) spherical glass beads particles.
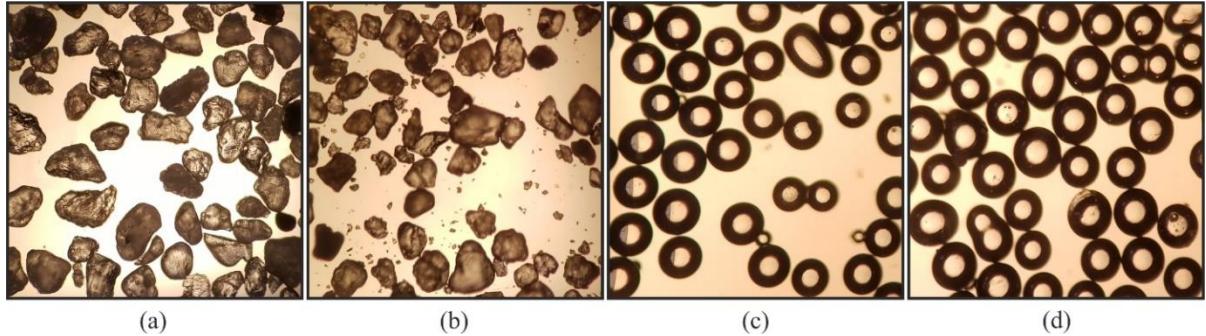
Figure III-5. Microscopic view of the particles: (a) fresh quartz sand particles and (b) reused for 2.5 hours; (c) fresh spherical glass beads particles and (d) reused for 5 hours.

3.2. Surface Roughness Measurements

The eroded surfaces were optically scanned by Tribotron AG and Nanovea Srl using a profilometer Nanovea JR25 with a PS3 sensor. The profilometer uses Chromatic Confocal optical technology. This technology uses a white light source (LED) which passes through a

series of lenses. These lenses have a high degree of chromatic aberration and vary the focal distance of each wavelength emitted by the LED in a way that only the region of interest on the surface is focused while the others are out of focus. The focused wavelength is then reflected to the sensor and passes through a CCD spectrometer, which indicates a specific distance for a single point on the surface. Thus, the height measurement is achieved by measuring the physical wavelength. The sensor has a height repeatability for the parameters R_a and R_z of 4.0 and 29.0 nm, respectively. The repeatability considers an average height variation for 1200 points in one fixed location on glass. The profilometer scans 25 mm of the sample.
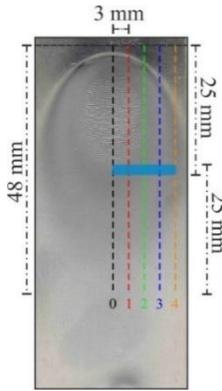
Figure III-6. Surface roughness measurement locations. Blue area: 2 mm overlapping area.

Two sets of 2D-Roughness measurements, composed by five roughness profiles each, were performed on each sample. Following the first set of measurement, the sample was moved 23 mm and the second set of measurement was carried out. The procedure considered a 2 mm overlapping, which allowed the roughness profiles from each set of measurement to be stitched together afterwards, resulting in one set of measurement. Consequently, a total of five roughness profiles distributed equally along the width of each sample were obtained. The spacing between each of the roughness profiles was 3 mm and all measurements started approximately 2 mm before the start of the erosion scar. Figure III-6 summarizes the applied procedure. A sampling distance of 2 µm was used for each optical measurement and the measurements were performed parallel to the impact direction of the particles.

Data processing from the profilometer was accomplished with Gwyddion 2.50, a free and open-source software which according to its founders[94], is modular program for scanning probe microscopy (SPM) data analysis. The software handles data not only from height fields

obtained by means of SPM techniques but also from any other height field and (greyscale) image processing, such as data obtained from profilometry techniques. Therefore, Gwyddion allows the user to obtain surface roughness profiles from profilometry data and easily compute numerous surface roughness parameters available. A standard cut-off length of 0.8 mm was applied to extract the surface roughness profiles from the raw data. At this cut-off, the texture profile is split into waviness and roughness. The former represents the low frequency components which define the overall shape of the surface and the latter characterizes the high-frequency components from which roughness parameters are extracted.

Parameters Analyzed

Several surface roughness parameters are available to assess material surface topography, which are classified into amplitude, spacing and hybrid parameters. While amplitude parameters quantify the vertical characteristics of the surface deviations, spacing parameters measure the horizontal characteristics. Hybrid parameters are a combination of both amplitude and spacing parameters. Gadelmawla et al.[95] published a very detailed review on several parameters available to describe surface roughness.

Surface roughness variation due to solid particle erosion was evaluated by quantifying the observed changes on the parameters R_a (arithmetic average height), RS_m (mean spacing at the mean line) and $\Delta\gamma$ (standard deviation of the roughness angle). R_a is an amplitude parameter which describes the mean absolute deviation of the roughness irregularities from the mean line over a sampling distance. RS_m is a spacing parameter which represents the mean spacing between peaks of the roughness profiles at the mean line. Following the work of Sommerfeld[76], $\Delta\gamma$ is a hybrid parameter which describes the roughness angle distribution and it depends on wall roughness structure and particle size. A method to estimate $\Delta\gamma$ is discussed further in Section 5.5. Figure III-7 details the definition of R_a and RS_m while Equations (III-1) and (III-2) describe their mathematical definition.
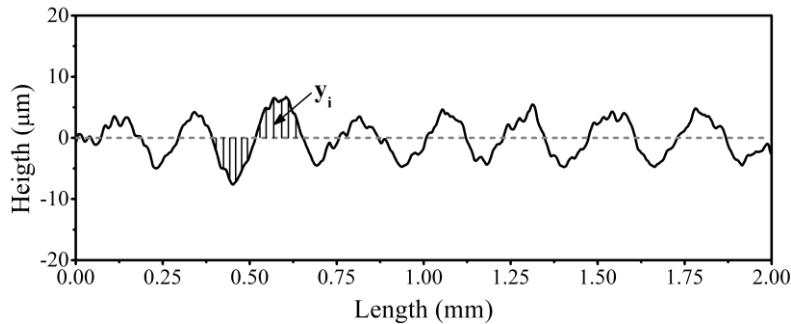
$$R_a = \frac{1}{n}\sum_{i=1}^{n}|y_i| \quad \text{(III-1)}$$
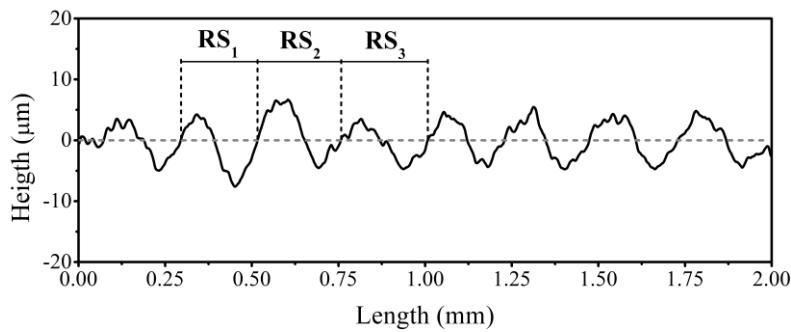
$$RS_m = \frac{1}{N}\sum_{i=1}^{n}RS_i \quad \text{(III-2)}$$

Figure III-7. Definition of parameters R_a (top) and RS_m (bottom) along with their mathematical description according to Gadelmawla et al.[95].

Nevertheless, R_a and RS_m were extracted from regions with most pronounced erosion, which also corresponds to regions against which most of the particles hit the surface of the sample. This prevents results from being damped by regions with insignificant or no erosion. For example, Figure III-8 shows five surface roughness profiles measured for aluminium 5754 considering an erosion time of 10 hours at an impact angle of 40°. The region most affected by erosion is the central area of the erosion scar which corresponds to the green area illustrated in the same figure. The same analysis was applied to all analysed samples, though different regions of interest for each impact angle were considered, as the erosion scar at an impact angle of 10° differs from the erosion scar at an impact angle of 40°, for example.
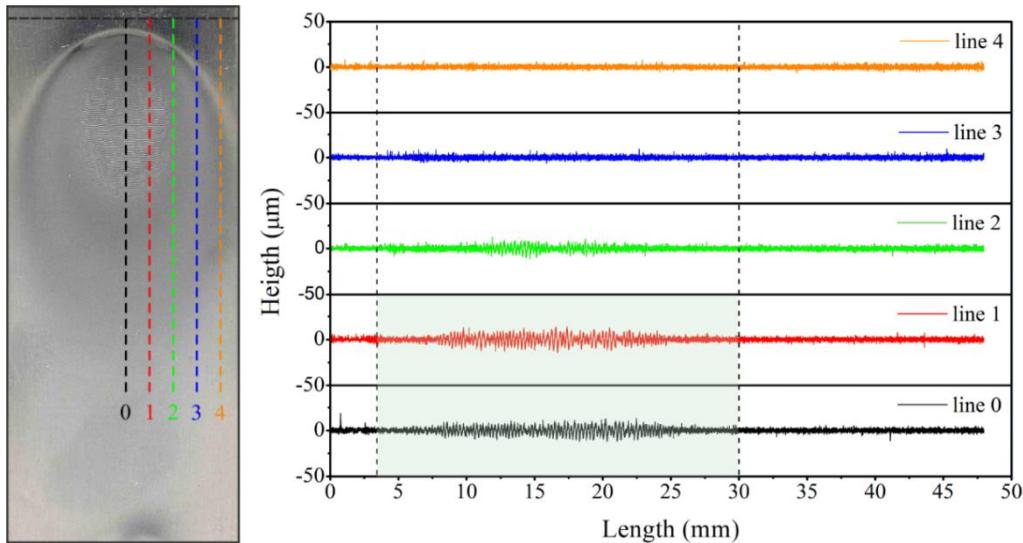
Figure III-8. Roughness profiles along the width of the sample (left) showing the region of interest (right). Inclination angle: 40°. Erosion time: 10 hours. Material: aluminium 5754.

3.3. Laser-Doppler Anemometry (LDA)

A single velocity component laser-Doppler anemometer (LDA) was used for measuring the continuous phase velocity distribution at the exit of the impingement jet. Since its invention, the LDA technique has been widely used for the characterization of local particle velocity distribution of several types of two-phase flows with a good spatial distribution. Spherical monosized seeding particles (type: spheromers® CA 6) with a diameter of 6 µm, refractive index of about 1.5 and density of 1.2 were fed into the flow to allow for the measurement of the continuous phase velocities. The optical system was mounted on a computer-controlled 3D traversing system operated by step motors, which allowed the precise positioning of the measuring system. The system was operating in backward scattering mode considering the parameters presented in Table III-2. For each measurement point a minimum of 8,000 samples were collected to allow for statically reliable measurements of the mean and fluctuating velocity components of air in the stream-wise direction. The velocity components were measured 2 mm away from the jet exit at its centre considering a spatial distribution of 1 mm, which resulted in 14 measurement points. It should be noted that due to the small distance between the sample (because of its inclination) and the upper region of the jet, one of the laser

beams was blocked by the sample. Therefore, some of the measurement points in the upper region of the jet could not be obtained.

Table III-2. Parameters of the LDA optical system.

Transmitting Optics		Receiving Optics	
Wavelength of the laser [nm]	633	Scattering angle [°]	180
Gaussian beam diameter [mm]	1	Polarization angle [°]	0
Focal length of front lens [mm]	310	Scattering mode option [-]	backward
Beam separation [mm]	38	Fringe rotation angle [°]	0
Fringe spacing [um]	5.1736		
Fringe number [-]	48		
Beam collimator exp. [-]	1		
Beam expander exp. [-]	1		

3.4. Shadow Image Velocimetry System

Particle motion at the exit of the jet flow was recorded by a CCD-Camera (type: PCO SensiCam QE) with a resolution of 1376 x 1040 pixels. The light intensity resolution of the CCD-Camera was 12 Bit, corresponding to grey levels between 0 and 255. A 50 mm Nikkor lens with an aperture of $f = 4$ was used and a 10 mm adapter ring was connected between the lens and the CCD-Camera in order to obtain a large magnification. The CCD-Camera was operating in double shutter mode which allowed the recording of two images within a very short time delay. A pulsed LED light source was applied for the visualisation of the particles, which was positioned perpendicularly to the direction of the flow allowing the full visualisation of the particle motion at the exit of the jet. An opaque plate was fixed in front of the LED to produce diffuse illumination. Due to the applied backlight illumination method, particles appeared as shadows on the recorded images. A representation of the measurement system is demonstrated in Figure III-9.
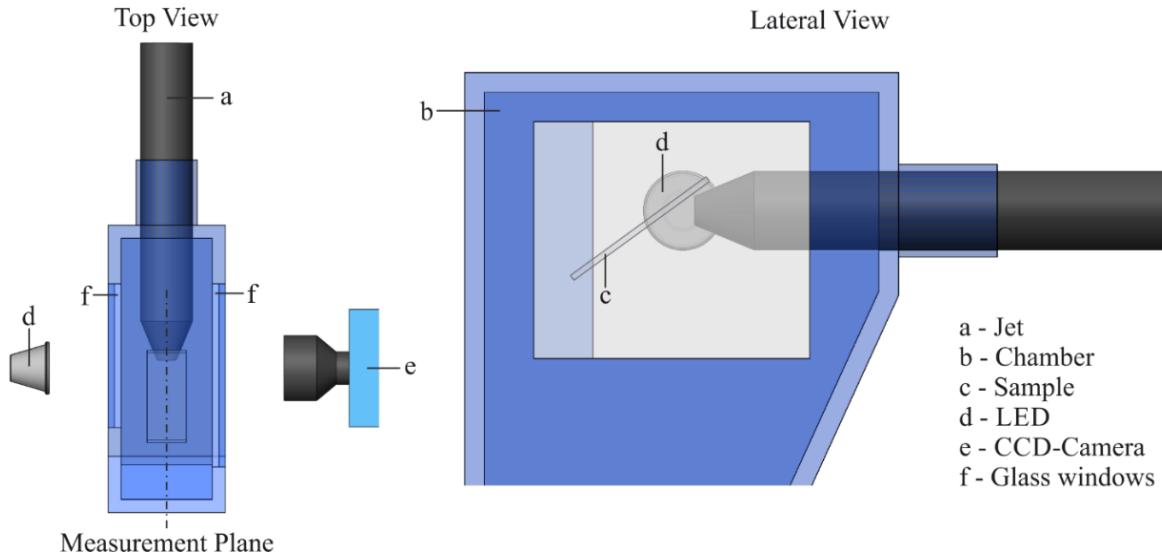
Figure III-9. Illustration of the measurement system.

The synchronisation of the CCD-Camera and the pulsed LED, as well as the pulse duration and the time delay between two pulses were performed by a 40MHz DDS function generator (Type: TG4001) with help of a signal controller. The duration of the light pulses was set to 10 µs while the time delay between two consecutive pulses was set to 20 µs. Additionally, a pair of images was recorded every 0.5 s, which allowed the recording of the particle motion for about 3 minutes before the memory of the CCD-Camera was full. Particle motion was recorded 5 times for each experiment totalizing a recording time of 15 minutes and 1,800 pair of images with a resolution of 1184 x 864 pixels. This procedure ensured that statistically reliable results for the particle velocity components were obtained. The calibrated pixel size was 20.83 µm, which resulted in a recording area of 24.66 x 18 mm. The recorded images were finally transferred from the CCD-Camera to the controlling computer. The particle image velocimetry (PIV) technique was applied to the recorded images to determine the velocity components of the particles, which required a digital image processing step. This step was accomplished by using an in-house image analysis tool, namely BIKO 3, together with the free and open-source software Fiji[96], which is a distribution of the free and open-source software ImageJ[97]. The in-house code BIKO 3 is written in DELPHI and based on the work of Bröder[98] and Bröder and Sommerfeld[99]. Firstly, the background was removed from the original images to remove all unnecessary objects, i.e. the plate and the jet. The background removal was performed using Fiji. Secondly, an edge detection filter (Marr and Hildreth[100]), namely Laplacian of Gaussian (LoG), was applied in order to detect particles on the images.

Thirdly, the images were binarized considering a constant threshold level since light intensity was practically constant for all images. Lastly, a median filter was used to remove remaining objects which were not removed by previously described filters. The application of these filters was carried out by using Biko 3. The same procedure was applied for quartz sand and spherical glass beads particles. Nevertheless, an additional morphological feature, namely fill holes, was applied to images containing spherical glass beads particles. Figure III-10 illustrates the described digital image processing step.
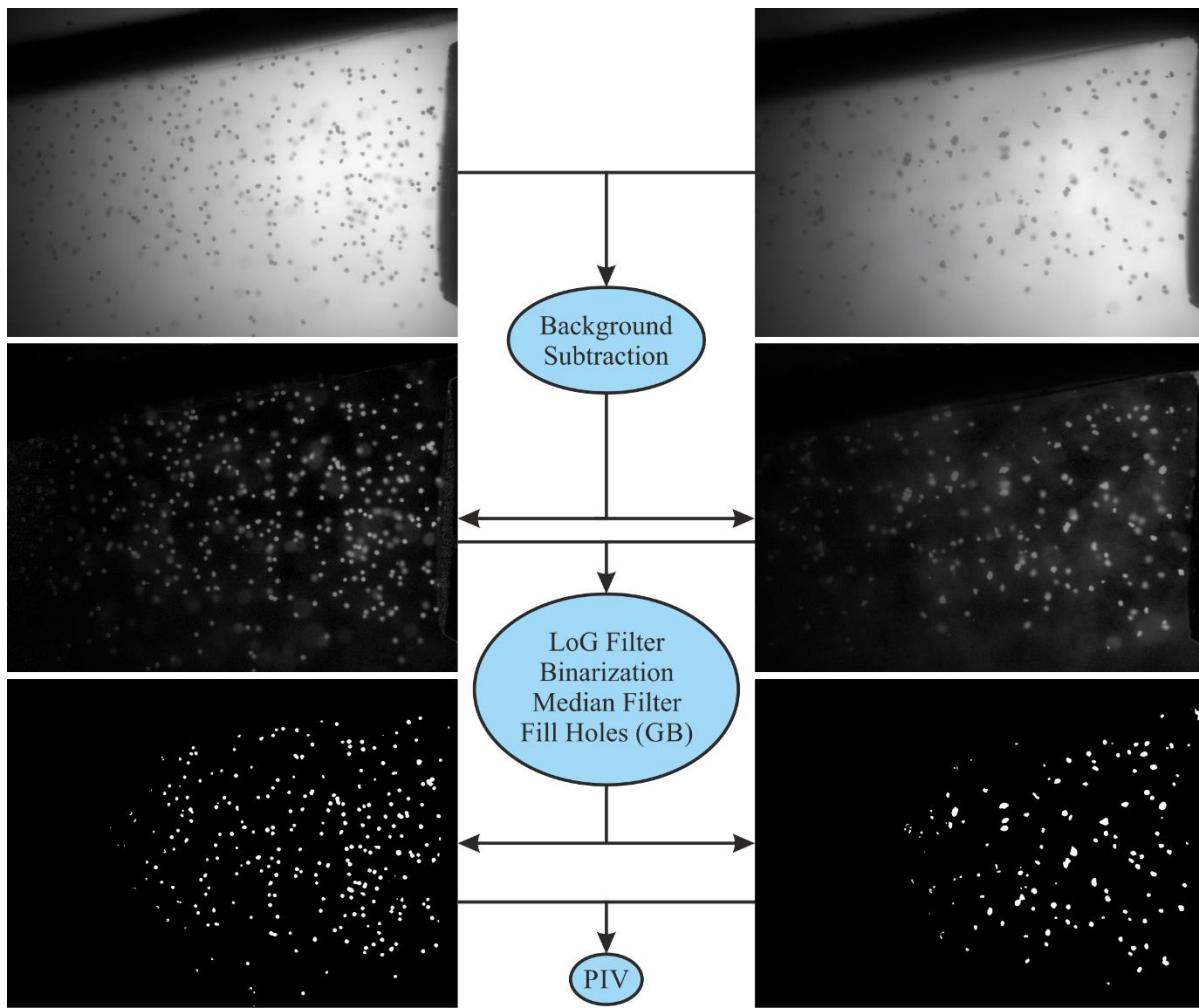
Figure III-10. Schematic diagram of filter operations for PIV. Left side: spherical glass beads. Right side: quartz sand. Impact angle: 10°. Top: raw images. Bottom: filtered images.

The application of PIV requires that images are split into several interrogation areas. Therefore, an in-house PIV algorithm[98,99] with iterative refinement of the interrogation area was utilized with an interrogation area size of 128 x 128 pixels (2.66 x 2.66 mm) for the first

step and 64 x 64 pixels (1.33 x 1.33 mm) for the second step with 50% overlapping of the interrogation areas, which yielded 34 x 24 vectors. The accuracy of PIV measurements mainly depends on the number of particles per interrogation area. Normally, particle concentration should be larger than about five particles per interrogation area for the application of PIV. This prerequisite was achieved in the measurements, especially in the jet exit, which is the region of interest in this work. A typical result of the mean particle velocity vector field obtained by the described method is shown in Figure III-11 for inclination angles of 10 and 20° considering spherical glass beads and quartz sand particles. The images were obtained by overlapping the original images with the particle velocity vector field. It should be noted that fluid and dispersed phase velocities were not measure simultaneously.
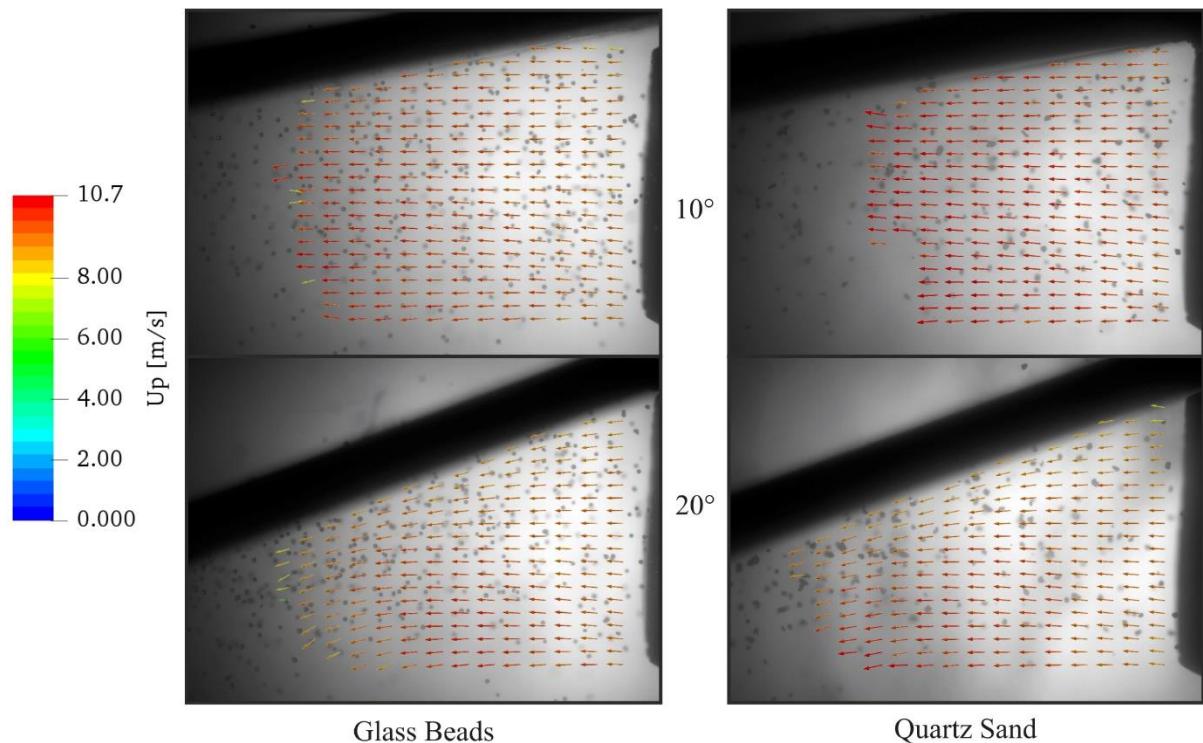
Figure III-11. Mean particle velocity field at the exit of the jet overlapped onto the original image containing the particles, the jet and the plate, coloured by the particle velocity magnitude and for impact angles of 10 and 20°.

Chapter IV

Pneumatic Conveying System – Bend Erosion

The pneumatic conveying system designed for obtaining experimental data on bend erosion along with the applied experimental techniques are presented in this chapter. Initially, the experimental facility is described. In the following, an experimental method for measuring erosion in terms of thickness loss is introduced. Finally, measurement techniques for acquiring fluid and dispersed phase velocities prior to the bends are presented.

4.1. Experimental Test Facility

For providing reliable data for erosion depth as well as air and particle velocity distributions, measurements were carried out in a pneumatic conveying test facility, as illustrated in Figure IV-1. The measuring section is composed of a 3.947 m long horizontal pipe, a 90° bend ($R_{bend,1} = 2.5D \pm 0.05D$), a 1.08 m long vertical pipe and a second 90° bend ($R_{bend,2} = 1.4D \pm 0.05D$). The inner diameter ($D$) and wall thickness of the pipes and bends

along the entire measuring section are 100 mm and 5 mm, respectively. The analysed bends were made of aluminium 6060-T66. In order to allow optical access for the application of laser-Doppler anemometer (LDA) and pulsed laser light sheet techniques, two 10 mm long glass pipes were inserted just before each one of the bends. The glass pipes were of the same inner diameter as the aluminium pipes to minimise disturbances of flow and particle motion.
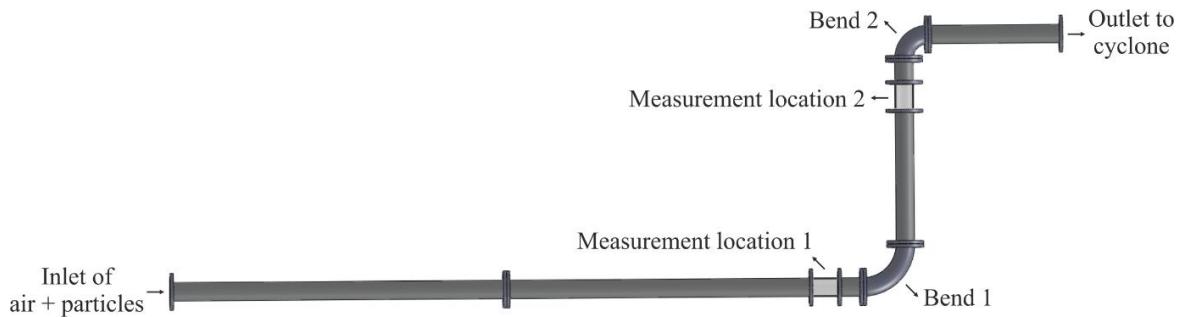
Figure IV-1. Representation of experimental pneumatic conveying system.

The required air flow rate of the system, which was provided by a blower, was adjusted to be almost constant during the measurements. The blower was connected to the measuring section by a 131 mm pipe and a cross section reducer. The air flow rate was monitored using an Annubar flow meter located 2 m before a mixing chamber. The air temperature at the measuring section entrance varied between 22 and 32 °C depending on the environmental temperature. This results in an air density deviation of approximately ± 1.7% around an average value of 1.176 kg/m³. An average air velocity of $U_0 = 37.9 \, m/s$ was considered in the experiments.

Prior to the pipe test section, particles were fed into the system by a screw feeder, which was connected to a mixing chamber mounted on the top of the 131 mm pipe. Air is injected into the mixing chamber at a lower pressure and higher velocity through a converging nozzle to ensure a continuous particle feeding. Particles exit the mixing chamber on the opposite side, in which a good particle dispersion within the pipe is achieved. Some fluctuations on the particle flow rate were produced by the screw feeder but became practically constant as a result of the mixing chamber. After the pipe system, particles were separated from the air using a cyclone separator and reinjected into the storage reservoir of the particle feeder through a rotary valve. Finally, the air from the cyclone flows through a bag filter to remove very fine

particles, mainly tracer particles or fine aluminium dust resulting from the erosion process and is released into the atmosphere thereafter.
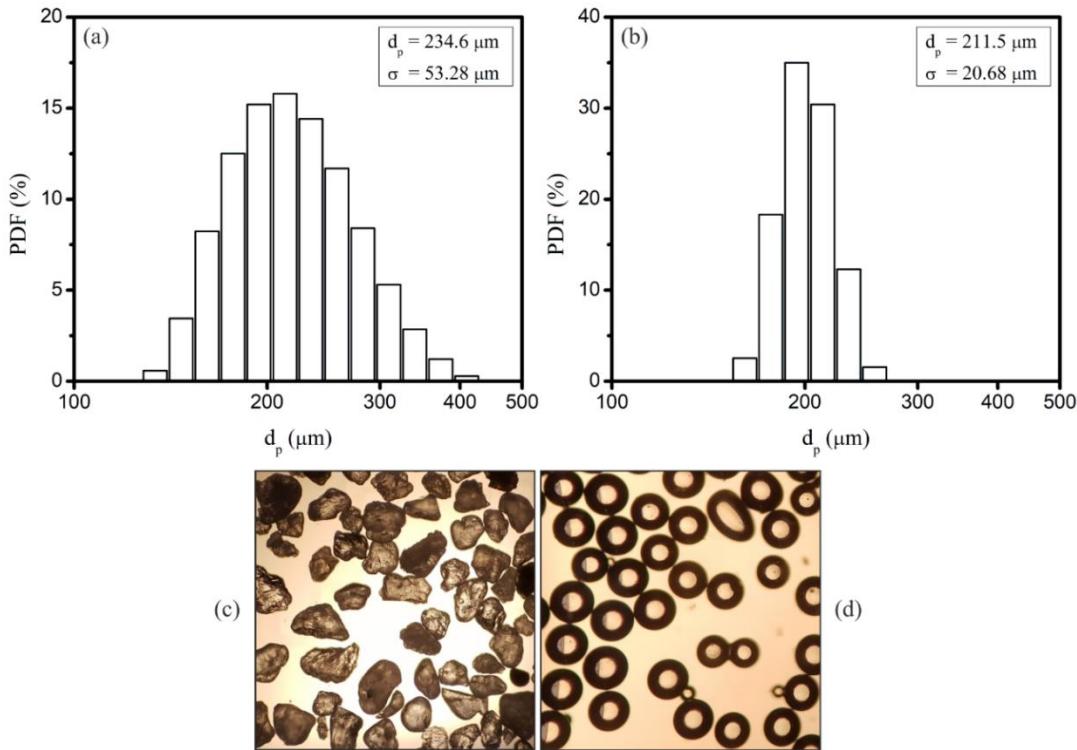
Figure IV-2. Measured number-based particle size distribution: (a) quartz sand and (b) spherical glass beads. Microscopic view of the particles: (c) quartz sand and (b) spherical glass beads.

The particles used in the present research were spherical glass beads ($\rho_p = 2500 \; kg/m^3$) and quartz sand ($\rho_p = 2650 \; kg/m^3$) with a number mean diameter, i.e. the sample mean diameter based on particle number, of 234.6 µm and 211.5 µm, respectively. The size distribution of both type of particles obtained by a laser diffraction particle size analyser is shown in Figure IV-2 together with their microscopic views. As rather large particles were used, adhesion forces could be neglected, and particles could be easily dispersed. Additionally, rope formation on the bottom of the horizontal pipe and particle sticking on walls were not observed due to high conveying velocity. Also, quartz sand particles were renewed 4 times during the experiments to avoid strong particle degradation. Moreover, two different mass loadings, i.e. η = 0.3 and 1.0 kg particles/kg air, were considered for both type of particles, which yields a particle mass flow of about 0.099 g/s and 0.33 g/s, respectively. Also, an error of about 2.1% was estimated in the particle mass loading. The experimental conditions as well as relevant wall material and particle properties are shown in Table IV-1.

Table IV-1. Experimental conditions and relevant properties.

Bulk air velocity [m/s]	37.9
Reynolds number [-]	$\approx 241{,}000$
Air temperature [°C]	27
Air pressure [Pa]	101325
Air density [kg/m^3]	1.176
Air viscosity [Pa·s]	18.46 10^{-6}
Mass loading of quartz sand [kg particles/kg air]	0.3 and 1.0
Quartz sand sphericity [-]	0.84
Quartz sand number mean diameter [μm]	234.6
Quartz sand density [kg/m^3]	2650
Mass loading of spherical glass beads [kg particles/kg air]	0.3 and 1.0
Spherical glass beads number mean diameter [μm]	211.5
Spherical glass beads density [kg/m^3]	2500
Bend material	Aluminium 6060-T66
Bend Vicker Hardness [GPa]	0.79
Glass beads with $\eta = 0.3$ and $\eta = 1.0$ – Experimental time [min]	580
Quartz sand with $\eta = 0.3$ – Experimental time [min]	580
Quartz sand with $\eta = 1.0$ – Experimental time [min]	300

4.2. Bend Erosion Measurements

For obtaining three-dimensional surface maps of the erosion scar resulting from particle impact by spherical glass beads and quartz sand for different particle mass loadings on the two 90° bends with different radii, an advanced, non-destructive testing ultrasonic wall thickness gauge, namely SONOWALL 70, was used together with two different measurement grids. The device uses ultrasonic technology, in which an ultrasonic wave is generated by a transducer. The ultrasonic wave is transmitted through the material structure and upon reaching a discontinuity, part of its energy echoes back to the transducer. Consequently, the thickness of the material may be obtained by correlating the time required for the ultrasonic wave to travel the material structure and the ultrasonic velocity, which is specific to each material. A SONOSCAN TXS10 EN probe with a centre frequency of 10 ±1 MHz and size of 8 mm was employed in this work. The transducer is composed of piezoelectric ceramics and allows

working temperatures between -20 °C and 60 °C. Additionally, a high precision mode was utilized with a resolution of 0.001 mm.

1.4D   2.5D

(a)   (b)   (c)
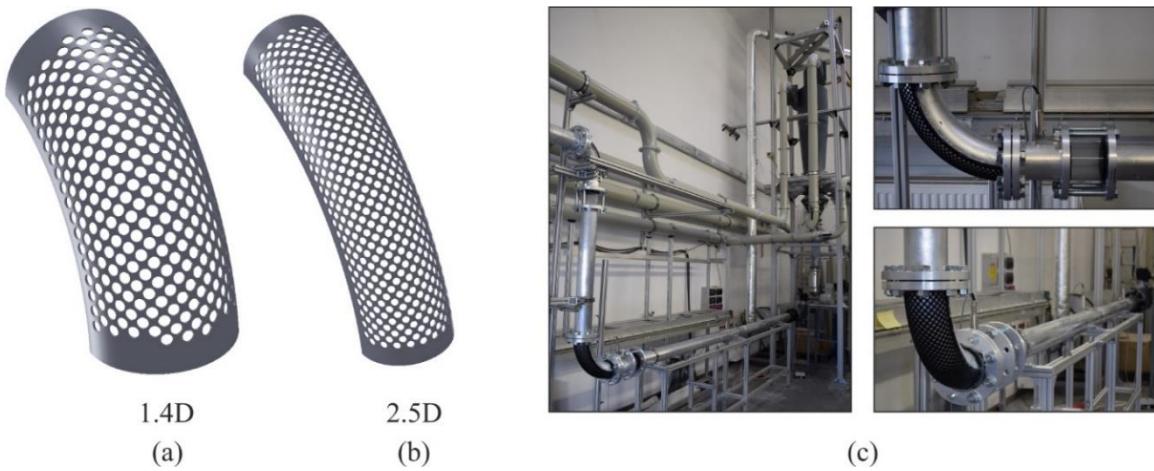
Figure IV-3. Details of the 3D-printed measurement grids for the (a) 1.4·D and (b) 2.5·D bends and (c) details of the pneumatic conveying facility and of the positioning of the 2.5·D grid on the outer bend surface.

In order to allow the precise positioning of the probe on the outer surface of the bends, two three-dimensional grids were 3D-printed and glued on each one of the bends, as shown in Figure IV-3. The grids were carefully glued as close as possible to the outer surfaces to minimize errors and movement of the probe. Moreover, the outer surface of the bends was polished to remove imperfections from the manufacturing process in order to reduce errors in the positioning of the measuring probe. The 1.4·D and 2.5·D grids are composed of 320 and 503 measurement points, respectively, allowing fine erosion profiles to be acquired. The bends are easily removable from the measurement sections and before each experiment the bends were fixed on a bench and all measuring points were acquired yielding the initial wall thickness profile. Then, after the experiments the bends were removed again, and the final state of erosion was obtained for all measurement points. Therefore, erosion depth was calculated by subtracting the final state from the initial state. An example of the initial and final state of bend 1 ($R_{bend,1} = 2.5 \cdot D$) eroded by quartz sand particles with a particle mass loading of $\eta = 1.0$ is illustrated in Figure IV-5. Additionally, by determining the three-dimensional location of each measuring point and applying a 2D Delaunay triangulation method, three-dimensional surface maps of the erosion scar for each experiment were generated. The location of each erosion profile on the outer wall of bend 1 is illustrated in Figure IV-4 (a) and (b), together

with the definition of the bend angle θ. The profiles are labelled 0, 1, 2, …, 9, in which 0 is the central profile along the bend. The angle between each profile is approximately 8.18°. The error associated with the positioning of the probe was estimated to be 30 µm. This value was obtained by averaging several measurements at a fixed location on the surface of the bend.
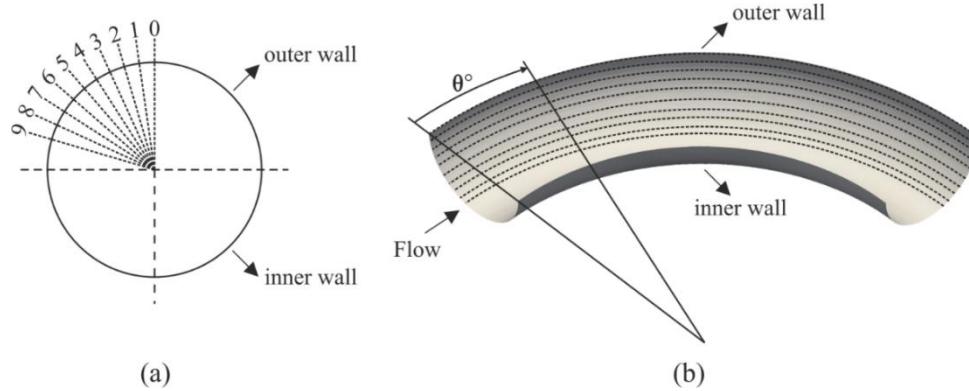
Figure IV-4. (a) location of each erosion profile on the outer surface of the bend, and (b) isometric view of the bend defining the bend angle θ ($R_{bend,1} = 2.5D$).
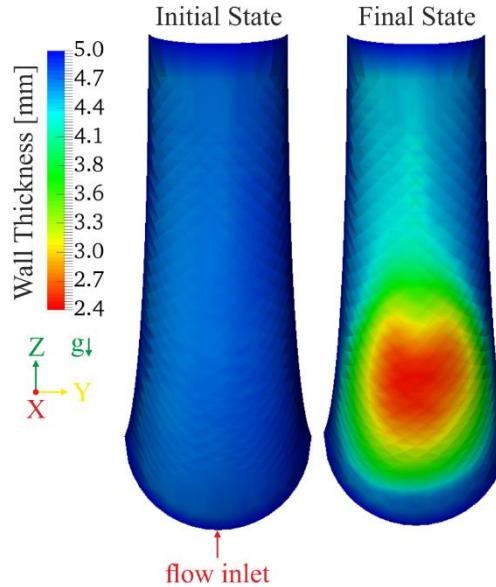
Figure IV-5. Visualization of the initial and final state of the bend 1 ($R_{bend,1} = 2.5 \cdot D$). Final state corresponds to 300 min of exposure to erosion. Results presented for a pneumatic conveying velocity of 37.9 m/s, quartz sand and $\eta = 1.0$.

4.3. Laser-Doppler Anemometry

For the measurement of air velocity distributions in both measurement locations a single velocity component laser-Doppler anemometer (LDA) was used as visualized in Figure IV-6 (a). To allow the precise positioning of the LDA beams within the glass pipe, the optical system was mounted on a computer-controlled 3D traversing system operated by step motors. Air velocity distributions were obtained by feeding glass spheres (type: Ballotini 5000 CP00) with a bulk density of 1.62 g/cm^3 and an average particle size of 7-10 µm into the system, which yields a particle response time and Stokes number of approximately 0.35 ms and of 0.16, respectively. Particle response time and Stokes number were calculated in accordance with Kussin and Sommerfeld[10]. In order to allow for statistically reliable measurements, a minimum of 15,000 samples were collected for each measurement point. It should be noted that the measurements of particles (laser-light sheet technique) and tracers (LDA) were performed separately.

4.4. Laser-Light Sheet Technique

For the visualization of particle motion within the pipe, the laser light sheet technique was used. For the first measurement area, the generated light sheet intersected the pipe from below at an angle of 90° with respect to the pipe central axis, and from left to right for the second measurement area, as shown in Figure IV-6 (b). The light sheet was produced by a 10W Argon-Ion laser which was mounted on a movable bench. A high-speed CMOS-Camera (type: FASTCAM SA4) with a resolution of 1024 x 1024 pixels and a light intensity resolution of 12 Bit was used for recording the particle motion. The lens used in the experiments was an 85 mm Nikkor with an aperture opening of $f = 1.4$. A 10 mm extension tube was connected between the CMOS-Camera and the lens in order to obtain a large magnification. The frame rate was set to 48,000 fps for all measurements and the calibrated pixel size was 84.4 µm, which resulted in a total recording area of about 10.8 x 31.06 mm (128 x 368 pixels) for the bottom measurement location and 48.61 x 10.8 mm (576 x 128 pixels) for the upper measurement location. As the measurement of the entire vertical plane across the horizontal

pipe, for example, was impossible, sets of measurements were performed in order to obtain a full description of the particle velocity distributions within the vertical plane across the pipe. For instance, this was achieved by positioning the camera at the bottom wall of the horizontal pipe and after completing the first measurement, the camera was moved upwards with a known distance with the help of the computer-controlled 3D traversing system and the second measurement was initiated. After acquiring all necessary sets of measurement, the images were stitched together and a full visualization of particle motion within the pipe was obtained.
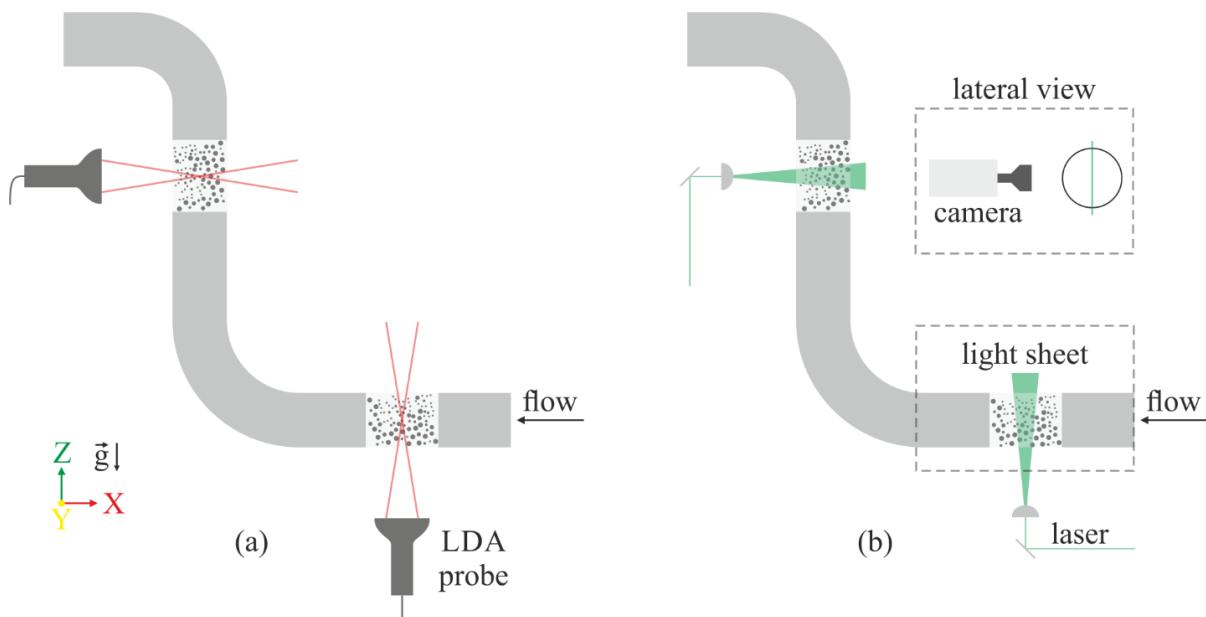
Figure IV-6. Illustration of the measurement system: (a) LDA measurements of air velocity and (b) laser-light sheet technique for measuring particle velocity. The measurements of particles (laser-light sheet technique) and tracers (LDA) were performed separately.

To extract the particle velocity distributions from the recorded images, the particle image velocimetry (PIV) method was applied. The application of PIV requires a digital image processing step, which is performed as follows:

- background subtraction from the images,
- detection of particles on the images by applying an edge detection filter (Marr and Hildreth[100]), namely Laplacian of Gaussian (LoG),
- binarization of the images with a constant threshold level,
- and application of a median filter.

The first step was performed by using the free and open-source software Fiji[96,97] while the remaining filters were applied by using an in-house image analysis tool (Biko 3), for which more details can be found in Bröder and Sommerfeld[98,99]. The same procedure was applied for both spherical glass beads and quartz sand particles. Figure IV-7 illustrates a final image obtained after the application of the described digital image processing step.
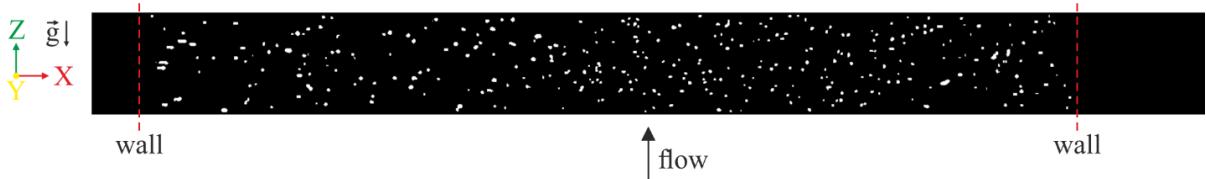
Figure IV-7. Image obtained after digital image processing step for quartz sand particles in the top measurement location with $\eta = 1.0$.

Additionally, in order to apply the PIV method, the images need to be split in several interrogation areas. Therefore, a PIV algorithm (Bröder and Sommerfeld[99]) with iterative refinement of the interrogation area was utilized. The first and second refinement steps considered an interrogation area size of 24 x 24 pixels (2.02 x 2.02 mm) and 16 x 16 pixels (1.35 x 1.35 mm), respectively. Moreover, a 50% overlapping of the interrogation areas was used. The PIV accuracy mainly depends on particle concentration per interrogation area, in which the number of particles should be normally higher than about 5 per interrogation area. This prerequisite was mostly achieved in all experiments.

Chapter V

The Euler-Lagrange Approach

The classical transient, three-dimensional and coupled Euler-Lagrange approach is adopted to model the pneumatic conveying systems presented in Chapter VI. Therefore, this chapter is aimed to present the fundamentals of the Euler-Lagrange approach. The chapter is divided into two major sections. The first section presents the governing equations for the fluid phase in its general form as well as the turbulence modeling. The second section is devoted to introducing the equations of motion for solid particles and to describe all relevant forces acting on them. Moreover, models for elementary processes such as turbulent dispersion of particles, particle-wall interaction with rough walls, particle-particle interaction and erosion modelling are detailed. All Euler-Lagrange calculations are performed by using the free and open-source code OpenFOAM® 4.1.

5.1. Continuous Phase

The fluid phase is predicted by solving the discretized form of the Reynolds-Averaged Navier-Stokes (RANS) equations in connection with the standard k-ε turbulence model. The

time-dependent, incompressible and three-dimensional governing equation for the continuous phase in its general form and including the influence of dispersed phase is written as:

$$(\rho\phi)_{,t} + (\rho U_i \phi)_{,i} = \left(\Gamma_{ik}\phi_{,k}\right)_{,i} + S_\phi + S_{\phi p} \qquad \text{(V-1)}$$

where ρ is the fluid density, U_i are the Reynolds-averaged velocity components and Γ_{ik} is an effective transport tensor. The temporal change and the convective term are represented by the first and the second term on left side of Equation (V-1) while on its right side the diffusion and source terms appear. S_ϕ summarizes the source terms of the fluid phase and $S_{\phi p}$ represents additional source terms due to phase interaction (detailed in Section 5.3). The effective transport tensor and the corresponding source terms are summarized in Table V-1 for different transport variables ϕ as presented by Laín and Sommerfeld[101].

Table V-1. Summary of the terms in the general transport equation for different transport variables that describe the fluid phase in connection with the standard k-ε turbulence model.

ϕ	Γ_{ik}	S_ϕ	$S_{\phi p}$
1	0	0	0
U_j	$(\mu + \mu_T)\delta_{ik}$	$P_{,k} + \left(\Gamma_{jk}U_{i,k}\right)_{,i} - \left(2/3\,\rho k + \mu_T U_{k,k}\right)_{,j} + \rho g_j$	$S_{U,p}$
k	$(\mu + \mu_T/\sigma_k)\delta_{ik}$	$P - \rho\varepsilon$	$S_{k,p}$
ε	$(\mu + \mu_T/\sigma_\varepsilon)\delta_{ik}$	$c_{\varepsilon 1}P\,\varepsilon/k - \rho c_{\varepsilon 2}\,\varepsilon^2/k$	$S_{\varepsilon,p}$

In Table 1, P is the mean pressure, μ is the dynamic fluid viscosity, μ_T is the turbulent viscosity and g_j is the gravitational acceleration. k and ε are the turbulent kinetic energy and turbulent dissipation rate, respectively. The resulting set of partial differential equations describe mass and momentum conservation. The remaining terms are expressed as follows:

$$\mu_T = \rho C_\mu\, k^2/\varepsilon \qquad \text{(V-2)}$$

$$P = -\rho R_{ij}U_{i,j} \qquad \text{(V-3)}$$

$$\rho R_{ij} = \left(2/3\,\rho k + \mu_T U_{k,k}\right)\delta_{ik} - \mu_T\left(U_{i,j} + U_{j,i}\right) \qquad \text{(V-4)}$$

$$C_\mu = 0.09 \qquad c_{\varepsilon 1} = 1.44 \qquad c_{\varepsilon 2} = 1.92 \qquad \sigma_k = 1.0 \qquad \sigma_\varepsilon = 1.3 \qquad \text{(V-5)}$$

The conservation equations are discretized by applying the finite volume method, which is naturally implemented in OpenFOAM®. Thus, the conservation equations are integrated over each control volume of the numerical domain, which results in a set of discrete equations that represents the conservation laws in each control volume. The time discretization is performed by using a transient and second order implicit numerical scheme, referred to as *backward* scheme. The discretization of gradient and divergence terms was performed by applying a second order numerical scheme, which is denominated as Gauss linear method. The Gaussian integration requires the interpolation of values from the cell centres to face centres, which is achieved via linear interpolation. The solution of the discretized equations is accomplished by using an iterative procedure which couples the momentum and mass conservation equations, namely the PIMPLE algorithm. This algorithm is a combination of PISO (Pressure Implicit with Splitting of Operator, Issa[102]) and SIMPLE (Semi Implicit Method for Pressure-Linked Equations, Patankar and Spalding[103]) algorithms. The SIMPLE algorithm is used for steady-state calculations whereas the PISO and PIMPLE algorithms are applied for transient computations. The PIMPLE iterative procedure is advantageous over PISO as it allows for large time steps and consequently, stable solutions even for a maximum Courant number above 1 may be achieved. As mentioned, the standard k-ε model is applied to model turbulence in the continuous phase and in order to reduce grid size and computational effort, wall functions are used to model near-wall regions. The necessity of wall functions rises from the fact that many computational cells need to be used to resolve the boundary layer in the vicinity of the walls, which requires the first computational cell in the near-wall region to be within the viscous sublayer, i.e. at approximately $y^+ = 1$. The implemented wall functions in OpenFOAM are based on the work of Kalitzin et al.[104] and they provide accurate results for any location of the centre of the first cell above the wall.

5.2. Dispersed Phase

The Lagrangian approach is applied to simulate the motion of the dispersed phase, in which particles are considered as point-masses and assumed to be spherical (except for the drag force for quartz sand particles). This approach relies on tracking a large number of particles throughout the flow field, yet the simulation of the real number of particles is

impossible due to the computational effort required. Instead, the parcel concept is generally used, in which a computational parcel represents several real particles with the same properties in order to achieve the correct particle mass flux injected into the system. This concept greatly reduces the number of particles to be tracked and consequently, the required computational effort. The dispersed phase is tracked transiently in the Lagrangian framework by solving the equations of motion for each computational parcel. Hence, the position as well as the linear and angular momentum may be predicted by solving the following set of ordinary first order differential equations:

$$\frac{dx_{pi}}{dt} = u_{pi} \tag{V-6}$$

$$m_p \frac{du_{pi}}{dt} = \frac{3}{4} \frac{\rho}{D_p} m_p C_D (u_i - u_{pi}) |\vec{u} - \vec{u}_p| + m_p g_i \left(1 - \frac{\rho}{\rho_p} \right) + \vec{F}_{lsi} + \vec{F}_{lri} \tag{V-7}$$

$$I_p \frac{d\omega_{pi}}{dt} = T_i \tag{V-8}$$

where u_{pi} are the linear velocity components of the particle, ω_{pi} are the angular velocity components of the particle, x_{pi} are the coordinates of particle position, D_p is the particle diameter and ρ and ρ_p are the fluid and particle density, respectively. Furthermore, $u_i = U_i + u_i'$ is the instantaneous velocity of the air and $I_p = 0.1 m_p D_p^2$ and $m_p = (\pi/6)\rho_p D_p^3$ are, respectively, the moment of inertia for a sphere and the particle mass. Finally, F_{lsi}, F_{lri} and T_i are the slip-shear lift force, the slip-rotational lift force and the torque acting on the rotating particle, respectively. By reason of high ratio of densities, other forces such as added mass or Basset force can be considered negligible. Therefore, the new parcel location, linear and angular velocities are calculated by integrating the described differential equations (V-6), (V-7) and (V-8). A brief description of all relevant forces acting on particles is presented in the following.

Drag Force

In most gas-solid flows the drag force is the main mechanism of particle transport and consists of a friction and form drag. The drag force is expressed for higher particle Reynolds

number by introducing a drag coefficient C_D, which is expressed by Crowe et al.[7] and Sommerfeld et al.[6] for spherical particle as:

$$C_D = \frac{\vec{F}_D}{\rho_f/2 \left(\vec{U}_f - \vec{u}_p\right)^2 A_p}$$

(V-9)

where $A_p = \pi/4 \, D_p^2$ is the cross-section area of a sphere, ρ_f is the fluid density, $\vec{U}_f$ and $\vec{u}_p$ are the fluid and particle velocity vectors, respectively. $\vec{F}_D$ corresponds to the drag force and is defined as:

$$\vec{F}_D = \frac{3}{4}\frac{\rho_f m_p}{\rho_p D_p} C_D \left(\vec{U}_f - \vec{u}_p\right)\left|\vec{U}_f - \vec{u}_p\right|$$

(V-10)

with m_p, ρ_p and D_p being the particle mass, density and diameter, respectively. The drag coefficient is expressed as a function of the particle Reynolds number Re_p according to the empirical correlation from Schiller and Naumann[105]:

$$Re_p = \frac{\rho_f D_p \left(\vec{U}_f - \vec{u}_p\right)}{\mu_f}$$

(V-11)

$$\begin{cases} Re_p < 0.5 & C_D = \dfrac{24}{Re_p} \\[2mm] 0.5 < Re_p < 1000 & C_D = \dfrac{24}{Re_p}\left(1 + 0.15Re_p^{0.687}\right) \\[2mm] Re_p > 1000 & C_D \approx 0.44 \end{cases}$$

(V-12)

where μ_f is the fluid dynamic viscosity. As quartz sand particles were used in the experiments, the empirical correlation from Haider and Levenspiel[106] is used for evaluating the drag coefficient for non-spherical particles:

$$\begin{aligned} C_D = \frac{24}{Re}&\left[1 + exp(2.3288 - 6.4581\phi + 2.4486\phi^2)Re^{(0.0964+0.5565\phi)}\right] \\ &+ \frac{Re \times exp(4.905 - 13.8944\phi + 18.4222\phi^2 - 10.2599\phi^3)}{Re + exp(1.4681 + 12.2584\phi - 20.7322\phi^2 + 15.8855\phi^3)} \end{aligned}$$

(V-13)

where ϕ is particle sphericity (see Table IV-1).

Gravity Force

The gravity force is a body force and is simply expressed as follows:

$$\vec{F}_g = m_p \vec{g}$$
(V-14)

where $\vec{g}$ is the gravitational acceleration.

Buoyancy Force

An additional force rises from the local pressure gradient in the flow in the direction of the pressure gradient, which may be expressed according to Crowe et al.[7] and Sommerfeld et al.[6] as:

$$\vec{F}_P = \frac{m_p}{\rho_p} (-\nabla P + \nabla \cdot \vec{\tau})$$
(V-15)

In Equation (V-15), ∇P and $\nabla \vec{\tau}$ are the pressure gradient and the divergence of the fluid shear stress, respectively, which are related to the fluid acceleration and the gravity force as follows:

$$-\nabla P + \nabla \vec{\tau} = \rho_f \left(\frac{D\vec{U}_f}{Dt} - \vec{g} \right)$$
(V-16)

In gas-solid flows the pressure force may be neglected as $\rho_f / \rho_p \ll 1$, which yields the buoyancy force:

$$\vec{F}_P = -m_p \frac{\rho_f}{\rho_p} \vec{g}$$
(V-17)

Nevertheless, in liquid-solid flows the pressure force is of importance as $\rho_f / \rho_p \approx 1$.

Slip-Shear Lift Force

Due to the non-uniform relative velocity over the particle and the resulting non-uniform pressure distribution, particles moving in a shear layer experience a transverse lift force, which is referred to as the Saffman force. The calculation of the slip-shear lift force is based on analytical results of Saffman[107] and extended for high particle Reynolds number according to Mei[108]:

$$\vec{F}_{ls} = 1.615 D_p \mu_f Re_s^{0.5} C_{ls}\left[(\vec{U}_f - \vec{u}_p) \times \vec{\omega}_f\right] \tag{V-18}$$

where $\vec{\omega}_f = \nabla \times \vec{U}_f$ is the fluid vorticity, $Re_s = \rho_f D_p^2 |\vec{\omega}_f|/\mu_f$ is the particle Reynolds number of the shear flow and $C_{ls} = F_{ls}/F_{ls,Saff}$ represents the ratio of the extended lift force to the Saffman force:

$$C_{ls} = \begin{cases} (1 - 0.331\sqrt{\beta})e^{-Re_p/10} + 0.331\sqrt{\beta} & Re_p \leq 40 \\ 0.0524 & Re_p > 40 \end{cases} \tag{V-19}$$

with β being a parameter given by $\beta = 0.5\, Re_s/Re_p$.

Slip-Rotation Lift Force

In pneumatic conveying systems high particle rotation may be induced by particle-wall and particle-particle interaction, which results in a deformation of the flow field around the particle, associated with a shift of the stagnation points and a transverse lift force (Sommerfeld et al.[6]). Therefore, particles may experience a lift force due to their rotation, the so-called Magnus force. The slip-rotation lift force is calculated based on the correlation given by Rubinow and Keller[109], which was extended to higher particle Reynolds number (Crowe et al.[7]):

$$\vec{F}_{lr} = \frac{\rho_f}{2}\frac{\pi}{4} D_p^2 C_{lr} |\vec{U}_f - \vec{u}_p| \frac{\vec{\Omega} \times (\vec{U}_f - \vec{u}_p)}{|\vec{\Omega}|} \tag{V-20}$$

In Equation (V-20), $\vec{\Omega} = 0.5\nabla \times \vec{U}_f - \vec{\omega}_p$ is the relative rotation and $\vec{\omega}_p$ is the particle angular velocity. The dependency of the lift coefficient C_{lr} on high particle Reynolds number is evaluated via the correlation proposed by Oesterlé and Bui Dinh[110]:

$$C_{lr} = 0.45 + \left(\frac{Re_R}{Re_p} - 0.45\right) e^{-0.05684Re_R^{0.4}Re_p^{0.3}} \quad for \quad Re_p < 140 \tag{V-21}$$

with Re_R being the Reynolds number of particle rotation:

$$Re_R = \frac{\rho_f D_p^2 |\vec{\Omega}|}{\mu_f} \tag{V-22}$$

Torque

The expression of Rubinow and Keller[109], which was extended to account for the relative motion between particle and fluid and higher Reynolds number, is used to calculate the torque acting on the rotating particle and is given by:

$$\vec{T} = C_R \frac{\rho D_p^5}{64} |\vec{\Omega}|\vec{\Omega} \tag{V-23}$$

where C_R is the rotational coefficient, which is obtained from Rubinow and Keller[109] for small Reynolds number of particle rotation ($Re_R < 32$) and the direct numerical simulations of Dennis et al.[111] and the experimental data of Sawatzki[112] for $32 < Re_R < 1000$ in the following form:

$$C_R = \begin{cases} \dfrac{64\pi}{Re_R} & for \quad Re_p \le 32 \\ \dfrac{12.9}{\sqrt{Re_R}} + \dfrac{128.4}{Re_R} & for \quad 32 < Re_R < 1000 \end{cases} \tag{V-24}$$

5.3. Influence of Particles on the Carrier Flow

The influence of particles on the fluid phase, i.e. the momentum exchange between both phases, is accounted for through an additional source term in the momentum equation of the continuous phase as follows:

$$S_{\phi p} = \overline{S_{U,p}} = -\frac{1}{V_{cv}\Delta t_E}\sum_{i=1}^{N}\left(\vec{F}_D + \vec{F}_{ls} + \vec{F}_{lr} - m_p\vec{g}\left(1 - \frac{\rho_F}{\rho_p}\right)\right)_i \Delta t_L \qquad (V\text{-}25)$$

where the summation is performed over all particles within a computational cell with volume V_{cv}, and Δt_E and Δt_L are the Eulerian and Lagrangian time steps, respectively. ρ_F and ρ_p are the density of the fluid and particle phase, respectively. $\vec{F}_D$ is drag force, $\vec{F}_{ls}$ defines the slip-shear lift force, and $\vec{F}_{lr}$ represents the slip-rotation lift force. Finally, m_p and $\vec{g}$ are the particle mass and the gravitational acceleration. In this work, the influence of particles on turbulent properties is neglected and therefore, no source terms appear in the equations for k and ε.

The source term in the conservation equation of the turbulent kinetic energy, k, is expressed in the Reynolds average procedure as:

$$S_{kp} = \overline{u_i S_{U,p}} - U_i\overline{S_{U,p}} \qquad (V\text{-}26)$$

whilst the source term in the ε-equation is modelled in the standard way:

$$S_{\varepsilon p} = C_{\varepsilon 3}\frac{\varepsilon}{k}S_{kp} \qquad (V\text{-}27)$$

with $C_{\varepsilon 3} = 1.8$ and the sum is implicit in the repeated sub-index i. Equations (V-26) and (V-27) are expressed as in Laín and Sommerfeld[101]. Although the modelling of the influence of the particles on turbulent properties is presented here, its effect was neglected in the simulations.

5.4. Turbulent Dispersion of Particle

The effect of turbulence on particle dispersion is described by a single-step isotropic Langevin model as proposed and validated by Sommerfeld et al.[113]. The model predicts the new fluctuating velocity of the fluid seen by the particle based on a correlated contribution from the previous time step and a stochastic influence which is sampled from a normal distribution function with a standard deviation of the local fluid velocity fluctuation:

$$u'^{n+1}_i = R_{P,i}(\Delta t_L, \Delta r)u'^n_i + \sigma_F\sqrt{1 - R^2_{P,i}(\Delta t_L, \Delta r)}\xi_i \qquad \text{(V-28)}$$

In Equation (V-28), the superscripts denote the time step and subscripts the spatial components. Δt_L is the Lagrangian time step and Δr is the spatial distance between the virtual fluid element and the Lagrangian particle during the time step Δt_L. Assuming isotropic turbulence σ_F represents the rms value of the fluid velocity fluctuation and ξ_i describes independent Wiener processes with zero mean and unit standard deviation, i.e. no correlation between the three velocity components is considered. The term $R_{P,i}(\Delta t_L, \Delta r)$ represents a correlation function which is predicted by Lagrangian and Eulerian components:

$$R_{P,i}(\Delta t_L, \Delta r) = R_L(\Delta t_L)R_{E,ij}(\Delta r) \qquad \text{(V-29)}$$

The Lagrangian correlation function $R_L(\Delta t_L)$ defines the instantaneous velocity fluctuation along the way of a virtual fluid element and depends on the Lagrangian integral time scale:

$$R_L(\Delta t_L) = \exp\left(-\frac{\Delta t_L}{T_L}\right) \qquad \text{(V-30)}$$

$$T_L = C_T\frac{\sigma_F^2}{\varepsilon} \qquad \text{(V-31)}$$

with $C_T = 0.24$ and $\sigma_F^2 = {}^2\!/_3\,k$. The Eulerian correlation function $R_{E,ij}(\Delta r)$, which describes the deviation of the particle trajectory from the path of the virtual fluid element, i.e. the so-called crossing trajectory effect, is expressed as:

$$R_{E,ij}(\Delta r) = \{f(\Delta r) - g(\Delta r)\}\frac{\Delta r_i \Delta r_j}{|\Delta r|^2} + g(\Delta r)\delta_{ij} \qquad \text{(V-32)}$$

where δ_{ij} is the Kronecker delta and $f(\Delta r)$ and $g(\Delta r)$ are the longitudinal and transverse two-points correlation functions[113,114]:

$$f(\Delta r) = \exp\left(-\frac{\Delta r}{L_E}\right) \qquad \text{(V-33)}$$

$$g(\Delta r) = \left(1 - \frac{\Delta r}{2L_E}\right)\exp\left(-\frac{\Delta r}{L_E}\right) \qquad \text{(V-34)}$$

where the Eulerian length scale L_E is calculated as:

$$L_E = C_L \sigma_F T_L \qquad \text{(V-35)}$$

with $C_L = 3.0$.

5.5. Particle-Wall Interaction with Rough Surfaces

Particle-wall interaction is an important process which influences particle transport behaviour in confined flows, such as in pneumatic conveying systems. For modelling the surface roughness effect Sommerfeld[76] adopted a stochastic approach by assuming that the particle impact angle with respect to the surface α_1 is composed of the particle trajectory angle α_0 and a stochastic contribution due to the surface roughness:

$$\alpha_1 = \alpha_0 + \xi\Delta\gamma \qquad \text{(V-36)}$$

Sommerfeld and Huber[115] carried out experiments which showed that the distribution of the roughness angle may be approximated by a normal distribution function with a standard deviation of $\Delta\gamma$. Herein, ξ represents a Gaussian random variable with zero mean and a standard deviation of one. Furthermore, $\Delta\gamma$ depends on surface roughness structure and particle size. In order to estimate $\Delta\gamma$ two different scenarios are considered: (1) particle diameter is smaller than the mean spacing between peaks of the roughness profile, i.e. $D_p < RS_m$, and (2)

particle diameter is bigger than the mean spacing between peaks of the roughness profile, i.e. $D_p \geq RS_m$. Hence, the surface roughness effect on the collision process is larger for small particles than for bigger particles, as illustrated in Figure V-1.
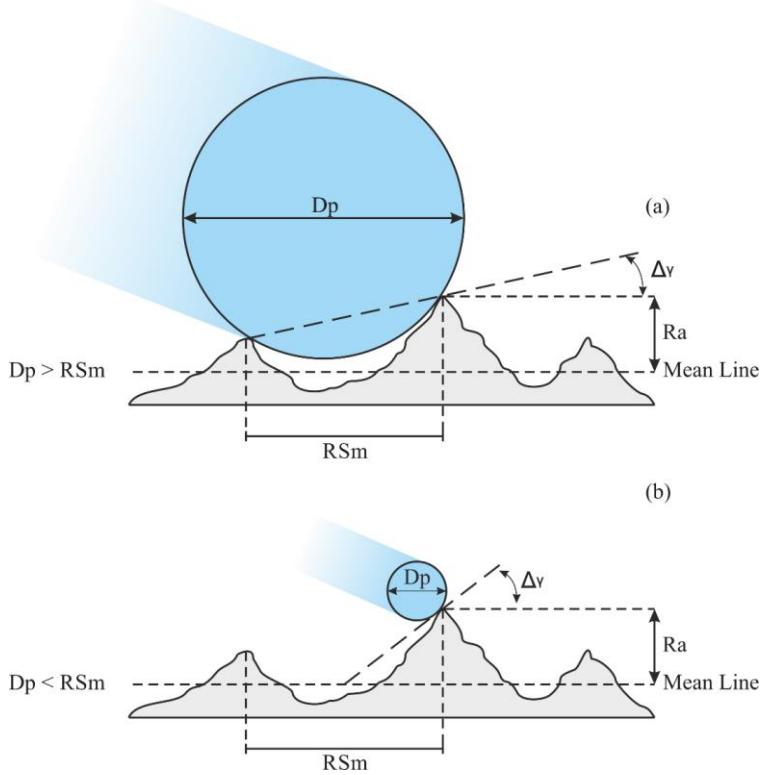
Figure V-1. Particle-wall interaction with rough surfaces: (a) large particles and (b) small particles.

Based on the described scenarios and the work of Sommerfeld[76] the standard deviation of the roughness angle may be estimated as follows:

$$\begin{cases} \Delta\gamma = \tan^{-1}\left(\dfrac{2R_a}{RS_m}\right) & if \quad D_p < RS_m \\[2ex] \Delta\gamma = \tan^{-1}\left(\dfrac{R_a}{2RS_m}\right) & if \quad D_p \geq RS_m \end{cases} \tag{V-37}$$

Moreover, small particles may not hit the lee side of a roughness structure, which results in a higher probability for the particle to hit the luff side, phenomenon which is referred to as shadow effect and it is illustrated in Figure V-2. The shadow effect shifts the probability distribution function of the effective roughness angle towards positive values. Based on Figure V-2 (b) and for a given combination of α_0 and γ, three regimes may be identified:

1   The probability of a particle to hit a roughness structure with $|\gamma^-| > \alpha_0$ is zero, which corresponds to the red region in Figure V-2 (b). Therefore, $f(\alpha_0, \gamma) = 0$.

2   In the interval $0 < |\gamma^-| > \alpha_0$, the probability to hit a roughness structure with negative inclination is smaller than that to hit a horizontal wall by the factor $f(\alpha_0, \gamma) = \frac{sin(\alpha_0 + \gamma^-)}{sin(\alpha_0)}$. This regime corresponds to the yellow region in Figure V-2 (b).

3   The probability to hit a positive inclination, i.e. $|\gamma^+| > \alpha_0$, becomes higher by the factor $f(\alpha_0, \gamma) = \frac{sin(\alpha_0 + \gamma^+)}{sin(\alpha_0)}$, which is illustrated by the green region in Figure V-2 (b).

According to the possible three regimes, the shadow effect is considered by multiplying the effective roughness angle distribution function P_{eff} by the following probability function:

$$f(\alpha_0, \gamma) = \frac{sin(\alpha_0 + \gamma)}{sin(\alpha_0)} \tag{V-38}$$

By applying Equation (V-38), P_{eff} is automatically shifted towards positive values and expressed as:

$$P_{eff}(\alpha_0, \Delta\gamma, \gamma) = P(\Delta\gamma, \gamma)\, f(\alpha_0, \gamma) = \frac{1}{\sqrt{2\pi\Delta\gamma^2}} exp\left(-\frac{\gamma^2}{2\Delta\gamma^2}\right) \frac{sin(\alpha_0 + \gamma)}{sin(\alpha_0)} \tag{V-39}$$
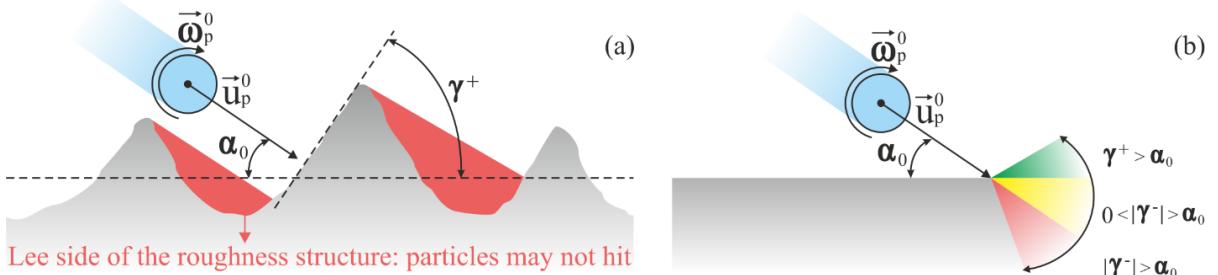
Figure V-2. Illustration of shadow effect due to wall roughness for small particles (a). Effective impact regime for stochastic modelling of rough surfaces (b).

The change of linear and angular momentum of the particle during a particle-wall interaction is based on the solution of the impulse equations coupled with Coulomb's law of friction, which yields a set of equation for a sliding and non-sliding collision process, as shown

by Sommerfeld[76] and Tsuji et al.[116]. The modelling approach is based on the so-called hard sphere model, which implies that particle deformation during the collision process is negligible. According to this approach, a compression and recovery period are identified for an inelastic collision process, in which collisions may be distinguished into three types:

- Type 1: the particle stops sliding in the compression period;

- Type 2: the particle stops sliding in the recovery period;

- Type 3: the particle slides during the entire collision process.
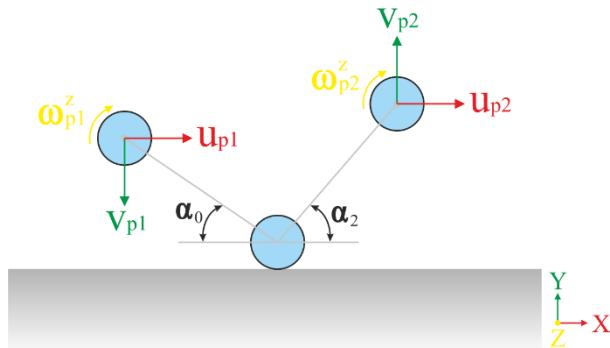
Figure V-3. Definition of particle velocity components and angles before impact and after rebound.

Collision Type 1 and 2 are referred to as *non-sliding collision* while collision Type 3 as *sliding collision*. For the description of equations that follows, the subscripts 1 and 2 refer to prior and after the collision, respectively. Additionally, u_P, v_P and w_P are the linear velocity components in the x-, y- and z-direction and ω_P^x, ω_P^y and ω_P^z are the angular velocity components of the particle in the co-ordinate system illustrated in Figure V-3. Consequently, a non-sliding collision occurs whether the following condition is met:

$$|u_{R1}| \leq \frac{7}{2} \mu_s (1 + e)\, v_{p1} \tag{V-40}$$

where u_{R1} is the velocity of the particle surface in relation to the contact point, μ_s is the static friction coefficient, and e is the normal restitution coefficient. If Equation (V-40) is not satisfied, a sliding collision occurs. u_{R1} is calculated as:

$$u_{R1} = \sqrt{\left(u_{P1} - \frac{D_P}{2}\omega_{P1}^z\right)^2 + \left(w_{P1} + \frac{D_P}{2}\omega_{P1}^x\right)^2} \qquad \text{(V-41)}$$

The set of equations which describes the change of linear and angular momentum of a particle during a particle-wall interaction considering a non-sliding and a sliding collision is presented in Equation (V-42).

non-sliding collision	**sliding collision**

$$u_{P2} = \frac{5}{7}\left(u_{p1} - \frac{D_P}{5}\omega_{P1}^z\right) \qquad\qquad u_{P2} = u_{P1} + \mu_d\,\epsilon_x\,(1+e)\,v_{p1}$$

$$v_{P2} = -e\,v_{p1} \qquad\qquad\qquad v_{P2} = -e\,v_{p1}$$

$$w_{P2} = \frac{5}{7}\left(w_{p1} + \frac{D_P}{5}\omega_{P1}^x\right) \qquad\qquad w_{P2} = w_{P1} + \mu_d\,\epsilon_z\,(1+e)\,v_{p1}$$

$$\text{(V-42)}$$

$$\omega_{P2}^x = \frac{2\,w_{P2}}{D_P} \qquad\qquad \omega_{P2}^x = \omega_{P1}^x - 5\,\mu_d\,\epsilon_z\,(1+e)\frac{v_{p1}}{D_P}$$

$$\omega_{P2}^y = \omega_{P1}^y \qquad\qquad\qquad \omega_{P2}^y = \omega_{P1}^y$$

$$\omega_{P2}^z = -\frac{2\,u_{P2}}{D_P} \qquad\qquad \omega_{P2}^z = \omega_{P1}^z + 5\,\mu_d\,\epsilon_x\,(1+e)\frac{v_{p1}}{D_P}$$

In Equation (V-42), μ_d is the dynamic friction coefficient, and ϵ_x and ϵ_z are factors which indicate the proportion and direction of the motion of the particle surface with respect to the wall:

$$\epsilon_x = \left(\frac{u_{P1} - \frac{D_P}{2}\omega_{P1}^z}{u_{R1}}\right) \qquad\qquad \text{(V-43)}$$

$$\epsilon_z = \left(\frac{w_{P1} + \frac{D_P}{2}\omega_{P1}^x}{u_{R1}}\right) \qquad\qquad \text{(V-44)}$$

In order to apply the described modelling approach, e, μ_s and μ_d need to be prescribed. These parameters are not only dependent on particle and wall material, but also on particle impact angle and velocity, as demonstrated by Sommerfeld and Huber[85]. Based on their

experimental work and on Laín and Sommerfeld[13], the restitution and dynamic friction coefficients are expressed as a function of the particle impact angle (in degrees) for spherical particles as:

$$e = max(1 - 0.0136\alpha_1, 0.7) \tag{V-45}$$

$$\mu_d = max(0.5 - 0.0175\alpha_1, 0.15) \tag{V-46}$$

In the case of quartz sand particles interacting with aluminium surfaces, the correlation proposed by Grant and Tabakoff[74] is used to compute the restitution coefficient. The correlation was obtained after analysing the post-collisional particle velocity by using a statistical approach and is computed as follows:

$$e = 0.993 - 1.76\alpha_1 + 1.56\alpha_1^2 - 0.49\alpha_1^3 \tag{V-47}$$

$$\sigma_e = 2.15\alpha_1 - 5.02\alpha_1^2 + 4.05\alpha_1^3 - 1.085\alpha_1^4 \tag{V-48}$$

where σ_e represents the standard deviation of the restitution coefficient. In Equations (V-47) and (V-48), the particle impact angle is given in radians.

5.6. Particle-Particle Interaction

In confined, gas-solid flows particle-particle interaction is of great importance especially for high mass loadings. In this work, particle-particle interaction is accounted for stochastically rather than deterministically, by applying the methodology described in detail in Sommerfeld[90]. The stochastic particle-particle interaction model relies on the generation of a fictitious collision partner based on the local properties of real particles within a computational cell. Therefore, during each time step of the particle tracking, the diameter, the size-dependent linear and angular velocity components of the fictitious particle are sampled from previously stored distribution functions of real particles. As no information on the real position and properties of all other surrounding particles during each time step is required, the stochastic approach requires much less computational effort than the deterministic approach. The stochastic model also assumes that only binary collision may occur during a Lagrangian

time step and no particle deformation is considered explicitly during a collision, i.e. hard sphere model assumption.

The size of the fictitious particle is randomly sampled from the local particle size distribution, which must be sampled and stored for each computational cell of the entire computational domain. The fictitious particle velocity is composed by the local mean velocity and fluctuating components of real particles. Moreover, the fluctuating components of the fictitious particle is sampled from a Gaussian velocity distribution with the local rms-value and correlated to the velocity of the considered particle due to turbulence, which depends on the Stokes number, i.e. the ratio of particle response time to the Lagrangian integral time scale of turbulence. Therefore, the fictitious particle velocity $u_{p,j}$ is expressed as:

$$u_{p,j} = \bar{u}_{p,i} + u'_{p,j}$$

(V-49)

$$u'_{p,j} = R(St)\, u'_{p,i} + \sigma_{p,i}\sqrt{1 - R(St)^2}\, \xi$$

(V-50)

where $\bar{u}_{p,i}$ is the local mean velocity, $u'_{p,j}$ are the fluctuating velocity components, $u'_{p,i}$ is the fluctuating velocity of the real particle, $\sigma_{p,i}$ is the local rms-value and ξ is a Gaussian random number with zero mean and a standard deviation of one. In the right-hand side of Equation (V-50), the first term is the correlated part while the second term is a random contribution. As presented by Sommerfeld[90], the correlation function $R(St)$ is found by comparing model calculation with large eddy simulation (LES) and it is expressed as follows:

$$R(St) = exp(-0.55\, St^{0.4})$$

(V-51)

By increasing the Stokes number, i.e. large particles, the correlated term is decreased while the random part is increased accordingly. The Stokes number St is computed accounting for non-linear drag and the Lagrangian integral time scale T_L is obtained from the turbulent dispersion model (Section 5.4):

$$St = \frac{\tau_p}{T_L}$$

(V-52)

$$\tau_p = \frac{\rho_p D_p^2}{18\mu_f f_D} \tag{V-53}$$

$$f_D = \frac{C_D Re_p}{24} \tag{V-54}$$

where τ_p is the particle response time. Additionally, whether a particle size distribution is considered, the particle mean and rms velocities are sampled and stored for each size class.

The local properties of the real particles are sampled and stored for each computational cell at the beginning of the Eulerian time step and are updated in the next one. Also, a fictitious particle is generated at each Lagrangian time step within a Eulerian time step. After sampling the fictitious collision partner the collision probability is calculated to decide whether a collision takes place or not. Therefore, in the following sections the calculation of the collision probability and impact efficiency, as well as the particle velocity change due to particle-particle interaction, are detailed.

Collision Probability and Impact Efficiency

To decide whether a collision between the real and fictitious occurs, a collision probability P_{coll} is defined which depends on particle size and fluctuating motion of particles as well as on particle concentration within a computational cell. The collision probability is a product of the collision frequency f_c and the Lagrangian time step according to the kinetic theory and is calculated as:

$$P_{coll} = f_c \Delta t_L = \frac{\pi}{4}\left(D_{pi} - D_{pj}\right)^2 \left|\vec{u}_{pi} - \vec{u}_{pj}\right| \frac{n_p}{V_c} \Delta t_L \tag{V-55}$$

in which the subscripts i and j refer to real and fictitious particle, respectively. D_p represents the particle diameter and $\vec{u}_p$ is the particle velocity. n_p describes the number of particle per volume of the computational cell V_c and, whether a particle size distribution is considered, it represents the number concentration of all particle fractions, as the fictitious particle is sampled from the particle size distribution which already accounts for the probability of a particle being in a certain size interval. The particle-particle collision is solved in a co-ordinate system where

the fictitious particle is stationary, in which a collision cylinder is defined with an axis aligned with the direction of the relative velocity between the real and fictitious particle, as shown in Figure V-4 (b).

The collision point is determined randomly, in which the fictitious particle is considered stationary. Thus, the point of impact in the longitudinal section of the collision cylinder is characterized by a non-dimensional lateral displacement L_a and the angle ϕ, which are determined randomly as:

$$L_a = \frac{2L}{D_{pc} + D_{ps}} = \sqrt{XX^2 + ZZ^2} \ \ with \ L_a < 1 \tag{V-56}$$

$$\phi = arcsin(L_a) \tag{V-57}$$

with L being the lateral displacement and XX and ZZ random numbers in the range [0,1]. Also, the orientation angle of the collision plane in the cross-sectional area of the collision cylinder is randomly predicted from a uniform distribution function in the range of $[0 < \Psi < 2\pi]$.
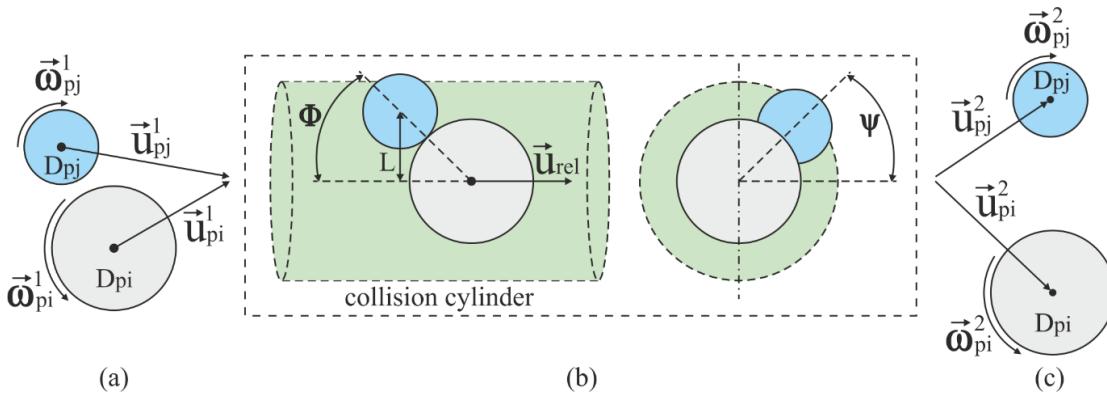
Figure V-4. (a) Representation of the real and fictitious particle before collision. (b) Illustration of particle-particle interaction in a co-ordinate system with a stationary collision partner. (c) Representation after collision.

Additionally, impact efficiency may be reduced for particles with different sizes as a small particle could follow the relative flow around a larger particle (collector) and not collide with the collector particle, as illustrated in Figure V-5. According to Sommerfeld[90], the impact efficiency defines the ratio of the circular cross-section with radius Y_c to the cross section of the collision cylinder, from where the small particle could come and still hit the collector

particle. Schuch and Löffler[117] proposed the following correlation to describe the impact efficiency η_p:

$$\eta_p = \left(\frac{2Y_c}{D_{pc} + D_{ps}}\right)^2 = \left(\frac{St_{Rel,i}}{St_{Rel,i} + a}\right)^b \tag{V-58}$$

where D_{pc} is the diameter of the collector particle, D_{ps} is the diameter of the smaller particle, Y_c is the radial distance, $St_{Rel,i}$ is the relative Stokes number, and a and b are parameter which depend on the Reynolds number of the collector (see Table V-2).
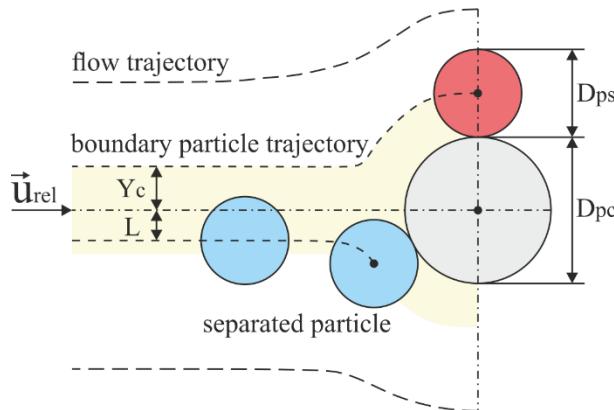
Figure V-5. (a) Illustration of the impact efficiency whether small particles are considered. The grey particle represents the collector particle, the red particle travels around the collector particle not colliding with it and blue particle collides with the collector particle.

Additionally, $St_{Rel,i}$ represents the ratio of the small particle response time to the time required to pass the collector, which is expressed as follows:

$$St_{Rel,i} = \frac{\rho_p \left|\vec{u}_{pc} - \vec{u}_{ps}\right| D_{ps}^2}{18 \, \mu_f \, f_D D_{pc}} \tag{V-59}$$

$$f_D = \frac{C_D Re_{pc}}{24} \tag{V-60}$$

$$Re_{pc} = \frac{\rho_f D_{pc} \left|\vec{U}_f - \vec{u}_{ps}\right|}{\mu_f} \tag{V-61}$$

Finally, a collision between a real and fictitious particle occurs if the following conditions are met:

$$RN < P_{coll} \quad and \quad L < Y_c \tag{V-62}$$

where RN is an uniform random number in the range [0,1]. Therefore, the prediction of post-collisional linear and angular velocities of the real particle are carried out in co-ordinate system where the fictitious particle is stationary by solving the momentum equation connected with the Coulomb`s law of friction, as detailed in the next section.

Table V-2. Constants for the impact efficiency proposed by Schuch and Löffler[117].

	a	b
$Re_{pc} < 1$	0.65	3.7
$1 < Re_{pc} < 20$	1.24	1.95
$20 < Re_{pc} < 40$	1.03	2.07
$40 < Re_{pc} < 80$	0.506	1.84
$Re_{pc} > 80$	0.25	2.0

Particle Velocity Change due to Particle-Particle Interaction

The set of equations which describes the change of linear and angular velocity components during a particle-particle interaction is obtained considering the following assumptions: (i) only binary collisions may occur, which is valid for most dispersed two-phase systems; (ii) the energy dissipation due to particle deformation during a collision is described by a normal restitution ratio (hard sphere model); (iii) a sliding collision is described by the Coulomb's law of friction. Therefore, the change in the particle linear and angular velocity due to particle-particle interaction is described by solving the momentum equation in connection with the Coulomb's law of friction, which yields relations for a sliding and a non-sliding collision. Thus, the change of particle linear and angular momentum is calculated by the following impulse equations:

$$m_{pi}\left(\vec{u}_{p2,i} - \vec{u}_{p1,i}\right) = m_{pj}\left(\vec{u}_{p2,j} - \vec{u}_{p1,j}\right) = \vec{J} \tag{V-63}$$

$$\frac{I_{pi}}{R_{pi}}\left(\vec{\omega}_{p2,i} - \vec{\omega}_{p1,i}\right) = \frac{I_{pj}}{R_{pj}}\left(\vec{\omega}_{p2,j} - \vec{\omega}_{p1,j}\right) = -\vec{n} \times \vec{J} \tag{V-64}$$

where m_p is the particle mass, $I_p = 0.1 m_p D_p^2$ is moment of inertia for a sphere, $\vec{n}$ is an unit vector and $\vec{J}$ is the impulse force vector. $\vec{u}_p$ and $\vec{\omega}_p$ are the particle linear and angular velocity vectors, respectively. The subscripts i and j denote real and fictitious particle, respectively, and 1 and 2 refer to before and after collision. By transforming the particle velocities into a coordinate system where the fictitious particle is stationary and the relative velocity vector corresponds to the axis of the collision cylinder, the following set of equations are obtained to calculate the new linear (Equation (V-65)) and angular (Equation (V-66)) velocity components of the real and fictitious particle in terms of the relative velocity components before collision:

<div align="center">

Real Particle i   **Fictitious Particle j**

</div>

$$u_{p2,i} = u_{p1,i} + \frac{J_x}{m_{pi}} \qquad\qquad u_{p2,j} = -\frac{J_x}{m_{pj}}$$

$$v_{p2,i} = v_{p1,i} + \frac{J_y}{m_{pi}} \qquad\qquad v_{p2,j} = -\frac{J_y}{m_{pj}} \qquad\qquad \text{(V-65)}$$

$$w_{p2,i} = w_{p1,i} + \frac{J_z}{m_{pi}} \qquad\qquad w_{p2,j} = -\frac{J_z}{m_{pj}}$$

<div align="center">

Real Particle i   **Fictitious Particle j**

</div>

$$\omega_{p2,i}^x = \omega_{p1,i}^x \qquad\qquad\qquad \omega_{p2,j}^x = \omega_{p1,j}^x$$

$$\omega_{p2,i}^y = \omega_{p1,i}^y - \frac{5 J_z}{m_{pi} D_{pi}} \qquad\qquad \omega_{p2,j}^y = \omega_{p1,j}^y + \frac{5 J_z}{m_{pj} D_{pj}} \qquad\qquad \text{(V-66)}$$

$$\omega_{p2,i}^z = \omega_{p1,i}^z + \frac{5 J_y}{m_{pi} D_{pi}} \qquad\qquad \omega_{p2,j}^z = \omega_{p1,j}^z - \frac{5 J_y}{m_{pj} D_{pj}}$$

with J_x, J_y and J_z being the components of the impulsive force. By defining a normal restitution ratio $e = (u_{p2,i} - u_{p2,j})/u_{p1,i}$, and with $J_x = -m_{pj} u_{p2,j}$, the impulsive force in the x-direction is expressed as:

$$J_x = -(1 + e)\, u_{p1,i} \frac{m_{pi}\, m_{pj}}{m_{pi} + m_{pj}} \qquad\qquad \text{(V-67)}$$

A relation for a sliding and non-sliding collision is obtained in terms of the velocities of both particles before collision by applying the Coulomb's law of friction:

$$|u_R| < \frac{2}{7}\mu_0(1 + e)\,|u_{\mathrm{p1},i}| \tag{V-68}$$

where μ_0 is the static coefficient of friction. Additionally, the relative velocity components at the point of contact u_R, u_{Ry} and u_{Rz} are computed in terms of the linear and angular velocity components of the real and fictitious particle as:

$$u_R = \sqrt{u_{Ry}^2 + u_{Rz}^2} \tag{V-69}$$

$$u_{Ry} = v_{\mathrm{p1},i} + \frac{D_{pi}}{2}\,\omega_{\mathrm{p1},i}^z + \frac{D_{pj}}{2}\,\omega_{\mathrm{p1},j}^z \tag{V-70}$$

$$u_{Rz} = w_{\mathrm{p1},i} - \frac{D_{pi}}{2}\,\omega_{\mathrm{p1},i}^y - \frac{D_{pj}}{2}\,\omega_{\mathrm{p1},j}^y \tag{V-71}$$

Finally, the components of the impulsive force in the y- and z-direction are calculated and distinguished into a sliding and non-sliding collision as follows:

non-sliding collision	**sliding collision**	
$J_y = -\dfrac{2}{7}\,u_{Ry}\,\dfrac{m_{pi}\,m_{pj}}{m_{pi}+m_{pj}}$	$J_y = -\mu_d\,\dfrac{u_{Ry}}{u_R}\,|J_x|$	
$J_z = -\dfrac{2}{7}\,u_{Rz}\,\dfrac{m_{pi}\,m_{pj}}{m_{pi}+m_{pj}}$	$J_z = -\mu_d\,\dfrac{u_{Rz}}{u_R}\,|J_x|$	(V-72)

where μ_d is the dynamic coefficient of friction.

5.7. Lagrangian Time Step

The Lagrangian time step Δt_L is calculated dynamically and was chosen to be 20% of the smallest of all relevant time scales to ensure stability of the numerical integration scheme (Göz et al.[118]). Therefore, Δt_L is computed as follows:

$$\Delta t_L = 0.2\min\left(\Delta t_{cv}, T_L, \tau_p, \tau_{coll}\right) \qquad\qquad\text{(V-73)}$$

Δt_{cv} is the time required for a particle to cross a control volume, which means that the selected Eulerian time step Δt_E should be small enough to ensure a Courant number smaller than one. T_L is the Lagrangian integral time scale of turbulence and is calculated according to Equation (V-31). The particle response time is defined as $\tau_p = \rho_p D_p^2 / 18\mu_f$. τ_{coll} is the average between inter-particle collisions and is computed as $\tau_{coll} = 1/f_c$, with f_c being the collision frequency which is detailed in Section 5.6 according to Equation (V-55).

5.8. Semi-unsteady Euler-Lagrange approach

The semi-unsteady Euler-Lagrange approach is used in this work, which reduces the computational cost in relation to the fully unsteady approach. The fully unsteady approach requires equal time step for both the Eulerian and Lagrangian parts, in which the overall time step is governed by the smallest time step of all calculated entities. Typically, the Eulerian time step for unsteady RANS simulations may be found in the range of $\Delta t_E = [10^{-4}s; 10^{-1}s]$, while the Lagrangian time step may lie in the range of $\Delta t_L = [10^{-10}s; 10^{-1}s]$ depending on particle response time, Lagrangian time scale and the local grid resolution[119]. Therefore, coupled calculations may be slowed down significantly when particles require a very small time step. However, as the time scales of the Eulerian phase are usually much higher than those of the Lagrangian phase, the temporal solution of each individual phase may be performed in a semi-unsteady approach.

In the semi-unsteady approach, the governing equations of the Eulerian phase are solved first for one Eulerian time step and the resulting flow field information is "frozen" and passed to the Lagrangian part. Afterwards, particles are tracked individually through the frozen fluid field. Within the Eulerian time step, particle tracking is sub-divided into several Lagrangian time steps, which are dynamically calculated considering all relevant time scales (see Section 5.7). In addition, if the size of the Lagrangian time step reaches beyond the end of the Eulerian time step, it will be reduced appropriately. Finally, after tracking the particles

within a Eulerian time step, the resulting source terms are transferred back to the Eulerian phase and solution continues. The semi-unsteady approach is illustrated in Figure V-6.
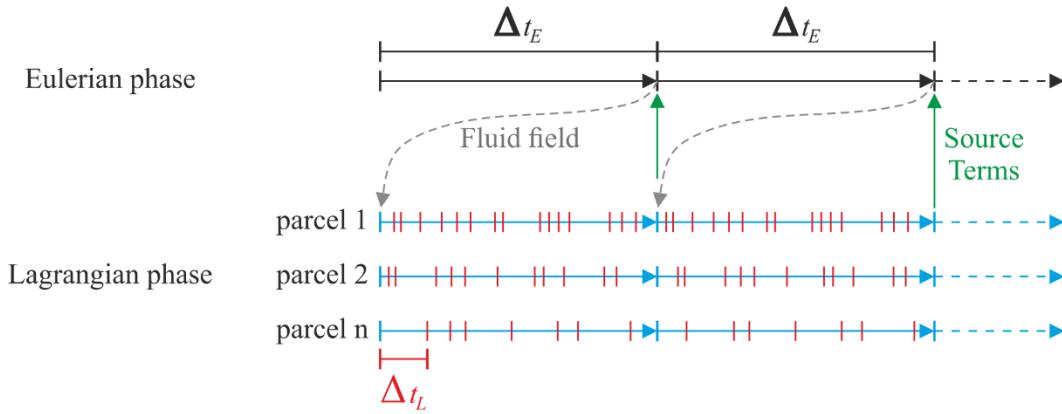
Figure V-6. Illustration of the semi-unsteady Euler-Lagrange approach[119]: the information of fluid field calculated for a Eulerian time step is given to the Lagrangian part. The particles are tracked with dynamically determined time steps in this "frozen" field. The calculated particle source terms are used in the calculation of the next Eulerian time step.

5.9. Erosion Models

This section details how erosion prediction is performed numerically and presents the erosion models used in this work. Erosion wear is generally defined as the mass or volume of removed material per mass of particle. Numerically, the wear is predicted as the sum of the damage caused by each individual particle-wall collision divided by the total injected mass of erodent:

$$E_S = \sum_{i=1}^{N_S} m_{pi} E_i \Big/ m_T \qquad \text{(V-74)}$$

where E_S is the total erosion ratio at each surface element area, E_i is the erosion caused by particle i and must be computed by an erosion correlation, m_{pi} is the mass of the particle i and m_T is the total injected mass of erodent. Herein the erosion damage is calculated numerically in terms of the penetration ratio, $E_{PR}\left(m/kg_p\right)$, given by:

$$E_{PR} = 10^{-9} \frac{E_S}{A_S} \tag{V-75}$$

with A_S being the surface element area and 10^{-9} is a constant that has the dimension of m^3/mm^3. The erosion correlations, expressed by E_i, are presented in the following. It should by noted that depending on the erosion correlation used, the units need to be converted accordingly. A brief description of the predictive equations used in this work is presented in the following sections.

Oka Model

The erosion model proposed by Oka et al.[31] and Oka and Yoshida[32] is applicable to many types of materials under various conditions involving particle impact angle and velocity as well as particle size and properties and therefore, is considered in this work and briefly described below. The predictive equation can be expressed as:

$$E(\alpha) = g(\alpha)E_{90} \tag{V-76}$$

In Equation (V-76), $E(\alpha)$ and E_{90} represent the volume of eroded material per mass of particle, in which E_{90} express the erosion damage at normal impact angle. $g(\alpha)$ is a function of the impact angle which describes the simultaneous phenomena of cutting and repeated deformation wear, and it is given by:

$$g(\alpha) = (\sin \alpha)^{n_1}[1 + Hv(1 - \sin \alpha)]^{n_2} \tag{V-77}$$

where Hv is initial Vickers hardness of the eroded material. The term $(\sin \alpha)^{n_1}$ is associated with repeated plastic deformation reaching its maximum at normal angle. On the other hand, the term $[1 + Hv(1 - \sin \alpha)]^{n_2}$ characterizes the cutting wear, which is more pronounced at shallower impact angles. The exponents n_1 and n_2 are determined by the eroded material hardness and other properties such as particle shape as follows:

$$\begin{cases} n_1 = s_1(Hv)^{q_1} \\ n_2 = s_2(Hv)^{q_2} \end{cases} \tag{V-78}$$

The erosion at normal angle E_{90} depends on the impact velocity, particle diameter and eroded material hardness accordingly to:

$$E_{90} = K(a \, Hv)^{k_1 b} \left(\frac{u_p}{u_{ref}} \right)^{k_2} \left(\frac{D_p}{D_{ref}} \right)^{k_3} \tag{V-79}$$

In Equation (V-79), u_p and D_p are respectively the impact velocity and particle diameter, u_{ref} and D_{ref} are the impact velocity and diameter used as reference in the experiments conducted by Oka et al.[31] and Oka and Yoshida[32]. K is a particle property factor which considers the particle shape, e.g. angularity, and particle hardness and it assumes an arbitrary unit. The exponents k_1 and k_3 are calculated based on the properties of the particle and are expressed in arbitrary units. k_3 is found by the authors to be roughly constant. k_2 depends on the Vickers hardness of the eroded material and on particle properties and can be expressed by:

$$k_2 = r(Hv)^p \tag{V-80}$$

According to the authors, the term $K(a \, Hv)^{k_1 b}$ in Equation (V-80) is highly dependent on the Vickers hardness of the eroded material and type of particle, which are not correlated with the impact conditions and other factors. The relationship between the Vickers hardness of the eroded material and E_{90} at the reference impact velocity for the materials investigated in this work are derived from the experimental data from the authors and are presented in Table V-3.

Table V-3. Parameters of the Oka model[31,32].

Particle Type	K	k_1	k_2	k_3	u_{ref}	D_{ref}	n_1	n_2
Quartz Sand	50	-0.12	$2.3(Hv)^{0.038}$	0.19	104	326	$0.71(Hv)^{0.14}$	$2.4(Hv)^{-0.94}$
Glass Beads	27	-0.16	2.1	0.19	100	200	$2.8(Hv)^{0.41}$	$2.6(Hv)^{-1.46}$

Finnie Model

Finnie[20] proposed the first single-particle erosion model for ductile materials, which assumes that a particle impacting on a surface with an impingement angle α removes material

from the surface by displacement or cutting action of the abrasive particle. Therefore, the surface of the material is assumed to deform plastically, and the particle does not break upon impact. The predictive equation is expressed as:

$$E = \begin{cases} \dfrac{M\vec{u}_p^2}{p\psi K}\left(\sin(2\alpha) - \dfrac{6}{K}\sin^2(\alpha)\right) & for \quad \alpha \le \dfrac{6}{K} \\[3mm] \dfrac{M\vec{u}_p^2}{p\psi K}\left(\dfrac{K\cos^2(\alpha)}{6}\right) & for \quad \alpha > \dfrac{6}{K} \end{cases} \tag{V-81}$$

where M is the total mass of particles, $\vec{u}_p$ is the particle impact velocity, p is flow stress of the material surface, ψ is the ratio of the depth of contact to the depth of cut, and K is the ratio of normal to tangential force. The first equation, i.e. for $\alpha \le 6/K$, corresponds to the case in which the particle leaves the material surface while still cutting while the second equation, this means for $\alpha > 6/K$, corresponds to the case in which the horizontal motion of the particle stops while cutting. In his work, Finnie assumed $K = 2$ and $\psi = 2$ and additionally, that many particles are not as effective as the idealized particle and therefore, Finnie arbitrarily chose a 50% off the predicted erosion. For erosion predictions with the Finnie model, a value of 2.7 GPa is assumed for p.

Zhang Model

Zhang et al.[68] proposed the flowing predictive erosion equation:

$$E = C(BH)^{-0.59}F_s V_p^n F(\alpha) \tag{V-82}$$

where C and n are empirical constants, BH is the Brinell hardness of the target material, F_s is a particle shape coefficient, V_p is the particle impact velocity, α is the impact angle and $F(\alpha)$ is a function of the impact angle. $F(\alpha)$ is modelled as follows:

$$F(\alpha) = 5.4\alpha - 10.11\alpha^2 + 10.93\alpha^3 - 6.33\alpha^4 + 1.42\alpha^5 \tag{V-83}$$

C and n assume values equal to $2.17 \cdot 10^{-7}$ and 2.41, respectively. The particle shape coefficient F_s assumes a value of 0.2 for spherical particle, 0.53 for semi-rounded particle and

1 for angular (sharp) particle. This predictive equation depends entirely on flow information and eroded material properties and consequently, as the Oka model, is very robust.

Neilson and Gilchrist Model

Neilson and Gilchrist[22] simplified the model proposed Bitter[16,21], which resulted in the following predictive equation for the total erosion:

$$E = E_C + E_D \tag{V-84}$$

in which E_C and E_D represent the combined contributions from cutting and deformation wear, respectively. As usual, the cutting wear is computed as a function of the particle impact angle in the following form:

$$E_C = \begin{cases} \dfrac{M\vec{u}_p^2 \cos^2(\alpha) \sin(n\alpha)}{2\phi_C} & for \quad \alpha < \alpha_0 \\[2ex] \dfrac{M\vec{u}_p^2 \cos^2(\alpha)}{2\phi_C} & for \quad \alpha > \alpha_0 \end{cases} \tag{V-85}$$

where M is the total mass of particles impacting the surface at a particle impact angle α and impact velocity $\vec{u}_p$. ϕ_C and α_0 are the cutting coefficient and the transition angle, respectively. The transition angle is normally set as $45°$. Moreover, the deformation wear is given by:

$$E_D = \frac{M[\vec{u}_p \sin(\alpha) - K]^2}{2\varepsilon_C} \tag{V-86}$$

with ε_C being the deformation coefficient and K the cut-off velocity below which no deformation occurs. The authors also point out that the cutting wear predominates in the erosion of aluminium and that K is often negligible, as it is usually small relative to the particle velocity. Therefore, the cut-off velocity is set to zero. Finally, ϕ_C and ε_C are specified as $3.332 \cdot 10^7$ and $7.742 \cdot 10^7$, respectively.

Chen Model

The predictive equation proposed by Chen et al.[71] assumes the form as expressed by Finnie[20]:

$$E = K\vec{u}_p^n f(\alpha) \tag{V-87}$$

where E is measured as mass of material eroded per unit mass of particle impacting the surface, $\vec{u}_p$ is the particle impact velocity, n is the velocity exponent, α is the particle impact angle, K is a scaling parameter and $f(\alpha)$ is a function which accounts for the influence of the impact angle on erosion. The function $f(\alpha)$ is expressed as follows:

$$f(\alpha) = \begin{cases} A\alpha^2 + B\alpha & for \quad \alpha \le \alpha_0 \\ X\cos^2(\alpha)\sin(W\alpha) + Y\sin^2(\alpha) + Z & for \quad \alpha > \alpha_0 \end{cases} \tag{V-88}$$

The parameters in Equation (V-88), i.e. $A, B, X, W, Y, Z, \alpha_0$, along with K and n, need to be experimentally adjusted. The values of these parameters were determined for sand particles impacting on aluminium by Wong et al.[86] and are reported accordingly in Table V-4.

Table V-4. Parameters of Chen model according to Wong et al.[86].

K	n	A	B	W	X	Y	Z	α_0
$1.44 \cdot 10^{-8}$	2.2	-7	5.45	-3.4	0.4	-0.9	1.556056	23°

Chapter VI

Surface Roughness Variation

This chapter is devoted to present the results obtained based on the experimental investigation described in Chapter III. In Section 6.1, measurements of the mean and fluctuating velocity components of air in the stream-wise direction at different inclination angles, i.e. 10°, 20° 30° and 40°, are reported. Then, in Section 6.2, the dependence of the particle mean and fluctuating velocity components in the stream-wise and transverse directions on the inclination angle is evaluated. Finally, Section 6.3 details the effect of solid particle erosion, inclination angle and particle shape on the parameters R_a, RS_m and $\Delta\gamma$, together with a simple correlation to estimate $\Delta\gamma$.

Herein, stream-wise and transverse components are denoted as U and V, in which the subscripts g and p denote air and particles, respectively. Please note that the velocity profiles are normalised by the mean flow velocity U_0 at the exit of the jet. Very often, experimental data is connected by line, intended merely to guide the eye.

6.1. Single Flow Velocity Measurements

Figure VI-1 (a) presents the measured mean and fluctuating velocities of air in the stream-wise direction as a function of the inclination angle of the plate. As previously mentioned, the measurement of all points in the upper region of the jet exit was not possible at inclination angles of $20°$, $30°$ and $40°$. Also, the point corresponding to $y/R = -1.0$ was not measured due to very poor data rate. Even though the air flow rate was kept constant, distinct velocity profiles in the stream-wise direction were obtained for both mean and fluctuating components. The results clearly show the influence of plate inclination on the fluid dynamics behaviour of air at the jet exit. Gradually increasing the inclination angle from $10°$ to $40°$ mainly affected regions in which the distance between the jet and the plate becomes significantly smaller with the increase in the inclination angle, i.e. the upper regions of the velocity profiles. In these regions, the air flow was blocked by the plate in such a way that its mean velocity component was considerably reduced, and its fluctuating component mostly enhanced. By increasing the inclination angle, on the other hand, the effective area available for the air flow becomes smaller, which results in a slightly increase in the mean velocity component in the lower regions. Furthermore, at higher inclination angles, air turbulence was mostly augmented in the lower regions.
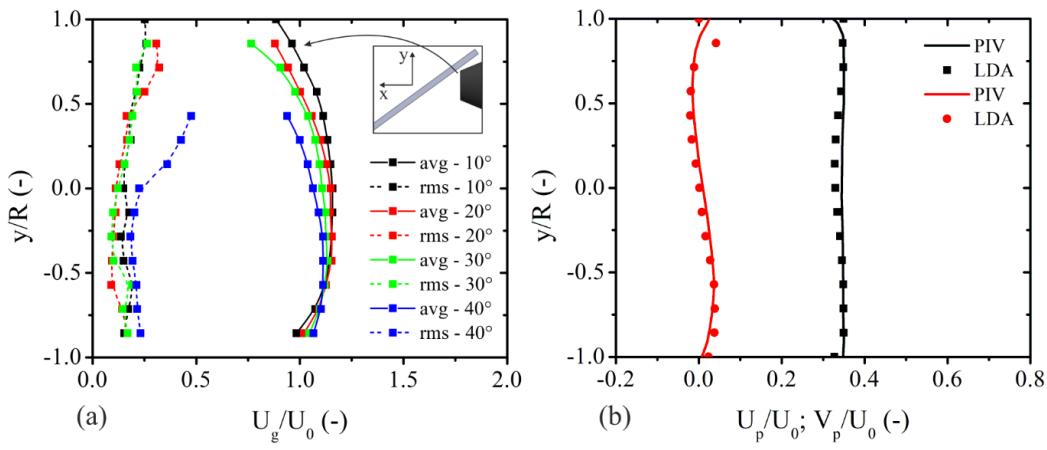
Figure VI-1. (a) Measured mean and fluctuating air velocity profiles in the stream-wise direction at different impact angles. (b) Measured mean particle velocity profiles in the stream-wise and transverse directions at an impact angle of $10°$ and for $211.5\ \mu m$ spherical glass beads particles, comparison between PIV and LDA. Measurement location: about 2 mm from jet exit. $U_0 = 26\ m/s$ and $D_{jet} = 14\ mm$.

Figure VI-1 (b) shows a comparison between the stream-wise and transverse velocity profiles obtained for spherical glass beads particles at an inclination angle of 10° using the LDA and PIV techniques. The intention of this comparison is merely to show that the method applied to measure the velocity components of particles, as described in Section 3.4, produces similar results to the LDA technique and is therefore considered reliable.

6.2. Dispersed Phase Velocity Measurements

Measured mean and fluctuating velocity components of particles in the stream-wise and transverse directions for 211.5 µm spherical glass beads particles at inclination angles of 10°, 20°, 30° and 40° are shown in Figure VI-2 (a) and (b), respectively. As presented in Figure VI-2 (a), increasing the inclination angle from 10° to 30° proved to have almost no influence on the mean and fluctuating velocity components of particles in the stream-wise direction, even though significant changes were detected on the continuous phase. The profiles are flat at these inclination angles, a characteristic normally observed with inertial particles, which respond slowly to changes on the flow. However, small changes were observed on the profiles in the upper regions due to the small distance between the plate and the jet. Also, the fluctuating velocity component is higher next to the jet walls than in jet core due to particle-wall collisions. Surprisingly, both velocity components were greatly affected at an inclination angle of 40°. While a considerable reduction was observed in the mean stream-wise velocity component, the fluctuating component increased significantly. The observed decrease could be attributed to the effect exerted by the inclination angle on the flow, as previously presented, and particles rebounding off the plate after a collision. These particles are not distinguished by the PIV algorithm from particles in a rectilinear collision path with the plate and consequently, the mean velocity component could be reduced in the stream-wise direction while it could be increase towards negative values in the transverse direction. The increment in the inclination angle up to 30° showed little influence on the mean and fluctuating velocity components of particles in the transverse direction, as demonstrated in Figure VI-2 (b). At inclination angles of 10°, 20° and 30°, the mean transverse velocity component is approximately zero in the core region of the jet, as expected. In the lower regions of the profiles positive values were measured, which indicates that particles are moving upwards as a result of particle-wall

collisions. Opposite to that, particles are moving downwards in the upper regions, and in addition, particle velocity is slightly influenced by the inclination angle. The fluctuating velocity component of particles in the transverse direction remained mostly similar at inclination angles of 10°, 20° and 30°, except for small perturbations in the upper regions resulting from the inclination angle. At an inclination angle of 40°, particles were forced to move slightly downwards rather than straight to the plate and therefore, the fluctuating velocity component was greatly enhanced.
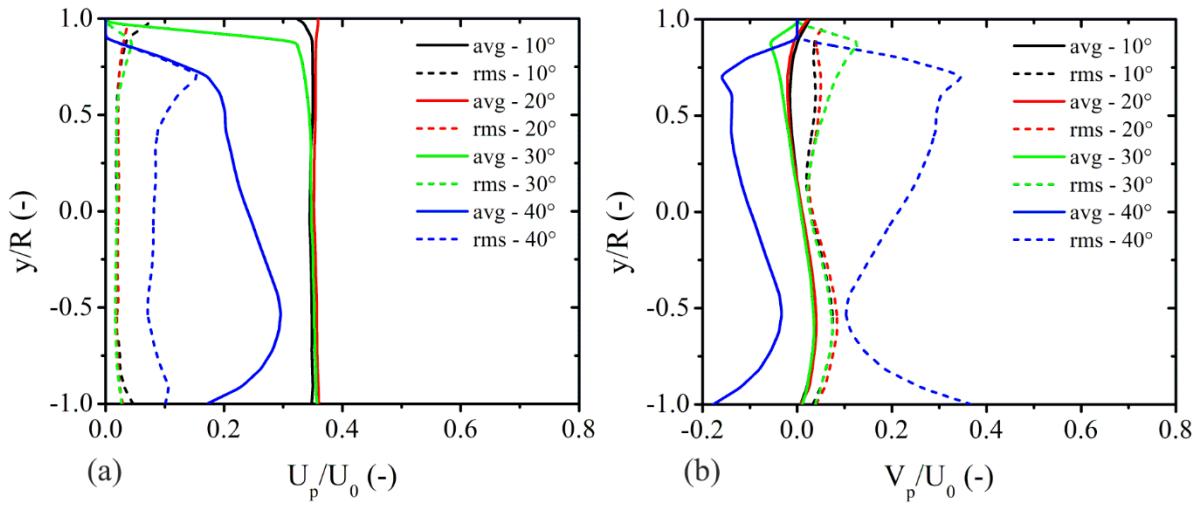
Figure VI-2. Measured mean and fluctuating particle velocity profiles at different inclination angles: (a) stream-wise and (b) transverse direction. Particle: 211.5 µm spherical glass beads. Measurement location: about 2 mm from jet exit. $U_0 = 26\ m/s$ and $D_{jet} = 14\ mm$.

Mean and fluctuating velocity components of particles in the stream-wise and transverse directions considering quartz sand particles are shown in Figure VI-3 (a) and (b), respectively. In the stream-wise direction (Figure VI-3 (a)), both mean and fluctuating velocity components at inclination angles of 10° and 20° are similar and are, in addition, slightly higher than those with spherical particles, as the drag force acting on non-spherical particles is higher than on spherical particles. Regarding the cases with inclination angles of 30° and 40°, the mean stream-wise velocity component underwent small reduction in the lower regions followed by a considerable reduction in the upper regions, showing the influence of the inclination angle on the results. Additionally, the fluctuating velocity component mainly increased in the upper regions. In the transverse direction (Figure VI-3 (b)), similar behaviours were obtained for the 10° and 20° cases for both mean and fluctuating velocity components.

The upper regions are composed of negative values while the bottom regions of positive values. Therefore, particles move downwards in the upper regions and upwards in the bottom regions as a result of particle-wall collisions. By increasing the inclination angle to 30° and 40°, particles are forced to move downwards in the upper regions as a result not only of particle-wall interaction but also due to the plate inclination, which increases the mean velocity component towards negative values. Nonetheless, the mean velocity component at an inclination angle of 40° is slightly higher in some regions than at 30°. Also, increasing the inclination angle to 30° and 40° contributes to the augmentation in particle velocity fluctuations. Some differences can be observed on particle velocity profiles between the cases involving non-spherical and spherical particles at inclination angles of 30° and 40°. These differences could be attributed to the irregular collision process of non-spherical particles. Due to their irregular shape, particles could bounce off the surface of the plate and the jet walls at angles much higher or lower than the particle incidence angle, possibly leading to distinct results.
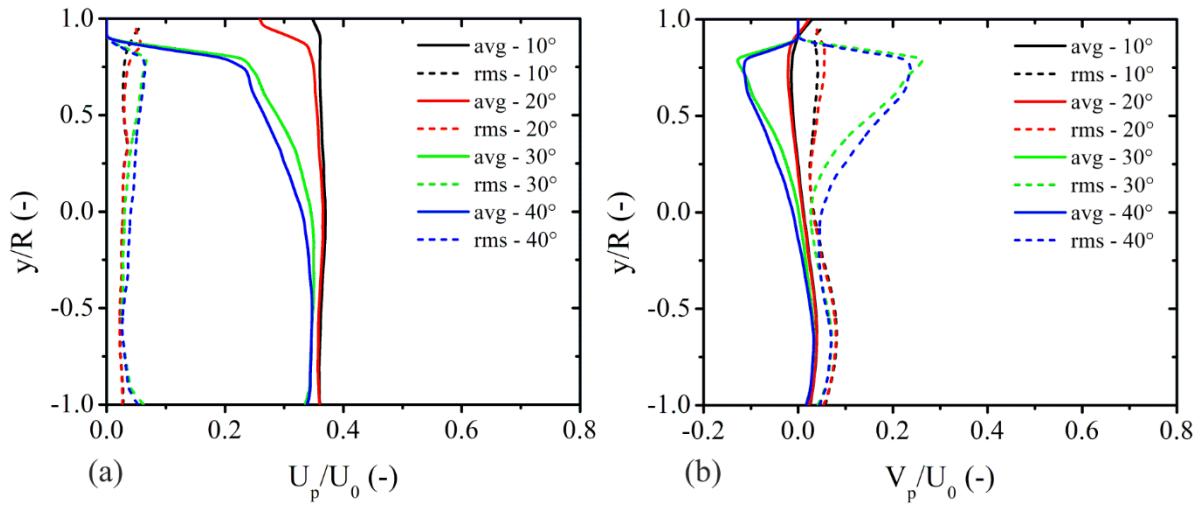
Figure VI-3. Measured mean and fluctuating particle velocity profiles at different inclination angles: (a) stream-wise and (b) transverse direction. Particle: 235.4 µm quartz sand. Measurement location: about 2 mm from jet exit. $U_0 = 26 \, m/s$ and $D_{jet} = 14 \, mm$.

6.3. Surface Roughness Measurements

This session is aimed at presenting and discussing the results obtained by optically scanning the eroded surfaces. Initially, results regarding each one of the materials eroded by quartz sand particles are presented and discussed in the following order: aluminium 5754, copper and brass 70/30. Then, results involving erosion by spherical glass beads particles are introduced and evaluated, following the same order.

Table VI-1. Summary of measured roughness parameters for aluminium 5754.

		Quartz Sand			*Spherical Glass Beads*		
	Time (h)	R_a (µm)	RS_m (µm)	$\Delta\gamma$ (°)	R_a (µm)	RS_m (µm)	$\Delta\gamma$ (°)
	0	0.51	18.34	3.18	0.51	18.34	3.18
	2.5	1.29	15.13	9.69	0.64	27.11	2.69
10°	5.0	1.27	14.76	9.73	1.18	52.92	2.56
	10.0	1.18	14.72	9.13	1.43	58.84	2.79
	2.5	1.30	15.66	9.45	1.07	34.77	3.51
20°	5.0	1.34	16.63	9.13	1.49	55.42	3.08
	10.0	1.61	18.57	9.86	1.82	64.92	3.20
	2.5	1.36	16.80	9.18	1.59	49.16	3.73
	5.0	1.49	18.33	9.23	1.93	47.80	4.63
30°	10.0	2.30	24.46	10.64	3.06	76.90	4.56
	20.0	2.71	28.20	10.87	-	-	-
	2.5	1.43	18.31	8.90	2.57	59.59	4.93
40°	5.0	1.47	17.91	9.31	2.80	56.37	5.69
	10.0	2.61	26.95	11.04	5.80	113.19	5.87

Additionally, the obtained experimental data are summarized in Table VI-1 for aluminium 5754, Table VI-2 for copper and Table VI-3 for brass 70/30. In these tables, empty cells indicate that no data was acquired. In terms of R_a, aluminium 5754 ($R_a = 0.51$ µm) and copper ($R_a = 0.52$ µm) present similar initial roughness while brass 70/30 is rougher than the other two ($R_a = 0.65$ µm). On the other hand, aluminium 5754 ($RS_m = 18.34$ µm) and brass 70/30 ($RS_m = 18.61$ µm) show similar initial mean distance between peaks while copper presents a higher value ($RS_m = 22.60$ µm).

Table VI-2. Summary of measured roughness parameters for copper.

	Time (h)	R_a (µm)	RS_m (µm)	$\Delta\gamma$ (°)	R_a (µm)	RS_m (µm)	$\Delta\gamma$ (°)
		Quartz Sand			*Spherical Glass Beads*		
	0	0.52	22.60	2.62	0.52	22.60	2.62
	2.5	1.11	14.64	8.62	0.44	20.22	2.50
10°	5.0	1.18	14.97	8.95	0.90	39.31	2.63
	10.0	1.19	14.59	9.25	1.25	50.01	2.87
	2.5	1.16	15.57	8.50	0.78	26.17	3.37
20°	5.0	1.25	17.14	8.31	1.46	53.03	3.17
	10.0	1.59	18.82	9.59	1.70	60.53	3.20
	2.5	1.27	17.72	8.17	1.66	49.25	3.86
30°	5.0	1.28	17.49	8.32	2.18	66.56	3.75
	10.0	1.84	22.70	9.22	2.81	74.28	4.32
	20.0	2.47	29.20	9.59	-	-	-
	2.5	1.30	17.33	8.55	2.59	72.01	4.12
40°	5.0	1.36	17.63	8.80	2.93	74.20	4.53
	10.0	2.27	27.19	9.47	4.24	98.99	4.89

Table VI-3. Summary of measured roughness parameters for brass 70/30.

	Time (h)	R_a (µm)	RS_m (µm)	$\Delta\gamma$ (°)	R_a (µm)	RS_m (µm)	$\Delta\gamma$ (°)
		Quartz Sand			*Spherical Glass Beads*		
	0	0.65	18.61	4.01	0.65	18.61	4.01
	2.5	1.06	14.50	8.31	0.49	20.48	2.75
10°	5.0	1.08	14.03	8.76	0.66	25.39	2.97
	10.0	1.04	14.20	8.37	0.62	30.62	2.31
	2.5	1.06	14.15	8.51	0.43	19.69	2.51
20°	5.0	1.11	13.88	9.08	0.61	29.26	2.39
	10.0	1.04	13.62	8.67	0.72	35.26	2.33
	2.5	1.05	14.43	8.30	0.56	21.86	2.95
30°	5.0	0.98	14.35	7.74	0.93	37.02	2.85
	10.0	1.01	14.08	8.18	1.16	42.41	3.13
	20.0	1.12	14.13	9.00	-	-	-
	2.5	1.06	14.09	8.55	0.68	32.00	2.41
40°	5.0	0.99	14.26	7.94	0.71	33.25	2.44
	10.0	0.97	13.75	8.05	2.09	61.32	3.92

Aluminium 5754 – Quartz Sand

Figure VI-4 shows macro images taken from the surface of aluminium 5754 after erosion by quartz sand particles for 2.5, 5 and 10 hours at an inclination angle of 10° and compares roughness profiles before and after erosion as well. The obtained erosion scars are long and narrow along the plate, a characteristic observed at shallow inclination angles. As the impact velocity and angle were considerably low, no ripples with large amplitude and wavelength were observed on the material surface, even for higher erosion. Therefore, the average roughness height and the distance between peaks are considerably smaller than at the other inclination angles analysed, which will be discussed shortly. Although no ripples were formed, the average roughness height is considerably higher than its initial state (see Table VI-1).
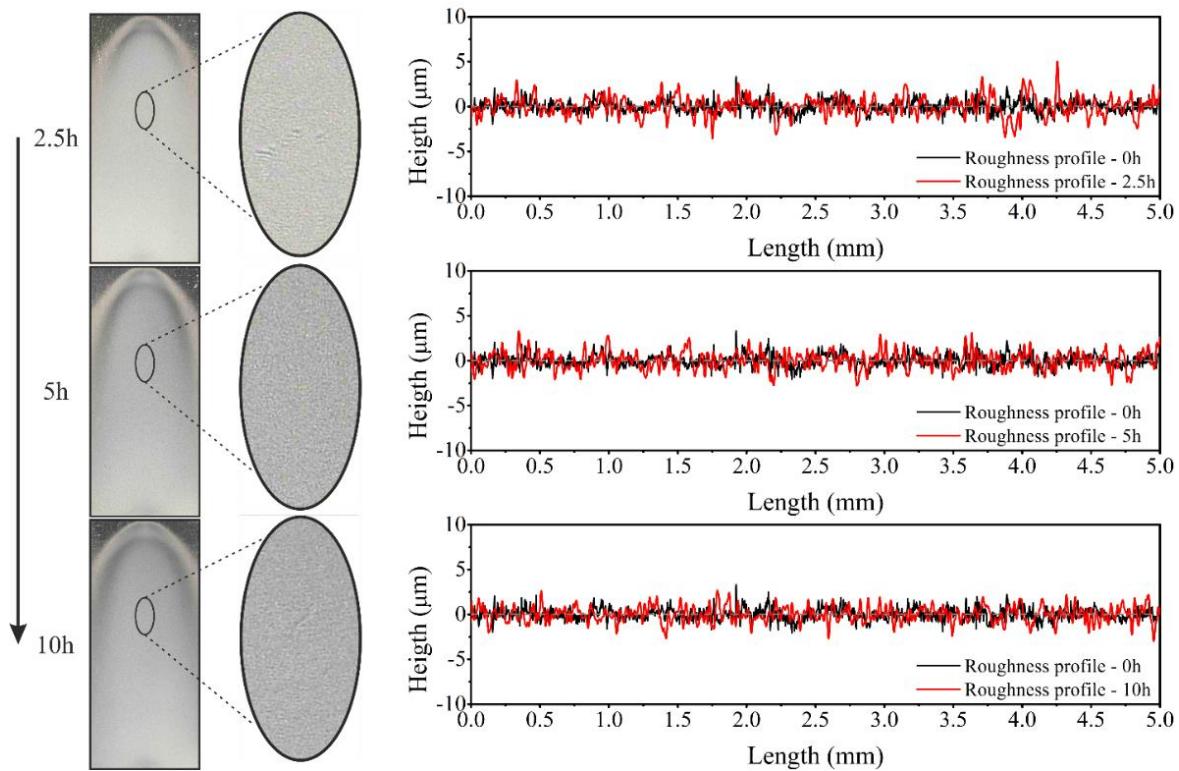
Figure VI-4. Changes on material surface (left) and roughness profiles (right) for different erosion times. Inclination angle: 10°. Particle: 235.4 µm quartz sand. Material: aluminium 5754.
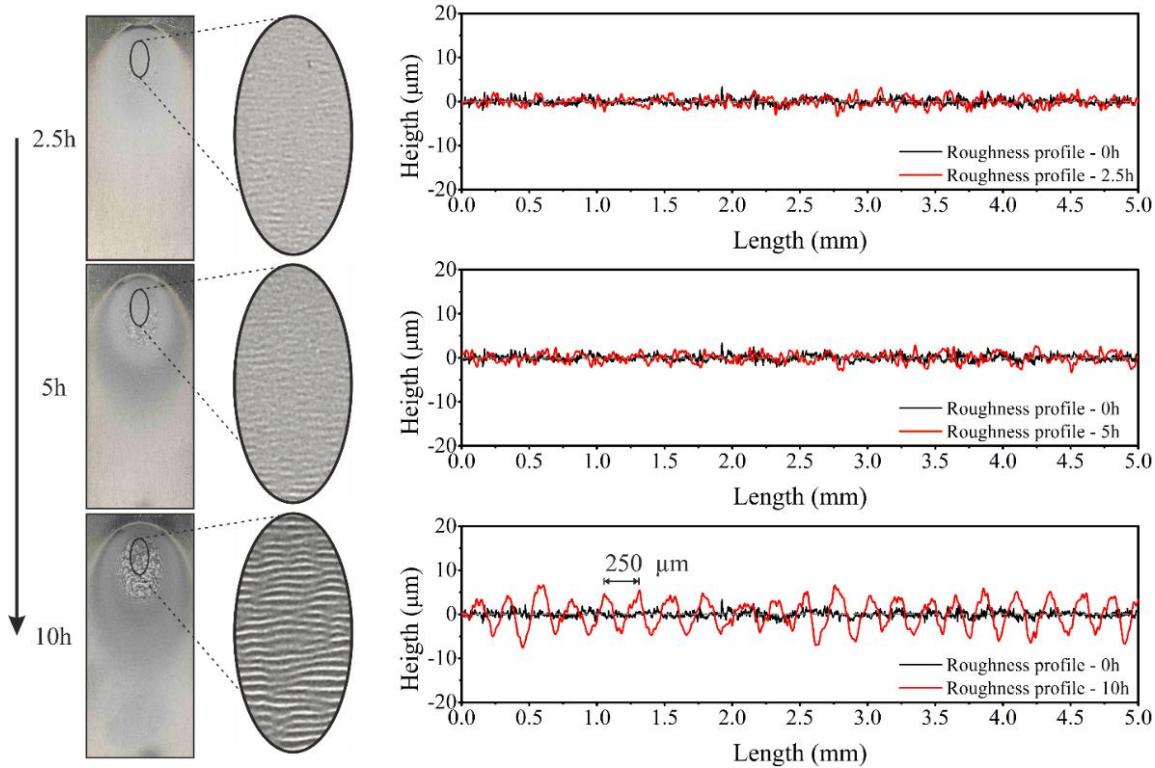
Figure VI-5. Changes on material surface (left) and roughness profiles (right) for different erosion times. Inclination angle: 40°. Particle: 235.4 µm quartz sand. Material: aluminium 5754.

By increasing the inclination angle from 10° to 40°, meaningful changes on both material surface and roughness profiles were observed, as shown in Figure VI-5. The developed erosion scar is characterized by an oval shape at which the maximum erosion is located just below its centre, as visualized in Figure VI-16. In the central region of the erosion scar, well-defined ripples were formed on the material surface after exposing it to erosion for 10 hours. Additionally, initial stages of ripple formation are detectable after 2.5 and 5 hours of erosion. This suggests that a threshold erosion time is necessary to produce enough surface deformation to allow the formation of well-defined ripples. The mechanisms of material removal by non-spherical particles commonly observed are cutting and ploughing deformation, in which lips are raised after particle impact and then removed by subsequent particle impacts. The mechanism of ripple formation is related to the raised lips formed around the crater left after each individual particle collision with the material surface[57,58], where subsequent particle impact near the original crater deepen and widen the raised lips generating peaks and valleys. Additionally, multiple particle impact displaces and removes material such that the individual peaks and valleys move in the direction of the flow meeting each other and,

finally, generating well-defined ripples. The amplitude and wavelength of the ripples are visualized in the bottom roughness profile presented in Figure VI-5. Both height and distance between peaks greatly increase due to solid particle erosion. The distance between peaks can achieve values as high as 250 μm, which is in the range of particle size used in the experiments and almost 14 times bigger than the initial value. This shows that the size of the wavelength of the ripples depends on particle size as well. Ripple formation on the surface of the material due to solid particle erosion will certainly affect particle-wall interaction process and erosion itself in confined, gas-solid flows.

Figure VI-6 (a) shows the dependence of the parameter R_a on erosion and inclination angle considering aluminium 5754 eroded by quartz sand particles. It is evidenced that surface roughness increases meaningfully in relation to its initial value even for low erosion and impact velocity. Additionally, the inclination angle demonstrated major influence on the surface roughness as well. At an impact angle of 10°, in which no ripples were formed (Figure VI-4), R_a initially increased, followed by a small decrease at higher erosion. By increasing the inclination angle to 20°, the average roughness initially increased due to erosion up to a similar value as at an impact angle of 10° and continued to increase slightly at higher erosion because of the formation of some ripples with low amplitude, which are not shown here. By increasing the inclination angle further to 30° and 40°, R_a greatly increased due to erosion as a result of the formation of well-defined ripples with higher amplitude, as observed in Figure VI-5. The normal velocity component of particles impacting on a surface with shallow angles such as 10° and 20° is small compared to 30° and 40°. Hence, particles could penetrate less into the material matrix reducing the amplitude of formed ripples or even no ripples could be formed. Ripples with low amplitude or the absence of them is the main reason for lower surface roughness at inclination angles of 10° and 20°. The relation between erosion, inclination angle and the parameter RS_m is illustrated in Figure VI-6 (b). As can be seen, RS_m expressed a different behaviour than R_a. After decreasing from its initial value, RS_m reached practically a constant value at an inclination angle of 10°, as no ripple formation was observed (Figure VI-4). At an inclination angle of 20°, RS_m was initially reduced due to erosion and thereafter, started to increase for higher erosion because of the formation of some ripples on the material surface with significant but short wavelength. At inclination angles of 30° and 40°, the spacing between peaks grew expressively for higher erosion reflecting the wavelength of the ripples

observed in Figure VI-5. In general, surface roughness of aluminium 5754 increased with the augmentation of the inclination angle up to 40°. Avcu et al.[63] observed similar surface roughness (R_a) dependence on the inclination angle by eroding an Ti6Al4V alloy by 120 mesh garnet particles under inclination angles of 15°, 30°, 45°, 60°, 75° and 90°. Their research showed that the surface roughness of Ti6Al4V alloy increased up to an inclination angle of 75° followed by a decrease at an inclination angle of 90°. Additionally, it was demonstrated that surface roughness increased with the increase of particle impact velocity. Kazarinov et al.[64] analysed the influence of particle impact velocity on surface roughness of ultrafine- and coarse-grained aluminium 1235 eroded by 100 µm corundum particles. It was also reported that surface roughness increased with impact velocity. By using a slurry impingement jet rig, Abedini and Ghasemi[67] also reported an increase in the surface roughness of an Al-brass alloy purely eroded by SiO_2 particles by increasing particle impact velocity. Moreover, by analysing different sand concentrations and inclination angles, the authors concluded that the variation in surface roughness of the Al-brass alloy regarding these parameters is higher at higher particle impact velocities. Therefore, it should be noted that other parameters have an effect on the surface roughness of materials.
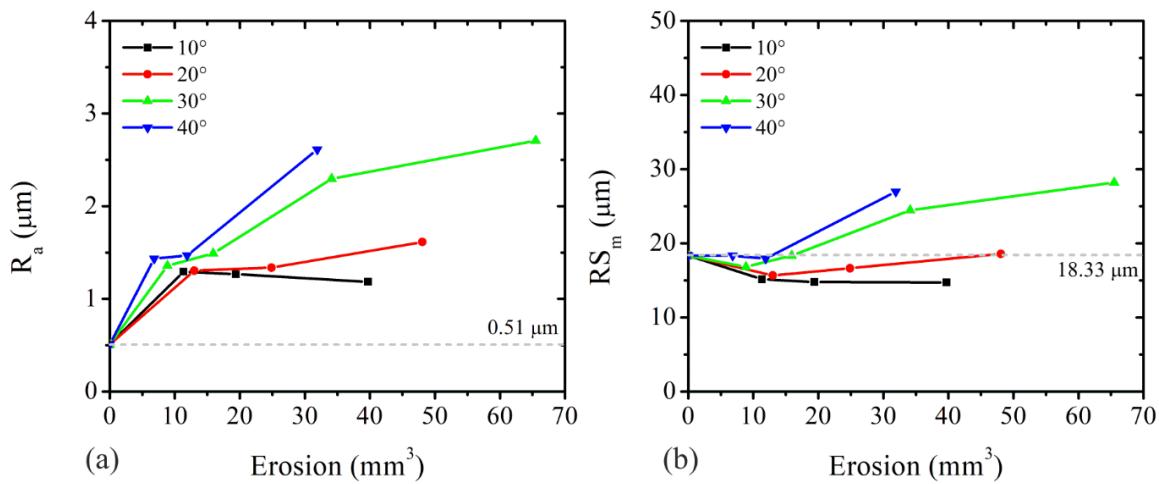
Figure VI-6. (a) R_a and (b) RS_m profiles as a function of erosion at different inclination angles. Particle: 235.4 µm quartz sand. Material: aluminium 5754. $H_v = 0.74\ GPa$.

The experimental and predicted values of the standard deviation of the roughness angle $\Delta\gamma$ are presented in Figure VI-7 for aluminium 5754 eroded by quartz sand particles at inclination angles of 10°, 20°, 30° and 40°. The experimental values of $\Delta\gamma$ were estimated

based on the parameters R_a and RS_m according to Equation (V-37). Although R_a and RS_m showed different behaviours at different inclination angles, $\Delta\gamma$ is similar throughout all inclination angles analysed. Nevertheless, higher values were obtained at inclination angles of 30° and 40° for higher erosion due to the formation of ripples. $\Delta\gamma$ reached values about 3 times higher than for a fresh sample of aluminium 5754 ($\Delta\gamma_0 = 3.18°$). Also, $\Delta\gamma$ in the range of 10° is considered as relatively high and will greatly influence particle transport behavior in confined, gas-solid flows, especially for small particles. $\Delta\gamma$ expressed an exponential growth for most of the cases, which will be discussed in the following, and consequently, can be modelled based on an exponential function as follows:

$$\Delta\gamma(E, \alpha, \Delta\gamma_0) = \Delta\gamma_0 \cdot exp\left(a + \frac{b_1}{E + c_1} + \frac{b_2}{\alpha + c_2}\right) \qquad \text{(VI-1)}$$

Equation (VI-1) accounts for both the influence of solid particle erosion and inclination angle and it additionally depends on the initial value of $\Delta\gamma_0$. $\Delta\gamma_0$ depends on the initial roughness structure which depends on manufacturing process and particle size. a, b_1, c_1, b_2 and c_2 are model parameters obtained from experimental data and are presented in Table VI-4 for each material and particle type considered. As shown in Figure VI-7, a good agreement between predicted and experimental values was obtained. Nonetheless, some minor deviations were obtained for other materials and particle type analysed.

Table VI-4. Parameters for Equation (VI-1).

	Aluminium 5754		Copper		Brass 70/30	
	Quartz Sand	Glass Beads	Quartz Sand	Glass Beads	Quartz Sand	Glass Beads
a	3.26258	28.93569	2.36154	7.55349	-0.68453	-0.47589
b_1	-1.70034	-1177.07754	-1.06388	-33.74396	-0.13096	-0.04654
c_1	1.50191	280.74034	0.83168	29.6261	0.1654	-1.53926
b_2	-1542.98053	-29962.4439	-1535.33871	-2923.69928	1383.19917	-6.73221E-5
c_2	724.33443	1193.92101	1422.98639	449.06924	936.90121	-1.51062E-4
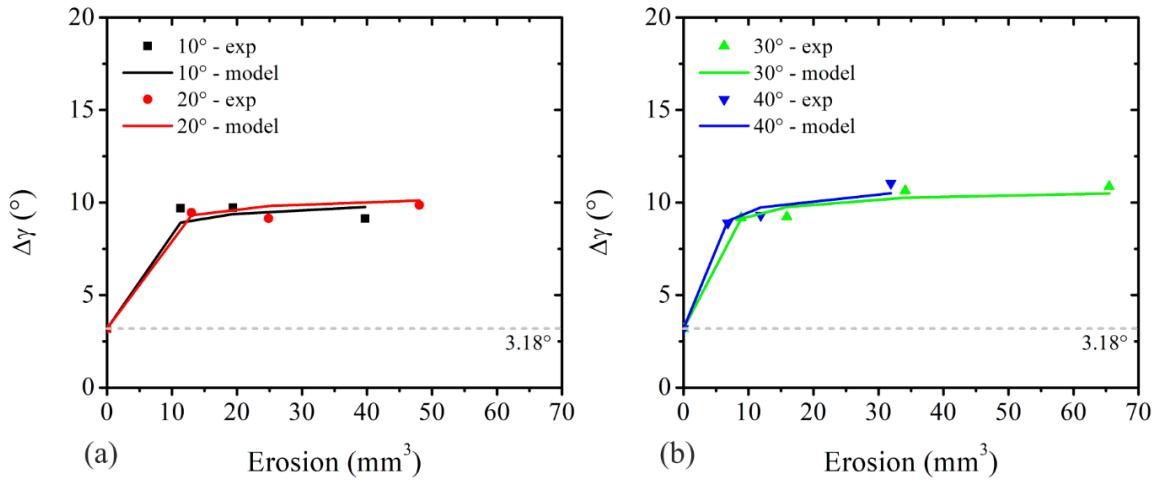
Figure VI-7. Comparison between experimental and predicted values of $\Delta\gamma$ according to Equation (VI-1) using the parameters presented in Table VI-4: (a) inclination angles of 10 and 20° and (b) inclination angles of 30 and 40°. Particle: 235.4 µm quartz sand. Material: aluminium 5754. $H_v = 0.74\ GPa$.

Copper – Quartz Sand

As shown in Figure VI-8, no ripple formation was observed on the surface of copper at an impact angle of 10°, though the average roughness height is considerably greater than its initial value (see Table VI-2). Even though copper is harder than aluminium 5754, a few well-defined ripples were formed on its surface after 2.5 and 5 hours of erosion by quartz sand particles at an impact angle of 40°, as shown in Figure VI-9. Then, ripples grew further in amplitude and wavelength for higher erosion (10 hours) over almost the entire central region of the erosion scar. As in the case considering aluminium 5754, the wavelength of ripples can reach values as high as 250 µm as well. In general, both materials presented similar behaviours in terms of ripple formation under the same impact conditions and erosion times, besides having different hardness.
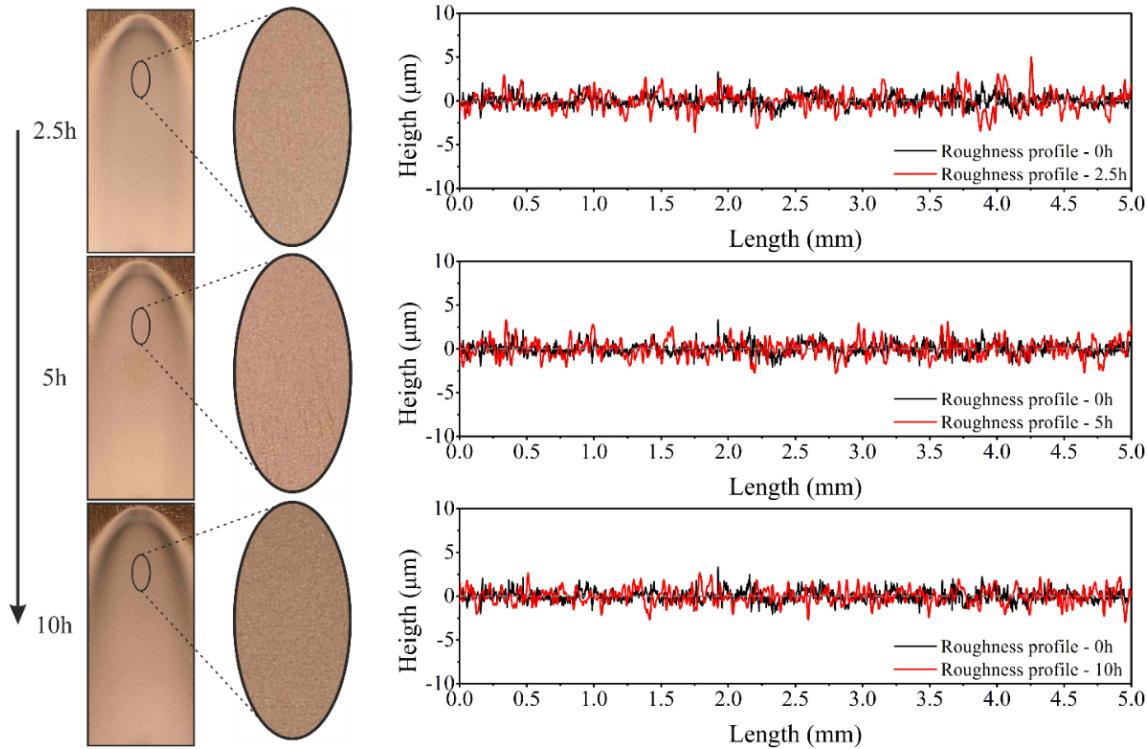
Figure VI-8. Changes on material surface (left) and roughness profiles (right) for different erosion times. Inclination angle: 10°. Particle: 235.4 µm quartz sand. Material: copper.
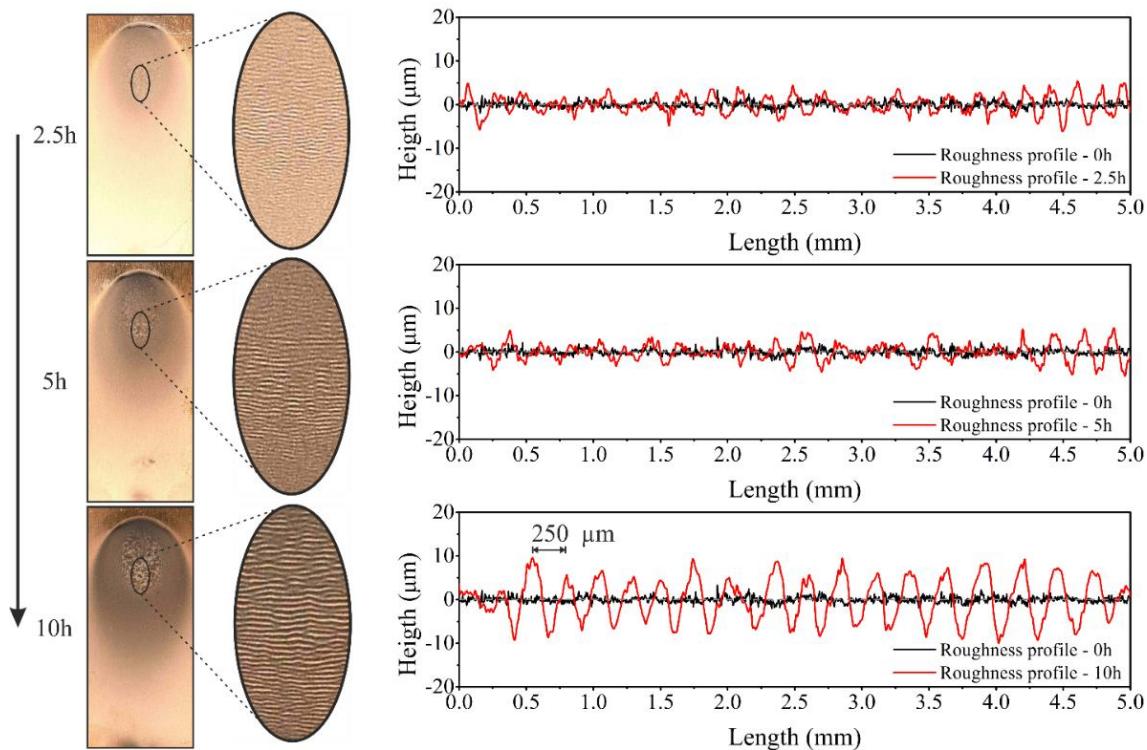
Figure VI-9. Changes on material surface (left) and roughness profiles (right) for different erosion times. Inclination angle: 40°. Particle: 235.4 µm quartz sand. Material: copper.

The dependence of R_a and RS_m for copper on erosion by quartz sand particles and inclination angle is presented in Figure VI-10 (a) and (b), respectively. At an inclination angle of 10°, R_a increased while RS_m decreased, in which both parameters reached an almost constant value, similarly to aluminium 5754. By increasing the inclination angle further to 20°, R_a and RS_m presented similar behaviours as at an inclination angle of 10° for erosion times of 2.5 and 5 hours. Nevertheless, both parameters increased further with an erosion time of 10 hours due to formation of ripples with low amplitude and short wavelength. Further increasing the inclination angle to 30° and 40°, both parameters increased expressively for higher erosion as a consequence of the formation of well-defined ripples with higher amplitude and longer wavelength, as observed in Figure VI-9. In addition, aluminium 5754 showed in general higher average roughness height than copper, specially at higher inclination angles such as 30° and 40° (see Table VI-1 and Table VI-2 for comparison). The harder nature of copper prevents particles from penetrating its surface as deeply as in the case of aluminium 5754, which in turn results in smaller average roughness height. Moreover, the average distance between peaks lies in the same range for both materials, suggesting that material displacement in the parallel direction of the particle impact is similar.
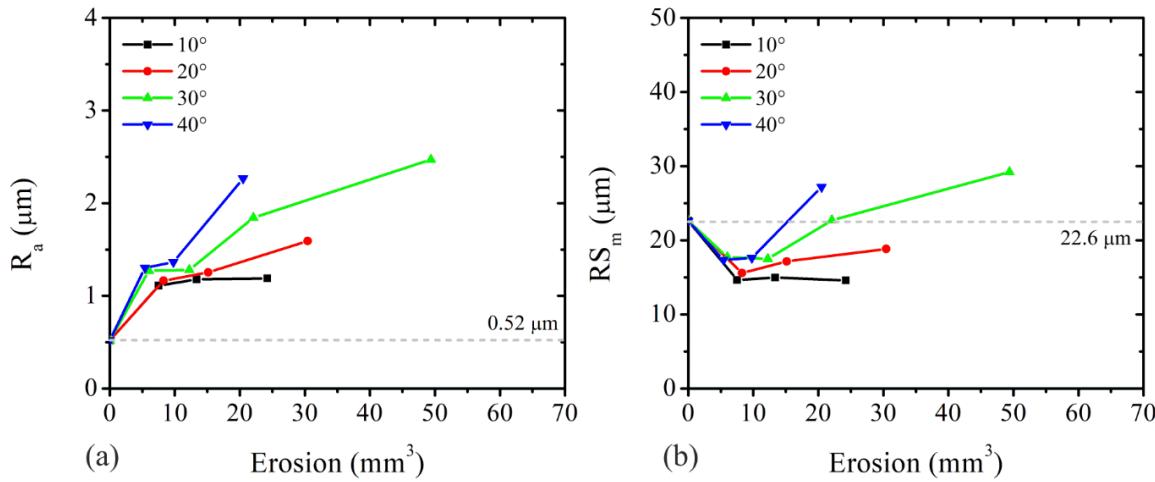
Figure VI-10. (a) R_a and (b) RS_m profiles as a function of erosion at different inclination angles. Particle: 235.4 µm quartz sand. Material: copper. $H_v = 0.9\ GPa$.

Figure VI-11 demonstrates the experimental and predicted $\Delta\gamma$ in the case of copper eroded by quartz sand particles at different inclination angles. As in the case of aluminium 5754, $\Delta\gamma$ increased rapidly up to a value and only small changes are observed for higher

erosion. Also, the influence of the inclination angle on $\Delta\gamma$ is not as significant as on the parameters R_a and RS_m. A mean reduction of about 8.2% was found in the $\Delta\gamma$ of copper compared to aluminium 5754, calculated by averaging all experimental values of $\Delta\gamma$ for both materials.
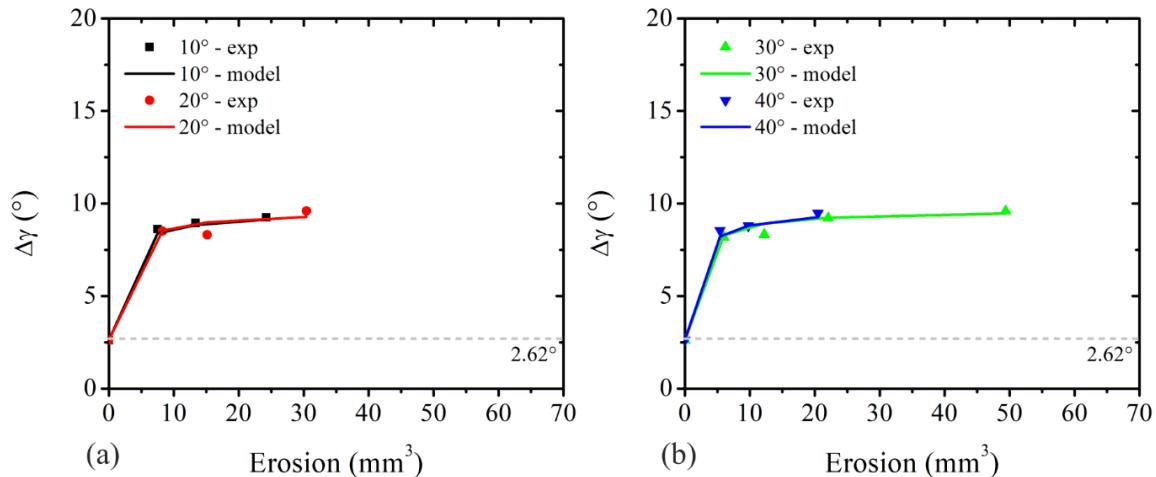
Figure VI-11. Comparison between experimental and predicted values of $\Delta\gamma$ according to Equation (VI-1) using the parameters presented in Table VI-4: (a) inclination angles of 10 and 20° and (b) inclination angles of 30 and 40°. Particle: 235.4 µm quartz sand. Material: copper. $H_v = 0.9\ GPa$.

Brass 70/30 – Quartz Sand

Brass 70/30 presented a different behaviour from aluminium 5754 and copper after being exposed to solid particle erosion, as visualized in Figure VI-12 regarding an inclination angle of 40°. The eroded surface as well as the roughness profiles remained very similar over time but differ from its initial state. The formation of well-defined ripples was not observed for this material in any of the impact conditions and erosion times analysed and therefore, changes on its surface are considered as part of the micro-roughness structure. Under the impact conditions considered, the kinetic energy of the particles was not enough to deeply penetrate the material surface to allow ripple formation.
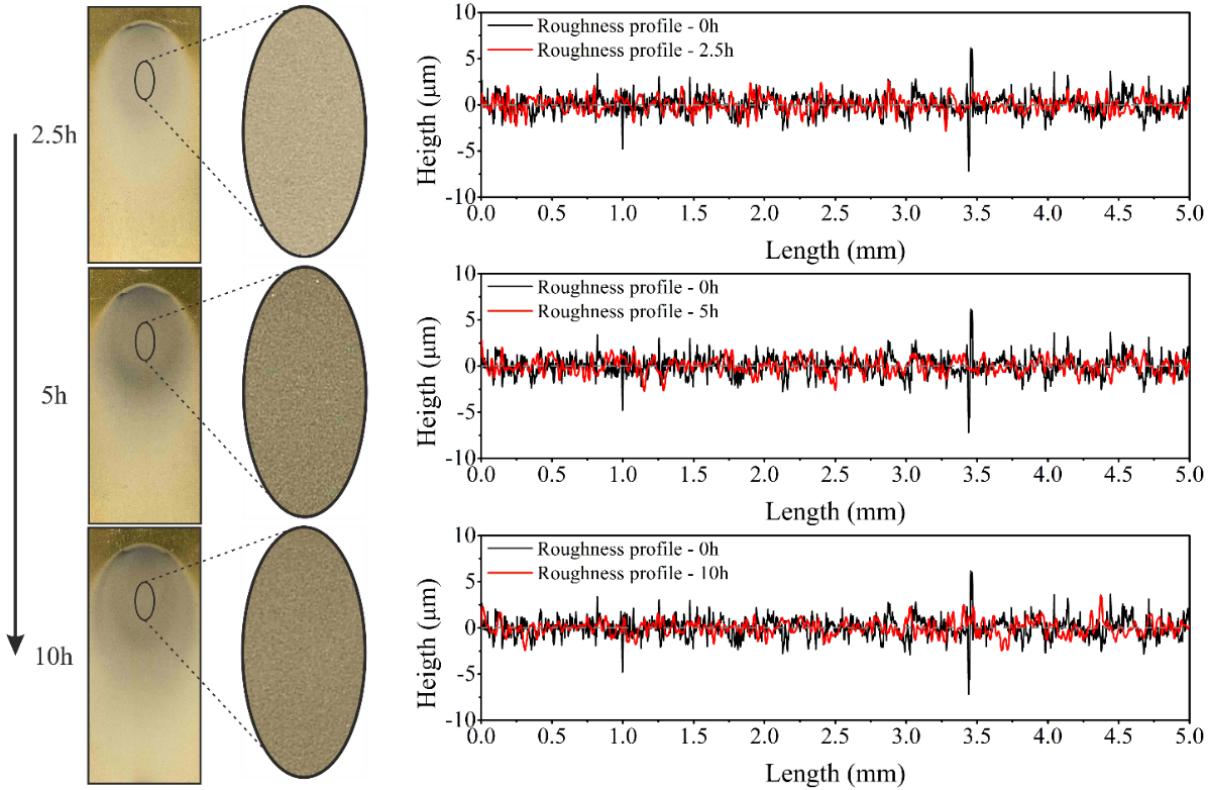
Figure VI-12. Changes on material surface (left) and roughness profiles (right) for different erosion times. Inclination angle: 40°. Particle: 235.4 µm quartz sand. Material: brass 70/30.

Nonetheless, meaningful changes were identified on the parameters R_a and RS_m, as illustrated in Figure VI-13 (a) and (b), respectively. R_a increased from its initial state reaching essentially a constant value with little influence of the inclination angle. In contrast, RS_m decreased up to a constant value at all inclination angles analysed. It should be noticed that at higher particle impact velocity, particle penetration into material surface could be greater enabling ripple formation, which could increase the parameters R_a and RS_m.

Figure VI-14 shows the experimental and predicted values of $\Delta\gamma$ for brass 70/30. Since R_a and RS_m reached constant values, it is natural that $\Delta\gamma$ presents similar behaviour. $\Delta\gamma$ reached an average value of 8.4° with small influence from the inclination angle. This represents a reduction of 12.8% and 5% with respect to aluminium 5754 and copper, respectively.
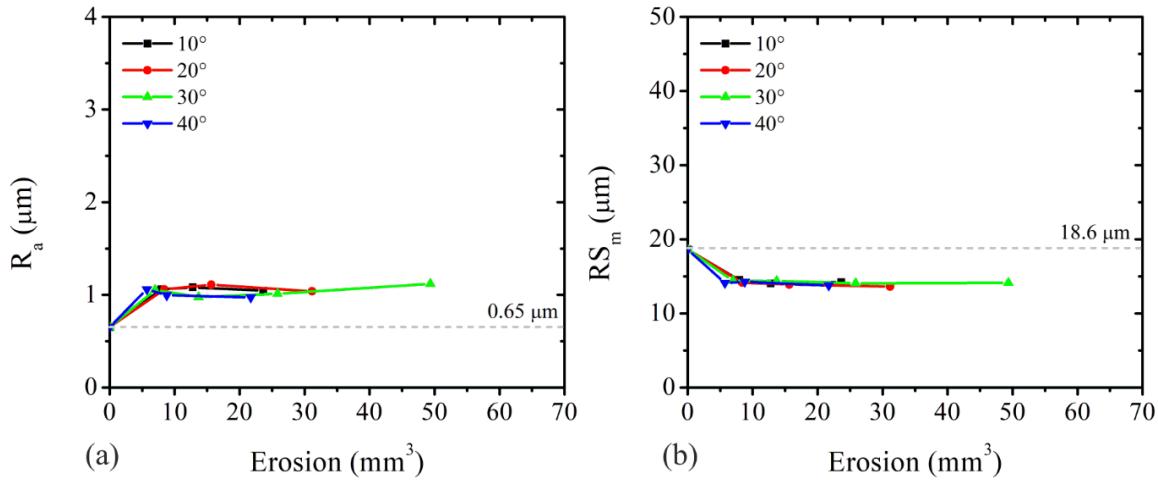
Figure VI-13. (a) R_a and (b) RS_m profiles as a function of erosion at different inclination angles. Particle: 235.4 µm quartz sand. Material: brass 70/30. $H_v = 1.2\ GPa$.
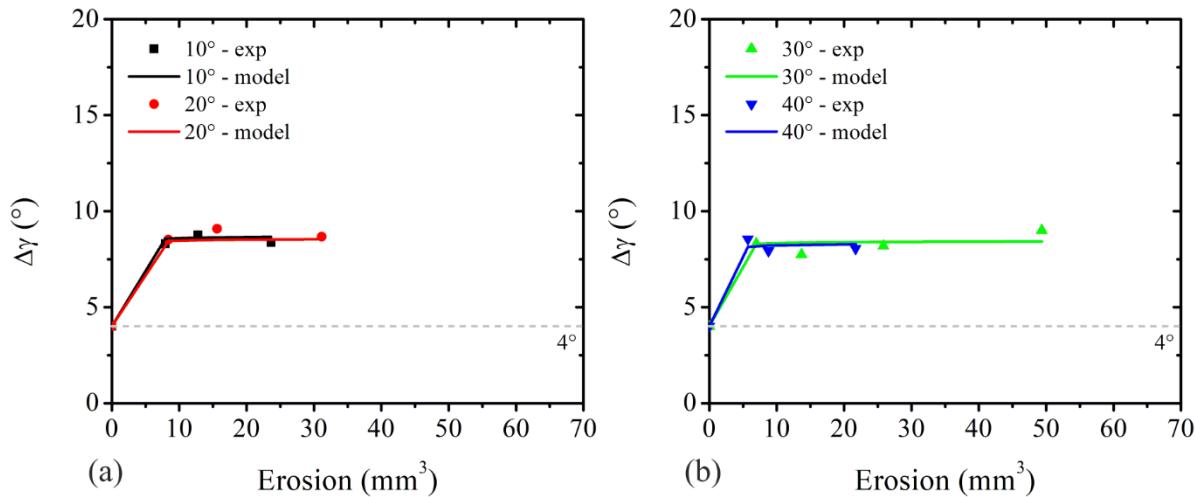
Figure VI-14. Comparison between experimental and predicted values of $\Delta\gamma$ according to Equation (VI-1) using the parameters presented in Table VI-4: (a) inclination angles of 10 and 20° and (b) inclination angles of 30 and 40°. Particle: 235.4 µm quartz sand. Material: brass 70/30. $H_v = 1.2\ GPa$.

Aluminium 5754 – Spherical Glass Beads

Solid particle erosion caused by spherical particles is considerably smaller than by non-spherical particles under the same operational conditions. Even though, the effect of spherical glass bead particles on the surface of the considered materials was substantially different from quartz sand particles, as presented in Figure VI-15 considering aluminium 5754 eroded by

spherical glass bead particles at an inclination angle of 40°. Ripples were formed on the eroded surface of aluminium 5754 even at early stages of erosion. Also, the amplitude and wavelength of the ripples were intensified by increasing erosion time. However, the ripples are irregular rather than well-defined as in the case with quartz sand particles. Moreover, the size of the amplitude and wavelength of the ripples are greater than in the case considering quartz sand particles, which can be easily seen in Figure VI-16. Erosion by spherical particle occurs mainly by ploughing deformation rather than cutting and material removal due to subsequent impacts is less effective than by non-spherical particle, as their sharp edges could easily cut off the vulnerable lips. Therefore, the size of the ripples is considerably higher both in amplitude and wavelength even if erosion is significantly reduced, which confirms that material removal is not necessarily the only mechanism responsible for ripple formation, as reported by other authors[57,61] as well. Additionally, maximum erosion depth is approximately 100 and 231 µm for spherical glass beads and quartz sand particles, respectively (Figure VI-16).
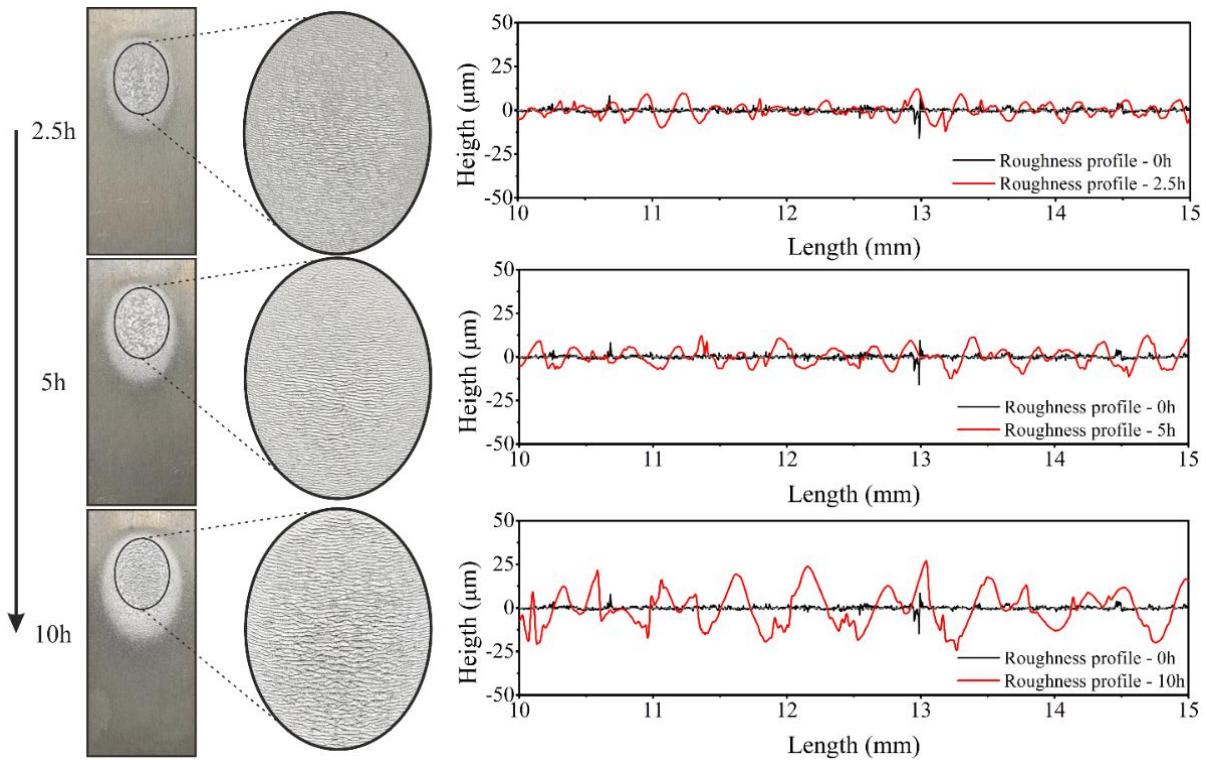
Figure VI-15. Changes on material surface (left) and roughness profiles (right) for different erosion times. Inclination angle: 40°. Particle: 211.5 µm spherical glass beads. Material: aluminium 5754.

Figure VI-17 (a) and (b) shows the relationship between erosion, inclination angle and the parameters R_a and RS_m considering aluminium 5754 eroded by spherical glass bead

particles. R_a increased with erosion at all inclination angles considered. At inclination angles of 10° and 20° similar trends were observed, in which R_a is slightly higher at an inclination angle of 20° than 10°. By increasing the inclination angle to 30°, R_a was enhanced even further while it reached maximum values at an inclination angle of 40°. Ripple formation was detected at all inclination angles analysed, increasing in amplitude towards higher inclination angles. At higher inclination angles, the normal component of particle impact velocity was high enough to cause deeper penetration into the material surface and therefore, bigger lips were formed and consequently, R_a became higher. In general, RS_m increased with erosion at all inclination angles considered. In comparison to the case considering quartz sand particles, the values of these parameters became strongly higher.
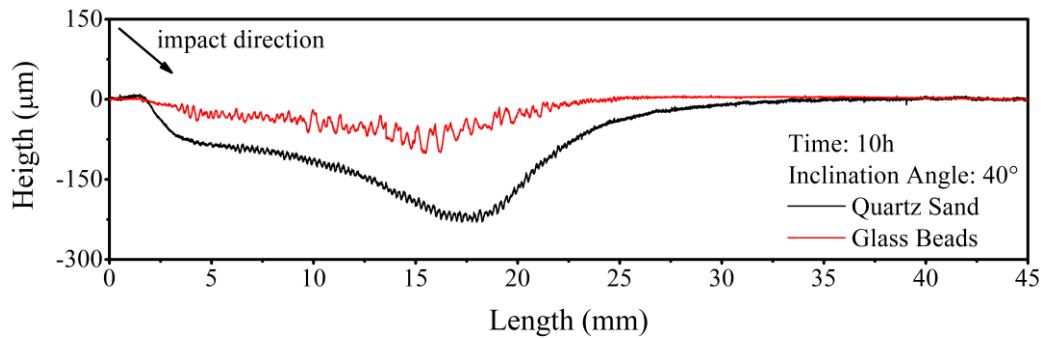
Figure VI-16. Comparison between erosion profiles after 10 hours of erosion by quartz sand and spherical glass beads particles measured along the centre of the erosion scar. Inclination angle: 40°. Material: aluminium 5754.
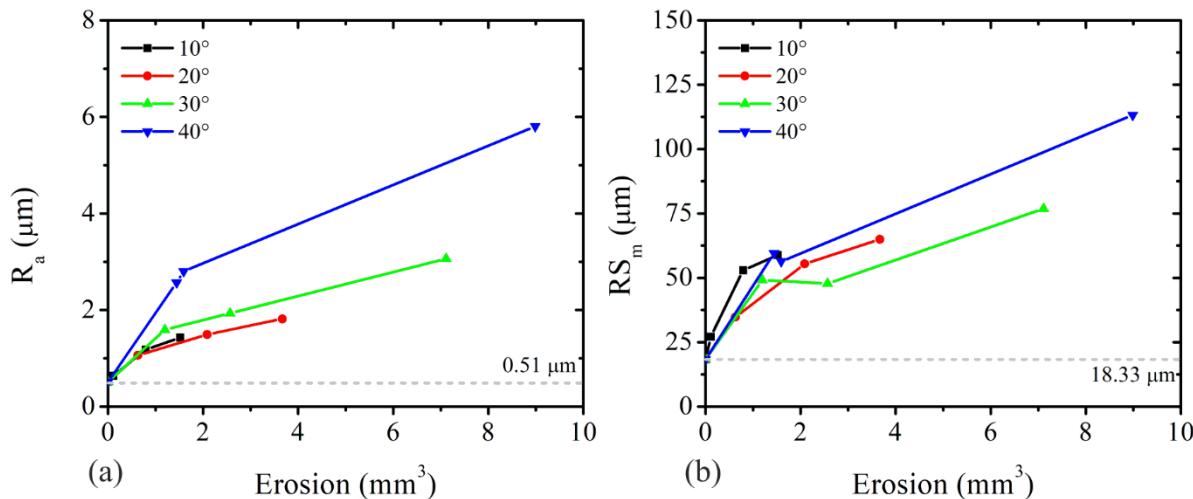
Figure VI-17. (a) R_a and (b) RS_m profiles as a function of erosion at different inclination angles. Particle: 211.5 µm spherical glass beads. Material: aluminium 5754. $H_v = 0.74\ GPa$.

Figure VI-18 demonstrates the experimental and predicted values of $\Delta\gamma$ for aluminium 5754 eroded by spherical glass bead particles at different inclination angles. At an inclination angle of 10°, $\Delta\gamma$ decreased from its initial value and it changed little at an inclination angle of 20°. On the other hand, $\Delta\gamma$ increased by increasing the inclination angle to 30° and 40°. Also, $\Delta\gamma$ is considerably smaller due to erosion by spherical glass beads than quartz sand particles even though R_a and RS_m were meaningful higher (see Table VI-1 for comparison), as the proportion at which RS_m changed due to erosion by spherical glass beads is greater than quartz sand particles. Equation (VI-1) underestimates the initial value of $\Delta\gamma$ but predicts its changes due to erosion and inclination angle well.
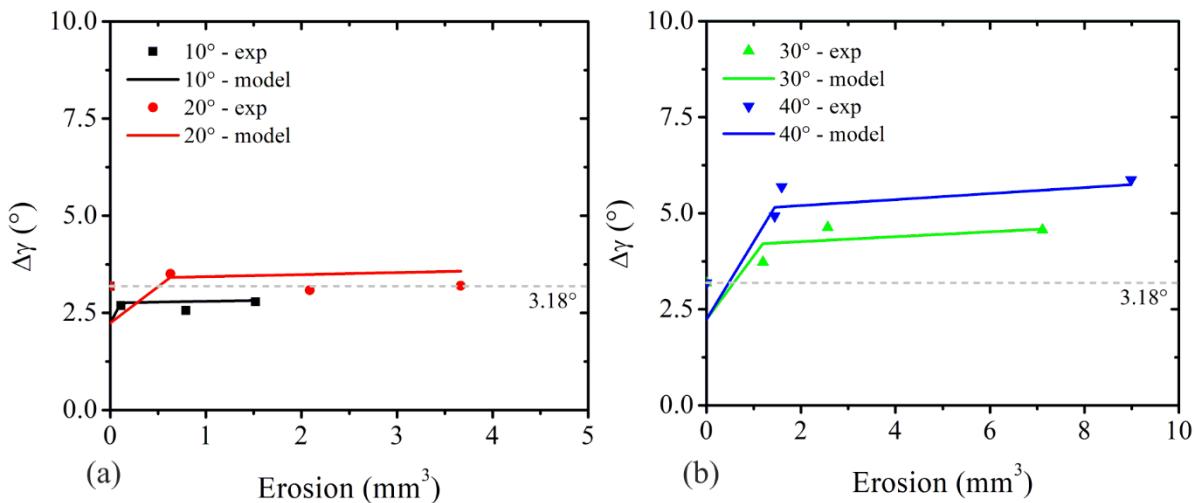

Figure VI-18. Comparison between experimental and predicted values of $\Delta\gamma$ according to Equation (VI-1) using the parameters presented in Table VI-4: (a) inclination angles of 10 and 20° and (b) inclination angles of 30 and 40°. Particle: 211.5 µm spherical glass beads. Material: aluminium 5754. $H_v = 0.74\ GPa$.

Copper – Spherical Glass Beads

Copper eroded by spherical glass beads particles at an inclination angle of 40° for different erosion times is shown in Figure VI-19. Copper exhibited similar behaviour to aluminium 5754, i.e. ripples were formed at early stages of erosion and became bigger both in amplitude and wavelength over time. R_a and RS_m increased with erosion at all inclination angles considered, in which higher values for both parameters were observed at higher

inclination angles, as shown in Figure VI-21 (a) and (b). With some exceptions, R_a and RS_m for copper are smaller than for aluminium 5754. Additionally, R_a and RS_m values are meaningfully greater than in the case with quartz sand particles due to the same reasons explained earlier for aluminium 5754.
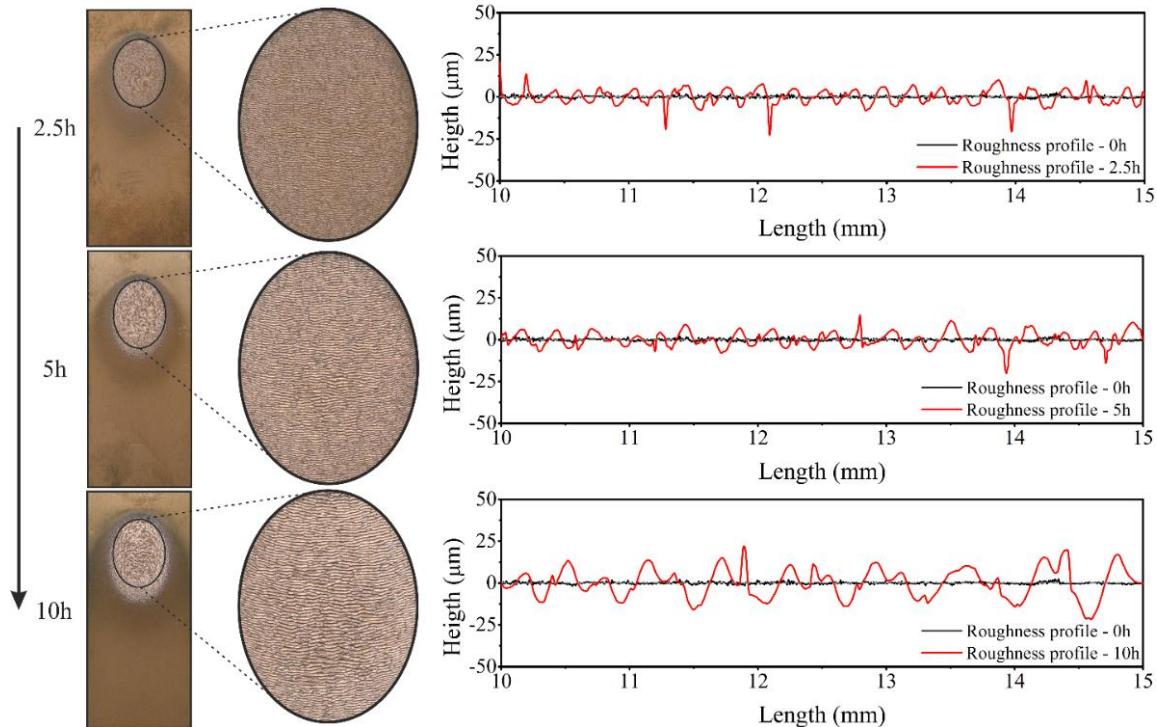

Figure VI-19. Changes on material surface (left) and roughness profiles (right) for different erosion times. Inclination angle: 40°. Particle: 211.5 µm spherical glass beads. Material: copper.
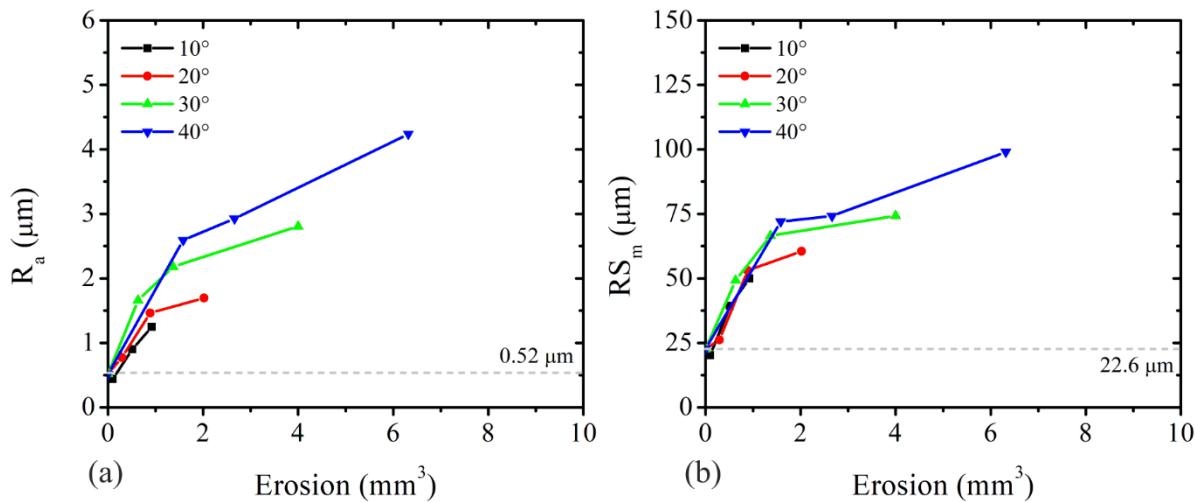

Figure VI-20. (a) R_a and (b) RS_m profiles as a function of erosion at different inclination angles. Particle: 211.5 µm spherical glass beads particles. Material: copper. $H_v = 0.9\ GPa$.

As shown in Figure VI-21, at an inclination angle of 10° $\Delta\gamma$ slightly decreased below its initial value and then increased with erosion. By increasing the inclination angle to 20°, 30° and 40°, $\Delta\gamma$ increased even further due to ripple formation. In comparison to the case with erosion by quartz sand particles, $\Delta\gamma$ is smaller since RS_m became much higher than R_a. Also, $\Delta\gamma$ is in general smaller for copper than aluminium 5754 and its prediction by Equation (VI-1) is in good agreement with the experimental values.
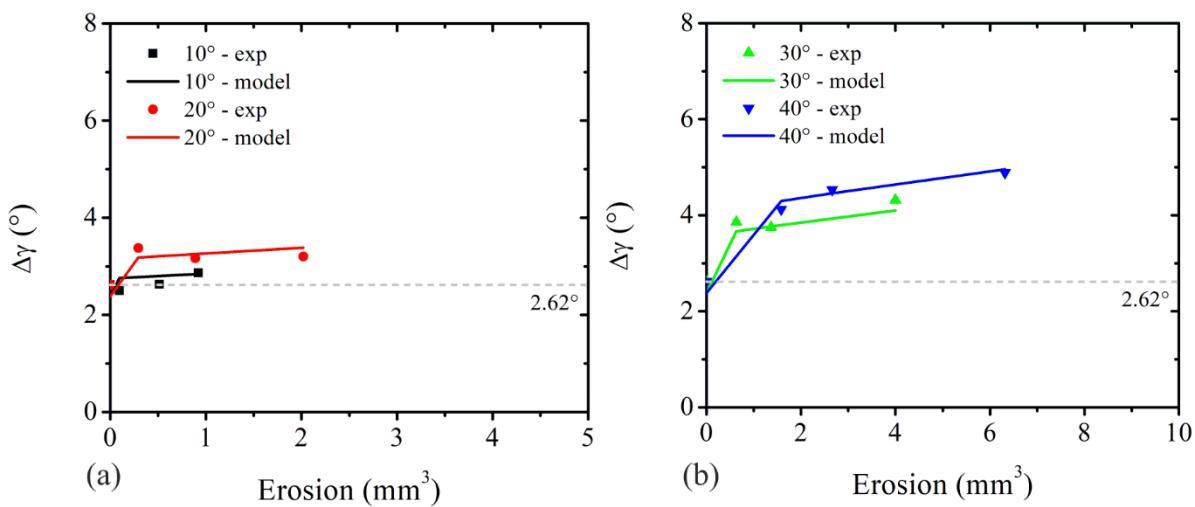
Figure VI-21. Comparison between experimental and predicted values of $\Delta\gamma$ according to Equation (VI-1) using the parameters presented in Table VI-4: (a) inclination angles of 10 and 20° and (b) inclination angles of 30 and 40°. Particle: 211.5 µm spherical glass beads. Material: copper. $H_v = 0.9\ GPa$.

Brass 70/30 – Spherical Glass Beads

Although no ripple formation was observed on the surface of brass 70/30 after eroding it by quartz sand particles, ripples were formed when eroding it by spherical glass beads particles, as visualized in Figure VI-22. Also, under the impact conditions considered, erosion by spherical glass beads is considerably smaller than by quartz sand particles, which states once more that material removal is not essentially the main mechanism of ripple formation. While small in amplitude and short in wavelength, ripples started to be formed after an erosion time of 2.5 hours and increased further after 5 and 10 hours. After an erosion time of 10 hours, ripples were mostly well-defined, differently from that observed for aluminium 5754 and copper considering the same erodent particle, which were considered mostly irregular. R_a and

RS_m in the case of brass 70/30 eroded by spherical glass beads particles are presented in Figure VI-23 (a) and (b), respectively. At inclination angles of 10°, 20° and 30°, R_a showed similar behaviours, i.e. it initially decreased and then increased for higher erosion times, specially at an inclination angle of 30°. The increase at 30° is bigger than at 10° and 20° as the ripples were higher in amplitude. At an inclination angle of 40° and for erosion times of 2.5 and 5 hours, R_a presented similar values as the initial state of the surface, as the amplitude of the ripples is similar to the initial roughness height, as can be seen in the roughness profiles in Figure VI-22 and in Table VI-3. After 10 hours of erosion, R_a increased greatly due to the increase in the amplitude of the ripples. RS_m, on the other hand, basically increased with erosion time at all inclination angle analysed, in which it presented higher values at 40°.
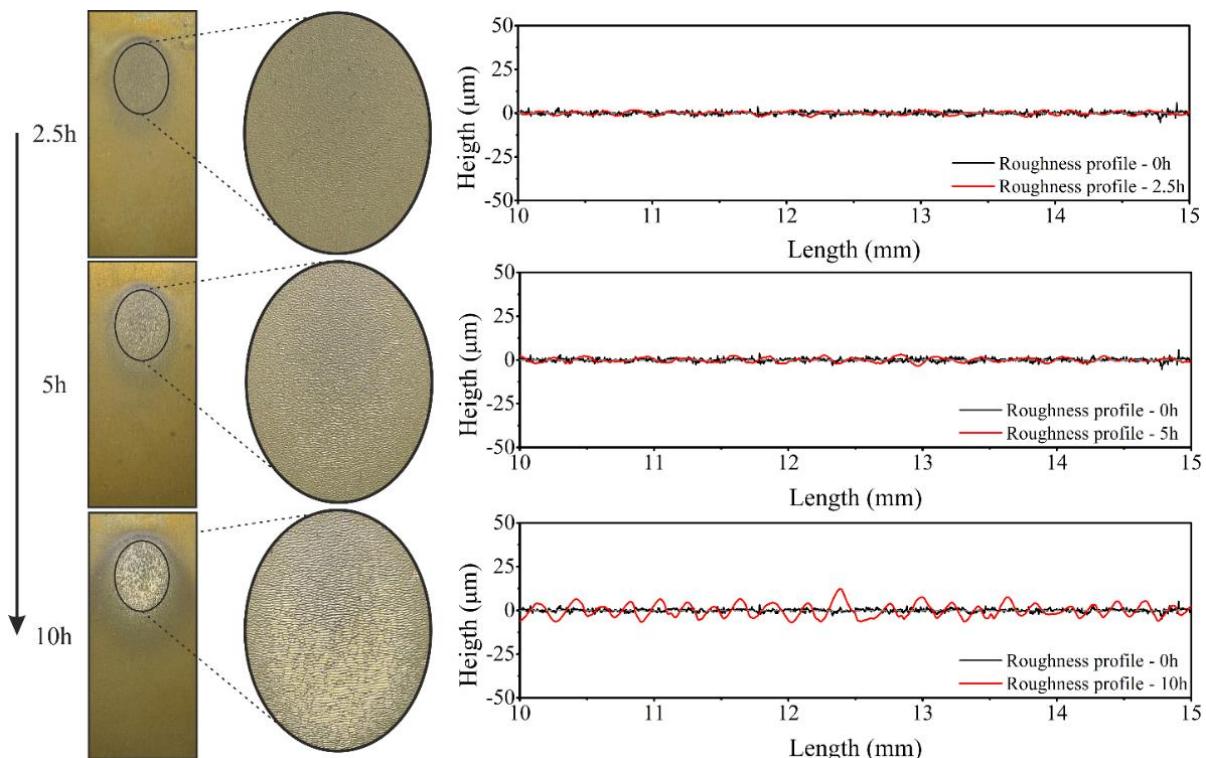
Figure VI-22. Changes on material surface (left) and roughness profiles (right) for different erosion times. Inclination angle: 40°. Particle: 211.5 µm spherical glass beads. Material: brass 70/30.

The experimental and predicted values of $\Delta\gamma$ for brass 70/30 eroded by spherical glass beads particles are presented in Figure VI-24. At shallow inclination angles such as 10° and 20°, $\Delta\gamma$ decreased from its initial value up to a point where only small variations were observed due to erosion. By increasing the inclination angle to 30° and 40°, $\Delta\gamma$ increased with erosion

after decreasing from its initial value. The predicted values of $\Delta\gamma$ by Equation (VI-1) showed good agreement with the experimental values.
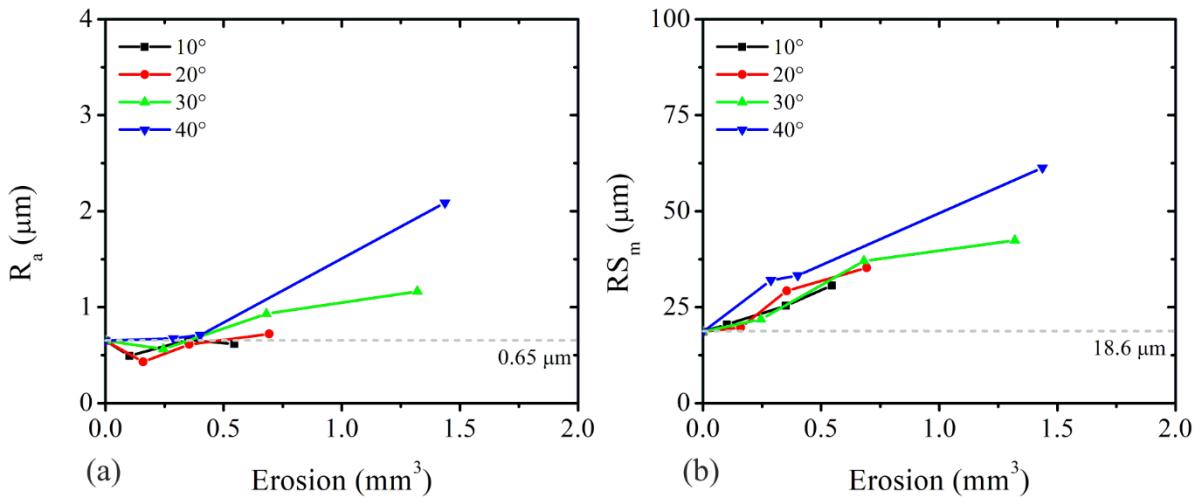
Figure VI-23. (a) R_a and (b) RS_m profiles as a function of erosion at different inclination angles. Particle: 211.5 µm spherical glass beads. Material: brass 70/30. $H_v = 1.2\ GPa$.
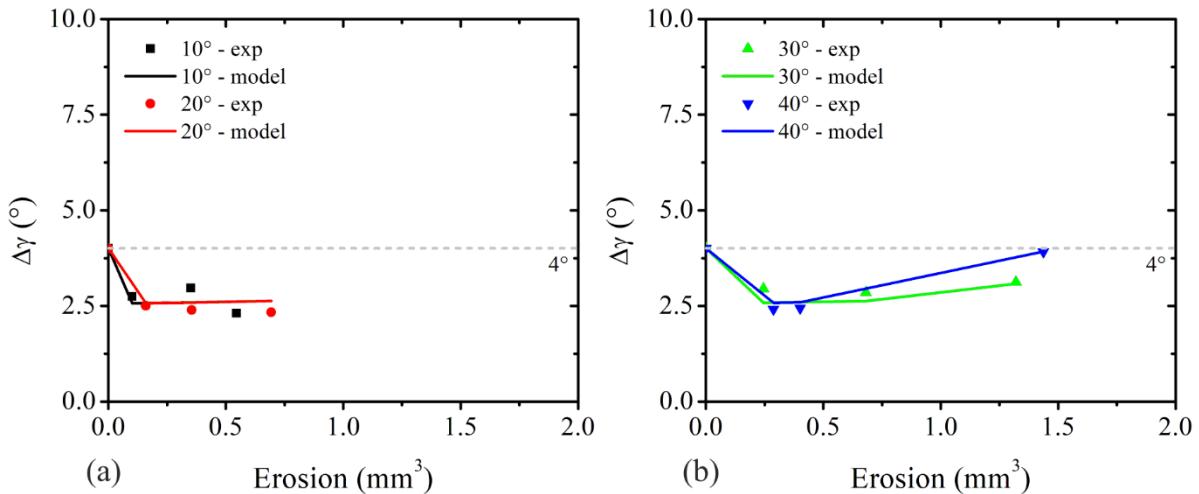

Figure VI-24. Comparison between experimental and predicted values of $\Delta\gamma$ according to Equation (VI-1) using the parameters presented in Table VI-4: (a) inclination angles of 10 and 20° and (b) inclination angles of 30 and 40°. Particle: 211.5 µm spherical glass beads. Material: brass 70/30. $H_v = 1.2\ GPa$.

Chapter VII

Numerical Validation of Gas-Solid Flows and Erosion Models

This chapter presents the ability of the previously described numerical approach to predict the behavior of gas-solid flows. Therefore, numerical results are compared with the experimental data provided by Huber[3] and Huber and Sommerfeld[4,5]. Initially, the numerical setup is presented, and the results are discussed in the following. It should be noted that a full analysis of the development of the dispersed two-phase flow considered in this chapter and parametric sensitivity studies are not attempted here. Laín and Sommerlfed[101] performed similar numerical validation using an in-house CFD code, namely FASTEST/Lag-3D. Therefore, the objective of the numerical investigation presented in this chapter is to validate and to achieve similar level of agreement between calculations and experimental data by using the CFD code OpenFOAM® 4.1. This is presented in Section 7.1. Additionally, a numerical validations of erosion models are provided in Sections 7.2 and 7.3.

7.1. Huber and Sommerfeld Case

The experimental data obtained by Huber[3] and Huber and Sommerfeld[4,5] in a pneumatic conveying system composed of a 5 m horizontal pipe, a 90° bend ($R_{bend} = 2.54D_{pipe} = 0.381\ m$) and 5 m vertical pipe is used to evaluate the ability of the numerical approach presented in Chapter V to predict gas-solid flows. The pipe is made of stainless steel with an inside diameter of 0.15 m. A one-component Phase-Doppler anemometer (PDA) was applied to determine the local particle mean number diameter, the stream-wise particle mean velocity and the associated mean fluctuation, as well as the particle mass flux in the stream-wise direction. The measurements were performed in the vertical pipe at distances of 0.3, 1.3 and 4.3 m from the bend exit with a particle mass loading of $\eta = 0.3$. The system as well as the measurement location are illustrated in Figure VII-1.
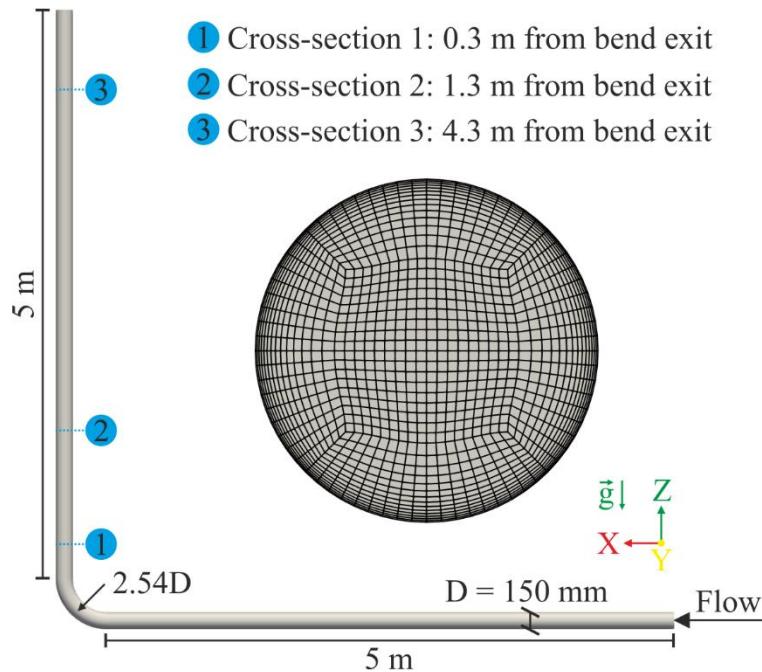
Figure VII-1. Computational grid and measurement locations according to Huber[3] and Huber and Sommerfeld[4,5].

Stainless steel is characterized by a high surface roughness degree and therefore a constant surface roughness angle distribution of $\Delta\gamma = 10°$ is chosen, as previously considered and validated by Laín and Sommerfeld[101]. The mean conveying velocity used in the experiments is 27 m/s, which yields a high pipe Reynolds number of 270,000. The air density

and dynamic viscosity are 1.2 kg/m^3 and 18·10^{-6} Pa·s, respectively. The air is injected uniformly at the horizontal pipe inlet. An outlet condition is applied at the vertical pipe exit whilst no-slip conditions are considered at the pipe walls. A medium level of turbulence, i.e. 5%, was adopted at the pipe inlet for the turbulent quantities. As mentioned earlier in Chapter V, wall functions are applied in near-wall region in order to solve the turbulent properties and therefore, extra refinement in the pipe walls is not necessary for a proper solution to be obtained. The geometry was discretized into approximately 950,000 hexahedral control volumes using an O-grid blocking method as presented in Figure VII-1. The refinement degree was found to be sufficient to produce grid-independent results.

$$\begin{cases} 15\ \mu m\ \leq class\ 1 < 25\ \mu m \\ 25\ \mu m\ \leq class\ 2 < 35\ \mu m \\ 35\ \mu m\ \leq class\ 3 < 45\ \mu m \\ 45\ \mu m\ \leq class\ 4 < 55\ \mu m \\ 55\ \mu m\ \leq class\ 5 < 65\ \mu m \\ 65\ \mu m\ \leq class\ 6 < 75\ \mu m \\ 75\ \mu m\ \leq class\ 7 \leq 85\ \mu m \end{cases}$$
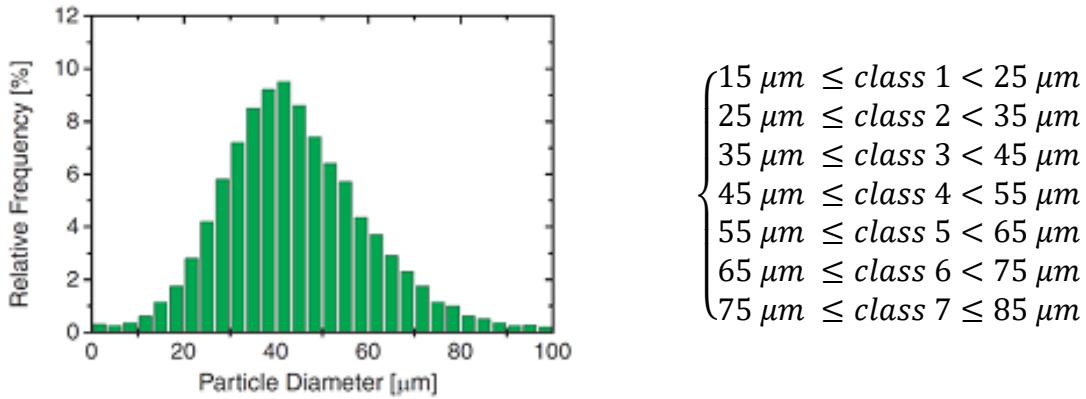
Figure VII-2. Particle size distribution of the glass beads according to the experiments of Huber and Sommerfeld[4].

Spherical glass beads particles with a density of 2,500 kg/m^3 are continuously injected at the pipe inlet. Particle linear and angular velocities are sampled from a Gaussian distribution with a constant mean and a rms value. The mean particle velocity in the stream-wise direction is the bulk air velocity of 27 m/s and zero in the transverse components. The rms value consists of 3% of the bulk air velocity in all three particle velocity components. The particle angular velocities are composed of a zero mean and a standard deviation of 1000 s^{-1} in all three components. The particle diameter is sampled from a continuous cumulative distribution function which is discretized into 7 class sizes ranging from 15 µm to 85 µm, as shown in Figure VII-2. This procedure also yields a variation of particle size within each class size. 600,000 parcels per second are injected continuously into the system and in order to allow for the correct mass flux of particles to be achieved, each parcel represents 2,000 real particles.

The calculations are performed for a mass loading of $\eta = 0.3$, which is the same of the experiments. As inelastic particle-wall interaction is considered, the restitution and friction coefficients are computed as a function of particle impact angle according to Equations (V-45) and (V-46), respectively. The restitution coefficient is assumed to be 0.9 during inter-particle collisions whereas a constant value of 0.4 is chosen for both static and dynamic friction coefficients. Gravity is applied in the opposite direction of the Z axis (see Figure VII-1).

Table VII-1. Summary of the experimental conditions and numerical setup.

Bulk air velocity, U_{av} [m/s]	27
Reynolds number, Re [-]	$\approx 270{,}000$
Air temperature, T_{air} [°C]	25
Air pressure, P_{air} [Pa]	101325
Air density, ρ_f [kg/m³]	1.18
Air viscosity, μ_f [Pa·s]	$18.0 \ 10^{-6}$
Mass loading, η [kg particles/kg air]	0.3
Number mean diameter, $D_{P,0}$ [µm]	40.0
Particle density, ρ_p [kg/m³]	2500
Parcels injected [parcels/s]	600,000
Particle per parcel [p/parcel]	2,000
Grid size	$\approx 950{,}000$
Pipe material	Stainless stell
Surface roughness, $\Delta\gamma$ [°]	10.0

Unsteady simulations were performed and a fixed time step of 0.0001 is selected for the solution of the Eulerian phase which ensured a maximum Courant number smaller than unity. As pointed out in Chapter V, Section 5.7, the Lagrangian time step for the particle tracking is dynamically calculated and chosen to be 20% of the smallest of all relevant time scales. All relevant forces acting on particles are considered as described in Chapter V as well. The single flow is computed for 1 s to ensure that a pseudo-steady state is achieved and thereafter, particles are injected into the system. The coupled fluid and dispersed phase are simulated for 1 s to achieve a constant number of parcels within the numerical domain, i.e. the number of parcels injected into the system is similar to the number of parcels which escape the

system. Subsequently, fluid and particle properties are sampled and averaged for 1 s to minimize statistical errors. Therefore, a total simulation time of 3 s is required, which takes between 2 and 3 days on 12-core CPU. Additionally, a summary of experimental conditions and the numerical setup is presented in Table VII-1.

Results

According to Laín and Sommerfeld[101], dispersed gas-solid flows in bends are generally characterized by phase segregation, in which particles accumulate on the outer wall of the bend mainly due to inertial effects. Consequently, rather dense ropes of particles are developed in bends leading to high local particle concentrations, which increases the probability of inter-particle collisions to occur. Hence, to which extent particles accumulate in the bend outer wall depends strongly on surface roughness and inter-particle collisions. Secondary flow formation in the bend and particle inertia are the most effective mechanisms which drive particles towards the outer wall of the bend. Upon impacting on the outer wall of the bend, particles are bounced off the surface to the core of pipe, a process which is intensified for higher surface roughness due to the associated shadow effect. The shadow effect implies that the average particle rebound angle is larger than the impact angle and consequently, momentum is transferred from the component parallel to the surface to the transverse components. Thus, particles should be distributed over a large portion of the vertical pipe cross-section as a surface roughness of 10° is considered relatively high. Even so, a moderately dense particle rope is observed at the outer wall of the bend. However, the secondary flow induced by the bend causes the particle rope to disintegrate along the vertical pipe. The emergence of a secondary flow in the bend is mostly caused by the high number of particle-wall collisions on the outer wall of the bend and the resulting focusing of particles trajectories towards the core of the pipe.

Figure VII-3 (a) presents a comparison of the numerical calculations for the particle mean velocity, normalised with the bulk flow velocity (i.e. $U_{av} = 27 m/s$), with measurements at 0.3 m, 1.3 m and 4.3 m from the bend exit. The outer wall of the bend is located at the right-hand side of the profiles. The numerical calculations accounting for particle-wall interactions with rough surfaces and inter-particle collisions can reproduce the experimental observations quite well. Nevertheless, particle mean velocities are slightly underpredicted in some regions,

especially at the right-hand side of the profiles located at z = 0.3 m and z = 1.3 m. By disregarding inter-particle collisions (2-way coupling), particles are not trapped within the particle rope formed just downstream of the bend exit (Figure VII-3 (b) at z = 0.3), which leads to a much wider rope prediction resulting in a reduced particle mean velocity over a large region of the profile as a consequence of the momentum transfer between the continuous and dispersed phases. Furthermore, calculations yielded similar results as the ones obtained by Laín and Sommerfeld[101] using FASTEST/Lag-3D.
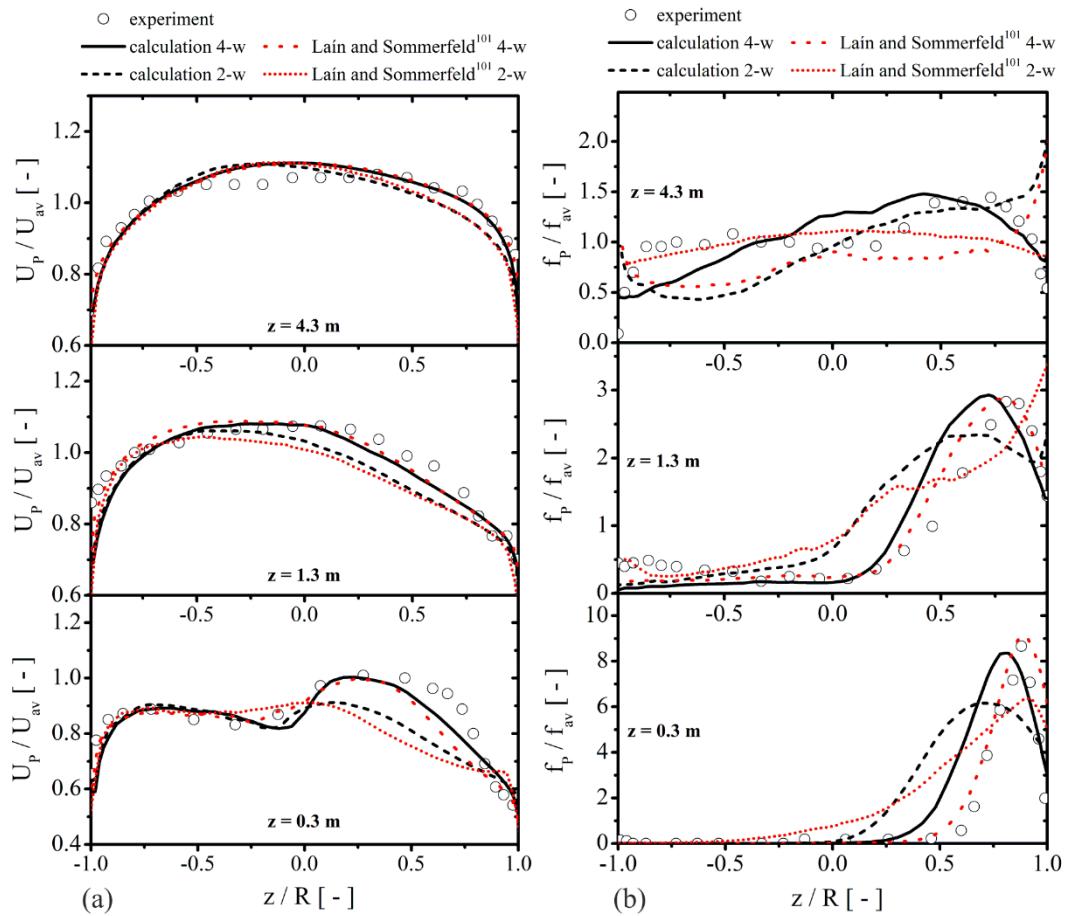
Figure VII-3. Calculated normalised particle mean velocity (a) and mass flux (b) compared to the experimental data of Huber and Sommerfeld[4] in the vertical pipe at z = 0.3, 1.3 and 4.3 m downstream of the bend exit ($D_{pipe} = 0.15\ m, R_{bend} = 2.54 D_{pipe}, U_{av} = 27\ m/s, \eta = 0.3, \Delta\gamma = 10°$). The particle mass flux is normalised by the mass flux at the inlet.

The comparison of the calculations with the measurements for the normalized particle mass flux is shown in Figure VII-3 (b). The agreement obtained is reasonably good for the cross-sections located at z = 0.3 m and z = 1.3 m when inter-particle collisions are considered,

and the numerical calculations were able to capture the magnitude of the particle mass flux peak. However, the calculations predict a slightly wider particle rope at these locations and therefore, both profiles are slightly shifted to the left, which may suggest that the surface roughness is strongly affecting the particle-wall collision process. Also, at z = 1.3 m the calculations underpredict particle mass flux in the region near the inner wall of the pipe (left-hand side of the profile). In the last profile (z = 4.3 m), measurements and calculations still show a region of higher particle mass flux near the outer wall and a good agreement was achieve for this region. Nonetheless, calculations overpredict the particle mass flux in the central region of the profile and underpredict in the region near the inner wall. Consequently, the selected numerical approach considering inter-particle collisions and particle-wall interactions with rough surfaces can capture the essential characteristics of the particle rope dispersion downstream of the bend exit. A much wider particle rope is obtained in the calculations when inter-particle collisions are not accounted for, resulting in unrealistic predictions of the particle mass flux. However, some discrepancies are observed in the particle mass flux in relation to the calculations of Laín and Sommerfeld[101] using FASTEST/Lag-3D, especially at z = 4.3 m.

The comparison between two- and four-way calculations and the measurements of the normalised number mean diameter is demonstrated in Figure VII-4. The numerical calculations considering inter-particle collisions show particle size segregation in the bend as observed in the experiments as well. Due to centrifugal effects, more inertial particles are forced to move towards the outer wall of the bend (right-hand side of the profiles). Therefore, in the cross-sections located at z = 0.3 m and z = 1.3 m a larger mean diameter is found on the right side of the profiles. Additionally, small particles are transported to the inner region of the pipe cross-section mainly due to the development of secondary flow in the bend. Particle number mean diameter is underestimated by the calculations in the left side of the core region of profile at z = 0.3 m while it is overpredicted in the right side. Nevertheless, the particle mass flux is very small in this region. In the cross-section located at z = 1.3 m the particle number mean diameter is overpredicted in the right side and the number of small particles is underpredicted near the inner wall. In the upper cross-section (z = 4.3 m) the particle mean number diameter is basically uniform in the experiments, but it is mostly overestimated in the simulations. In general, the trends in the profiles of the particle number mean diameter in all

cross-sections are well predicted and a good agreement of all predicted particle phase properties was obtained by applying the numerical approach presented in Chapter V using OpenFOAM® 4.1. Nonetheless, some deviations are observed in the particle number mean diameter in relation to the computations performed by Laín and Sommerfeld[101] using FASTEST/Lag-3D.
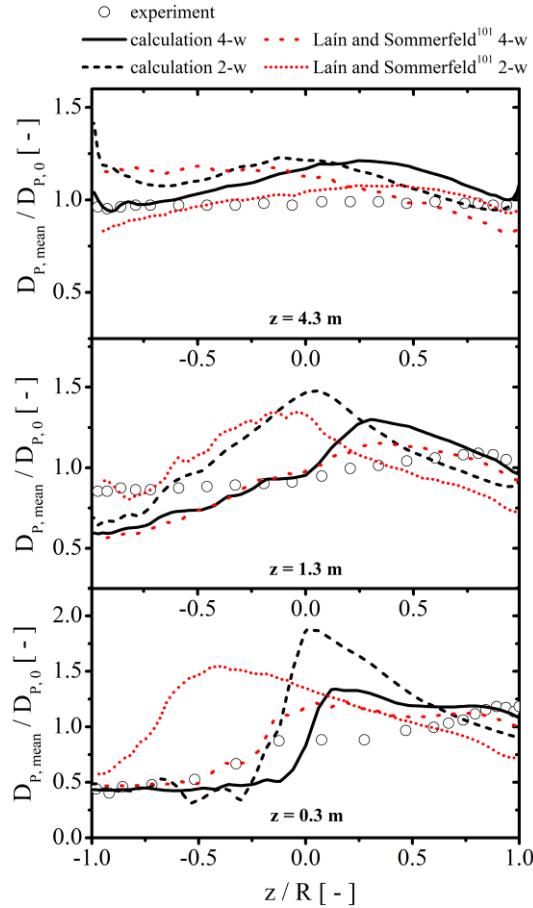
Figure VII-4. Calculated normalised particle mean number diameter compared to the experimental data of Huber and Sommerfeld[4] in the vertical pipe at z = 0.3, 1.3 and 4.3 m downstream of the bend exit ($D_{pipe} = 0.15\ m, R_{bend} = 2.54 D_{pipe}, U_{av} = 27\ m/s, \eta = 0.3, \Delta\gamma = 10°, D_{P,0} = 40\ \mu m$).

7.2. Mazumder Case

The goal of this section is to provide a numerical validation of erosion calculations regarding different predictive equations available in the literature. Mazumder et al.[1] experimentally investigated the magnitude of erosion at different locations of an elbow

specimen to determine the location of maximum erosion. Experiments were performed in a vertical to horizontal two-phase flow. The elbow used in the experiments was made of aluminum 6061-T6, which has a density and Vickers hardness of 2700 kg/m^3 and 1.049 GPa, respectively. The bulk velocity of air in the experiments was 34.1 m/s, which results in a Reynolds number of about 57,750. Sand particles with a mean diameter of 182 µm and a mass loading of 0.013 (kg of particles/kg of air) were injected into the vertical pipe at about 1.22 m below the test elbow. The test specimen was a 90° elbow with a diameter of 25.4 mm and a curvature radius of 38.1 mm, as illustrated in Figure VII-5. A horizontal pipe with 10 diameters long is considered after the elbow and details of the numerical mesh used in the calculations is presented in Figure VII-5 as well.
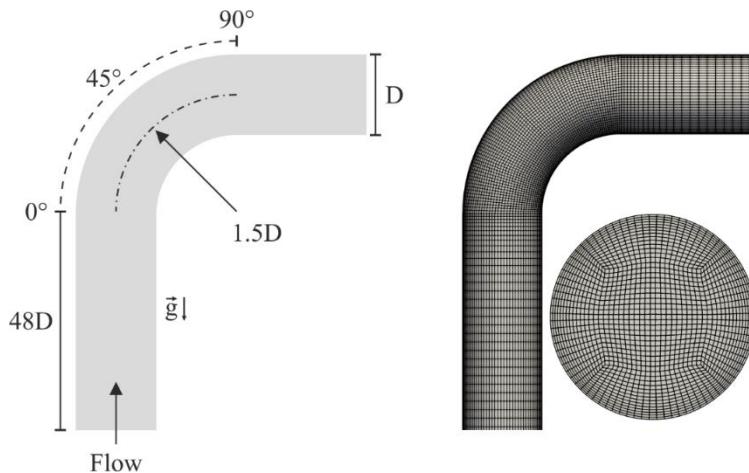
Figure VII-5. (left) Sketch of the experimental testing facility of Mazumder et al.[1] and (right) details of the numerical mesh.

The numerical domain was discretized into approximately 1,000,000 hexahedra elements, which produces less numerical diffusion then elements such as tetrahedra and pyramids. In the near-wall region the elements were gradually refined due to the existence of high velocity gradients and the boundary layer. The numerical mesh refinement yielded mesh-independent results. 4,953,000 parcels per second were tracked through the flow field using the forces and Lagrangian time step restrictions described in Chapter V. The Eulerian time step was set to $1.0 \cdot 10^{-5}$ s. Inter-particle collisions as well as flow modification by the particles are neglected in the calculations as the experiments were conducted with a very low mass loading of 0.013. Particles were injected into the system with the mean fluid velocity of 34.1 m/s and

a fluctuating velocity for all three components of 4.5% of the bulk flow velocity was considered.

Inelastic particle-wall collisions are considered and therefore, the restitution model of Grant and Tabakoff[74] is applied according to Equations (V-47) and (V-48), as such model was originally derived for sand particles impacting on an aluminium surface. The friction coefficient is calculated depending on the particle impact angle according to the empirical correlation obtained by Sommerfeld and Huber[85], i.e. Equation (V-46). Additionally, the pipe surfaces were considered as perfectly smooth as no information about the degree of surface roughness was reported. However, it important to highlight that the effect of surface roughness on erosion behaviour is of major importance, as previously discussed in other sections. In this brief numerical analysis, the Oka model was applied with the parameters presented in Table VII-2 while the parameters concerning the other models are the same as presented in Chapter V, Section 5.9. Also, the particle shape coefficient was set to 0.53 in the Zhang model.

Table VII-2. Parameters used in the Oka model for the SiO_2 particles and aluminium wall.

K	k_1	k_2	k_3	u_{ref}	D_{ref}	n_1	n_2
65	-0.12	$2.3(Hv)^{0.038}$	0.19	104	326	$0.71(Hv)^{0.14}$	$2.4(Hv)^{-0.94}$

Results

A quantitative comparison of the numerical results predicted by different erosion models with the measured thickness loss along the central line of the outer wall of the bend is presented in Figure VII-6. The vertical bars indicate the standard deviation of the measurements. Here, the bend inlet is set to a bend angle of 0° whereas a bend angle of 90° corresponds to the bend outlet. Qualitatively speaking, all erosion models predicted similar thickness loss curves, although their magnitude are different. As the flow field is the same for all erosion correlations and most of them depend mainly on particle impact velocity and angle, the behaviour of the curves is expected to be similar. Alternatively, the thickness loss magnitude depends mainly on material and particle properties as well as other parameters, such as velocity exponent. Therefore, the models performed well in predicting the location of maximum thickness loss, which is between bend angles of 50° to 55° in this case. The slightly

difference in the location of maximum erosion between measured and calculated values can be attributed to the predictions of the two-phase flow rather than to the erosion correlations, as all of them predicted similar erosion peak along the bend. Nonetheless, considering the complexity of the phenomena involved in two-phase flows, the quality of the results is reasonably good. Among the models analysed, the Oka model provided the best agreement with the experimental data. All other models overpredicted the maximum thickness loss. Therefore, the Oka model is considered the most suitable among the models tested and it will be applied for all erosion calculations presented in Chapter VIII. Additionally, results obtained with numerical approach adopted in this work and considering the Oka model are similar to the numerical results obtained by Laín and Sommerfeld[92] using FASTEST/Lag-3D, as illustrated in the same figure.
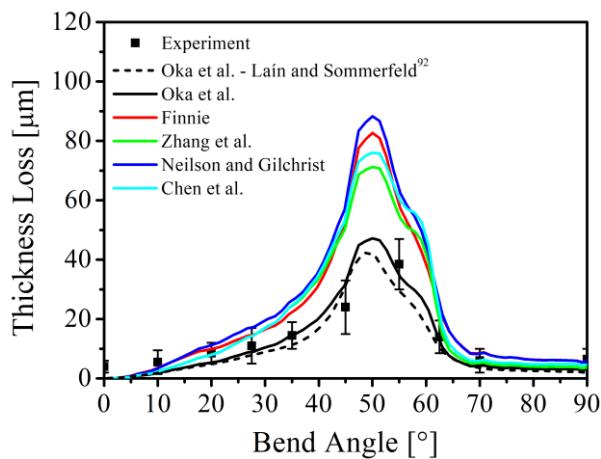
Figure VII-6. Comparison of the predicted thickness loss by different erosion models with the experimental data from Mazumder et al.[1].
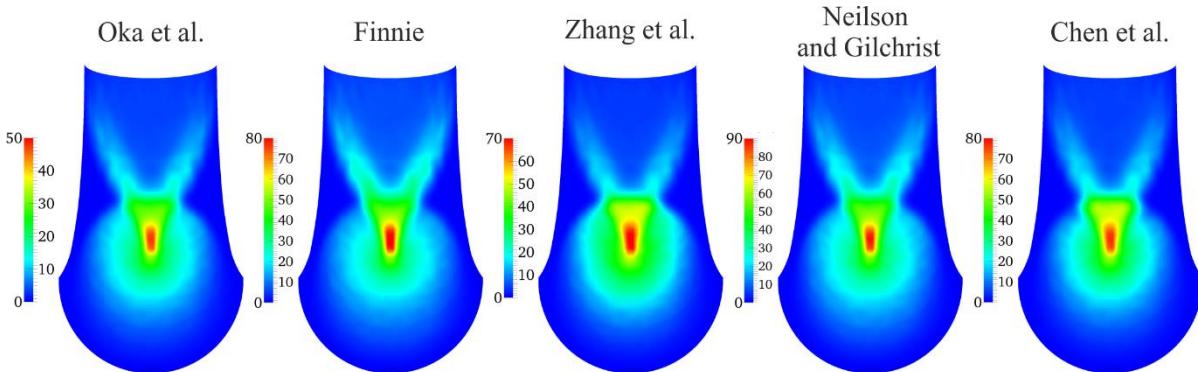
Figure VII-7. Predicted erosion scar by different erosion models for the Mazumder et al.[1] two-phase flow. Flow enters at the bottom of the image.

Figure VII-7 illustrates the predicted erosion scar on the outer wall of the bend by the considered erosion models. Please note that the scales are different to emphasize the similarities of the erosion patterns. The flow direction is upwards and gravity acts in the opposite direction of the flow (see Figure VII-5). The erosion scars are characterized by a narrow, elongated region of high thickness loss, which is surrounded by a wide area of moderate erosion. The region of high thickness loss arises mainly due to primary particle-wall collisions with high particle impact velocity. Downstream of the location of high erosion a V shaped structure is observed, which is caused mainly due to secondary particle-wall collisions. This behaviour has been numerically observed by a number of other investigators[2,18,71,87,89,92]. Nevertheless, according to Solnordal et al.[2], a V shaped structure is normally not observed experimentally. The purpose of the comparison presented in Figure VII-7 is to demonstrate that the erosion models considered predict very similar erosion patterns, but with different magnitudes, as previously discussed.

7.3. Solnordal Case

As previously described in Chapter II, Section *Numerical Studies of Solid Particle Erosion*, Solnordal et al.[2] conducted an experimental analysis of bend erosion caused by sand particles in a pneumatic conveying system. The authors provided experimental data on erosion depth obtained in a 90° elbow ($R_{elbow} = 1.5D$) by conveying 200 kg and 300 kg of sand with a mean number diameter of 184 µm with air at 80 m/s. They obtained a detailed three-dimensional surface map of erosion scar by using a Sheffield Discovery II D-8 coordinate measurement machine (CMM). The data is additionally used for validating erosion predictions based on the numerical approach presented in Chapter V.

The experimental facility is consisted of an open circuit, in which the main test section has a diameter of 102.5 mm and air is injected into a 200 mm horizontal pipe close to the floor. Sand is injected at a constant rate into the horizontal pipe before transitioning two 90° elbows and a reducer and entering a vertical pipe. The vertical pipe is 25.8 D long and ends at the experimental elbow. The elbow is machined out of two aluminum blocks (Al grade 6061) that are bolt together. Sand was introduced far upstream of the test section to ensure relatively uniform distribution of the particles upon arriving at the measurement elbow. Figure VII-8

illustrates the experimental facility. The dimensions of the experimental facility are reported in Table VII-3.
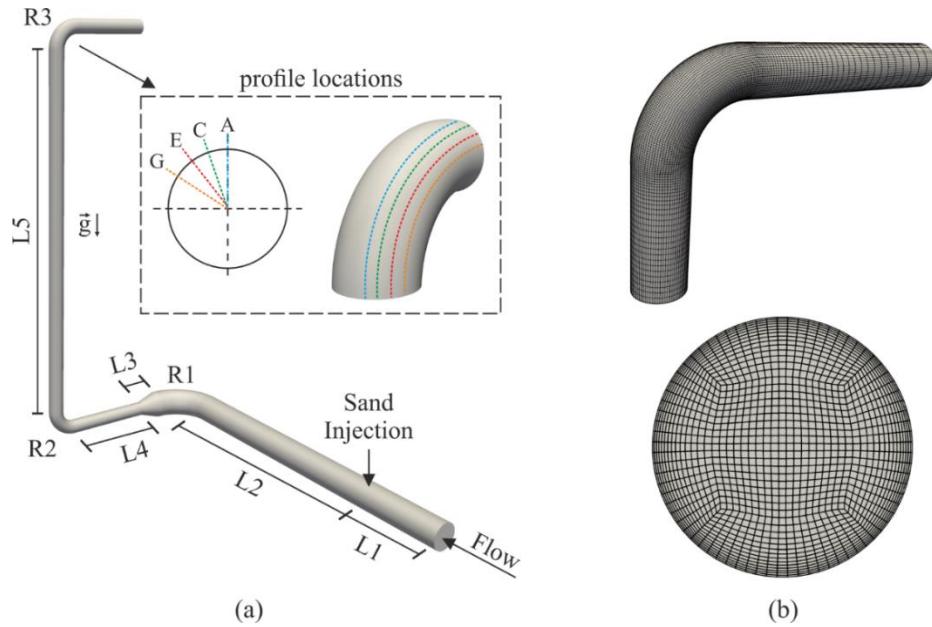
Figure VII-8. (a) Schematic representation of the experimental facility according to Solnordal et al.[2] and profiles used for comparison in the current work. (b) Numerical mesh visualization.

Surface profile measurements were first performed with a fresh elbow and after the passage of 200 kg and 300 kg of sand through the elbow. The authors extracted twenty erosion profiles labelled from A to V along the left side of the elbow surface. However, only profiles A, C, E and G are used for comparison with numerical calculations in the current work as shown in Figure VII-8. In fact, profiles A and C are more interesting for comparison as they represent the region with maximum erosion. Profiles are separated by an angle of 18.95°. As a considerably low particle mass loading of $\eta = 0.0384$ was used in the experiments, particle-particle interactions and the effect of the particles on the continuous phase were neglected.

Table VII-3. Dimensions of the experimental facility from Solnordal et al.[2].

L1	L2	L3	L4	L5	R1	R2	R3
500 mm	1950 mm	150 mm	600 mm	2644 mm	300 mm	153 mm	153 mm

The entire system was considered in the calculations to prevent errors due to geometry simplifications, despite the increase in the computational cost. On the other hand, the computational effort is considerably reduced by neglecting two- and four-way coupling. The

numerical domain consists of 983,250 hexahedra elements, which yield more numerical stability and less numerical diffusion. The numerical mesh is refined in the near-wall region due to high velocity gradients. Mesh independent results were obtained with the respective refinement.

Table VII-4. Summary of the experimental conditions and numerical setup for the Solnordal et al.[2] case.

Air flow rate, $\dot{m}_f$ [kg/s]	0.78
Bulk air velocity entering the elbow, U_{av} [m/s]	80
Reynolds number in the elbow, Re [-]	538,000
Air temperature, T_f [°C]	25
Air pressure, P_f [Pa]	101325
Air density, ρ_f [kg/m^3]	1.18
Air viscosity, μ_f [Pa·s]	$18.0\ 10^{-6}$
Sand flow rate, $\dot{m}_p$ [kg/s]	0.030
Amount of sand passing, [kg]	300
Mass loading, η [kg particles/kg air]	0.0384
Mean volume fraction, α_p [-]	$1.746 \cdot 10^{-5}$
Sand mean diameter, $D_{P,50}$ [µm]	184
Sand density, ρ_p [kg/m^3]	2650
Parcels injected [parcels/s]	1,734,000
Particle per parcel [p/parcel]	2
Grid size	983,250
Pipe material	Al grade 6061
Surface roughness, $\Delta\gamma$ [°]	7.0

Air is injected into the horizontal pipe at a constant velocity of 22.01 m/s and a 5% turbulence intensity was chosen at the inlet for the turbulent quantities. A gauge pressure of 0 Pa was prescribed at the outlet of the system and the no-slip condition is employed at the pipe walls. Mono-sized particles with a mean diameter of 184 µm are injected into the system perpendicularly to the particle inlet with a constant velocity of 1 m/s. Particle inlet has a diameter of 40 mm and the initial rotation of the particles was neglected. The number of parcels injected per second was 1,734,000 and each parcel represents 2 real particles. The restitution

and friction coefficients were calculated according to Grant and Tabakoff[74] (Equations (V-47) and (V-48)) and Sommerfeld and Huber[85] (Equation (V-46)), respectively. Additionally, the static coefficient of friction was set as 0.5 while a surface roughness degree of 7.0° was adopted, as no experimental information was provided regarding those parameters. The fluid time step is set to $5.0 \cdot 10^{-5}$ s and the time step of the particles is dynamically calculated according to Equation (V-73). Also, material and particle properties as well as model parameters were chosen to be the same as the previously case (Section 7.2). Finally, the experimental conditions and the numerical setup are summarized in Table VII-4.

Results

Figure VII-9 compares predicted erosion distributions obtained with different erosion models to the experimental data provided by Solnordal et al.[2]. The origin of the profiles, i.e. at a bend angle of 0°, is set at the bend inlet, whilst a bend angle of 90° corresponds to the bend outlet. As with the case discussed earlier (Section 7.2), the erosion models predicted very similar erosion curves, qualitatively speaking, but with different magnitude. Similar qualitative behaviours are obtained in this case for the same reasons discussed in the previous case, i.e., as most of the correlations depend mainly on the particle impact angle and velocity, and as the flow field is the same for all correlations, it is expected the erosion curves to be similar. The prediction of the region with maximum thickness loss is in very good agreement with the measurements, showing the quality of the predictions not only for the particle impact angle and velocity but also for the distribution of the particles within the bend.

The region of maximum erosion is located along the centre line (profile A) between bend angles of 55° to 60° in this case. The best results were obtained using the Oka model, whereas all other models overestimated erosion. In general, the Oka model provided very good agreement with the experimental data for regions comprehended between 40° to 90° for all profiles, although the maximum thickness loss is slightly overpredicted for profile A. However, values are mostly underpredicted for all profiles for bend angles between 0° to 40°. Such behaviour has been also observed by other authors[89,91]. This short numerical analysis shows once more that the application of the Euler-Lagrange approach together with an appropriate erosion model allows accurate predictions of erosion on bends in dispersed gas-

solid flows. Due to the quality of the numerical results obtained once again through the Oka model, it will be used in the numerical analysis presented in Chapter VIII.
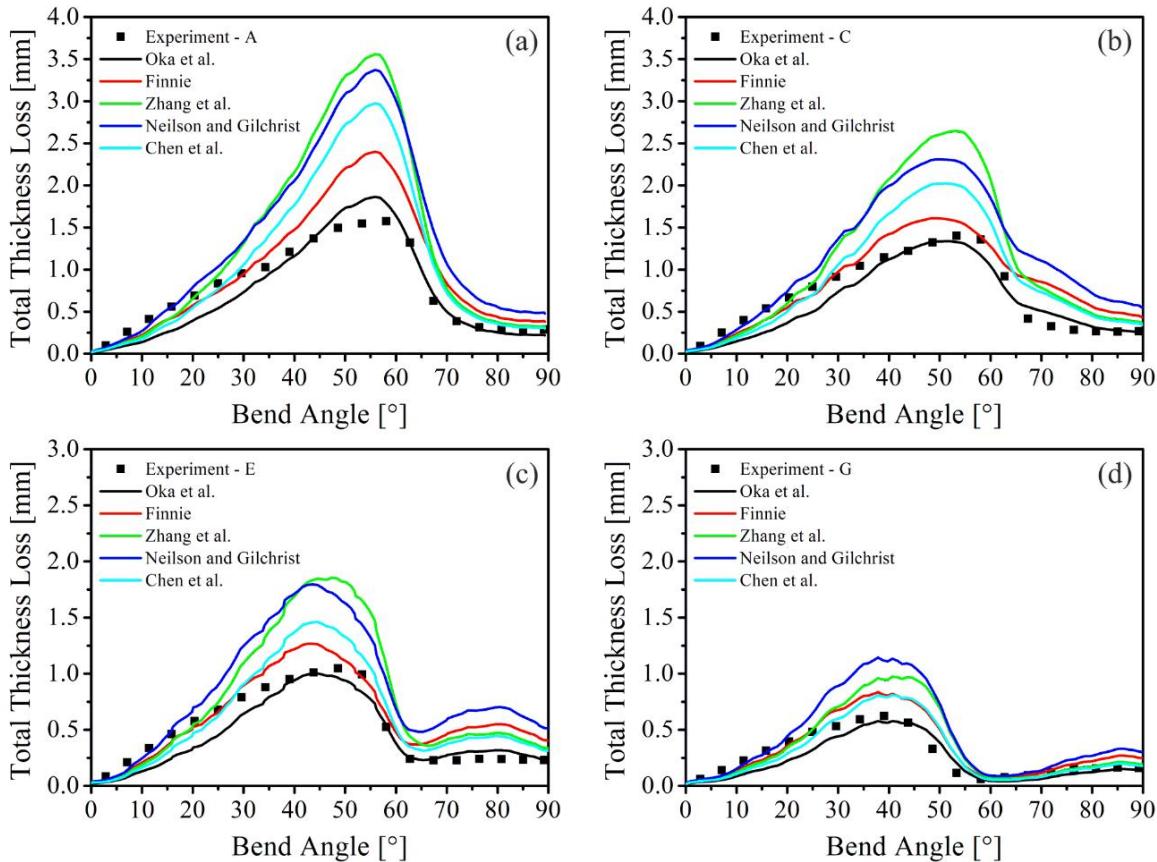
Figure VII-9. Predicted erosion distributions compared to the measurements from Solnordal et al.[2] for different erosion models. Profiles: (a) A, (b) C, (c) E, and (d) G.

The predicted erosion map with the Oka model after the passage of 300 kg of sand is demonstrated in Figure VII-10. As observed in the experiments, erosion decreases in all directions from the region of maximum erosion, which is represented by the red spot on the figure and located between bend angles of 55° to 60°. The numerical erosion scar resembles the one measured in the experiments quite well (the reader is referred to figure 6b from Solnordal et al.[2] for comparison), as may also be seen quantitatively in Figure VII-9 for different profiles.
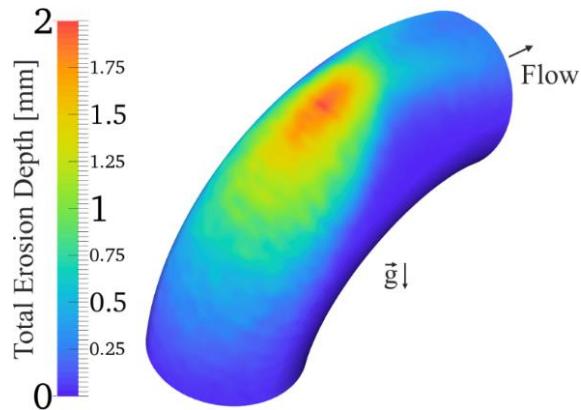
Figure VII-10. Predicted erosion map on the outer wall of the bend for the Solnordal et al.[2] case with the Oka model.

Chapter VIII

Bend Erosion – Experimental and Numerical Validation

This chapter provides a detailed numerical analysis of bend erosion and presents the experimental results obtained in the pneumatic conveying facility detailed in Chapter IV. The numerical setup as well as a grid independence test is initially presented in Section 8.1. Single phase flow calculations are validated by comparison with the experimental data and are reported in Section 0. In Section 8.3 a detailed numerical validation regarding the dispersed phase is provided.

8.1. Numerical Setup

In order to provide a detailed numerical validation of the numerical approach and erosion predictions, the measurement section of the pneumatic conveying facility was computationally constructed as presented in Figure VIII-1. The discretization of the measurement section consists of a structured O-grid with 1,157,184 elements, selected based

on a preliminary grid independence test, which is described further on. A cross-sectional visualization of the internal mesh is presented in Figure VIII-1 as well. For all numerical calculations presented in this chapter a Eulerian time step of $\Delta t_E = 5 \cdot 10^{-5}s$ was adopted, which ensured a Courant number smaller than unity and consequently numerical stability was achieved. As previously mentioned in Chapter V, Section 5.7, the Lagrangian time step is calculated based on all relevant time scales but never exceeds the Eulerian time step.
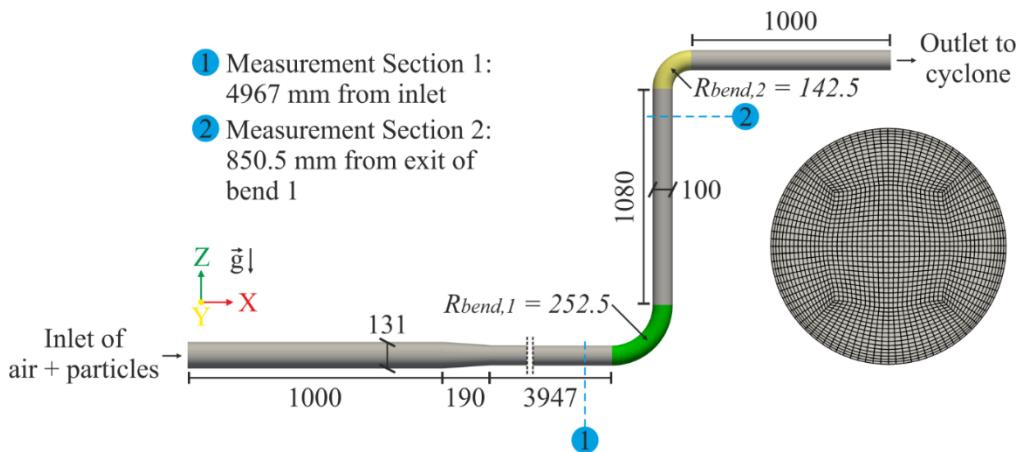
Figure VIII-1. Schematic representation of the computational geometry and internal mesh with all relevant dimensions and measurement locations. Units in millimetre.

An uniform air conveying velocity at the inlet of the system of 22.1 m/s was prescribed yielding a mean conveying velocity of 37.9 m/s in the horizontal pipe with an inside diameter of 100 mm. The flow was considered incompressible under the experimental conditions considered and therefore, a constant air density and dynamic viscosity of 1.176 kg/m³ and 18.46 10^{-6} Pa·s were chosen, respectively. A 5% turbulence intensity was adopted at the inlet for the turbulent quantities, which is referred to as a medium level of turbulence. As already mentioned, turbulence was modelled with the standard k-ε model. A quasi-steady state for the flow field calculations was achieved after 20,000 Eulerian time steps, which equals to 1s of simulation time. Thereafter, parcels were injected into the system.

An injection rate of 1,800,000 and 1,825,000 parcels per second was selected when considering spherical glass beads and quartz sand particles, respectively. As the injection rate does not represent the real number of particles, each parcel represents 5 real particles in the case of spherical glass beads considering a particle mass loading of 0.3 and 16 real particles when considering a particle mass loading of 1.0. By considering quartz sand particles, a

computational parcel represents 3 and 10 real particles when considering particle mass loadings of 0.3 and 1.0, respectively. This ensured the correct mass flow rate of particle obtained in the experiments. Particle linear and angular velocities were randomly sampled from a Gaussian distribution function with a fixed mean velocity and a prescribed rms (root mean square) value. A mean linear velocity of 22.1 m/s (bulk air velocity) was considered for the stream-wise velocity component, while for the transverse components, a value of zero was assumed. The rms value for the linear velocity was chosen to be 3% of the bulk air velocity for all three velocity components. Additionally, a mean value of zero and a rms value of 10^3 s^{-1} were assumed for all three components of the particle angular velocity.

The discrete phase was simulated for 0.5 s (10,000 Eulerian time steps) in order to achieve a constant number of parcels within the computational domain, i.e. the number of parcels injected into the system is similar to the number of parcels which escape the system. Thereafter, fluid and particle properties were sampled for 1 s (20,000 Eulerian time steps). Erosion predictions were performed over this simulation time as well. Therefore, the entire simulation time is 2.5 s (50,000 Eulerian time steps) and one simulation takes approximately 3 days in 12-cores CPU. Particle size distribution was discretized into 6 computational size classes when considering spherical glass beads (Figure IV-2 (a)) and 15 when considering quartz sand particles (Figure IV-2 (b)). Additionally, particle size was sampled from a continuous cumulative distribution, which results in a variation of the particle size within a computational size class.

When considering particle-particle interaction, both static and dynamic friction coefficients are assumed to be 0.4 whilst a value of 0.9 is selected for the restitution coefficient. The analysis of the influence of the change of surface roughness due to erosion on dispersed phase flow and erosion itself is performed after reaching a steady state condition with a constant number of parcels within the numerical domain. A constant number of parcels is achieved after computing the dispersed phase for 0.5 s. Thereafter Equation (VI-1) is applied with the appropriated constants (see Table VI-4) to generate a surface roughness field which depends on erosion and particle impact angle. Then, dispersed phase properties are sampled for statistical analysis as well as erosion is computed.

Table VIII-1. Numerical setup for the simulations considering spherical glass beads.

Case Identification	e [-]	μ_s [-]	μ_d [-]	$\Delta\gamma_0$ [°]	2-way	4-way	η [-]
GB1	Eq. (V-43)	0.4	Eq. (V-44)	2.5	✓	✓	0.3
GB2	Eq. (V-43)	0.4	Eq. (V-44)	2.5	✓	✗	0.3
GB3	Eq. (V-43)	0.4	Eq. (V-44)	2.5	✗	✗	0.3
GB4	Eq. (V-43)	0.4	Eq. (V-44)	10	✓	✓	0.3
GB5	Eq. (V-43)	0.4	Eq. (V-44)	20	✓	✓	0.3
GB6	Eq. (V-43)	0.4	Eq. (V-44)	Eq. (VI-1), $\Delta\gamma_0 = 2.5°$	✓	✓	0.3
GB7	Eq. (V-43)	0.4	Eq. (V-44)	2.5	✓	✓	1.0

Based on the described numerical approach, the influence of coupling degree and surface roughness on erosion predictions and dispersed phase velocity are investigated and compared with the experimental data for spherical glass beads and a particle mass loading of $\eta = 0.3$ according to Table VIII-1. The influence of coupling degree is represented by the cases GB1, GB2 and GB3 in the same table, while cases GB1, GB4, GB5 and GB6 describe the numerical setup for analysing the effect of surface roughness. Case GB7 considers the same parameters as case GB1, but for a higher particle mass loading of $\eta = 1.0$.

The effect of surface roughness variation due to erosion on the results is analysed for quartz sand particles and a particle mass loading of $\eta = 0.3$ according to Table VIII-2 (Cases SAND1, SAND2 and SAND3). The numerical setup of the case SAND4 is equal to the case SAND1, although the case SAND4 considers a higher particle mass loading of $\eta = 1.0$.

Table VIII-2. Numerical setup for the simulations considering quartz sand particles.

Case Identification	e [-]	μ_s [-]	μ_d [-]	$\Delta\gamma_0$ [°]	2-way	4-way	η [-]
SAND1	Eq. (V-45)	0.4	Eq. (V-44)	2.5	✓	✓	0.3
SAND2	Eq. (V-45)	0.4	Eq. (V-44)	Eq. (VI-1), $\Delta\gamma_0 = 2.5°$	✓	✓	0.3
SAND3	Eq. (V-45)	0.4	Eq. (V-44)	Eq. (VI-1), $\Delta\gamma_0 = 5.0°$	✓	✓	0.3
SAND4	Eq. (V-45)	0.4	Eq. (V-44)	2.5	✓	✓	1.0

Grid Independence Test

A grid independence test was performed using three different grids as presented in Table VIII-3. The grid refinement is performed in the transverse direction of the geometry.

The results are considered independent from grid size when only minimal differences from grid to grid are observed. The grid independence test was based on the standard numerical setup previously described for spherical glass beads and a particle mass loading of $\eta = 0.3$. Therefore, particle velocity profiles were extracted from the bottom and top measurement locations for the three numerical grids and compared to the experimental results, as shown in Figure VIII-2. Additionally, in Table VIII-3, Error 1 and Error 2 refer to the bottom and top measurement locations, respectively. M_{12} is the error from grid M1 to M2, and M_{23} is the error from grid M2 to M3. As can be seen, the error is smaller than 1% when comparing M2 to M3. As only small differences were observed in the numerical results, the intermediate grid was chosen for performing all the simulations presented in this section.
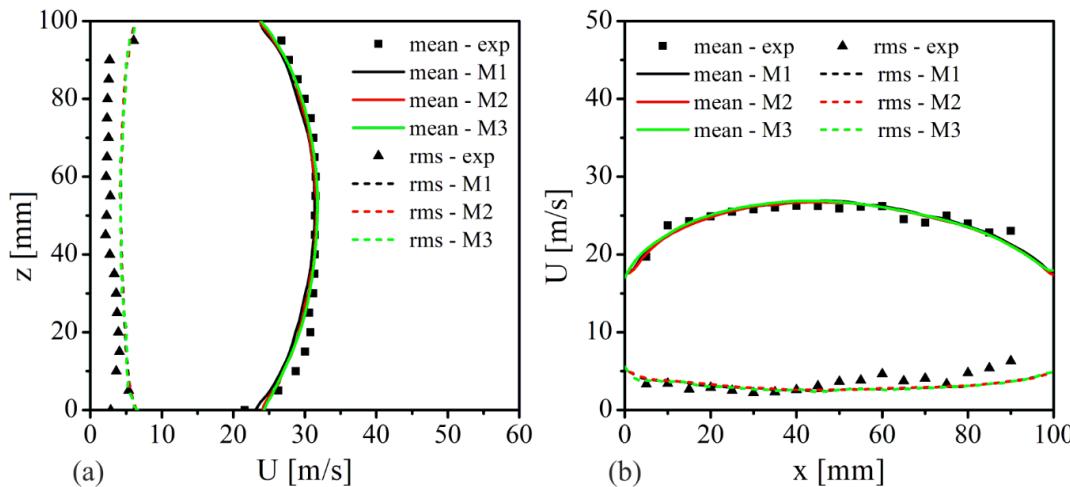
Figure VIII-2. Grid independence test. Comparison between numerical and experimental results for particle mean and fluctuating velocity components in the stream-wise direction. (a) Bottom and (b) top measurement locations considering spherical glass beads particles and $\eta = 0.3$.

Table VIII-3. Mesh resolution average y^+ values for grid independence test.

Identification	Refinement	Number of Elements	Average y^+	Error 1	Error 2
M1	Coarse	599,256	82.33	$M_{12} = 1.05\%$	$M_{12} = 0.62\%$
M2	Intermediate	1,157,184	55.33	$M_{23} = 0.77\%$	$M_{23} = 0.45\%$
M3	Fine	2,074,436	30.73	-	-

8.2. Single Phase Flow Validation

This section aims at presenting a comparison between single-phase calculations with the experimental data obtained in the test facility described in Chapter IV. Figure VIII-3 shows the mean fluid velocity in the stream-wise direction compared with the measurements performed at the measurement locations 1 and 2 (see Figure VIII-1). Henceforth, measurement locations 1 and 2 will be referred to as bottom and top locations, respectively.
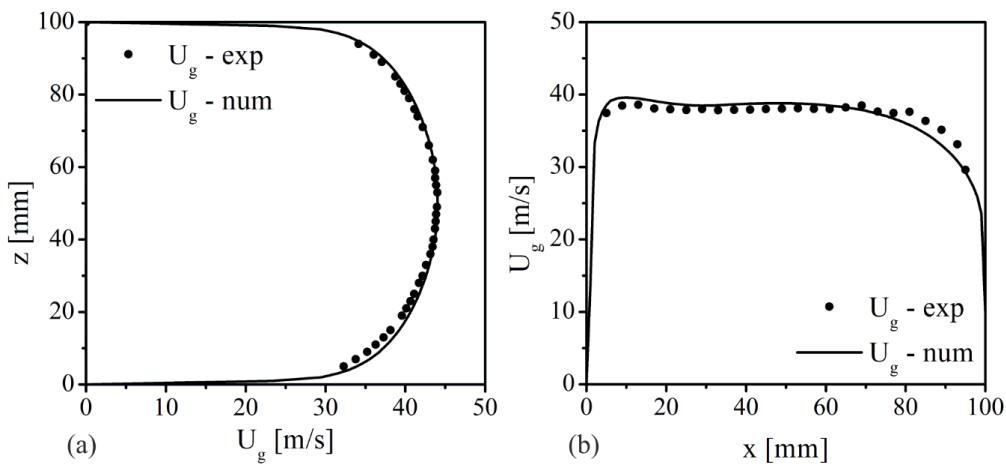
Figure VIII-3. Comparison of measured and calculated mean velocity component in the stream-wise direction for the single flow: (a) bottom and (b) top measurement locations. Results presented for a pneumatic conveying velocity of 37.9 m/s.

The quality of the numerical calculations is very good for both locations. The mean fluid velocity profile at the bottom location is characterized by a turbulent profile and the numerical values are slightly overestimated at the lower region. Nevertheless, the rest of profile, i.e. for $30\ mm < x < 100\ mm$, is quite well predicted. The numerical predictions at the top measurement location are qualitatively good, although the values are slightly overestimated for the region between $x = 0\ mm$ and $x = 70\ mm$ and underestimated for $x \geq 70\ mm$. The velocity profile at the top is not developed as at the bottom measurement location due to the geometric characteristics of system. After conveying through the first bend, the air flows through a rapid transition from the vertical section (10.8·D) to a new horizontal pipe through a 90°, short radius bend (1.4·D). The short length vertical pipe prevents the air flow to fully develop and the existence of the short radius bend modifies the behaviour of flow as well. Therefore, the fluid velocity is increased close to the inner wall (left-hand side of Figure VIII-3

(b)). Please note that the inner wall of the vertical pipe in relation to the second bend is located on the right side of the vertical pipe presented in Figure VIII-1. The calculations were able to capture the behaviour observed experimentally quite well. Based on the quality obtained for the single-phase flow predictions compared to the experimental measurements, the single-phase numerical calculations may be considered as validated.

8.3. Dispersed Phase Validation

This section is reserved for presenting the experimental and numerical results obtained for the dispersed phase. A detailed numerical analysis is conducted based on the experimental data acquired in a pneumatic conveying system (description in Chapter IV) for spherical glass beads and a particle mass loading of $\eta = 0.3$. The influence of phase interaction and surface roughness is deeply evaluated for this case. Then, the experimental and numerical results regarding the case considering spherical glass beads and a particle mass loading of $\eta = 1.0$ are presented and compared with the case considering a particle mass loading of $\eta = 0.3$, although only the standard numerical setup is compared with the experimental data, as previously detailed. Afterwards the effect of surface roughness variation due to erosion on the results is evaluated for quartz sand particles and a particle mass loading of $\eta = 0.3$. Finally, the case involving quartz sand particles and a particle mass loading of $\eta = 1.0$ is discussed based on the standard numerical setup, in which a comparison between $\eta = 0.3$ and $\eta = 1.0$ is provided as well. It should be noted that although 10 erosion profiles, which includes the profile in the centre of the surface, were acquired, only 5 profiles are presented and discussed.

All erosion predictions presented in this section are performed by applying the predictive equation proposed by Oka et al.[31] and Oka and Yoshida[32], as it yielded better erosion prediction among all the models tested (Sections 7.2 and 7.3). Therefore, the dependence of the function $g(\alpha)$ on the particle-wall impact angle for both quartz sand particles and spherical glass beads is demonstrated in Figure VIII-4. Parameters are available in Table V-3. For quartz sand particles, the function $g(\alpha)$ increases rapidly to a maximum of about 1.70 at an impact angle of 25° and then decreases to a value of 1.0 at an impact angle of 90°. This behavior is commonly observed in soft materials such as aluminum and indicates that the cutting wear is the main erosion mechanism. For spherical glass beads, on the other hand, the function $g(\alpha)$

continuously increases from zero at an impact angle of 0° until it reaches a maximum value of 1.0 at an impact angle of 90°. This behavior shows the poor cutting action of spherical particles at oblique impact angles, where the dominant erosion mechanism is ploughing rather than cutting, as previously described in Chapter II, Section Erosion Mechanisms.
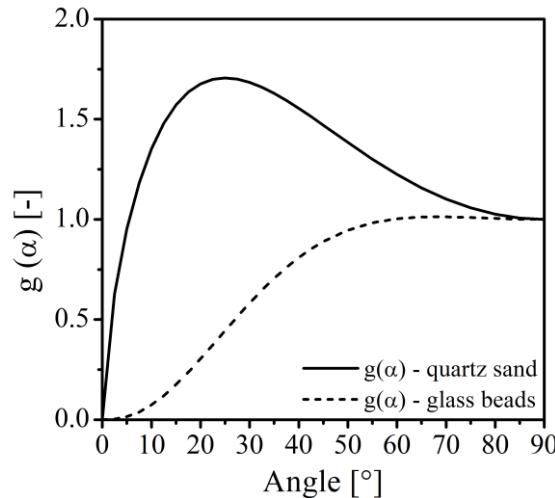
Figure VIII-4. Dependence of the function $g(\alpha)$ on the particle-wall impact angle for different particle types: quartz sand and spherical glass beads.

Spherical Glass Beads – η = 0.3

The experimental and numerical results obtained based on the methods described in Chapter IV and Chapter V are presented in the following for spherical glass beads and a particle mass loading of $\eta = 0.3$.

Influence of Phase Interaction

The influence of phase interaction on dispersed phase velocity profiles is depicted and compared to the measurements in Figure VIII-5. The z- and x-axes are the same as in Figure VIII-1. The locations z = 0 mm and z = 100 mm indicate the bottom and top wall of the horizontal pipe in Figure VIII-5 (a), respectively, whereas in Figure VIII-5 (b), z = 0 mm represents the outer wall of the vertical pipe in relation to bend 1, and z = 100 mm defines the inner wall of the same pipe regarding bend 1 (see Figure VIII-1). Unless otherwise specified,

the same considerations are valid for all images presented in this section which present experimental and numerical results concerning dispersed phase velocity profiles within the pipes.

The mean particle velocity profile obtained experimentally at the lower measurement site (see Figure VIII-5 (a)) exhibits almost symmetrical behavior, in which higher velocities are observed in the central region of the profile which decrease towards the upper and lower walls. However, the mean velocity fluctuation showed a slightly asymmetrical behavior, where higher fluctuations were measured near the pipe walls, an effect caused mainly due to the collisions between the particles and the pipe walls. The mean fluctuation values in the lower portion of the profile are slightly higher than the values in the upper portion. This suggests that the particle-wall collision frequency is higher for the lower wall of the pipe than for the upper wall due to the gravitational settling of larger particles. In addition, gravitational settling may generate regions of high local concentration near the bottom wall of the pipe and consequently, particle-particle collision frequency becomes higher yielding slightly higher fluctuations. Although the particle mass loading is relatively high in this case, small differences were observed between 1- and 2-way coupling. The values of the mean velocity were overestimated in both cases, although the behavior of the numerical profile is very similar to the experimental one. Thus, this shows a weak coupling between the fluid and dispersed phase in this region of the horizontal pipe, which also leads to only slight modifications in the velocity profile of the continuous phase. Interestingly, the effect of particle-particle interaction proved to be very significant. When colliding, particles lose part of their momentum, which produces a reduction in the average velocity profile of the particles. Very good agreement between both numerical and experimental profiles was obtained for the mean particle velocity by considering inter-particle collisions. Nevertheless, small differences are observed near the lower wall of the pipe, which may be associated with experimental errors as the rest of the data match quite well. Regarding the mean velocity fluctuation, the numerical predictions showed very similar behaviors and values for all cases, although the values are slightly higher than the experimental values in the upper portion of the profiles. Nonetheless, a reasonable agreement was obtained in the lower portion of the profiles.
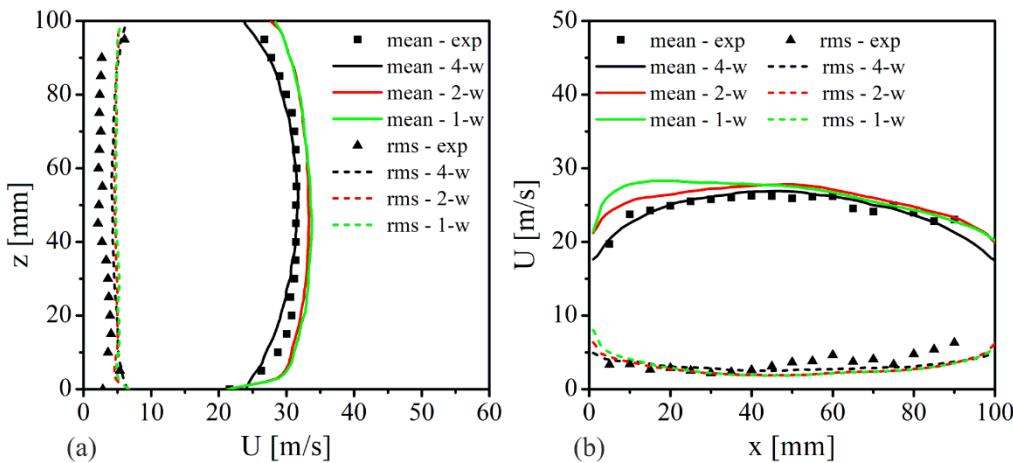
Figure VIII-5. Influence of phase interaction on the mean and fluctuating velocity components of the dispersed phase in the stream-wise direction: (a) bottom and (b) top measurement locations. Results presented for a pneumatic conveying velocity of 37.9 m/s, spherical glass beads, $\Delta\gamma = 2.5°$ and $\eta = 0.3$. Please refer to Table VIII-1 for case description: 4-w (GB1), 2-w (GB2), 1-w (GB3).

The mean velocity profile measured at the upper measurement site (Figure VIII-5 (b)) is slightly more asymmetric when compared to that obtained at the lower measurement site, yet both have similar characteristics, i.e. higher velocities are observed at the center of the profile and decrease towards the pipe walls. The small asymmetry observed is based on the fact that the vertical pipe is not long enough to allow complete dispersion of the particles within the pipe after conveying through the first bend. Similarly, the mean velocity fluctuation is higher near the pipe walls. In addition, the fluctuation is slightly higher in the region to the right of the profile, which corresponds to the inner wall of the vertical pipe with respect to bend 1. Significant changes are observed when considering the interaction between the fluid and dispersed phase. While in the right portion of the graph there is a slight increase in the mean particle velocity, in the left portion the average velocity is considerably reduced. As stated by Laín and Sommerfeld[101], dense ropes are likely to form on the outer wall of bends mainly due to inertial effects. Those dense ropes normally disintegrate along the vertical pipe whether its length is enough. Since measurements were carried out only a short distance after bend 1, the dense rope did not completely disintegrate, resulting in higher local concentration near the outer wall of the vertical pipe. The higher concentration in this region contributes to a stronger coupling with the fluid phase and hence fluid and particle velocity are reduced. The reduction in particle velocity is even greater when considering particle-particle interaction, particularly in the region where the dense rope is located, as inter-particle collision frequency

becomes higher due to the high local particle concentration. The entire particle velocity profile is reduced due to the momentum loss because of inter-particle collisions. Moreover, in the region near the inner wall of the vertical pipe, particles bouncing off the wall collide with particles near the wall such that the reduction in velocity of the particles in such region is even more pronounced. In general, a very good agreement was achieved between the measurements and calculations for the mean particle velocity at the top measurement location by considering inter-particle collisions. Small variations are found near the outer wall with respect to the mean velocity fluctuation. The fluctuations are lightly damped when considering 2- and 4-way coupling, mostly because particles become trapped within the dense rope. Apart from these slight variations, the fluctuation predictions are quite similar for 1-, 2- and 4-way couplings. Finally, the numerical results are reasonably consistent with the experimental data, especially in the region $0 < x < 50$ mm.

Figure VIII-6 presents the influence of phase interaction on erosion scar for bend 1 (a) and bend 2 (a). Please note that both scales are fixed based on the experimental data and that the gravity acts on the opposite direction of the Z-axis, which is coloured as green. The flow inlet is also distinct by colours which are related to the axes as well. Additionally, no experimental data was acquired exactly at the inlet and outlet of the bends due to the existence of the flanges (20 mm thick) and therefore, the positioning of the ultrasonic probe on the surface of the bends was not possible in those regions. Nevertheless, values equal to zero were assumed for those regions to allow the three-dimensional reconstruction of the experimental bends in the same size as of the numerical bends. These considerations are valid for all images related to erosion patterns which are presented further on in this section. The erosion maps acquired for the outer surface of bends 1 and 2 show that the erosion is close to symmetrical, and that there is a region of maximum erosion located at the centre of the surfaces. Moreover, the erosion depth decreases in all directions from the maximum for both bends. Similar behaviour has been also observed by other researchers[2], although quartz sand was used as erodent particle in their experiments. The region of maximum erosion depth for bend 1 corresponds to bend angles from about 35° to 45°, whereas the region of maximum erosion depth for bend 2 lies from circa 42.5° to 52.5°. Additionally, the maximum erosion depth measured for bend 1 is higher than that for bend 2.
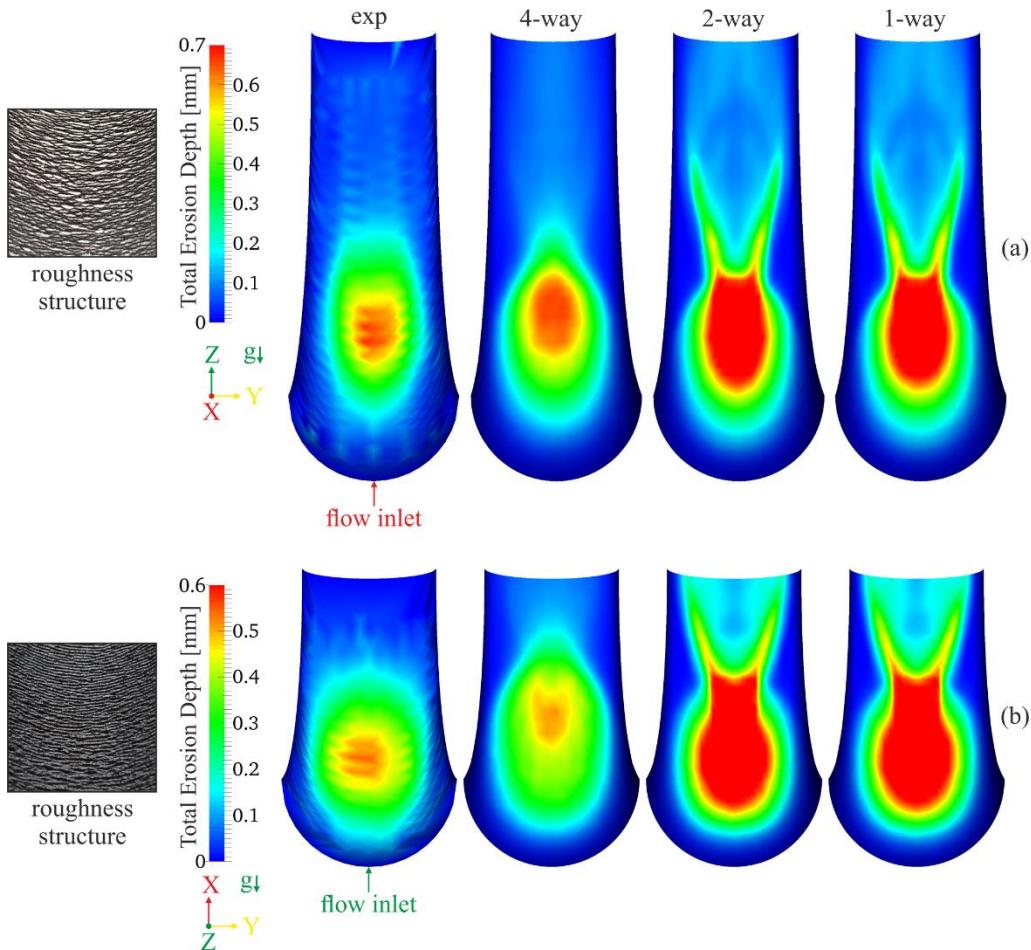
Figure VIII-6. Influence of phase interaction on erosion pattern: (a) bend 1 ($R_{bend,1} = 2.5 \cdot D$) and (b) bend 2 ($R_{bend,2} = 1.4 \cdot D$). Results presented for a pneumatic conveying velocity of 37.9 m/s, spherical glass beads, $\Delta\gamma = 2.5°$ and $\eta = 0.3$. Please refer to Table VIII-1 for case description: 4-w (GB1), 2-w (GB2), 1-w (GB3).

The erosion observed for bend 2 is lower compared to bend 1 because the particle velocity is lower when bend 2 is reached (see Figure VIII-5). Moreover, the difference in the location of the region of maximum erosion occurs mainly due to the flow characteristics, since particle distribution within the horizontal pipe is different from the vertical one, as will be highlighted further on among other particle impact parameters. For both bends analysed, no significant differences were detected between 1 and 2-way coupling calculations for the erosion maps. Erosion maps on both curves are characterized by an oval-shaped maximum erosion region, which is surrounded by an area with moderate erosion. The maximum erosion region is formed by primary particle-wall collisions at high impact velocity. Downstream from the maximum erosion region, a V-shaped erosion pattern is formed, which results mainly from

secondary particle-wall collisions[87]. Comparison shows that in this case only the 1- and 2-way couplings are not adequate to correctly represent the experimental erosion map. However, the quality of the results was improved by considering particle-particle interactions. By interacting with each other, particles have their velocities and trajectories changed. Thus, particle distribution, as well as particle impact velocity and angle, are also modified upon reaching the surface of the bends, and consequently, erosion scar may be significantly different. As can be seen from the figure, the numerical erosion scar from bend 1 when considering 4-way coupling closely resembles that observed experimentally. That is, the erosion scar is characterized by a region of high erosion depth which decreases in all directions from this region and the V-shaped structure disappears. The same behaviour is observed experimentally. However, the region of high erosion in the simulation is slightly shifted to larger bend angles compared to the experimental one. In addition, the region downstream of the region with higher erosion is narrower in the numerical calculations than that observed in the experiments. Even so, considering the complexity of the phenomena involved, it can be concluded that the applied models can reproduce the experimentally observed behaviour very well.
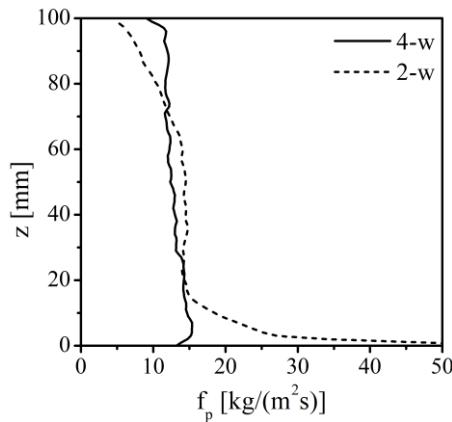
Figure VIII-7. Influence of phase interaction on mean particle mass flux at the bottom measurement location. Results presented for a pneumatic conveying velocity of 37.9 m/s, spherical glass beads, $\Delta\gamma = 2.5°$ and $\eta = 0.3$. Please refer to Table VIII-1 for case description: 4-w (GB1), 2-w (GB2).

The improvement in the numerical calculations when considering 4-way coupling, with consequent reduction of the erosion peak to values closer to the experimental ones, is mainly a result from the redispersion of particles (see Figure VIII-7, for instance) and augmentation in wall collision frequency, followed by a reduction in the impact velocity of the particles

caused by collisions. With respect to bend 2 and the consideration of 4-way coupling, the region of high erosion in the numerical calculations is considerably shifted towards higher bend angles in relation to the measurements. Nevertheless, the size of the region with higher erosion is well predicted. The reason why the erosion peak is shifted to higher bend angles is mainly related to the particle distribution within the vertical pipe.
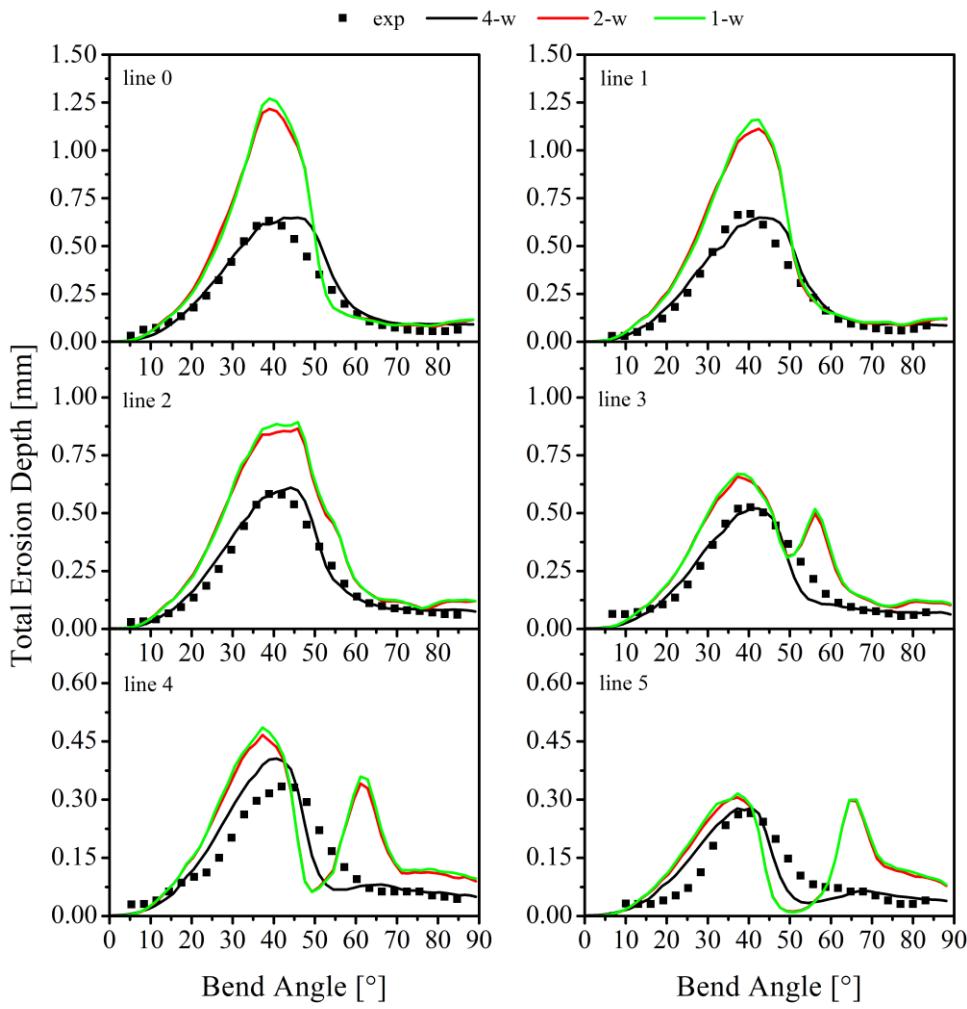
Figure VIII-8. Influence of phase interaction on total erosion depth distribution for bend 1 ($R_{bend,1} = 2.5 \cdot D$). Results presented for a pneumatic conveying velocity of 37.9 m/s, spherical glass beads, $\Delta \gamma = 2.5°$ and $\eta = 0.3$. Please refer to Table VIII-1 for case description: 4-w (GB1), 2-w (GB2), 1-w (GB3). See Figure IV-4 for line location.

The impact of phase interaction on total erosion depth distribution for bend 1 is quantitatively illustrated in Figure VIII-8. For experimental and numerical results presented in this section as a function of bend angle, as in Figure VIII-8, the bend inlet in always located at

a bend angle of 0° whilst its exit is located at a bend angle of 90°. This is valid for both bends. In the case of bend 1, in both simulations considering 1- and 2-way coupling, the erosion peak is clearly overestimated, as well as the erosion in the vicinity of the region of high erosion (lines 1 to 5). The same trend is observed for both cases, although erosion is slightly lower in some regions for the case involving 2-way coupling. These small differences is caused by small variations observed in the particle impact conditions, i.e. particle impact velocity and angle as well as wall collision frequency, although no significant differences were observed in the particle velocity profile, as presented in Figure VIII-5 (a). Additionally, from line 3 onwards, two erosion peaks are detected which are a consequence of the formation of the V-shaped structure which results from secondary particle-wall collisions, as discussed earlier and shown in Figure VIII-6. As stated above, inter-particle collisions reduce the velocity of the particles and modify their impact angle as well as influence their dispersion within the pipes. Consequently, there is a large reduction in the erosion peak such that the numerical predictions for this case represent the experimental data adequately for almost all lines analysed, although, as already mentioned, the erosion peak is slightly shifted. Still, the qualitative and quantitative behaviour of the numerical profiles in relation to the experimental ones is very good. Small discrepancies are noted for lines 4 and 5.

Figure VIII-9 shows the influence of phase interaction on erosion depth distribution for bend 2. Similar to bend 1, the erosion depth is significantly overestimated when considering only 1- and 2-way coupling, as well as two erosion peaks are identified from line 3 onwards due to the V-shaped structure formed. Only minor differences are observed when considering 2-way coupling, for the same reasons discussed for bend 1. By accounting for collisions between particles, a significant reduction in erosion depth is observed mainly due to the decrease in particle velocity and particle redistribution within the vertical pipe, coupled with changes in the particle impact angle. Even though the prediction of the site of maximum erosion is shifted relative to the experimental one, the numerical calculations are able to estimate the maximum erosion correctly, as observed in the centreline. The discrepancies associated with the prediction of erosion for bend 2 are more pronounced than for bend 1, even though the numerical predictions of the particle velocity profile are good (see Figure VIII-5 (b)). Nevertheless, the numerical results are considered as reasonable when accounting for inter-particle collisions.
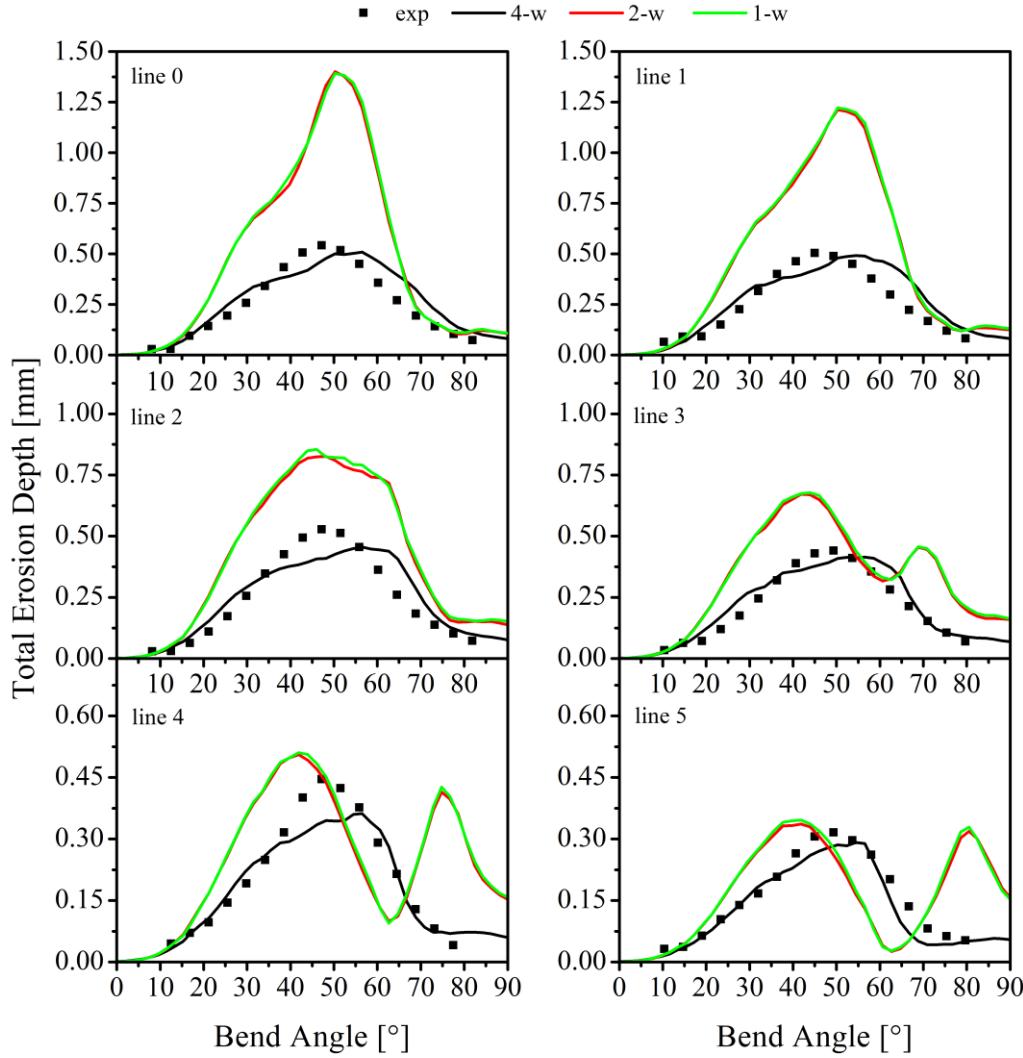
Figure VIII-9. Influence of phase interaction on total erosion depth distribution for bend 2 ($R_{bend,2} = 1.4 \cdot D$). Results presented for a pneumatic conveying velocity of 37.9 m/s, spherical glass beads, $\Delta\gamma = 2.5°$ and $\eta = 0.3$. Please refer to Table VIII-1 for case description: 4-w (GB1), 2-w (GB2), 1-w (GB3). See Figure IV-4 for line location.

The influence of phase interaction on erosion-related variables such as particle impact velocity and angle, collision frequency and impacted mass on bend 1 is presented in Figure VIII-10. Regarding 1- and 2-way couplings, there are no significant differences in the results, except for the mean particle impact velocity at bend angles greater than approximately 55°, at which a reduction is observed. It can be seen from Figure VIII-10 (c) and (d) that inter-particle collisions increase wall collision frequency and the amount of mass that reaches the surface of bend 1 for bend angles higher than about 42.5°, besides shifting the region in which most particles collide with the bend from about 37.5° to 47.5°. The increase in the wall collision

frequency occurs because the particles get trapped inside the dense rope of particles which is formed on the outer surface of the bend. For angles below 42.5 °, there is a reduction in both variables due to particle redispersion caused by particle-particle interactions, as illustrated in Figure VIII-7.
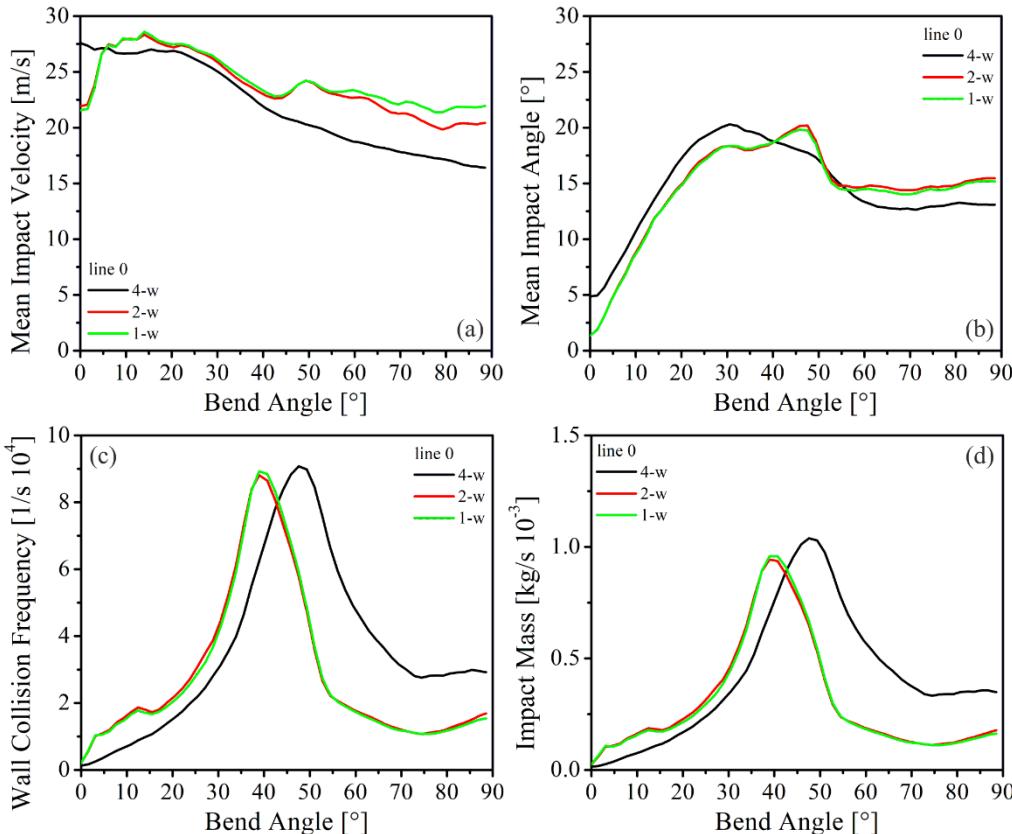
Figure VIII-10. Influence of phase interaction on erosion-related variables for bend 1 ($R_{bend,1} = 2.5 \cdot D$): (a) mean impact velocity, (b) mean impact angle, (c) wall collision frequency and (d) impacted mass. Results presented for a pneumatic conveying velocity of 37.9 m/s, spherical glass beads, $\Delta\gamma = 2.5°$ and $\eta = 0.3$. Please refer to Table VIII-1 for case description: 4-w (GB1), 2-w (GB2), 1-w (GB3). See Figure IV-4 for line location.

The mean particle impact velocity is generally reduced by considering inter-particle collisions (Figure VIII-10 (a)), in which the reduction is more pronounced at bend angles larger than circa 42.5°. Higher wall collision frequency also implies more momentum loss by the dispersed phase and therefore, lower mean impact velocity is obtained at bend angles higher than 42.5° in relation to lower angles. Due to the collisions, the mean impact angle is in turn increased up to a bend angle of about 40° relative to the 1- and 2-way cases, followed by a

decrease at larger angles. As can be seen in Figure VIII-8 with respect to the centreline and for bend angles greater than 50°, all three cases showed erosion depths not much different from each other, although significant differences were observed in the erosion-related variables. Figure VIII-4 shows lesser erosion at shallower impact angles, which connected with lower mean impact velocity, should yield lesser erosion. However, the reduction of these variables was offset by an increase in the wall collision frequency such that similar values were obtained for the erosion depth. Below this angle, the reduction in erosion depth (Figure VIII-8) is a result of the decrease in the mean particle impact velocity and wall collision frequency, although higher impact angles contribute to an increase in erosion in this case (Figure VIII-4).
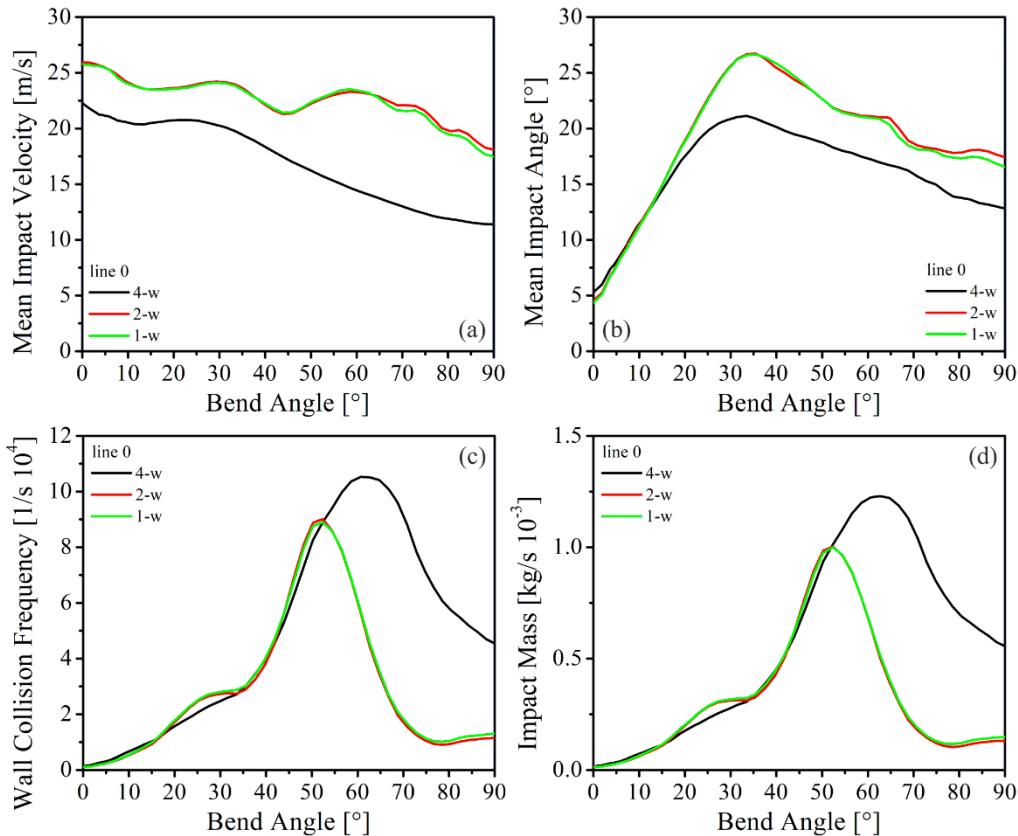
Figure VIII-11. Influence of phase interaction on erosion-related variables for bend 2 ($R_{bend,2} = 1.4 \cdot D$): (a) mean impact velocity, (b) mean impact angle, (c) wall collision frequency and (d) impacted mass. Results presented for a pneumatic conveying velocity of 37.9 m/s, spherical glass beads, $\Delta\gamma = 2.5°$ and $\eta = 0.3$. Please refer to Table VIII-1 for case description: 4-w (GB1), 2-w (GB2), 1-w (GB3). See Figure IV-4 for line location.

The dependence of erosion-related variables on phase interaction is presented in Figure VIII-11 for bend 2. Only very small differences are observed between 1- and 2-way coupling for all erosion-related variables analyzed. Due to the collisions between particles and consequently the particles trapped within the dense particle rope, there is a substantial increase in the wall collision frequency as well as the amount of mass reaching the surface of bend 2 for bend angles greater than approximately 50°, as shown in Figure VIII-11 (c) and (d). Bellow this angle only minor differences are apparent. Additionally, the site at which most particles hit the surface of the bend 2 is dislocated from about 52.5° to 62.5°. The mean impact velocity is decreased along the entire profile when 4-way coupling is considered, where the differences are more pronounced with respect to the case with only 2-way coupling at angles greater than 50°, as observed in Figure VIII-11 (a). Since the wall collision frequency in the range of 0° to 50° is basically the same for all three cases, it is suggested that the reduction observed in the mean impact velocity is only a consequence of particle-particle interactions, i.e. particles simply reach the surface of the bend with less velocity due to collisions. For bend angles above 50°, the increase in the wall collision frequency influences the mean impact velocity, decreasing it even further. The mean impact angle, which is presented in Figure VIII-11 (b), suffer no influence from inter-particle collisions up to a bend angle of 15°, yet it is meaningfully reduced at higher bend angles. Hence, the remarkable reduction in the erosion depth through inter-particle collisions results from shallower impact angles (see Figure VIII-4) as well as reduced impact velocity.

Influence of Surface Roughness

The influence of surface roughness on dispersed phase velocity profiles is presented and compared with the measurements in Figure VIII-12. It has been already been demonstrated that surface roughness affects directly particle motion within pipes and strongly modifies wall collision frequency[14,15]. Therefore, a sensitive analysis regarding the impact of surface roughness degree on particle velocity profile, erosion depth and erosion-related variables is carried out in the following. Additionally, only results accounting for inter-particle collisions are presented from now on, as it was previously demonstrated that particle-particle interactions are of great importance. As demonstrated in Figure VIII-12 (a), the mean particle velocity profiles for the cases considering an initial surface roughness of 2.5° (standard case) and the

surface roughness as a function of erosion and impact angle are very similar, where only very small differences are observed. Please note that the initial surface roughness is also set to $2.5°$ for the case where surface roughness varies with erosion and impact angle. The reason for this behavior relies on the fact that the observed erosion on the horizontal pipe is minimal and moreover, the angles at which particles collide with the walls of the horizontal pipe are generally shallow. From Figure VI-18 is clear that erosion caused by spherical glass beads at small impact angles modifies surface roughness very little in terms of $\Delta\gamma$. Thus, since the impact of erosion on surface roughness is small in this case, it is only natural that both cases have similar results. Nevertheless, particle velocity is remarkably decrease by increasing surface roughness even further, i.e. $\Delta\gamma = 10°$ and $\Delta\gamma = 20°$. Particles bounce from wall to wall more frequently as a result from higher surface roughness, i.e. wall collision frequency is greatly increased in the horizontal pipe, and accordingly, mean particle velocity is reduced due to higher momentum loss[120]. In the horizontal pipe, velocity fluctuations are somewhat similar except for those of the case with $\Delta\gamma = 20°$, in which fluctuations are higher at the core of the pipe.
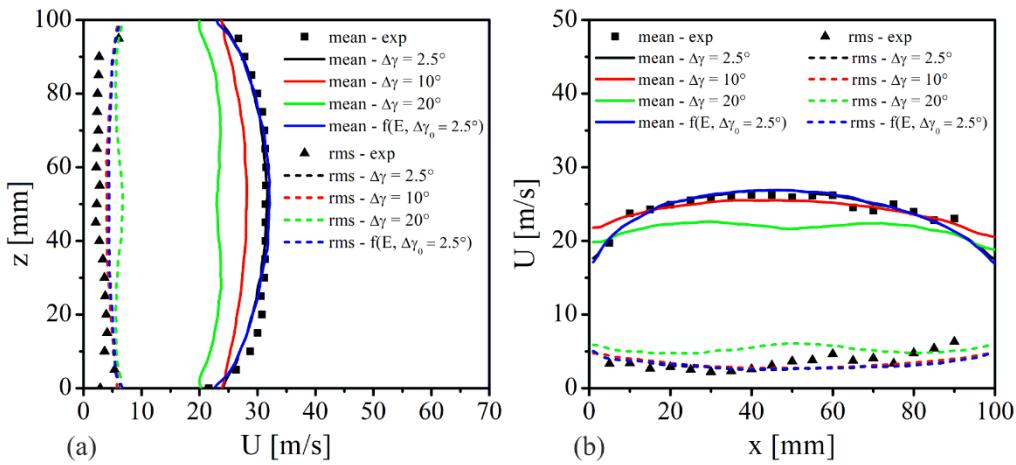
Figure VIII-12. Influence of surface roughness on the mean and fluctuating velocity components of the dispersed phase in the stream-wise direction: (a) bottom and (b) top measurement locations. Results presented for a pneumatic conveying velocity of 37.9 m/s, spherical glass beads, and $\eta = 0.3$. Please refer to Table VIII-1 for case description: $\Delta\gamma = 2.5°$ (GB1), $\Delta\gamma = 10°$ (GB4), $\Delta\gamma = 20°$ (GB5), $f(E, \Delta\gamma_0 = 2.5°)$ (GB6).

Similar trends are obtained with respect to the mean particle velocity profiles in the upper measurement location, as shown in Figure VIII-12 (b). Hence, the same observations

are applied. Even so, the magnitude of reduction observed for the vertical pipe is smaller than that for the horizontal pipe for the cases involving larger surface roughness. Since the vertical pipe is shorter in length than the horizontal pipe, the momentum loss by the particles due to collisions with the walls of the vertical pipe is lower by the time particles reach the measurement location. Also, velocity fluctuations are very similar for all cases, except for the case with $\Delta\gamma = 20°$, where higher fluctuations are identified.
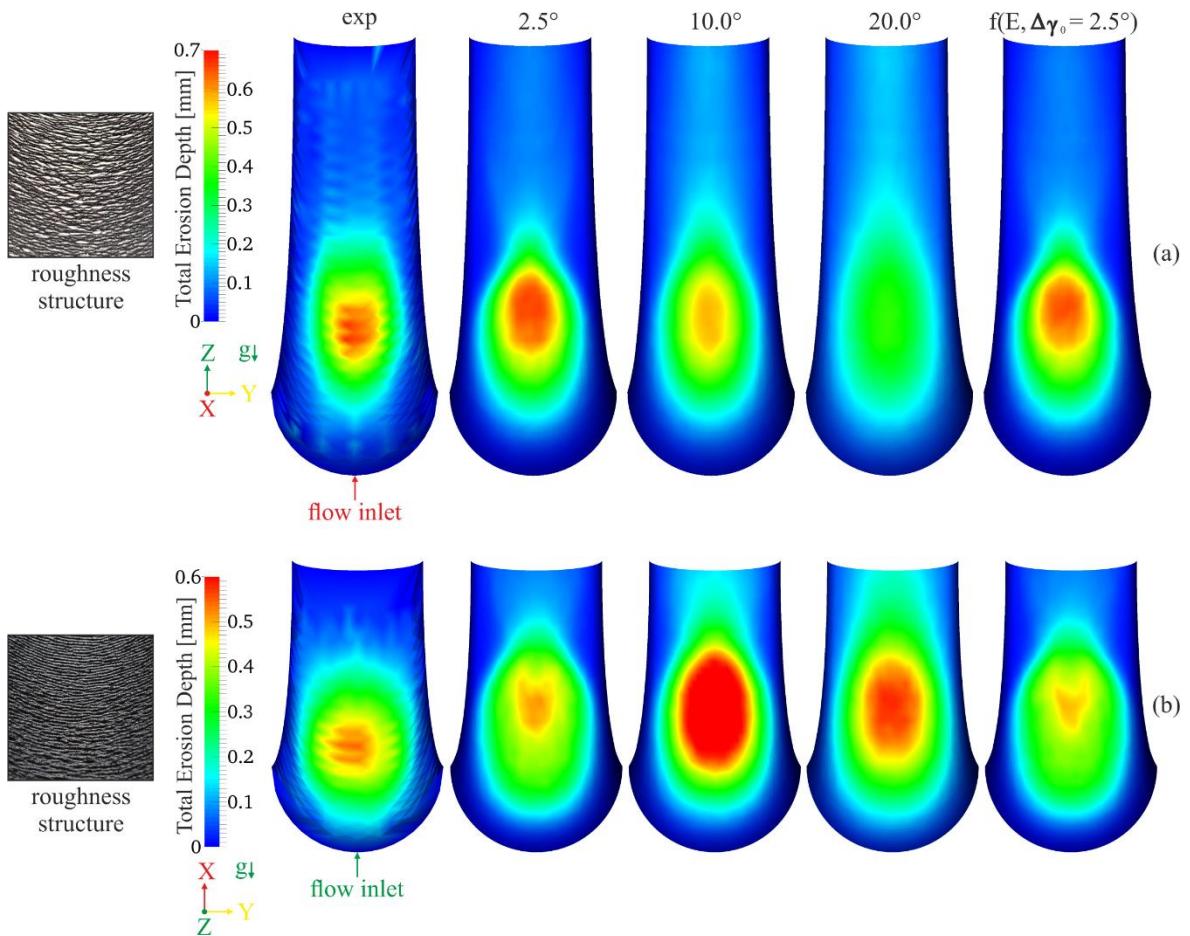
Figure VIII-13. Influence of surface roughness on erosion pattern: (a) bend 1 ($R_{bend,1} = 2.5 \cdot D$) and (b) bend 2 ($R_{bend,2} = 1.4 \cdot D$). Results presented for a pneumatic conveying velocity of 37.9 m/s, spherical glass beads, and $\eta = 0.3$. Please refer to Table VIII-1 for case description: 2.5° (GB1), 10.0° (GB4), 20.0° (GB5), f(E, $\Delta\gamma_0 = 2.5°$) (GB6).

Figure VIII-13 (a) and (b) illustrates the influence of surface roughness on erosion scar for bend 1 and 2, respectively. As can be seen in Figure VIII-13 (a), the erosion patterns from bend 1 for the cases considering rough walls with $\Delta\gamma = 2.5°$ and as a function of erosion and impact angle are quite similar. Even though changes in the surface roughness of bend 1 are

more pronounced due to higher erosion and larger impact angles as those in the horizontal pipe, for instance, they are not sufficient to cause significant changes not only in the erosion pattern of bend 1, but also in the total erosion depth (see Figure VIII-14) and in the erosion-related variables (see Figure VIII-15). By increasing the surface roughness to 10° the dispersion of the particles becomes greater as the collision frequency is reduced in the bend such that the region of maximum erosion becomes narrower relative to the other cases and the total erosion is reduced. By further increasing the surface roughness, the maximum erosion is reduced, as well as the region of maximum erosion becomes even wider. Such behaviour was also observed by Laín and Sommerfel[92], Duarte et al.[91] and Solnordal et al.[2], for example. However, this effect is more pronounced in their work, probably because each investigator used a different CFD code and moreover, the simulated systems and conditions are different. Figure VIII-13 (b) shows the results obtained for bend 2. Regarding bend 2, only small variations are detected when considering surface roughness as a function of erosion and impact angle when compared to the case with $\Delta\gamma = 2.5°$. However, these modifications are subtle and can be attributed to the small modifications observed in the mean particle impact velocity and wall collision frequency, according to Figure VIII-17 (a) and (c). Again, the progressive increase in surface roughness makes the maximum erosion region wider but contrary to expectations, a considerable increase in the total erosion depth is detected for this bend, especially for the case with $\Delta\gamma = 10°$. This unexpected behavior will be discussed later based on the erosion-related variables. Additionally, erosion depth is meaningfully augmented downstream of the region of maximum erosion for higher surface roughness.

The effect of surface roughness on total erosion depth distribution for bend 1 is quantitively expressed in Figure VIII-14. As already mentioned, the case with a variable surface roughness yields results very similar to the case with a constant value of 2.5° (standard case), and therefore, both are in good agreement with the experimental data. The results are similar as the changes in surface roughness caused by erosion are small such that there are only very small modifications in the particle impact velocity and angle, as well as in the wall collision frequency and in the amount of mass which collide with the surface of the bend, as may be confirmed in Figure VIII-15 (a), (b), (c) and (d). For the cases with $\Delta\gamma = 2.5°$ and as a function of erosion, the particle impact velocity is maximal at the bend inlet, i.e. 0°, and practically decreases until the particles exit the bend at a bend angle of 90°, where the decrease

is more accentuated from a bend angle of 30° to 90° as a result of the large increase in wall collision frequency. On the other hand, the particle impact angle continuously increases up to a bend angle of 30° mostly due to the gravitational settling, which is followed by a reduction up to a bend angle of 65°. From 65° to 90°, it remains mostly constant. The wall collision frequency as well as the impacted mass on the surface increase with bend angle up to about 47.5° and then start to decrease up to 75°, from which they remain practically constant. Therefore, the peak of erosion located at bend angles between 37.7° and 47.5° results from a combination of high wall collision frequency, moderate impact velocity and high impact angle. Erosion is greatly reduced downstream of the erosion peak due to lower impact velocity, impact angle and wall collision frequency. It can be observed from Figure VIII-14 that the maximum of total erosion depth is substantially reduced by increasing surface roughness and, additionally, that the spot of the erosion peak is slightly displaced toward lower bend angles. As particle bounce off the walls with higher angles due to surface roughness, this results in a remarkably increase in the mean particle impact angle along the bend, as shown in Figure VIII-15 (b). This effect alone should increase erosion depth in accordance with Figure VIII-4. However, the effect of increasing surface roughness on the redispersion of particles within the domain is high such that the particles reach the surface of bend 1 widely spread, which in turn yields a reduction in the wall collision frequency. In addition, the increase in surface roughness helps the particles to break free of the dense particle rope which is formed in regions near the outer wall of the bend, reducing the wall collision frequency even further. The magnitude of the wall collision frequency reduction can be clearly observed in Figure VIII-15 (c). Naturally, similar behaviour is identified for the amount of mass colliding with the outer surface of the bend, as visualized in Figure VIII-15 (d). The increase in surface roughness from 2.5° to 10° contributes to an increase in the mean particle impact velocity for bend angles greater than about 30°, where for lower bend angles, values similar to those of the case with 2.5° were obtained. The increase in particle impact velocity for a surface roughness of 10° is related to the fact that particles can escape the dense particle rope, which reduces the particle concentration near the bend walls and, consequently, reduces wall collision frequency, allowing the particles to collide with the bend at higher velocities. The same trend is observed for a surface roughness of 20°. Nevertheless, for the latter, there is a reduction in the particle impact velocity for bend angles below 45° with respect to the case with surface roughness of 10°. The reason for that is probably due to the great reduction observed in particle velocity

profile as presented earlier in Figure VIII-12 (a), as a consequence the particles reach the bend at lower velocities. Therefore, despite the particles colliding with the surface at higher impact velocity and angle, the erosion peak is reduced due to the remarkable reduction in the wall collision frequency. Also, at higher bend angles, erosion is increased as particle impact velocity and angle become higher with increasing surface roughness, though wall collision frequency is relatively decreased. Besides particle impact velocity, similar tendencies with increasing surface roughness were also observed by Laín and Sommfeld[92] and Duarte et al.[91].
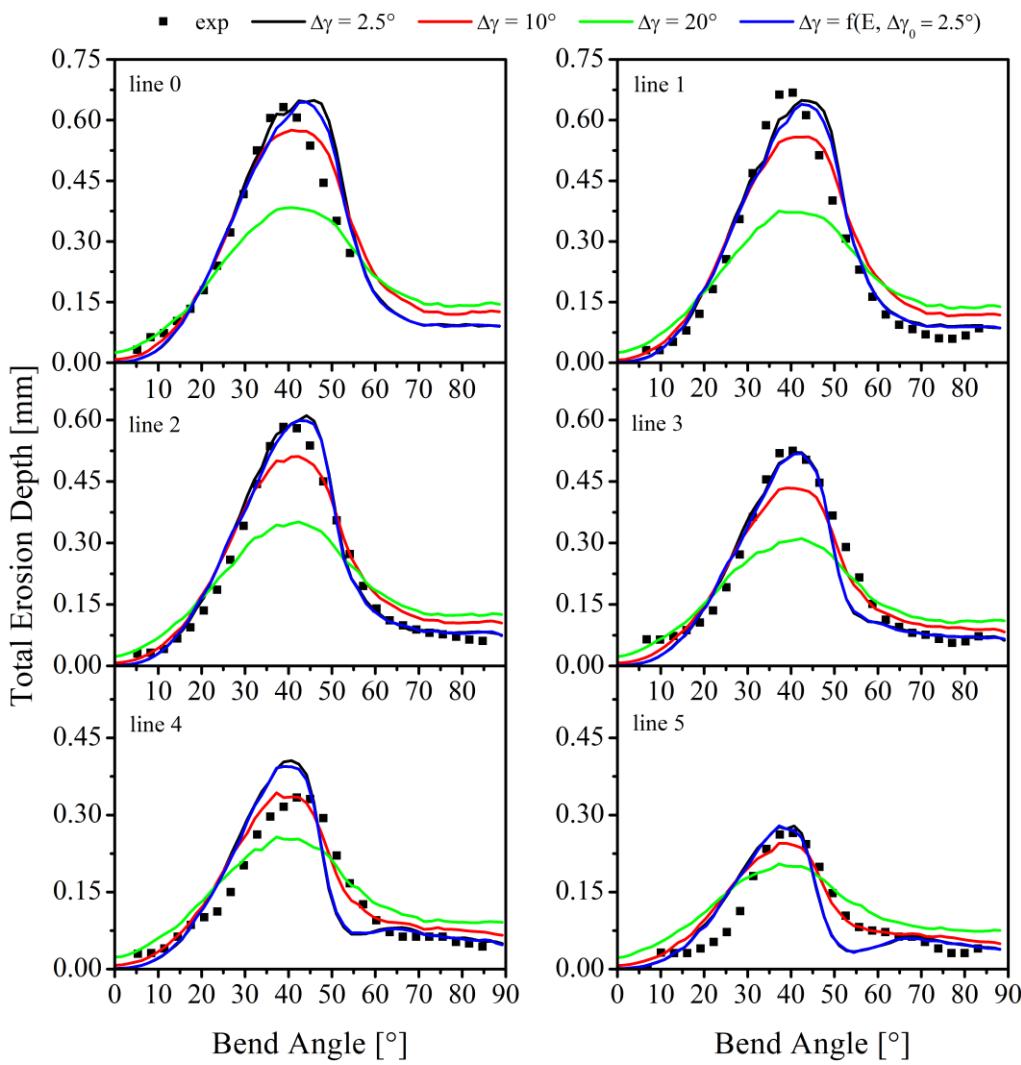
Figure VIII-14. Influence of surface roughness on total erosion depth distribution for bend 1 ($R_{bend,1} = 2.5 \cdot D$). Results presented for a pneumatic conveying velocity of 37.9 m/s, spherical glass beads, and $\eta = 0.3$. Please refer to Table VIII-1 for case description: $\Delta\gamma = 2.5°$ (GB1), $\Delta\gamma = 10°$ (GB4), $\Delta\gamma = 20°$ (GB5), $\Delta\gamma = f(E, \Delta\gamma_0 = 2.5°)$ (GB6). See Figure IV-4 for line location.
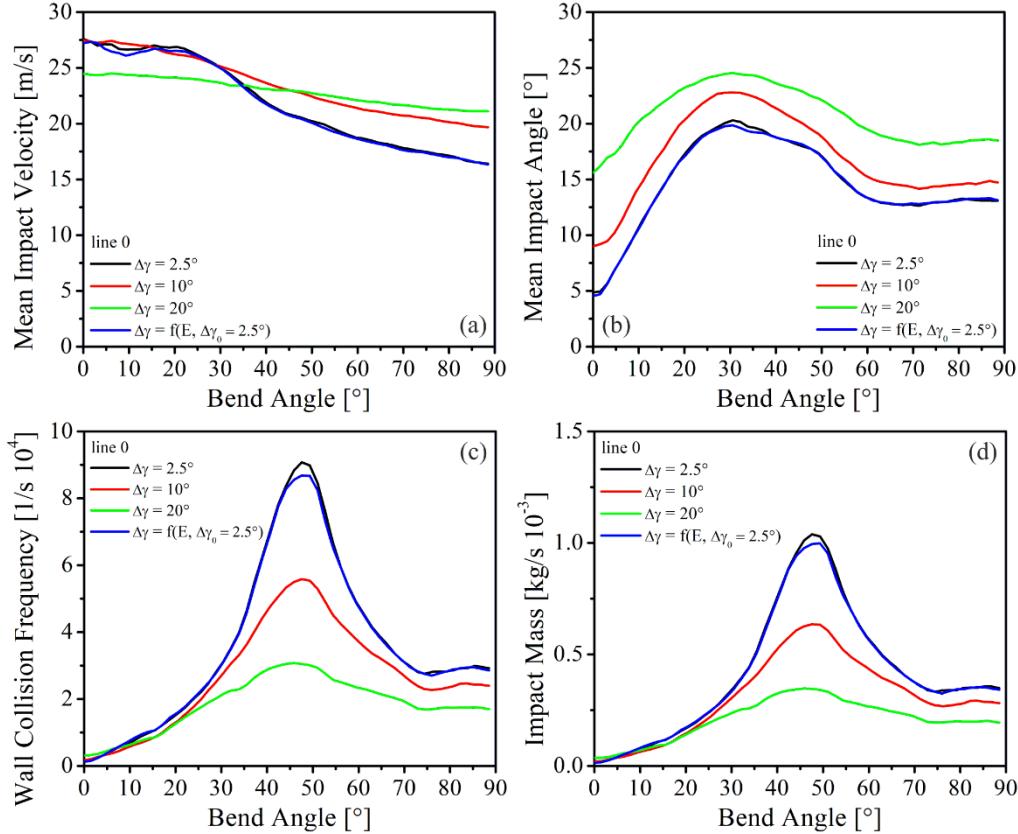
Figure VIII-15. Influence of surface roughness on erosion-related variables for bend 1 ($R_{bend,1} = 2.5 \cdot D$): (a) mean impact velocity, (b) mean impact angle, (c) wall collision frequency and (d) impacted mass. Results presented for a pneumatic conveying velocity of 37.9 m/s, spherical glass beads, and $\eta = 0.3$. Please refer to Table VIII-1 for case description: $\Delta\gamma = 2.5°$ (GB1), $\Delta\gamma = 10°$ (GB4), $\Delta\gamma = 20°$ (GB5), $\Delta\gamma = f(E, \Delta\gamma_0 = 2.5°)$ (GB6). See Figure IV-4 for line location.

Distinct trends are identified for the erosion depth profiles with increasing surface roughness regarding bend 2 as illustrated in Figure VIII-16. As can be seen from the figure, all erosion depth profiles presented for the cases with a constant surface roughness of 2.5 ° and variable are similar both in behaviour and magnitude. However, a small reduction is observed in the maximum erosion region as a consequence of slight variations present in the erosion-related variables, as shown in Figure VIII-17. The slight variations are due to minor disturbances which occur in the particle distribution within the pipes, which in turn are caused by small changes in surface roughness due to erosion, especially regarding bend 1. The magnitude of the erosion peak for these two cases is very close to that measured experimentally, yet the erosion peak in the numerical calculations is shifted to a bend angle of

approximately 55 °, whilst the experimental peak is located at a bend angle of around 47°. Nonetheless, in the region comprehended between bend angles of 35° to 50° the predicted values are mostly underestimated and for higher bend angles, erosion depth is slightly overestimated.
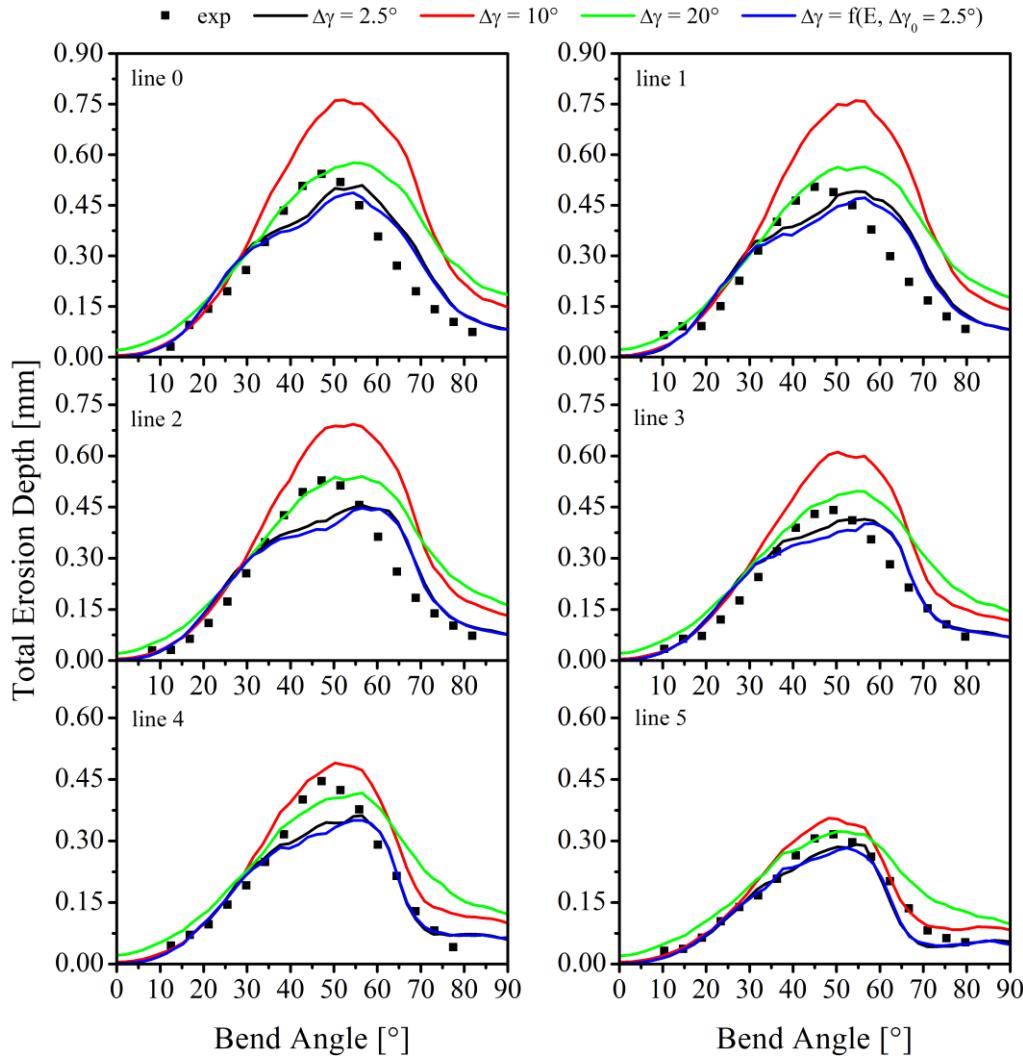
Figure VIII-16. Influence of surface roughness on total erosion depth distribution for bend 2 ($R_{bend,2} = 1.4 \cdot D$). Results presented for a pneumatic conveying velocity of 37.9 m/s, spherical glass beads, and $\eta = 0.3$. Please refer to Table VIII-1 for case description: $\Delta\gamma = 2.5°$ (GB1), $\Delta\gamma = 10°$ (GB4), $\Delta\gamma = 20°$ (GB5), $\Delta\gamma = f(E, \Delta\gamma_0 = 2.5°)$ (GB6). See Figure IV-4 for line location.

Similar trends are obtained for bend 2 when compared to bend 1 with respect to the mean particle impact velocity and angle, i.e. the impact velocity is maximal at the inlet of the bend and minimum at its exit, while the impact angle continuously grows to a bend angle of

about 30° and then subtly decreases at higher bend angles. These tendencies can be observed in Figure VIII-17 (a) and (b). By comparing bend 1 and 2 regarding $\Delta\gamma = 2.5°$ and $\Delta\gamma = f(E)$ the mean particle impact velocity is reduced from about 27.5 m/s to 22.5 m/s at the bend inlet and from 16 m/s to 11 m/s at its exit, while the mean particle impact angle is similar. However, due to the small radius of bend 2, the maximum wall collision frequency as well as the amount of mass reaching the surface is shifted from a bend angle of about 47.5° to 65°. This justifies the erosion peak in the simulations being located at the region around a bend angle of 55°. Increasing surface roughness from 2.5° to 10° increases the maximum erosion as well as the erosion located in the region downstream of the erosion peak. By further increasing the surface roughness to 20°, the maximum erosion decreases with respect to the 10° case but is still higher than in the 2.5° case. This behaviour is contradictory to the behaviour that is generally observed. The trends observed in relation to the mean particle impact angle, wall collision frequency, and the amount of mass which collides with the surface, are the same as those observed for bend 1 and are in good agreement with the observations of other researchers[91,92]. Therefore, the main reason for such behaviour lies in the mean particle impact velocity. It can be seen from Figure VIII-17 (a) that the mean particle impact velocity increases considerably for greater surface roughness. Also, the impact velocity for the case with surface roughness of 20° is lower compared to the case with 10° for bend angles less than 45° and higher for bend angles greater than 45°. The concentration of the particle rope is considerably reduced with increasing surface roughness, as observed in Figure VIII-18, where the particle concentration in the mid-plane of bend 2 is illustrated in logarithmic scale. As can be seen, there is a large increase in particle dispersion such that virtually the entire section of bend 2 is filled with particles. As a result of the reduction in the particle concentration near the bend walls, inter-particle collision frequency is reduced as well as the coupling between phases becomes weaker. Due to the weak coupling between the phases, the air velocity, especially near the outer wall of the bend, is higher, which results in an increase in the mean particle impact velocity. Additionally, the disintegration of the particle rope due to higher surface roughness contributes to a reduction in the number of inter-particle collisions within the rope, which, consequently, decreases wall collision frequency yielding higher particle impact velocity. However, the reduction in the wall collision frequency for the case with surface roughness of 10° is not sufficient to compensate the increase in particle impact velocity and angle and therefore, the predicted erosion is higher. Even though minor changes are observed in the mean

particle impact velocity and the increase in the mean particle impact angle is considerable, the reduction observed in the wall collision frequency for the case with a surface roughness of 20° is even higher so that the predicted erosion is reduced regarding the case with 10°, but still higher than in the other cases described in this analysis. The results also show that the variation of surface roughness as a function of erosion and impact angle has little impact on the presented results. This behaviour is obtained because significant variations on surface roughness occur only on the outer surface of the bends and not in the entire system. However, by increasing the surface roughness for the entire system, as in the cases with surface roughness of 10° and 20°, the influence of this parameter on the results is quite significant, as presented.
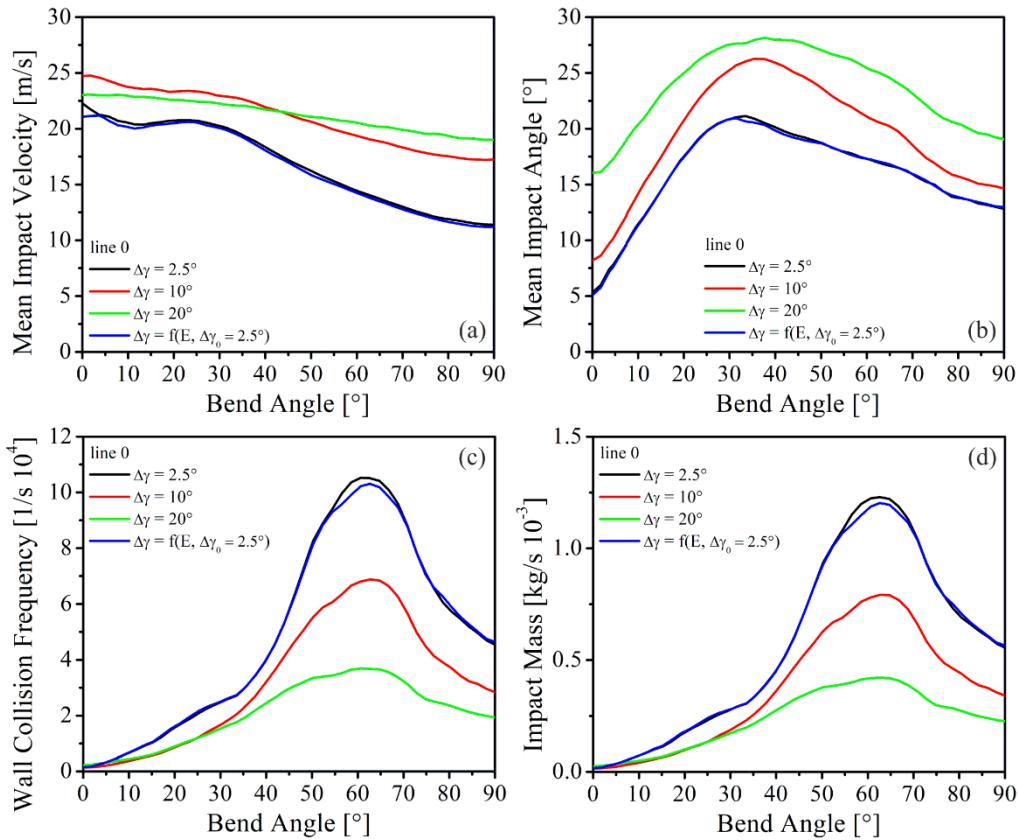

Figure VIII-17. Influence of surface roughness on erosion-related variables for bend 2 ($R_{bend,2} = 1.4 \cdot D$): (a) mean impact velocity, (b) mean impact angle, (c) wall collision frequency and (d) impacted mass. Results presented for a pneumatic conveying velocity of 37.9 m/s, spherical glass beads, and $\eta = 0.3$. Please refer to Table VIII-1 for case description: $\Delta\gamma = 2.5°$ (GB1), $\Delta\gamma = 10°$ (GB4), $\Delta\gamma = 20°$ (GB5), $\Delta\gamma = f(E, \Delta\gamma_0 = 2.5°)$ (GB6). See Figure IV-4 for line location.
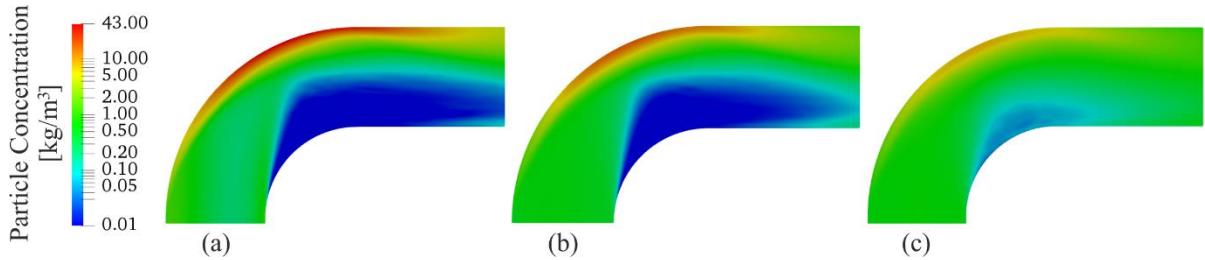
Figure VIII-18. Particle concentration in the bend 2 mid-plane ($R_{bend,2} = 1.4 \cdot D$): (a) $\Delta\gamma = 2.5°$ (GB1), (b) $\Delta\gamma = 10°$ (GB4), and (c) $\Delta\gamma = 20°$ (GB5). Results presented for a pneumatic conveying velocity of 37.9 m/s, spherical glass beads, and $\eta = 0.3$.

Spherical Glass Beads – η = 1.0

The experimental and numerical results obtained based on the methods described in Chapter IV and Chapter V are presented in the following for spherical glass beads and a particle mass loading of $\eta = 1.0$. In addition to the numerical and experimental comparison for the case with $\eta = 1.0$, a comparison between particle mass loadings of $\eta = 0.3$ and $\eta = 1.0$ is also provided. Please note that the comparison is based on the standard numerical setup.

Figure VIII-19 compares the measured and calculated mean and fluctuating velocity components of the particles in the stream-wise direction for different particle mass loadings, i.e. $\eta = 0.3$ and $\eta = 1.0$. As observed in Figure VIII-19 (a), the mean velocity profile of the particles obtained experimentally with a mass loading of $\eta = 1.0$ shows very similar behavior to the case with a mass loading of $\eta = 0.3$, in which a slight reduction is identified in the central and lower portion of the profile. The reduction is a result of the increased local particle concentration which leads to an increased inter-particle collision frequency and a stronger coupling between the fluid and dispersed phases. The fluctuating velocity component, in addition, is reasonably reduced by increasing particle mass loading to 1.0, especially in the lower region of the profile located between 0 < z <50 mm. The increase in the inter-particle collision frequency for higher particle mass loading causes the mean velocity fluctuation to be reduced due to isotropisation of the fluctuating behavior of the particles and the associated energy dissipation[120,121]. The numerical predictions of mean particle velocity for a particle mass loading of 1.0 are underestimated relative to measurements while the mean particle

velocity fluctuation is overestimated, although the experimental and numerical behavior are very similar. This slightly difference is most probably originating from wrongly predictions of particle dispersion within the pipes, which may be producing, in this case, somewhat higher inter-particle collision frequency and hence, reduced particle velocity. Moreover, the increase in particle mass loading contributes to the increase in the wall collision frequency which in turn may contribute to the reduction in particle velocity. As demonstrated in Figure VIII-19 (b), similar experimental behavior is obtained for the mean and fluctuating particle velocity components at the upper measurement location with respect to the lower region. Thus, a slight reduction in mean velocity is observed in the central region of the profile which tends to fade toward the pipe walls, whilst the rms values reasonably decrease throughout the profile. However, the reduction in the mean velocity is slightly higher in the vertical pipe, as the particles are not completely dispersed due to the reduced length of the vertical pipe and consequently, regions with locally higher concentration may appear contributing to higher inter-particle collision frequency and stronger coupling between phases. Numerically speaking, significant discrepancies are obtained with respect to measurements. For $x < 40$ mm, the mean particle velocity is distinctly underestimated, while for $x > 40$ mm it is overestimated. When transported through bend 1 and due to the formation of a dense particle rope arising from inertial effects, particles get trapped within that rope due to the high inter-particle collision frequency which increases with particle mass loading (see Figure VIII-22 (a)). The increase in the number of collisions contributes to a greater loss of kinetic energy by the particles which consequently reduces their velocities. In addition, as particles become trapped within the rope, they collide more often with the outer wall of the vertical pipe, further reducing their velocities. However, particle concentration in the region toward the inner wall of the vertical pipe is smaller than in the outer wall, as particles trapped in the rope are hardly transported to this region. Thus, the velocity of the particles is higher in this region due to the reduction in the inter-particle collision rate and the weak coupling between the phases. Thus, it seems that in the numerical simulation performed for $\eta = 1.0$ the dense rope of particles is not disintegrated as rapidly as in the experiments. Regarding the velocity fluctuation, numerical calculations with $\eta = 1.0$ overestimate the experimental values and are similar to the case with $\eta = 0.3$, with small exceptions near the outer wall of the pipe, where a slight reduction is observed.
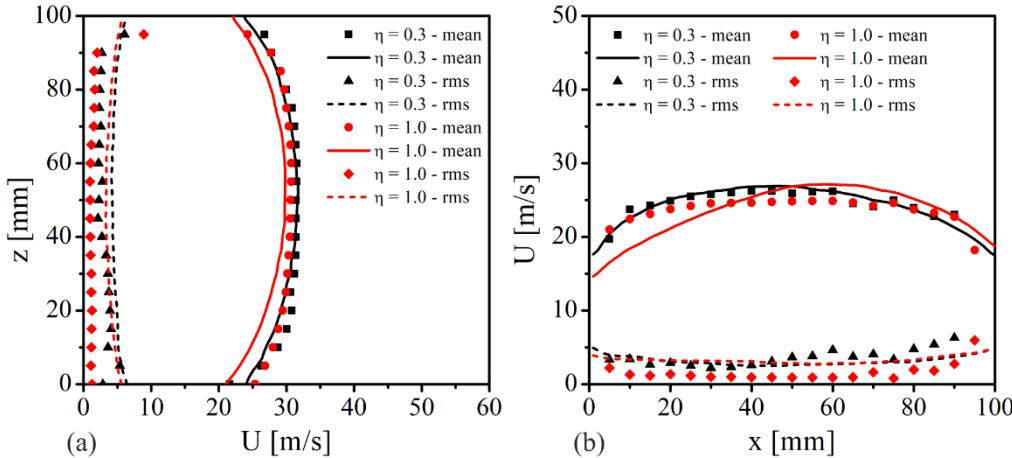
Figure VIII-19. Comparison of measured and calculated mean and fluctuating velocity components of the dispersed phase in the stream-wise direction for $\eta = 0.3$ and $\eta = 1.0$: (a) bottom and (b) top measurement locations. Results presented for a pneumatic conveying velocity of 37.9 m/s, spherical glass beads and $\Delta\gamma = 2.5°$. Symbols: measurements. Solid lines: numerical predictions. Please refer to Table VIII-1 for case description: $\eta = 0.3$ (GB1), $\eta = 1.0$ (GB7).

A comparison between experimental and calculated erosion patterns for a particle mass loading of $\eta = 0.3$ and $\eta = 1.0$ is illustrated in Figure VIII-20 (a) and (b), respectively. The erosion maps obtained for both bends considering $\eta = 1.0$ also showed behaviour close to symmetrical. The experimental erosion patterns of bend 1 differ not only in magnitude but also in their shape when increasing particle mass loading. The observed region of maximum erosion is wider for higher particle mass loading, as well as the region with moderate erosion. The lower portion of the region of maximum erosion is characterized by an oval shape while the upper portion slightly resembles a V-shaped structure. It can also be observed that by increasing particle mass loading the region of maximum erosion is shifted to lower bend angles because the gravitational settling is more effective. Although not apparent due to scale fixation relative to experimental data, the numerical erosion map is reasonably similar to the experimental one. Nevertheless, the absolute values for the total erosion depth are underestimated. Furthermore, the V-shaped structure is also present in the numerical calculations and is more pronounced. Contrary to what is generally observed experimentally, the region of maximum erosion for bend 2 has a V-shaped structure. The reason for this behaviour lies probably in the geometric characteristics of the system under analysis. As already mentioned, the vertical pipe is short to allow complete particle dispersion such that unusual behaviours may be obtained for bend 2, which may be unique to this system. However,

the simulations also predicted a V-shaped structure, which is, however, longer downstream of the bend. Moreover, in the numerical calculations the maximum erosion does not occur along the centre line in this case, as commonly observed. Again, this behaviour results from a set of factors that are probably related to the geometrical characteristics of the system.
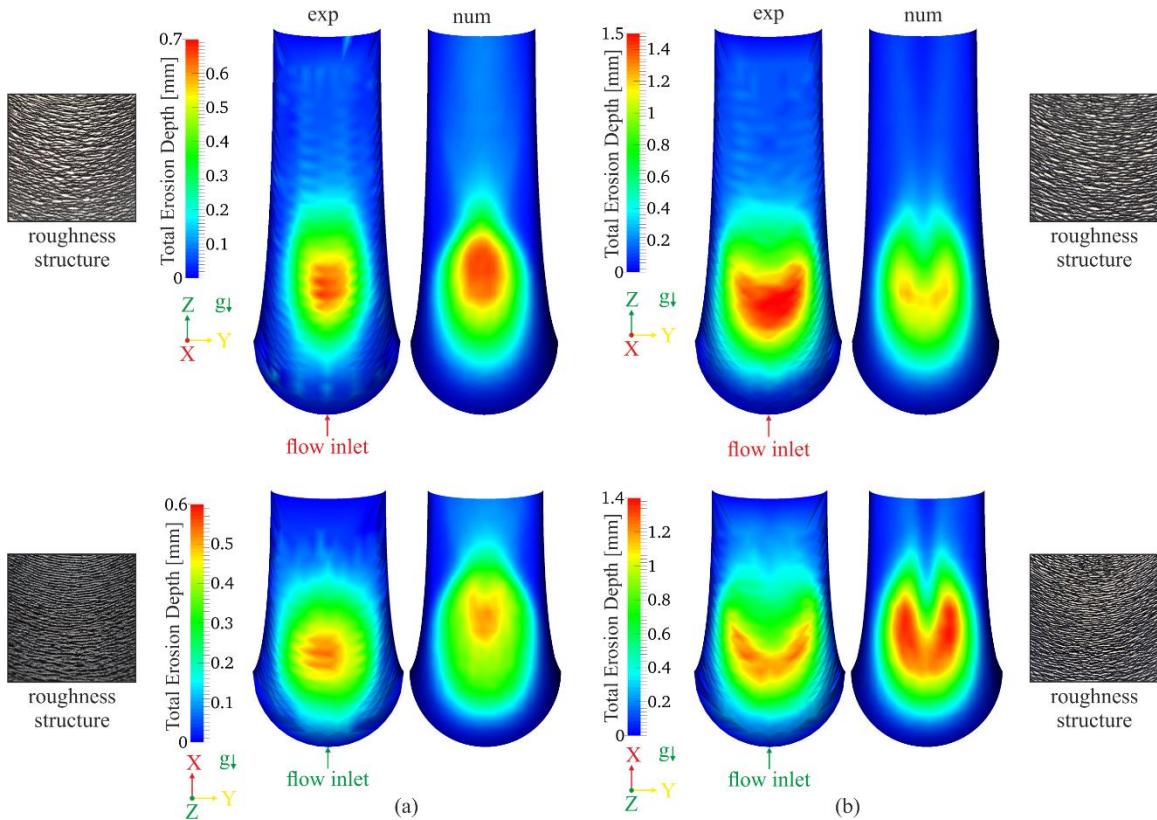
Figure VIII-20. Comparison of measured and calculated erosion patterns: (a) η=0.3 and (b) η=1.0. Results presented for a pneumatic conveying velocity of 37.9 m/s, spherical glass beads and Δγ=2.5°. Please refer to Table VIII 1 for case description: η=0.3 (GB1), η=1.0 (GB7).

The measured and calculated erosion distribution profiles are demonstrated in Figure VIII-21 for bend 1 comparing both particle mass loadings considered in the experiments. Please note that the results are presented in terms erosion ratio in this case, i.e. µm per kilogram of particle mass injected (µm/kg). An increase in erosion ratio could be expected due to the higher particle number density at higher particle mass loading, however, by comparing the experimental profiles represented by lines 0 to 3, a reduction in the erosion ratio is observed when increasing particle mass loading, a phenomenon which is referred to as shielding effect[51]. This means that for high mass loading, particle traveling into the bend will mostly collide with

particles which are trapped within the dense rope and not with the bend outer wall. This phenomenon acts as shield against incoming particles and hence, it protects the surface from further erosion. The observed decrease becomes relevant from a bend angle greater than approximately 30°, which continues to 90°. Nonetheless, at higher bend angles the decrease is more subtle. In contrast, an increase in the erosion ratio is observed for profiles 4 and 5, which are farther from the central region of the bend than the other profiles (see Figure IV-4). This suggests that the local concentration in regions far from the central portion of the bend outer wall is not high enough for the shielding effect to be effective, at least for this case. The main reason for this reduction in erosion ratio may be explained based on the formation of the dense particle rope moving along the outer wall of the bend. At first, particles trapped within the rope cause an increase in wall collision frequency and thereby particle impact velocity is considerably reduced due to momentum loss during collisions. In addition, the formation of a dense particle rope at higher particle mass loadings contributes to a stronger coupling between phases reducing the velocity of the fluid phase in the regions near the outer wall of the bend, which leads, consequently, to a reduction in the particle velocity which are moving in these regions[92]. The increase in the wall collision frequency as well as the decrease in the mean particle impact velocity are shown in Figure VIII-22 (a) and (c) for line 0, which are found to occur along the entire profile, i.e. from 0° to 90°. Also, it is obvious that the increase in wall collision frequency results in an augmentation in the impacted mass on the bend surface, as shown in Figure VIII-22 (d). As pointed out by Laín and Sommerfeld[15], at higher particle mass loading a stronger gravitational settling is observed in the horizontal pipe whereby just after entering the bend a concentrated and laterally wide rope develops which is compressed through inter-particle collisions. As a result, the mean particle impact angle is also reduced from bend angles higher than 25°, as according to Figure VIII-22 (b). Therefore, the resulting reduction in erosion ratio with increasing particle mass loading is observed due to the damping of the particle motion within the rope due to inter-particle collisions[92]. It should be noted that similar erosion ratio was obtained experimentally for both particle mass loadings up to a bend angle of 30°, which suggests that in the experiments, both mean particle impact velocity and angle are somewhat similar, although calculations show here different trends, i.e. lower erosion ratio up to a bend angle of 30° in case of a particle mass loading of 1.0, which is caused especially by the reduction in the mean particle impact velocity observed in the simulations (see Figure VIII-22 (a)).
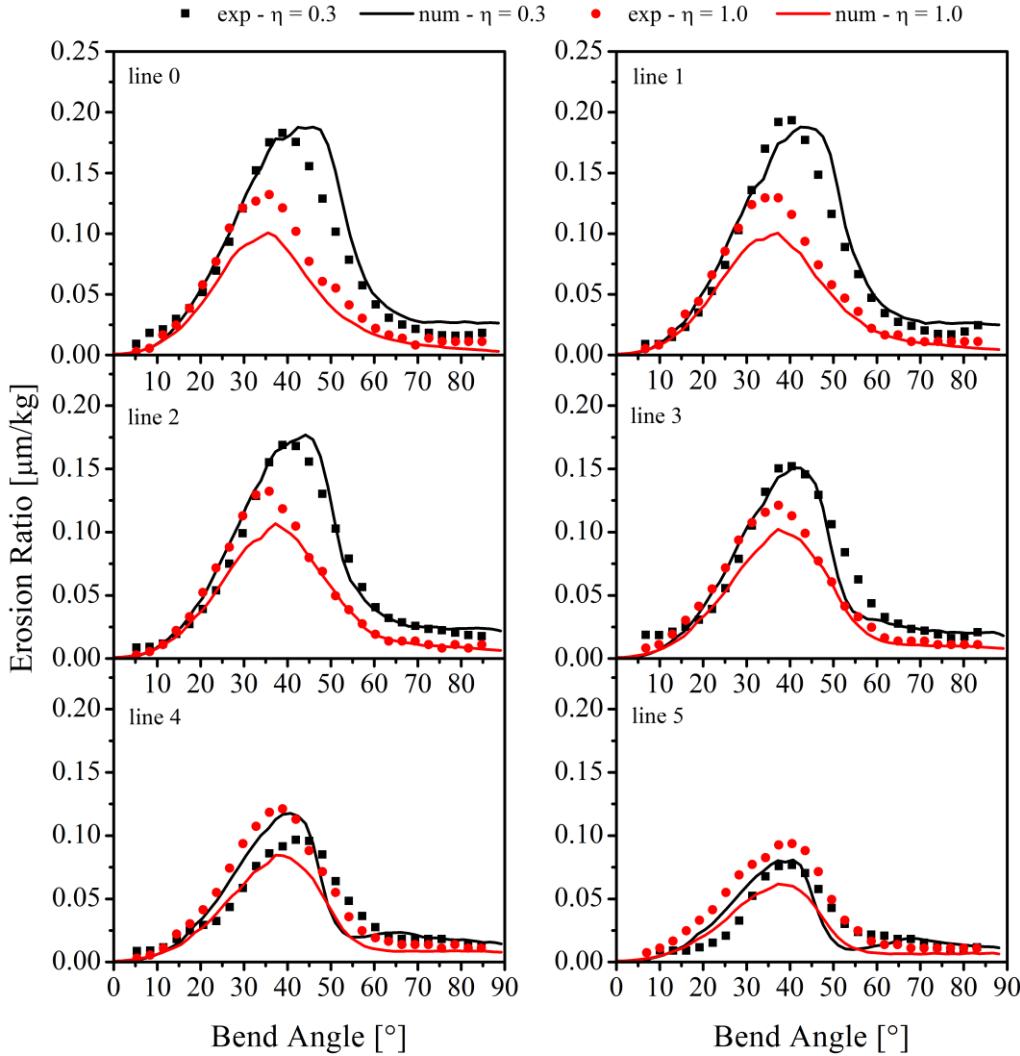
Figure VIII-21. Comparison of measured and calculated erosion ratio distribution for bend 1 ($R_{bend,1} = 2.5 \cdot D$) and for $\eta = 0.3$ and $\eta = 1.0$. Results presented for a pneumatic conveying velocity of 37.9 m/s, spherical glass beads and $\Delta\gamma = 2.5°$. Please refer to Table VIII-1 for case description: $\eta = 0.3$ (GB1), $\eta = 1.0$ (GB7). See Figure IV-4 for line location.

Due to the shielding effect, a reduction of about 27.8% is detected in the erosion peak for bend 1 when increasing particle mass loading from 0.3 to 1.0. Nevertheless, the numerical predictions for this case unfortunately underestimate the values measured experimentally for the region of maximum erosion, as a likely consequence of the mean particle velocity profile itself being slightly underestimated, as shown earlier in Figure VIII-19 (a). Even so, the qualitative behaviour of the predicted erosion ratio profiles for bend 1 is reasonably good, and

in addition to that, the Euler-Lagrange approach, in connection with the consideration of inter-particle collisions, is able to capture the shielding effect observed experimentally.

Finally, it is emphasised that although erosion ratio, which is expressed herein in terms of µm/kg, decreases with augmenting particle mass loading, this does not necessarily imply lower total erosion (e.g., µm) or erosion rate (e.g., µm/hr). For instance, by multiplying the erosion ratio (µm/kg) by the particle mass flow (kg/s), one obtains an erosion rate expressed in terms of µm/s which becomes higher with increasing particle mass loading, i.e. erosion velocity is larger at higher particle mass loadings.
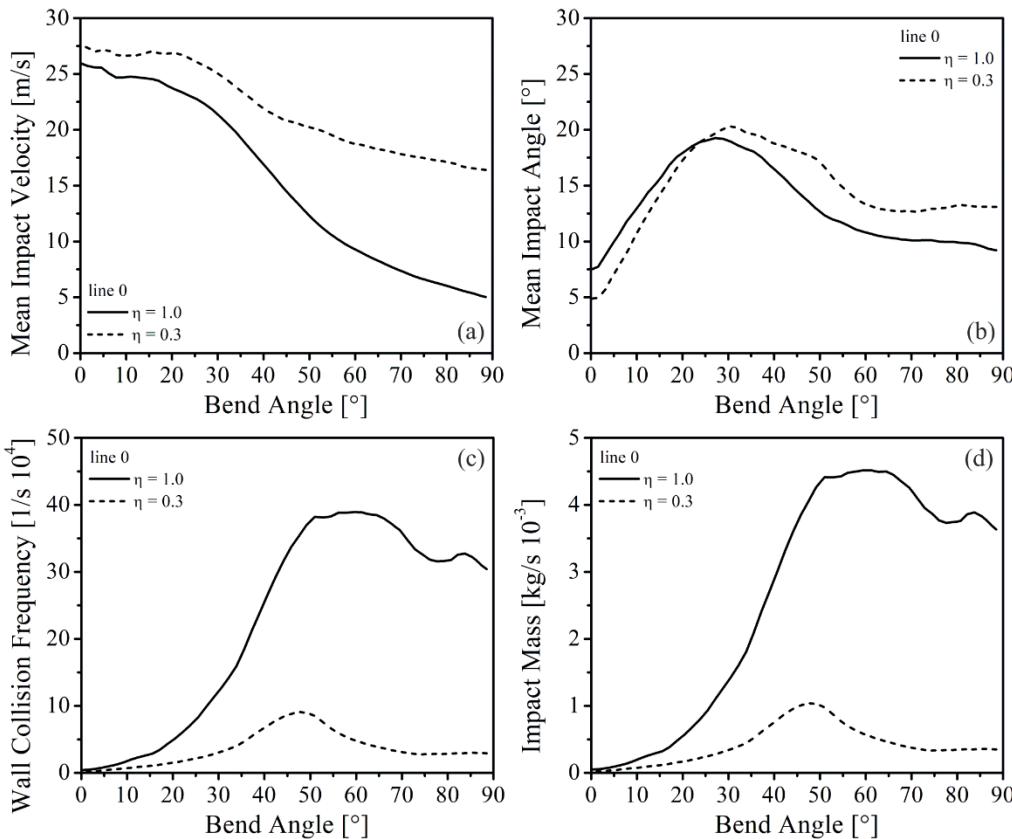
Figure VIII-22. Comparison of predicted erosion-related variables for bend 1 ($R_{bend,1} = 2.5 \cdot D$) considering $\eta = 0.3$ and $\eta = 1.0$: (a) mean impact velocity, (b) mean impact angle, (c) wall collision frequency and (d) impacted mass. Results presented for a pneumatic conveying velocity of 37.9 m/s, spherical glass beads and $\Delta\gamma = 2.5°$. Please refer to Table VIII-1 for case description: $\eta = 0.3$ (GB1), $\eta = 1.0$ (GB7). See Figure IV-4 for line location.
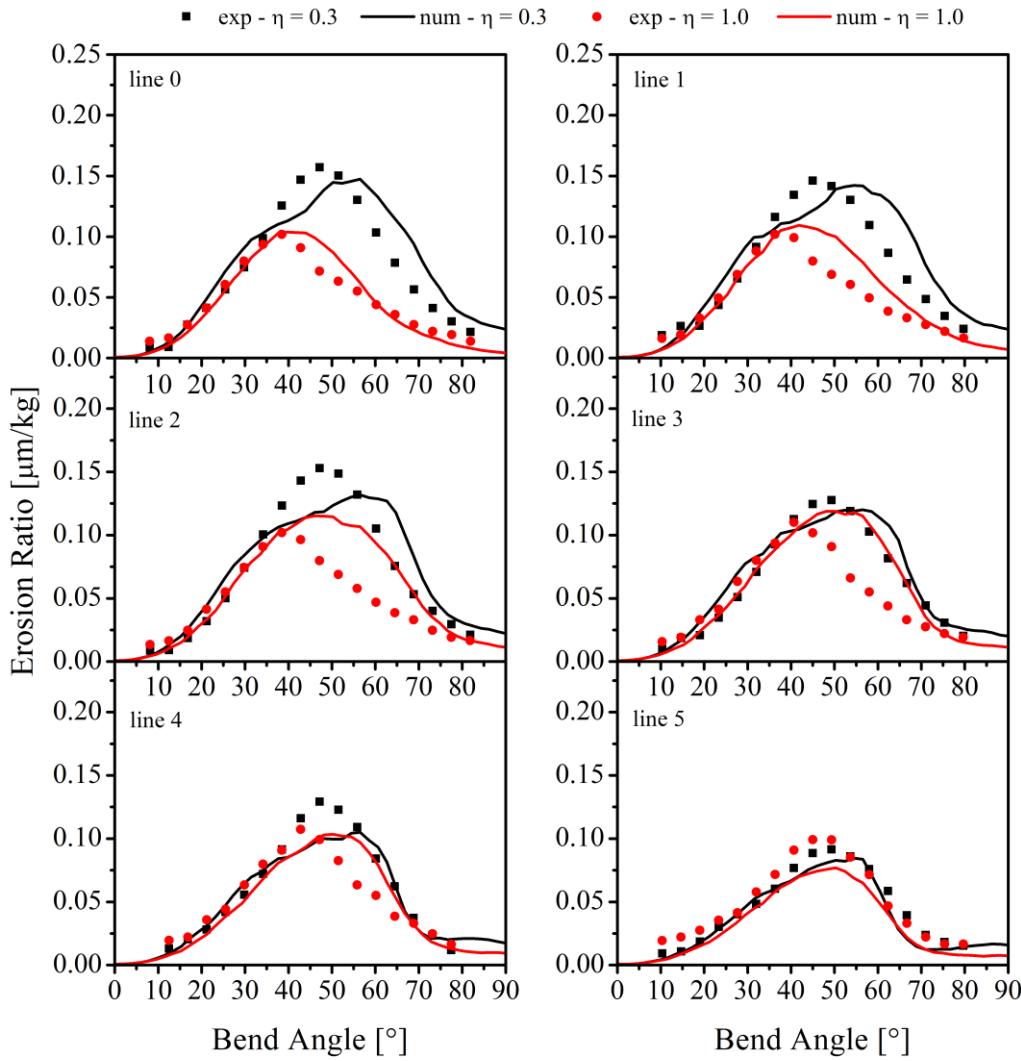
Figure VIII-23. Comparison of measured and calculated erosion ratio distribution for bend 2 ($R_{bend,2} = 1.4 \cdot D$) and for $\eta = 0.3$ and $\eta = 1.0$. Results presented for a pneumatic conveying velocity of 37.9 m/s and spherical glass beads. Results presented for a pneumatic conveying velocity of 37.9 m/s, spherical glass beads and $\Delta\gamma = 2.5°$. Please refer to Table VIII-1 for case description: $\eta = 0.3$ (GB1), $\eta = 1.0$ (GB7). See Figure IV-4 for line location.

Figure VIII-23 compares the measured and calculated erosion ratio (µm/kg) distribution profiles for bend 2 for both particle mass loadings utilized in the experiments. The erosion ratio for bend 2 is also reduced at higher mass loading as a consequence of the shielding effect. In this case, the shielding effect is extended to profile 4 and is no longer relevant thereafter. The shielding effect starts to become of great relevance from a bend angle higher than about 35°, in which its magnitude decreases towards a bend angle of 90°. Bellow a bend

angle of 35°, similar erosion ratios were obtained in the experiments for both particle mass loadings. In case of bend 2, a reduction of about 35.2% is detected in the erosion peak when increasing particle mass loading from 0.3 to 1.0, suggesting a stronger shielding effect mostly due to the short bend radius and flow characteristics within the vertical pipe and the bend itself. Additionally, the erosion peak is displaced to lower bend angles at higher particle mass loading, i.e. from approximately 47° to 37° regarding profile 0. It should be noted that a dense particle rope is formed on the outer wall of bend 2 as well, which is expected to be slightly more concentrated in some regions because of the short radius of this bend. Interestingly, the value of the erosion peak and the trends observed experimentally for profile 0 and $\eta = 1.0$ are slightly better predicted by calculations, even though not so good predictions were obtained for bend 1 and the mean particle velocity profile prior to bend 2 (see Figure VIII-19 (b)). Reasonably good agreement was also obtained between experiments and calculations with $\eta = 1.0$ for profiles 1 to 4 up to a bend angle of about 40°. Nevertheless, erosion ratio is mostly overestimated in the range of bend angles from 40° to 70° for those profiles. Regarding profile 5, erosion ratio is underestimated by the calculations.

Also, the shielding effect tends to disappear in the simulations from profile 3 onwards. In the calculations, somewhat similar erosion ratios were also obtained up to a bend angle of 35°, since predictions show similar mean particle impact velocity and angle in this region, as observed in Figure VIII-24 (a) and (b) for profile 0. Also, Figure VIII-24 (a) and (b) show significant reduction in mean particle impact velocity and angle at bend angles higher than 40° with increasing particle mass loading. The reduction in those impact parameters is responsible for decreasing erosion ratio at higher particle mass loadings. Naturally, by increasing particle mass loading, wall collision frequency as well as the amount of mass colliding with the bend surface are increased as well, as reported in Figure VIII-24 (c) and (d). Finally, the numerical calculations accounting for 2-way coupling and inter-particle collisions generally capture the trends observed experimentally, and demonstrates the emergence of the shielding effect.
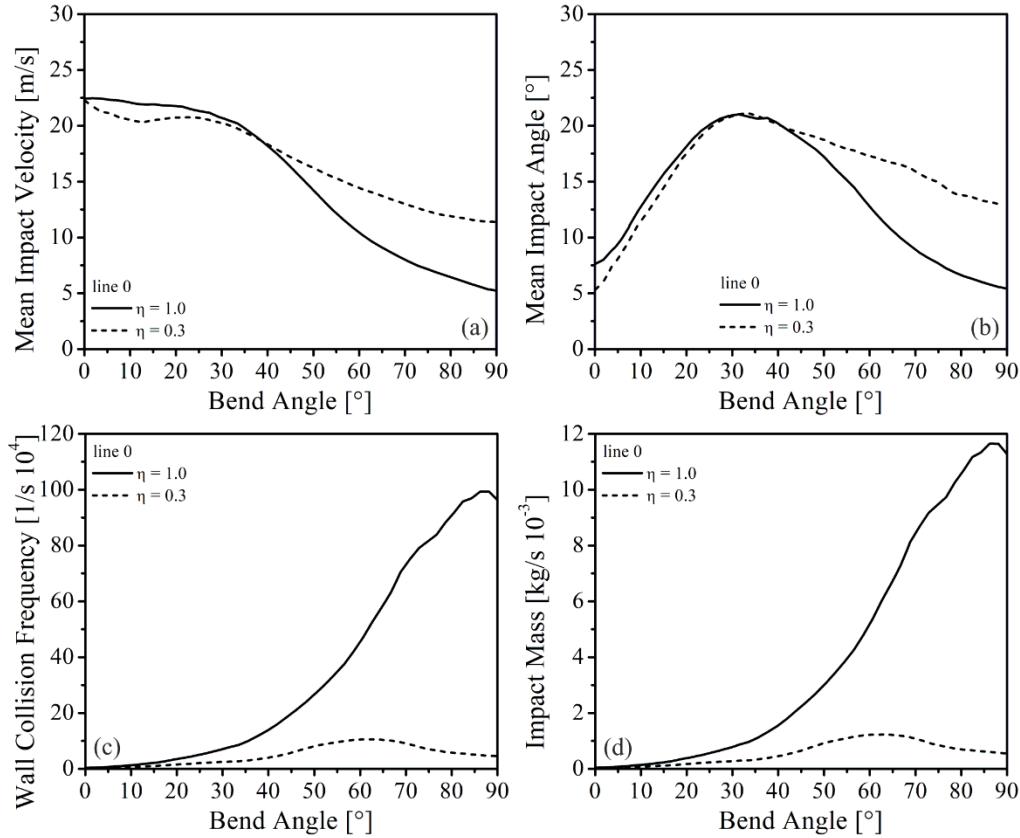
Figure VIII-24. Comparison of predicted erosion-related variables for bend 2 ($R_{bend,2} = 1.4 \cdot D$) considering $\eta = 0.3$ and $\eta = 1.0$: (a) mean impact velocity, (b) mean impact angle, (c) wall collision frequency and (d) impacted mass. Results presented for a pneumatic conveying velocity of 37.9 m/s, spherical glass beads and $\Delta\gamma = 2.5°$. Please refer to Table VIII-1 for case description: $\eta = 0.3$ (GB1), $\eta = 1.0$ (GB7). See Figure IV-4 for line location.

Quartz Sand – η = 0.3

The experimental and numerical results obtained based on the methods described in Chapter IV and Chapter V are presented in the following for quartz sand particles and a particle mass loading of $\eta = 0.3$. The discussion of the results is mostly based on the dependence of surface roughness on erosion and particle impact angle.

As in the same way as for the case with spherical glass beads, the mean particle velocity profiles at both measurement locations exhibit almost symmetrical behavior, showing higher velocities in the core of the pipes which decrease towards the walls, as shown in Figure

VIII-25. Also, higher velocity fluctuations are observed close to the bottom wall of the horizontal pipe and near the outer wall of the vertical pipe, as wall collision frequency is naturally larger in those regions. In this analysis, the influence of surface roughness on the results is discussed mainly regarding surface roughness as a function of erosion and particle impact angle, as also demonstrated in Figure VIII-25. Please note that the surface roughness regarding the standard case is constant and set to 2.5°, while for the other cases, in which surface roughness is not constant, the initial surface roughness is visualized on the image within the parentheses. Only very small differences are observed in both mean and fluctuating particle velocity profiles in the stream-wise direction when considering surface roughness as a function of erosion and impact angle with an initial value of 2.5°, as shown in Figure VIII-25 (a). The same behavior was obtained when considering spherical glass beads. Although erosion by quartz sand particles is meaningfully higher than by spherical glass beads, the erosion on the horizontal pipe is still minimal to cause large changes on surface roughness and therefore, very little influence on the results is obtained.
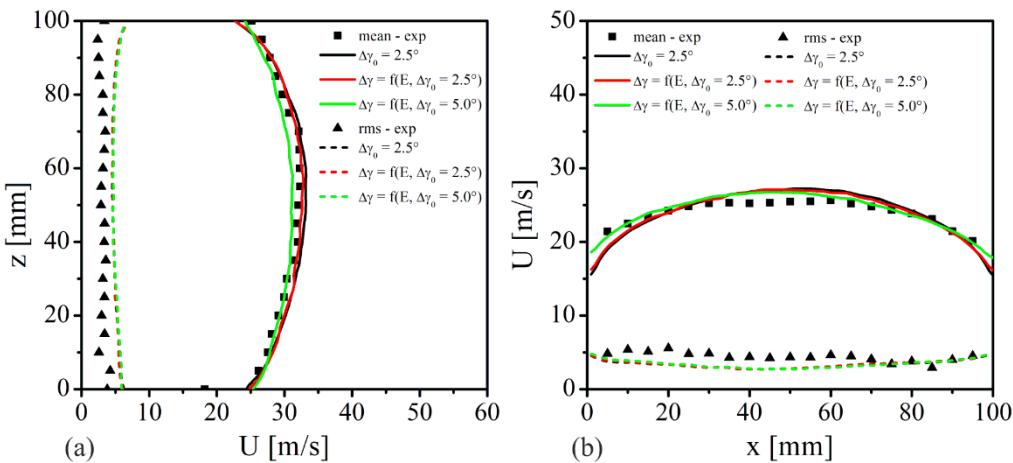
Figure VIII-25. Influence of surface roughness on velocity profiles of the dispersed phase: (a) bottom and (b) top measurement locations. Results presented for a pneumatic conveying velocity of 37.9 m/s, quartz sand, and $\eta = 0.3$. Please refer to Table VIII-2 for case description: $\Delta\gamma = 2.5°$ (SAND1), $\Delta\gamma = f(E, \Delta\gamma_0 = 2.5°)$ (SAND2), $\Delta\gamma = f(E, \Delta\gamma_0 = 5.0°)$ (SAND3).

For instance, the developed surface roughness field is visualized in Figure VIII-26. As can be seen, the increase in surface roughness on the horizontal pipe is small, reaching a mean value of approximately 3.4°. This value is calculated based on the entire horizontal pipe section and is not high enough to cause significant changes on the results. Naturally, particle velocity

decreases when increasing the initial surface roughness to 5° for basically the same reasons previously discussed for spherical glass beads. Also, a very good agreement with the experimental data was obtained for both the cases with $\Delta\gamma_0 = 2.5°$ and $\Delta\gamma = f(E, \Delta\gamma_0 = 2.5°)$ regarding the mean particle velocity, although velocity fluctuations are overestimated in both cases. Likewise, only minimal variations are obtained numerically with respect to the mean particle velocity profile in the upper measurement location for the cases with $\Delta\gamma_0 = 2.5°$ and $\Delta\gamma = f(E, \Delta\gamma_0 = 2.5°)$. The surface roughness reaches a mean value of about 4° for the vertical pipe while the surface roughness of the outer wall of bend 1, as well as in the case of bend 2, increases considerably, reaching values between 8° and 9° at the region of maximum erosion (see Figure VIII-26).
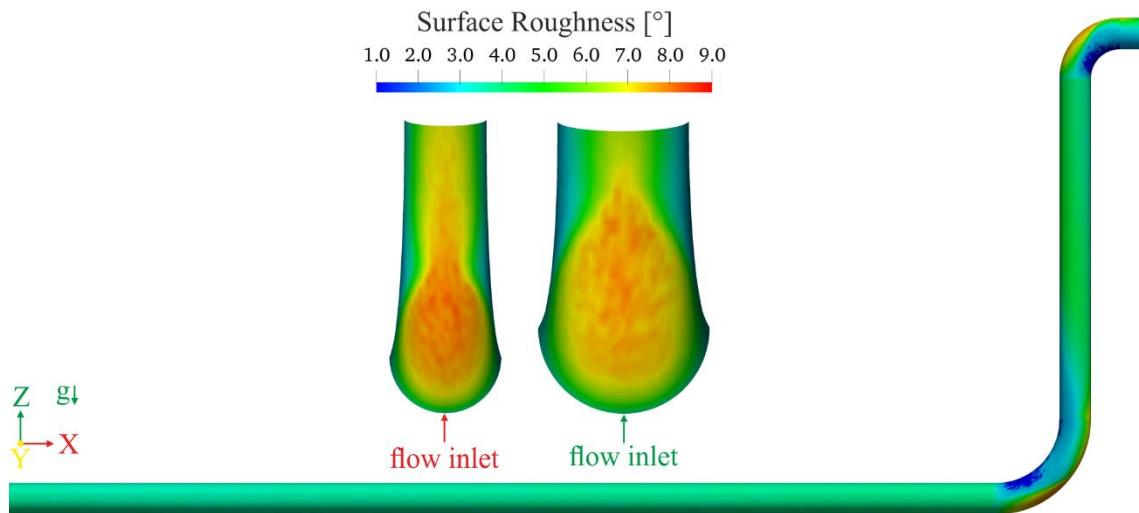
Figure VIII-26. Surface roughness field developed on the surfaces of the system according to Equation (VI-1) considering an initial surface roughness of 2.5° (case SAND2 in Table VIII-2). Results presented for a pneumatic conveying velocity of 37.9 m/s, quartz sand, and $\eta = 0.3$.

The region of higher surface roughness is characterized by an oval shape, where a strip of high surface roughness is also observed downstream of this region. In the vicinity of these regions, the surface roughness is not so high due to the reduction in erosion. Even though erosion changes the surface roughness considerably in some regions of the bends, this was not enough to cause very significant changes on the mean particle velocity in this case. Nonetheless, by increasing the initial surface roughness to 5°, particles are likely to move away from the outer wall of the vertical pipe in direction to the core and the inner wall of pipe, which

reduces particle concentration near the outer wall. This behavior reduces inter-particle collision frequency and weakens the coupling between the phases in such a way that particle velocity is slightly increased in that region. As can be seen from Figure VIII-25 (b), the case with an initial surface roughness of 5° presents a slightly better agreement with the measurements close to the outer wall of the vertical pipe. Additionally, no significant modification is obtained for the velocity fluctuations with increasing surface roughness up to 5° and the calculations mostly underestimate the measured values for the velocity fluctuations.
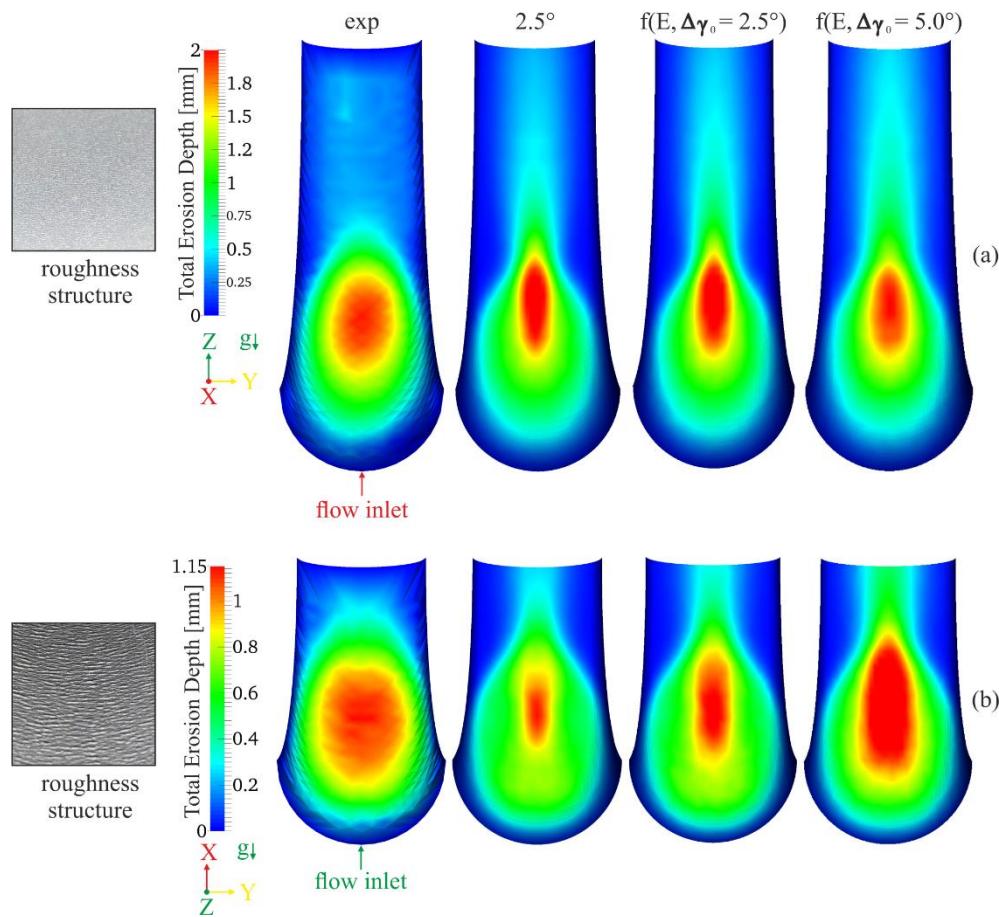
Figure VIII-27. Influence of surface roughness on erosion pattern: (a) bend 1 ($R_{bend,1} = 2.5 \cdot D$) and (b) bend 2 ($R_{bend,2} = 1.4 \cdot D$). Results presented for a pneumatic conveying velocity of 37.9 m/s, quartz sand, and $\eta = 0.3$. Please refer to Table VIII-2 for case description: 2.5° (SAND1), f(E, $\Delta\gamma_0 = 2.5°$) (SAND2), f(E, $\Delta\gamma_0 = 5.0°$) (SAND3).

Figure VIII-27 (a) and (b) illustrates the influence of surface roughness on erosion scar for bend 1 and 2, respectively. The erosion scars measured for the outer surface of bends 1 and 2 considering quartz sand as abrasive particles are also nearly symmetrical and show that the

region of maximum erosion is located at the centre of the surfaces. The maximum erosion region in both bends is characterized by an oval-shaped structure which is wider for bend 2. Furthermore, erosion decreases in all directions from the region of maximum erosion for both bends. Similar behaviour has been also observed by other researchers[2]. Furthermore, the region of maximum erosion when quartz sand particle is utilized is relatively wider compared to spherical glass beads. It is worth noticing that the size distribution of quartz sand particles is wider than the distribution of spherical glass beads and therefore the behaviour of particle motion and distribution within the system is different. Moreover, the collision process is quite different for quartz sand particles due to their irregular shape, which when colliding with a surface, the rebound angle depends mainly on the orientation of the particles relative to the surface, where relatively higher or smaller rebound angles may be obtained. As a result, there may be considerable differences in the shape of erosion patterns. The region of maximum erosion depth for bend 1 corresponds to bend angles from about 32.5° to 47.5°, whereas the region of maximum erosion depth for bend 2 lies from circa 30° to 60°. The erosion peak is located at a bend angle of approximately 42° for bend 1 and of 52° in the case of bend 2. Moreover, the measured erosion for bend 1 is higher compared to bend 2 mainly due to the higher mean particle velocity observed prior to bend 1 (see Figure VIII-25). Numerical calculations are compared with measurements regarding bend 1 in Figure VIII-27 (a). As can be seen, the numerically predicted erosion scar unfortunately contains characteristics that differ from those observed experimentally for the three simulated cases. The maximum erosion region obtained numerically is narrower for all cases analysed, however, by increasing the initial surface roughness, this region becomes slightly more dispersed. This is expected as particle dispersion increases with increasing surface roughness. Also, downstream of the region of maximum erosion a strip of moderate erosion is developed which is not observed experimentally. Similar characteristics are observed in the case of bend 2, as shown in Figure VIII-27 (b), i.e. the maximum erosion area is narrower than the one observed experimentally, and a moderate erosion strip is formed downstream of this area for higher surface roughness as well. In addition, the maximum erosion area becomes relatively longer and wider with increasing surface roughness. In qualitative terms, the numerical calculations involving spherical glass beads produced erosion patterns which most closely resemble those obtained experimentally. Due to the complexity of the phenomena involved, especially when irregularly shaped particles are used, it is difficult to detect a specific cause which justifies the differences

observed between experimental and numerical behaviour. For example, particles are numerically tracked from correlations developed primarily for spherical particles, except for the drag force correlation. As already mentioned, the particle-wall collision process for non-spherical particles has a higher degree of complexity than for spherical particles, even more so when surface roughness is involved. However, the behaviour of irregular collisions is somewhat implicitly accounted for in the collision model by the surface roughness parameter, nonetheless, the particle shape effect should ideally be accounted for regardless of this parameter. In addition, the continuous variation of the surface profile may change not only the angle at which particles impact upon the surface, but also their post-impact trajectories and erosion itself.

The influence of surface roughness on total erosion depth distribution is quantitatively demonstrated in Figure VIII-28 for bend 1. Only small differences are observed in the cases with $\Delta\gamma_0 = 2.5°$ and $\Delta\gamma = f(E, \Delta\gamma_0 = 2.5°)$. For such cases, the erosion depth profile 0 is reasonably well predicted for bend angles between 0° and 40°. At higher bend angles, the numerical calculations overestimate the experimental values, which includes the erosion peak. Except for profile 1, the erosion peak is underestimated for the remaining profiles. Nevertheless, by increasing the initial surface roughness to 5°, the erosion peak of profile 0 decreases to values close to the experimental ones, although erosion is still overestimated at higher bend angles. The reduction is obtained due to the increase in particle dispersion through the increase in surface roughness and, as previously discussed for other cases, this modifies the behavior of erosion-related variables. From profile 3 onwards, only minor changes are observed among all cases. Even though the numerical predictions do not represent the experimental data perfectly, it is important to emphasize that the prediction of the erosion peak of profile 0 is reasonably good with an initial surface roughness of 5°. From an industrial point of view the correct prediction of maximum erosion is very important for preventing pipe rupture and product leakage, for instance, and the applied approach is able to accomplish this reasonably well.
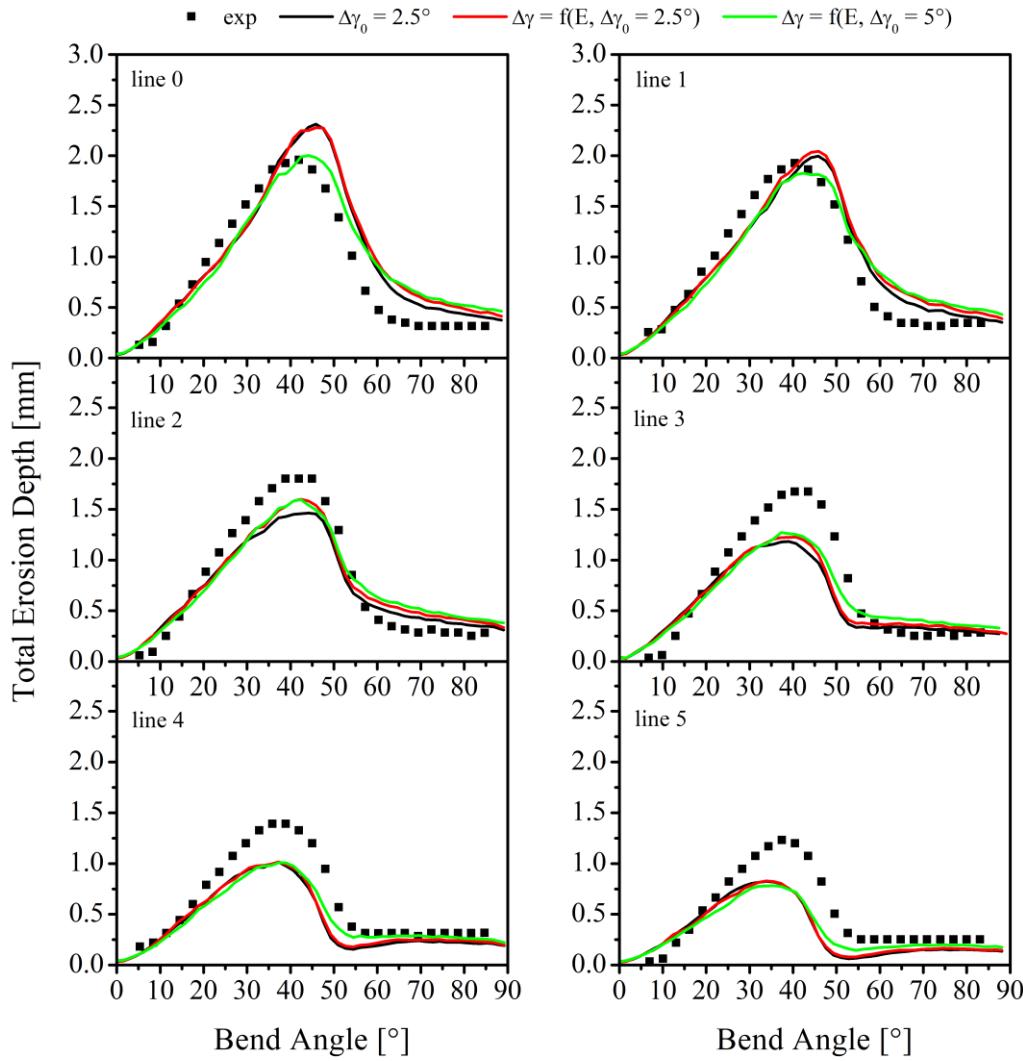
Figure VIII-28. Influence of surface roughness on calculated total erosion depth distribution for bend 1 ($R_{bend,1} = 2.5 \cdot D$). Results presented for a pneumatic conveying velocity of 37.9 m/s, quartz sand, and $\eta = 0.3$. Please refer to Table VIII-2 for case description: $\Delta\gamma = 2.5°$ (SAND1), $\Delta\gamma = f(E, \Delta\gamma_0 = 2.5°)$ (SAND2), $\Delta\gamma = f(E, \Delta\gamma_0 = 5.0°)$ (SAND3). See Figure IV-4 for line location.

Although only minimal variations were observed in the results so far discussed for bend 1 when considering the erosion effect on surface roughness, stronger modifications are observed for bend 2, as visualized in Figure VIII-29. As can be seen in the figure, the predicted erosion depth regarding the standard case ($\Delta\gamma_0 = 2.5°$) shows a reasonable agreement with the measurements in relation to profile 0, specially regarding the erosion peak, however, between bend angles of about 30° to 42°, the values are to some extent underestimated. Profile 1 is reasonably good predicted as well, except in the range of approximately 27.5° to 52.5°, at which values are underestimated. For the remaining erosion depth profiles good predictions

are obtained up to a bend angle of about 25°, although at higher bend angles, the predicted values are basically underestimated. By considering the effect of erosion on surface roughness and an initial surface roughness of 2.5°, erosion depth for profiles 0 and 1 is enhanced for bend angles higher than about 35°. In the case of the profiles 2, 3, 4 and 5, erosion depth is marginally increased in the central region of the profiles, which is considered a small improvement in the results. These variations are caused by the augmentation in surface roughness due to the erosion, as previously demonstrated in Figure VIII-26. The effect of changing surface roughness is stronger for bend 2 as particles flow through bend 1 and the vertical pipe, as they experience stronger surface roughness modifications than the horizontal pipe, even though only minimal variations were observed in the mean particle velocity profile prior to bend 2. Nevertheless, significant changes are identified in erosion-related variables as presented in Figure VIII-30 for $\Delta\gamma_0 = 2.5°$ and $\Delta\gamma = f(E, \Delta\gamma_0 = 2.5°)$. Both wall collision frequency and the amount of mass impacted on the surface are reduced for bend angles from 40° to 90°, resulting from the increase in the surface roughness due to erosion. The increase in surface roughness also contributes to the increase in the mean particle impact velocity in the range of 0° to 90° as well as in the mean particle impact angle from bend angles of about 20° to 70°. Therefore, the augmentation in erosion depth is a result of the increase in mean particle impact velocity and angle, although wall collision frequency is reduced. As previously presented, similar behavior with increasing surface roughness was also obtained for erosion-related variables considering spherical glass beads and the same explanations discussed earlier are valid for quartz sand particles as well. Additionally, the resultant surface roughness due to erosion becomes much higher by increasing the initial surface roughness to 5°, which in turn increases erosion even further. This effect, as well as the reasons why it manifests itself, were already discussed earlier when considering spherical glass beads, which are mainly related to the reduction in the particle concentration within the dense particle rope. For $\Delta\gamma = f(E, \Delta\gamma_0 = 5°)$, erosion depth is meaningfully overestimated at bend angles higher than about 40° in the case of profiles 1 and 2, whilst profile 2 is quite well predicted. Moreover, the trends of the experimental profiles are better captured by the calculations in this case, i.e. the almost flat behavior in the central region of profiles 2, 3, 4 and 5 disappears. Finally, it should be noted that the effect of particle impact velocity is not accounted for in Equation (VI-1). This effect should ideally be included in the model since roughness height is found to increase with increasing particle impact velocity, as already demonstrated by Avcu et al.[63], Kazarinov et

al.[64], and Abedini and Ghasemi[67]. Nevertheless, the effect of particle impact velocity on surface roughness in terms of $\Delta\gamma$ is unclear as it also depends on the mean spacing between the peaks of the roughness profile (RS_m).
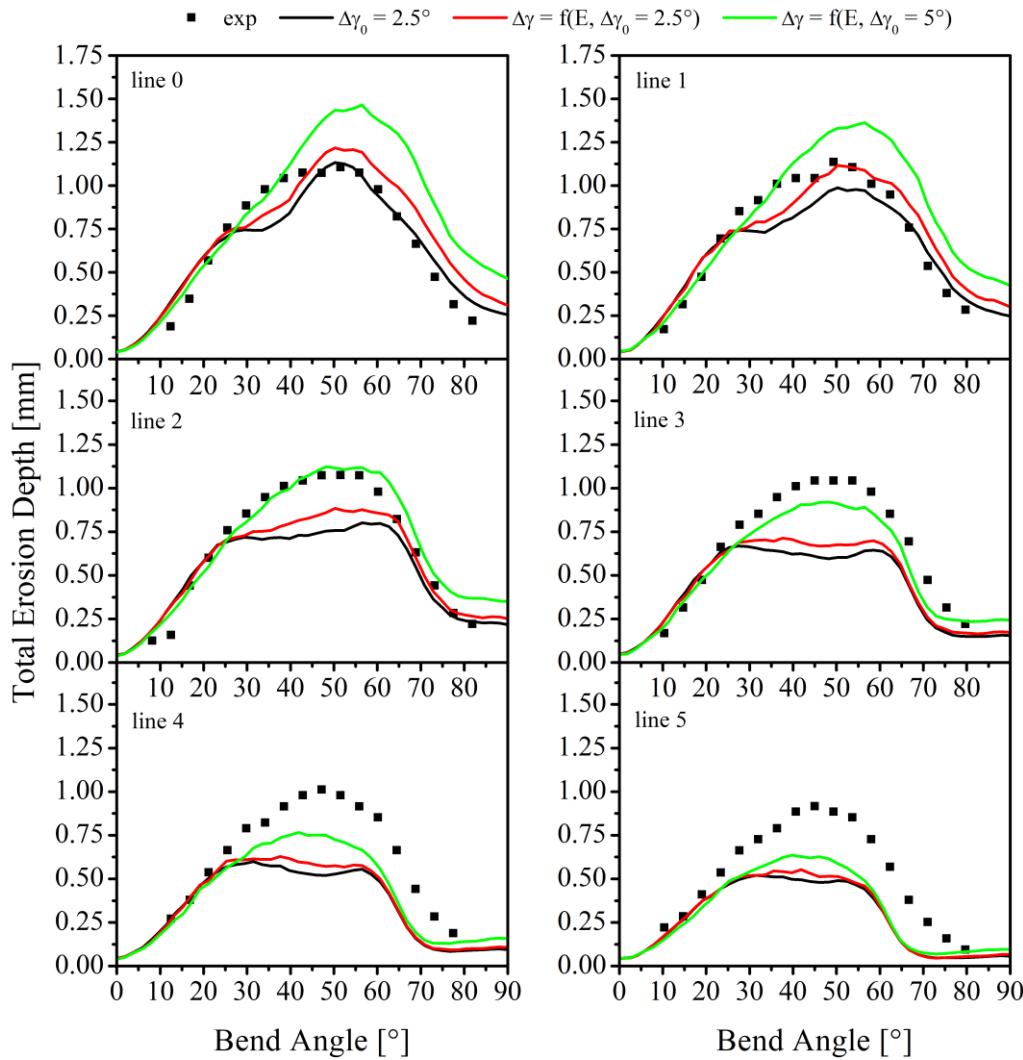
Figure VIII-29. Influence of surface roughness on calculated total erosion depth distribution for bend 2 ($R_{bend,2} = 1.4 \cdot D$). Results presented for a pneumatic conveying velocity of 37.9 m/s, quartz sand, and $\eta = 0.3$. Please refer to Table VIII-2 for case description: $\Delta\gamma = 2.5°$ (SAND1), $\Delta\gamma = f(E, \Delta\gamma_0 = 2.5°)$ (SAND2), $\Delta\gamma = f(E, \Delta\gamma_0 = 5.0°)$ (SAND3). See Figure IV-4 for line location.
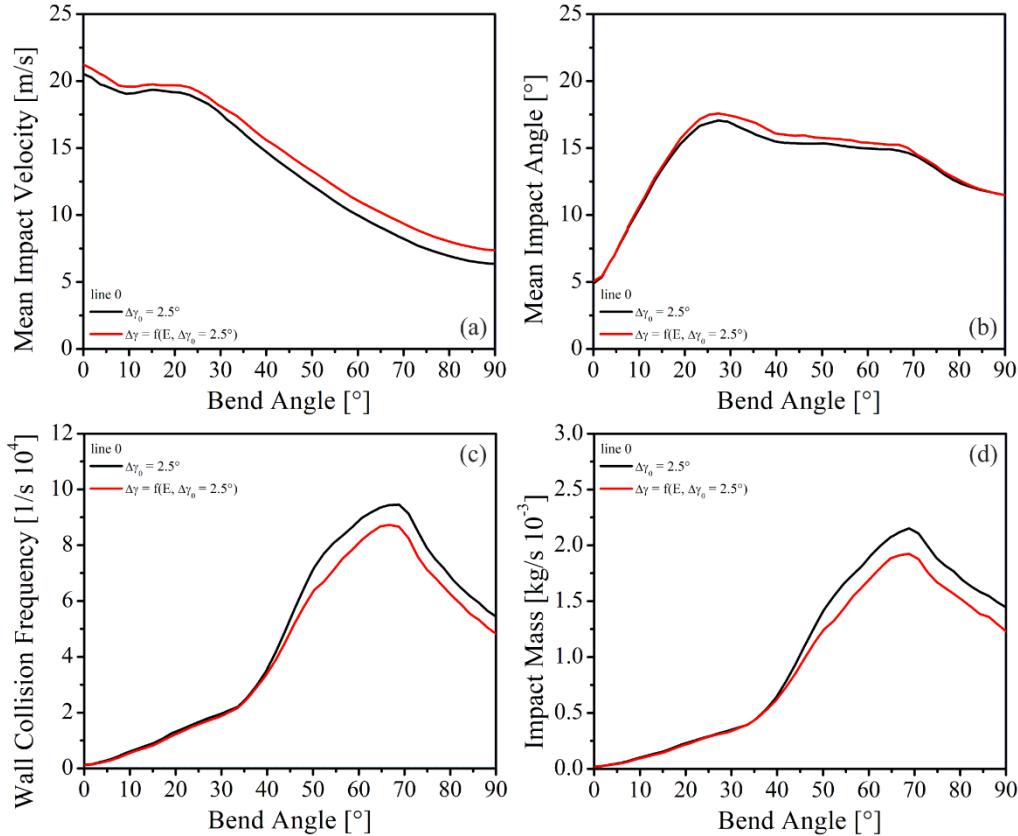
Figure VIII-30. Influence of surface roughness as a function of erosion on calculated erosion-related variables for bend 2 ($R_{bend,2} = 1.4 \cdot D$): (a) mean impact velocity, (b) mean impact angle, (c) wall collision frequency and (d) impacted mass. Results presented for a pneumatic conveying velocity of 37.9 m/s, quartz sand and $\eta = 0.3$. Please refer to Table VIII-2 for case description: $\Delta\gamma = 2.5°$ (SAND1), $\Delta\gamma = f(E, \Delta\gamma_0 = 2.5°)$ (SAND2). See Figure IV-4 for line location.

Quartz Sand – η = 1.0

The experimental and numerical results regarding the case considering quartz sand particles and a particle mass loading of $\eta = 1.0$ is presented next. Additionally, the cases with a particle mass loading of $\eta = 0.3$ and $\eta = 1.0$ are compared to highlight once again the phenomenon referred to as shielding effect. Please note that the comparison is based on the standard numerical setup.
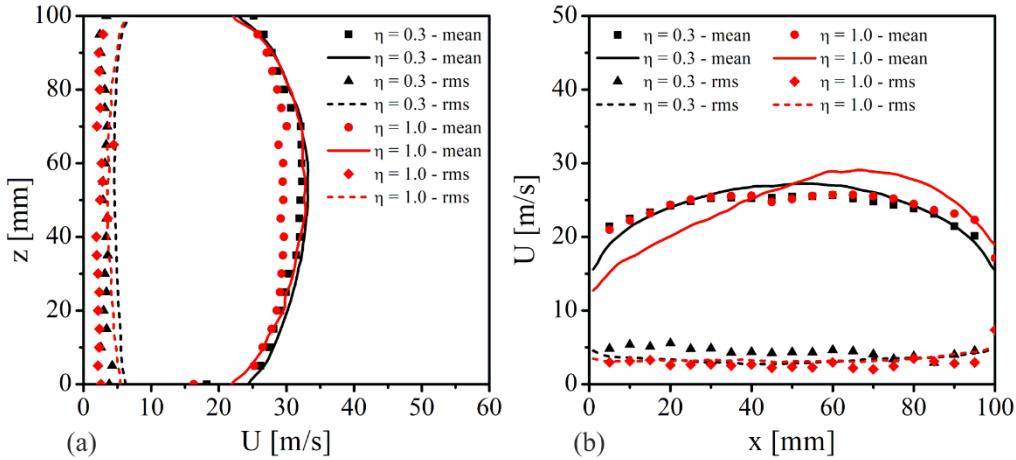
Figure VIII-31. Comparison of measured and calculated mean and fluctuating velocity components of the dispersed phase in the stream-wise direction for $\eta = 0.3$ and $\eta = 1.0$: (a) bottom and (b) top measurement locations. Results presented for a pneumatic conveying velocity of 37.9 m/s, quartz sand and $\Delta\gamma = 2.5°$. Symbols: measurements. Solid lines: numerical predictions. Please refer to Table VIII-2 for case description: $\eta = 0.3$ (SAND1), $\eta = 1.0$ (SAND4).

A comparison of measured and calculated mean and fluctuating particle velocity components in the stream-wise direction is demonstrated in Figure VIII-31 for distinct particle mass loadings, i.e. $\eta = 0.3$ and $\eta = 1.0$. As a result of the augmentation in the local particle concentration as particle mass loading increases to 1.0, which leads to an increase in the number of inter-particle collisions as well as a stronger coupling between the fluid and dispersed phases, the mean particle velocity decreases slightly in the regions close to the walls of the horizontal pipe, whereas a moderate reduction is observed at the core of pipe, as observed in Figure VIII-31 (a). The fluctuating velocity component is only slightly lowered towards the bottom wall of the horizontal pipe with increasing particle mass loading due to the enhancement in inter-particle collision frequency and the associated energy dissipation through inelastic collisions[120,121]. Also, this is only vaguely caused by the damping of fluid turbulence as rather inertial particles are considered[10]. The mean particle velocity considering a particle mass loading of 1.0 is mainly overestimated by the numerical computations in the core of the pipe. Numerically speaking, a notable yet small reduction in the mean particle velocity is only identified for z < 60 mm when comparing both particle mass loadings, which becomes more meaningful towards the bottom wall. It seems that in the experiments the particle concentration in the core of the pipe is somehow higher than in the simulations and therefore, particle velocity is smaller in the experiments than in the simulations mainly due to

phase interaction and increased inter-particle collision frequency. The particle velocity fluctuation is mainly overestimated by the simulations near the walls of pipe. Even so, the particle velocity fluctuation predicted numerically with $\eta = 1.0$ is diminished regarding the case with $\eta = 0.3$, behavior also observed experimentally. The experimentally obtained particle velocity profile at the top measurement location for a particle mass loading of 1.0 is closely similar to that obtained for a particle mass loading of 0.3, as presented in Figure VIII-31 (b). Nevertheless, close to the inner wall of the pipe, i.e. $90 < x < 100$ mm, particle velocity is larger at higher particle mass loading. Alternatively, particle velocity fluctuation is mostly reduced with increasing particle mass loading. Unfortunately, the numerical predictions for the particle velocity profile are not able to follow the trends observed experimentally in this case, as particle velocity is underestimated in the region defined by $x < 40$ mm while it is overestimated for $x > 40$ mm. By comparing Figure VIII-31 (b) and Figure VIII-19 (a), it can be seen that both spherical glass beads and quartz sand particles presented similar behavior numerically. Therefore, the same explanations given for the case with spherical glass beads are applicable to quartz sand particles. Nevertheless, the variations observed for quartz sand particles are stronger than in the case with spherical glass beads (compare Figure VIII-31 (b) and Figure VIII-19 (a)), as particle size distribution differs from one type of particle to the other. Interestingly, particle velocity fluctuation is well predicted in this case, and it is slightly reduced close to the outer wall in relation to numerical case with a particle mass loading of 0.3.

Measured and calculated erosion maps for a particle mass loading of $\eta = 0.3$ and $\eta = 1.0$ are presented in Figure VIII-32 (a) and (b), respectively. Just as for the experimentally obtained erosion maps already presented, the erosion maps acquired for both bends considering a particle mass loading of 1.0 and quartz sand particles are generally nearly symmetrical. Nonetheless, some small asymmetries are detected in the region of maximum erosion, which are probably a result of the irregular collision process experienced by irregular particles. The characteristics of the erosion maps change both in magnitude and in shape at higher particle mass loading for both bends. For instance, the area of maximum erosion of bend 1 becomes wider at higher particle mass loading and is displaced to lower bend angles, resulting from a stronger gravitational settling. The region with moderate erosion is somewhat similar in both experimental cases, differing from each other in magnitude, naturally. Most of the region of

maximum erosion is described as an oval shape while the upper portion vaguely resembles a small V-shaped structure. More importantly, the predicted erosion map resembles the measured one reasonably well, although its shape slightly differs in the region of maximum erosion, which presents an oval shape in its entirety. Furthermore, the region with moderate erosion downstream of the site with maximum erosion is marginally narrower and more elongated in the calculations as that in the experiments, such that it resembles a drop-shaped structure.
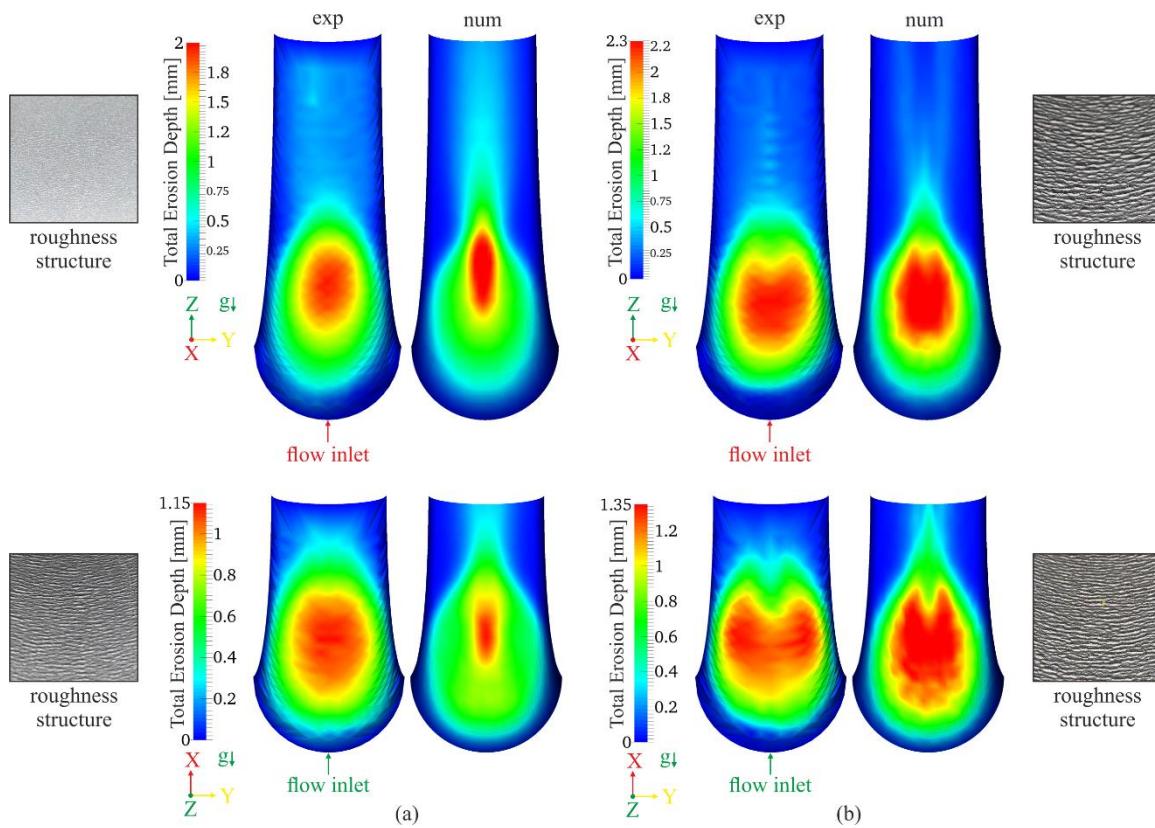
Figure VIII-32. Comparison of measured and calculated erosion patterns: (a) $\eta = 0.3$ and (b) $\eta = 1.0$. Results presented for a pneumatic conveying velocity of 37.9 m/s and quartz sand. Results presented for a pneumatic conveying velocity of 37.9 m/s, quartz sand and $\Delta\gamma = 2.5°$. Please refer to Table VIII-2 for case description: $\eta = 0.3$ (SAND1), $\eta = 1.0$ (SAND4).

Unexpectedly, the spot of maximum erosion is not located at the centre line along bend 2, as generally measured experimentally, but on its surroundings instead. This unexpected behaviour results probably from the geometric characteristics of the system connected with the irregular bouncing of irregular particles and consequently, might be unique to the system and

conditions presented herein. Except in its upper portion, the area of maximum erosion is characterized in the numerical calculations mostly by an oval shape, which is surrounded by a drop-shaped structure with moderate erosion. Although it is not clearly visible in the figure due to the colour scale used, the erosion peak in the simulations is also not located on the central line along the bend.

Figure VIII-33 presents a quantitative comparison of measured and calculated erosion ratio (µm/kg) distribution profiles for bend 1 considering both particle mass loadings used in the experiments. The experimental comparison clearly highlights once more the shielding effect, which was already described and discussed earlier for spherical glass beads. In the case of quartz sand particles, the shielding effect is present in all the profiles presented, however, it is more effective in the central region of the surface of the bend. At bend angles lower than approximately 30°, the erosion ratio is only slightly reduced for all profiles, where a more meaningful reduction is obtained at bend angles higher than 30°, especially in the region at which the erosion peaks are located. The shielding effect is more effective at higher bend angles because the particle rope formed in this region becomes quite dense and therefore, erosion is significantly reduced. At lower bend angles the particle rope is naturally formed but its local particle concentration is not high enough to cause great reduction in the erosion ratio. Additionally, the explanations given in terms of erosion-related variables for spherical glass beads are valid for this case as well, although minor modifications are expected due to distinct particle size distribution. A reduction of about 33.4% is obtained in the peak of erosion ratio for bend 1 when increasing particle mass loading from 0.3 to 1.0, which is higher than that observed for spherical glass beads (27.8%). The predicted erosion ratio by the calculations for bend 1 is in reasonable agreement with the measurements for all profiles. Nevertheless, the peak of erosion ratio is marginally overpredicted for the profile 0, for instance, as the mean particle velocity profile is slightly overestimated by the computations (see Figure VIII-31 (a)). The shielding effect begins to disappear in the numerical simulations from profile 3 onwards, where it is still active only for bend angles greater than about 55°.
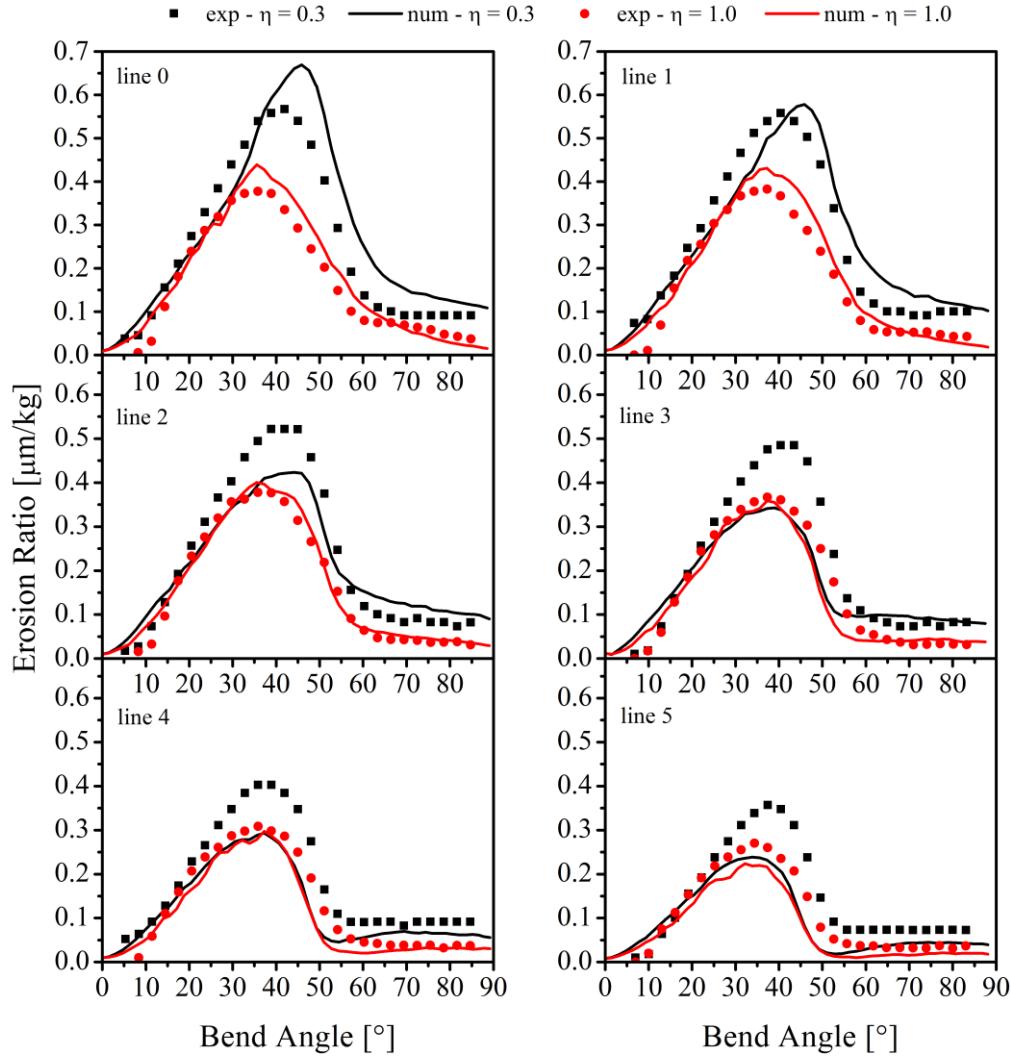
Figure VIII-33. Comparison of measured and calculated erosion ratio distribution for bend 1 ($R_{bend,1} = 2.5 \cdot D$) and for $\eta = 0.3$ and $\eta = 1.0$. Results presented for a pneumatic conveying velocity of 37.9 m/s, quartz sand and $\Delta\gamma = 2.5°$. Please refer to Table VIII-2 for case description: $\eta = 0.3$ (SAND1), $\eta = 1.0$ (SAND4). See Figure IV-4 for line location.

A quantitative comparison of measured and calculated erosion ratio (µm/kg) distribution profiles for bend 2 considering both particle mass loadings used in the experiments is presented in Figure VIII-34. The measured erosion ratio for bend 2 is reduced at higher particle mass loading as a result of the shielding effect as well. The impact of the shielding effect is extended to all profiles presented, as it was also observed for bend 1. Unlike the behaviour observed regarding bend 1, the shielding effect is also very relevant at shallow bend angles and becomes even more relevant in the central region of all profiles. The stronger

influence at shallow bend angles occurs due to the shorter radius of bend 2. A shorter radius favours the increase of the local particle concentration within the rope immediately in regions close to the bend inlet, which makes the shielding effect more effective through the increase in the inter-particle collision frequency. As also observed for the other cases, the shielding effect weakens as it moves away from the central region of the bend. A reduction of approximately 35.2% is observed in the erosion peak when increasing particle mass loading from 0.3 to 1.0 by comparing the maximal erosion obtained for profile 0, for instance. However, it should be noted the maximal erosion is not located at profile 0 in case of bend 2, as previously mentioned, but at profile 4 instead. The reduction in erosion ratio through the shielding effect is slightly higher for bend 2 when compared to bend 1, mainly due to the shorter bend radius as the associated increase in the local particle concentration within the particle rope. When concerning profile 0, the erosion peak is somewhat displaced to lower bend angles. As can be seen in the figure, the numerical simulations in relation to profiles 0, 1, 2 and 3 capture the experimental trends relatively well, but the values are generally slightly overestimated, probably due to the fact that the particle velocity is also overestimated by the calculations for x > 40 mm (see Figure VIII-31 (b)). With respect to profiles 4 and 5, the erosion ratio is basically underestimated for bend angles higher than about 37.5° and 32.5°, respectively. By comparing the numerical profiles 0 and 1 considering both particle mass loadings, it is noted that the shielding effect is also weaker at shallow bend angles and becomes more effective at intermediate bend angles, whereas at higher angles, the shielding effect is again reduced. These trends were also observed experimentally. However, there is a very large reduction in the erosion ratio for the case with 0.3 in such a way that the erosion ratio with 1.0 is greater at intermediate curvature angles. Unfortunately, this behaviour is not consistent with the experimental data obtained.
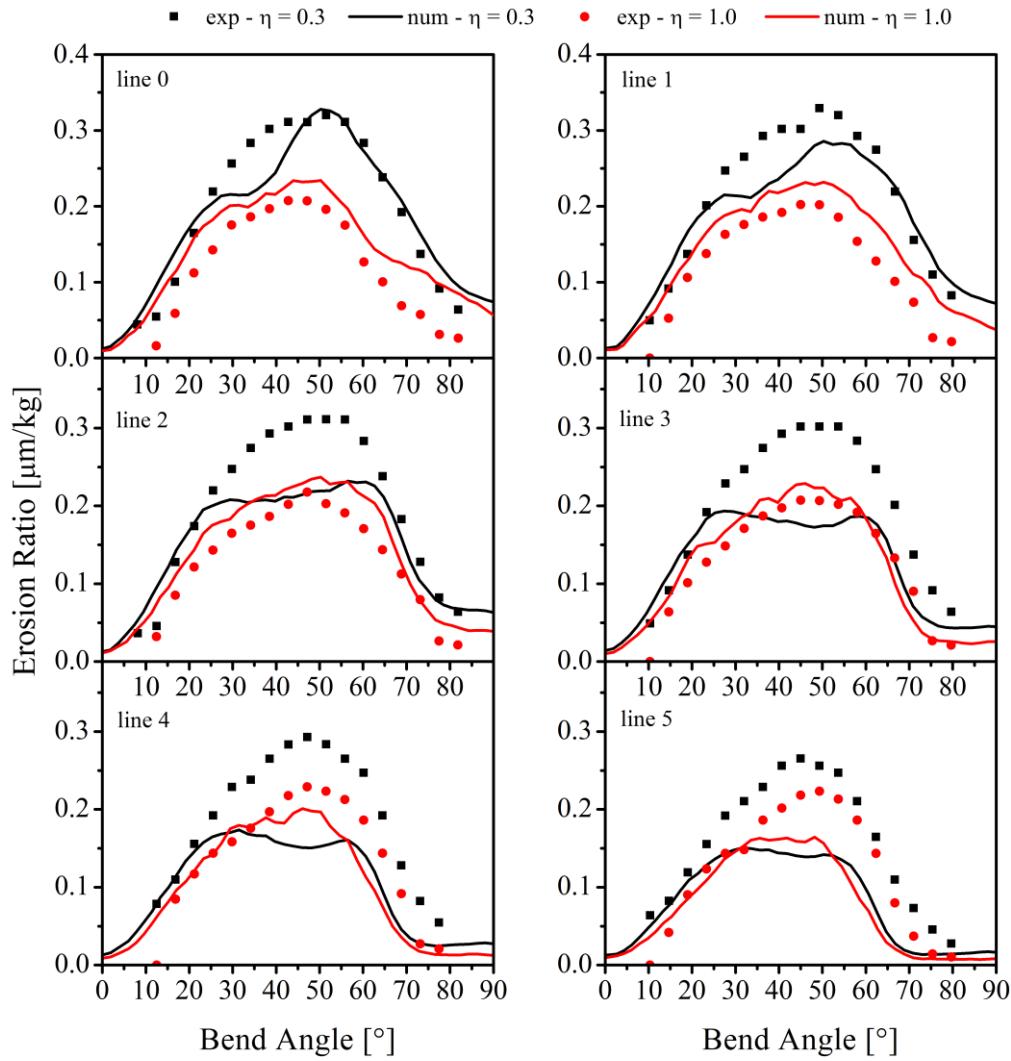
Figure VIII-34. Comparison of measured and calculated erosion ratio distribution for bend 2 $(R_{bend,2} = 1.4 \cdot D)$ and for $\eta = 0.3$ and $\eta = 1.0$. Results presented for a pneumatic conveying velocity of 37.9 m/s, quartz sand and $\Delta\gamma = 2.5°$. Please refer to Table VIII-2 for case description: $\eta = 0.3$ (SAND1), $\eta = 1.0$ (SAND4). See Figure IV-4 for line location.

Chapter IX

Conclusions and Outlook

A great deal of information, both numerical and experimental, was developed and presented throughout the current work. Experimental data was acquired in two different experimental facilities as well as the standard Lagrangian libraries from OpenFOAM® 4.1 were extended to account for inter-particle collisions and the effect of roughness on the particle-wall interactions. In addition, four erosion models were implemented and five were tested, as well as a correlation which describes the effect of erosion and particle impact angle on the surface roughness was developed and implemented. General conclusions from the work and presented in the following. Lastly, the suggestions for future work are presented.

9.1. General Conclusions

The influence of solid particle erosion on the surface roughness behavior of different materials under different erosion times and impact conditions, considering particles of different shapes, was investigated by performing erosion tests in an impingement jet facility

and optically scanning the material surface after erosion. The eroded surfaces were characterized in terms of three different parameters: R_a, RS_m and $\Delta\gamma$. The measurements revealed that the surface roughness of the considered materials was majorly affected by erosion time, inclination angle and particle shape. In general, the following conclusions may be drawn from the experimental investigation conducted:

- Erosion by quartz sand is significantly higher than by spherical glass beads particles for all considered materials, as the cutting action of non-spherical particles is more effective over the ploughing deformation of spherical particles. Naturally, differences in particle properties may contribute to changes on erosion intensity as well.

- Ripple formation is a result of the erosion process and does not result exclusively from mechanisms of material removal but also from material displacement. Therefore, particle shape is an important parameter in evaluating to which extent surface roughness of materials could change due to solid particle erosion. As far as ripple formation is concerned, the amplitude and wavelength of the ripples were considerably higher after erosion by spherical glass beads than by quartz sand particles, and moreover, ripples were intensified by increasing erosion time.

- In addition, it was shown that the inclination angle affects ripple formation as well. For instance, no ripples were observed on the surface of aluminium 5754 after erosion by quartz sand particles at an inclination angle of 10°. By increasing the inclination angle up to 40°, on the other hand, ripples were formed with growing amplitude and wavelength at higher inclination angles.

- Furthermore, material properties such as hardness certainly influences ripple formation, as no ripples were formed on the surface of brass 70/30, which is harder than aluminium 5754 and copper, by using quartz sand particles. Nonetheless, ripples were observed on the surface of brass 70/30 by using spherical glass beads particles as result of their ploughing action, though erosion is greatly reduced. Even though copper is harder than aluminium 5754, both materials presented similar behaviour in terms of ripple formation for both particle shapes considered.

- In general, ripple formation is the main factor responsible for the significant increase in the parameters R_a and RS_m. An increase in the R_a parameter was also observed in cases where ripple formation was not detected, as regards brass 70/30 eroded by quartz sand particles, for example. On the other hand, RS_m mostly decreased when no well-defined ripples were formed.

- Except for the case of brass 70/30 eroded by quartz sand particles, in which R_a and RS_m achieved constant values, the highest average roughness height and the largest average distance between peaks were observed at higher impact angles and erosion times. Therefore, it can be assumed that, in general, R_a and RS_m increase with increasing inclination angle up to 40° and erosion time. Nonetheless, increasing the inclination angle further to 90° could reduce the values of R_a, as reported by Avcu et al.[63].

- Based on the work of Sommerfeld[76] as well as on the measurements and evaluation of the parameters R_a and RS_m, a simple correlation was proposed to estimate the dependence of $\Delta\gamma$ on solid particle erosion accounting for the effect of the inclination angle up to 40°. The model predictions were in good agreement with the obtained experimental data.

- Nevertheless, it should be noted that other parameters such as particle impact velocity (Avcu et al.[63], Kazarinov et al.[64], Abedini and Ghasemi[67]) and concentration (Abedini and Ghasemi[67]), for instance, affect surface roughness as well.

Additionally, air and particle velocity measurements were conducted at the exit of the impingement jet at different inclination angles. The measurements revealed that both mean and fluctuating air velocity components in the stream-wise direction were significantly affected by the inclination angle of the plate. By increasing the inclination angle the mean air velocity in the stream-wise direction is meaningfully reduced in the upper region, as a result of the small distance between the plate and the jet, and slightly increased in the bottom region. The fluctuating component, on the other hand, was mostly enhanced. In addition, the mean and fluctuating velocity components in the stream-wise and transverse directions for spherical glass beads particles were little modified by increasing the inclination angle from 10° to 30°. In contrast, at an inclination angle of 40° the mean velocity component was greatly reduced by the presence of the plate in the stream-wise direction while it was increased towards

negative values in the transverse direction. The fluctuating velocity component, on the other hand, was enhanced. At inclination angles of 10° and 20°, little influence on mean and fluctuating velocity components in the stream-wise and transverse directions for quartz sand particles was observed. Nevertheless, the mean velocity component in the stream-wise direction was reduced by increasing the inclination angle to 30° and 40° and the fluctuating velocity component was intensified. In the transverse direction, while the mean velocity component was increased towards negative values in the upper regions of the jet by the increase in the inclination angle, no significant changes were observed in the bottom regions. Once more, the fluctuating velocity component was intensified at inclination angles of 30° and 40°. Rebounding particles from the plate, which are not distinguish by PIV algorithm from other particles, may also contribute to the reduction observed in particle velocity at an inclination angle of 40°.

The transient, three-dimensional and coupled Euler-Lagrange approach together with the standard k-ε model was chosen to perform the all numerical analysis which were addressed to in the current work. The standard code libraries from OpenFOAM® 4.1 were used as a basis for the numerical implementation of other mathematical models necessary to adequately predict the behaviour of diluted gas-solid flows and estimate solid particle erosion. Among which, the models that stand out the most are the stochastic inter-particle collision model and the model which describes the particle-wall collision process considering the effect of surface roughness. These models were crucial for obtaining numerical results capable of representing the trends observed experimentally, both qualitatively and quantitatively. In addition, other erosion models have been included in the standard code library, apart from Finnie's model, which is already part of the standard source code. Also, the possibility of considering the surface roughness as a function of erosion and impact angle is now available as well, although modelling improvement to account for the effect of other parameters is still a necessity. The implementation of such models is unfortunately not straightforward, which demands a high amount of work towards its validation. Therefore, the numerical calculations including the aforementioned models were initially tested and compared with the experimental data provided by Huber[3] and Huber and Sommerfeld[4,5], in which results showed very good agreement with the measurements. The good quality of the numerical results demonstrated that the applied approach accounting for inter-particle collisions and surface roughness are essential to

correctly predict the phase segregation on the outer wall of bends caused mainly due to inertial effects, on which particles accumulate forming a dense particle rope which moves along the bend. Inter-particle collisions contributed to a compression of the particle rope and the arising of the shielding effect in such a way that the numerical results approached considerably the measurements regarding the particle mass flux downstream of the bend. Moreover, the disintegration of the particle rope along the vertical pipe is also predicted by calculations when inter-particle collisions is accounted for, as observed in the experiments. A great improvement in the particle velocity profiles, as well as in the particle size distributions, along the cross-sections of the vertical pipe was also achieved via the consideration of inter-particle collisions and surface roughness. Based on the good results obtained for this system, it can be concluded that the implementations have been validated and other gas-solid systems can be explored.

Likewise, the erosion models implemented were evaluated through a validation process to ensure the best prediction of erosion. This objective was achieved by comparing the erosion estimates with the experimental data acquired by Mazumder et al.[1] and Solnordal et al.[2]. When comparing the numerical data with the case from Mazumder, it was demonstrated that all the tested models predict very similar erosion profiles and maps, which are distinguished from each other only in magnitude. This is natural as all models strongly depend on particle impact velocity and angle and these were the same for all erosion computations. Also, the Oka model performed better in predicting the measured thickness loss compared to other models, probably because this model is more recently developed and accounts for material hardness and was additionally developed under several impact conditions considering different erodent particles. Solnordal et al.[2] provided a detailed experimental map of erosion, with which the results from the implemented erosion models were also compared. The numerical results were compared with 4 profiles obtained along the outer wall of the measurement bend and, once more, all models estimated similar erosion profiles but of different magnitudes. The predictive equation from Oka showed a better performance compared to the other models and, consequently, it was chosen as a standard model for the rest of the numerical simulations presented. However, the evaluation of the ability of predictive equations to correctly predict erosion was carried out in very diluted gas-solid flows, in which the effects of inter-particle collisions as well as the influence of particles on the fluid phase were neglected. These effects were discussed based on the experimental data obtained by the author in a pneumatic conveying facility.

An experimental pneumatic conveying facility was developed with the objective of obtaining erosion profiles and three-dimensional maps on two geometrically different bends, as well as measuring the velocity distributions of the fluid and dispersed phase in regions which precede both bends. Therewith, the influence of the particle mass loading and particle shape on the erosion pattern as well as on particle velocity profile was characterized. The greatest contribution of this analysis was to provide simultaneously experimental data regarding bend erosion and particle velocity in a single experimental facility, as such measurements are normally not available in the literature, according to the author's knowledge. The simultaneous obtaining of erosion and particle velocity data in the same experiment allows a more precise validation of the numerical methods and the available erosion models, since in most cases, the flow dynamics are validated based on experimental data from an author and the erosion models are compared with measurements provided by another author. Although this is commonly practiced and generally produces good results, prediction errors and uncertainties may be higher, as the associated experimental errors and uncertainties may differ considerably from author to author. in addition to showing the appearance of the shielding effect, the measurements highlighted the differences between the erosion maps obtained with different particle shapes and particle mass loading. It was also shown that the shielding effect is stronger in the central region of the bend due to the high local concentrations observed in this region, yet its effect is reduced as the profiles move away from the central region. Also, the reduction in erosion ratio through the shielding effect is more meaningful for quartz sand particles than spherical glass beads in the case of bend 1, whilst in the case of bend 2, similar reduction was identified. The measured particle velocity profiles for spherical glass beads showed similar behaviours for both particle mass loadings considered at both measurement locations, where small reductions were observed for the case with a particle mass load of 1.0 mainly due to the increase in the local particle concentration and, consequently, to the increase in the inter-particle collision frequency. Although the reduction in the particle velocity with respect to the profile at the bottom measurement location is greater in the case of quartz sand particles, which is attributed mainly to the irregular bouncing of non-spherical particles. Nevertheless, only minor differences were observed for the particle velocity at the top measurement location. Particle velocity fluctuation is mainly reduced with increasing particle mass loading. As expected, the velocity profile of the fluid phase at the bottom measurement location showed classic characteristics of a developed turbulent profile. On the contrary, the velocity profile of

the continuous phase at the top measurement location is asymmetric, where higher velocities were measured at the regions close to the outer wall of the vertical pipe, while at the regions close to the inner wall, the fluid velocity is lower. The central region of the profile, in turn, showed generally a flat behaviour. The asymmetry observed is a function of the short length of the vertical pipe, which quickly converges to a new horizontal section through a 90° bend with a shorter radius.

The predictions of single-phase flow are very good, where only small discrepancies were obtained in relation to the velocity profile at the top measurement location. Furthermore, an extensive evaluation and validation was provided by comparing the numerical results obtained with the application of the Euler-Lagrange approach with the experimental results. The influence of the degree of coupling between the phases on particle velocity profile and erosion was analysed in detail for the case considering spherical glass beads with a particle mass loading of 0.3 allowing to demonstrate the importance of the 4-way coupling. By neglecting particle-particle interactions, the particle velocity distribution was generally overestimated, whereas erroneous predictions were obtained in relation to the erosion maps for both bends, where a V-shaped structure appeared. Naturally, erosion distribution on the bend surface was therefore overestimated as well. Through the 4-way coupling, particle velocity is generally reduced due to the loss of momentum through collisions causing a significant reduction in erosion, in which an immense improvement in the results was obtained. In addition, the V-shaped structure completely disappears due to the redispersion of the particles within the pipes as a result of collisions. Furthermore, collisions contribute mainly to a reduction in the particle impact velocity and angle because of the increase in the wall collision frequency. Therefore, accounting for inter-particle collisions together with an appropriate erosion model is essential in prediction gas-solid flows as well as in estimating erosion. In general, a very good agreement was obtained regarding the predictions of particle velocity and erosion for bend 1. The region of maximum erosion was mostly displaced in the case of bend 2, but predictions were reasonably good quantitatively.

The impact of surface roughness on particle velocity and erosion was evaluated for the case considering spherical glass beads and a particle mass loading of 0.3. A numerical case showing the influence of the dependence of surface roughness on erosion and particle impact

angle considering an initial surface roughness of 2.5° was discussed as well. On average, particle velocity decreased with the increase in surface roughness as a result of the augmentation in the wall collision frequency and the consequent loss of kinetic energy by the particles. However, there were insignificant differences when considering the surface roughness as a function of erosion and particle impact angle, as the contribution of these both parameters to the change of the surface roughness in terms of $\Delta\gamma$ is not so high. Regarding bend 1, the region of maximum erosion was found to be reduced with increasing surface roughness as wall collision frequency is remarkably reduced, although particle impact angle is considerably augmented. Particle impact velocity, on the other hand, was found to be increased in some regions of bend while it was reduced in others, depending on the surface roughness degree. Numerically speaking, bend 2 showed unique trends in which the increase in surface roughness from 2.5° to 10° increased erosion, which then decreased with a surface roughness of 20°. This behaviour is related to the dispersion of the particle rope through higher surface roughness, which in turn reduces the local particle concentration resulting in a reduction in the wall and inter-particle collision frequency and the weakening the coupling between the phases. Consequently, particle impact velocity and angle are increased yielding higher erosion, although wall collision frequency is reduced. Thus, it is concluded that the surface roughness has a major influence on the prediction of confined gas-solid flows and on the erosion itself and its modelling is of paramount importance[2,5,91,92,101,10,12–15,76,85,87].

A comparison was presented between the cases involving spherical glass beads and particle mass loadings of 0.3 and 1.0, both from an experimental and numerical point of view. The shielding effect was also captured numerically by increasing particle mass loading through the consideration of inter-particle collisions, which shows, once again, the importance of particle-particle interactions. The reduction in erosion ratio was found mainly to occur due to remarkable increase in the wall collision frequency followed by a reduction in the particle impact velocity. The prediction of the erosion scar for bend 1 was reasonably good qualitatively, yet erosion ratio was principally underestimated, as particle velocity prior to bend 1 was underestimated as well. In the case of particle mass loading of 1.0, the particle velocity profile at the top measurement location was erroneously calculated, although the erosion ratio for profile 0 was predicted relatively good. Also, the estimated erosion scar for bend 2 presented higher differences compared to the experimental erosion scar.

The effect of changing the surface roughness as a function of erosion and particle impact angle was examined mainly for the case considering quartz sand particles and a particle mass loading of 0.3. It was reported that changes in the surface roughness are higher on the outer surface of both bends, naturally, since erosion is higher in these regions than in the horizontal and vertical pipes. The comparison between cases $\Delta\gamma = 2.5°$ and $\Delta\gamma = f(E, \Delta\gamma_0 = 2.5°)$ revealed that the changes suffered by the surface roughness due to the erosion and particle impact angle cause only minor disturbances in both particle velocity and erosion, with respect to the bottom measurement location and the bend 1. Nevertheless, the erosion on the strip formed downstream of the region with maximum erosion is relatively higher for the case with $\Delta\gamma = f(E, \Delta\gamma_0 = 2.5°)$ and the region of maximum erosion is slightly wider as well. It was found for this case that surface roughness reached values between 8° to 9° for both bends in the region of maximum erosion while a mean value of 3.4° and 4° was obtained for the horizontal and vertical pipes, respectively. The effect of changing surface roughness was found to be stronger for bend 2 as particles flow through bend 1 and the vertical pipe and they experience stronger surface roughness modifications than the horizontal pipe. Although only minimal variations were observed in the mean particle velocity profile prior to bend 2. In the case of variable surface roughness ($\Delta\gamma = f(E, \Delta\gamma_0 = 2.5°)$) erosion generally increased due to the observed increase in the particle impact velocity and angle, although wall collision frequency was decreased, which was considered as a minor improvement in the results. Also, it was observed that by increasing the initial surface roughness to 5°, erosion is reduced for bend 1 and increased for bend 2. The erosion trends of bend 2 were better captured in this case, although erosion peak was overestimated. Hence, it is concluded that the change of surface roughness due to erosion and particle impact angle have an impact on the behaviour of gas-solid flows and erosion itself. Unfortunately, the dissimilarities between calculations and measurements were more pronounced for quartz sand particle and a particle mass loading of 0.3. Nevertheless, the region of maximum erosion was reasonably good predicted. Additionally, predictions of particle velocity were very good, especially at the bottom measurement location.

The cases considering quartz sand particles and particle mass loading of 0.3 and 1.0 were also compared both from an experimental and numerical point of view. Simulation results proved once more the ability of the numerical approach in predicting the shielding effect by

considering 4-way coupling. Moreover, the erosion scar for bend 1 as well as the erosion ratio distribution were very well predicted for a particle mass loading of 1.0, even though particle velocity profile was minorly overestimated at the bottom measurement location. The experimental trends were also well captured by the numerical calculations related to bend 2, however, the values of the erosion ratio were generally overestimated. This could be somehow expected as the particle velocity, in the case of a particle mass loading of 1.0, was wrongly predicted prior to bend 2.

The results obtained by applying the transient, three-dimensional and coupled Euler-Lagrange approach in connection with the standard k-ε model and accounting for all relevant forces which act on the particles are in general in good agreement with the measurements performed by the author as well as with the experimental data available in the scientific literature. This was naturally achieved by taking into account inter-particle collisions and the effect of surface roughness, both as a constant value and as a function of erosion and particle impact angle, indicating that those models are essential for an accurate prediction of dispersed gas-solid flows, in which solid particle erosion is also involved, especially at high particle mass loading. Hence, the numerical methods presented in the current work may be directly applied to industrial applications involving gas-solid flows in pipes with the consideration of solid particle erosion. Lastly, the good quality of the obtained numerical results shows also the reliability of the applied methodology.

9.2. Suggestions for Future Work

Based on the experimental and numerical work developed, some suggestions for future work are presented below.

- The effect of erosion considering the influence of the particle impact angle up to 40° on the surface roughness of three ductile materials was investigated. It is suggested to evaluate and include in the proposed correlation the impact of other parameters related to erosion, such as the effect of particle impact velocity as well as of the particle diameter. It has been shown in the current work that the distance between the peaks (RS_m) of the roughness profile can reach values as high as the particle size. Hence, the impact of particle size on

the roughness angle distribution may be significant. It has also been reported by other researchers[63,64,67] that the average height (R_a) of the roughness profile increases with increasing particle impact velocity. Thus, this parameter could also modify the distance between peaks and, consequently, the parameter $\Delta\gamma$. Naturally, the influence of particle impact angle greater than 40° should ideally be accounted for. Another suggestion would be to carry out the same analysis considering brittle materials, as the erosion mechanisms for these materials are completely different from those of ductile materials and therefore, the mechanism of ripple formation is probably different as well.

- The influence of surface roughness, both as a constant value and as a function of erosion and particle impact angle, on the behaviour of a gas-solid flow in a pneumatic conveying system as well as on solid particle erosion was explored in detail. However, it is already known that severe erosion, in addition to modifying the surface roughness, also alters the surface of the bend. It would be interesting to include and analyse numerically the effect of the surface change, coupled with the effects already discussed, on the development of the gas-solid flow as well as on the erosion itself.

References

1. Mazumder, Q. H., Shirazi, S. A. & McLaury, B. Experimental investigation of the location of maximum erosive wear damage in elbows. *J. Press. Vessel Technol.* **130**, 1–7 (2008).

2. Solnordal, C. B., Wong, C. Y. & Boulanger, J. An experimental and numerical analysis of erosion caused by sand pneumatically conveyed through a standard pipe elbow. *Wear* **336**–**337**, 43–57 (2015).

3. Huber, N. Zur Phasenverteilung von Gas-Feststoff-Strömungen in Rohren. (Ph. D. Thesis, University Erlangen-Nürnberg, 1997).

4. Huber, N. & Sommerfeld, M. Characterization of the cross-sectional particle concentration distribution in pneumatic conveying systems. *Powder Technol.* **79**, 191–210 (1994).

5. Huber, N. & Sommerfeld, M. Modelling and numerical calculation of dilute-phase pneumatic conveying in pipe systems. *Powder Technol.* **99**, 90–101 (1998).

6. Sommerfeld, M., van Wachem, B. & Oliemans, R. Best Practice Guidelines for Computational Fluid Dynamics of Dispersed Multiphase Flows. in *ERCOFTAC (European Research Community on Flow, Turbulence and Combustion)* (2008).

7. Crowe, C. T., Schwarzkopf, J. D., Sommerfeld, M. & TsujiY. *Multiphase flows with droplets and particles*. (CRC Press, 2012).

8. Elghobashi, S. On predicting particle-laden turbulent flows. *Appl. Sci. Res.* **52**, 309–329 (1994).

9.   Sommerfeld, M. Numerical simulation of the particle dispersion in turbulent flow. The importance of particle lift forces and particle/wall collision models. *Am. Soc. Mech. Eng. Fluids Eng. Div. FED* **91**, 11–18 (1990).

10. Kussin, J. & Sommerfeld, M. Experimental studies on particle behaviour and turbulence modification in horizontal channel flow with different wall roughness. *Exp. Fluids* **33**, 143–159 (2002).

11. Laín, S., Sommerfeld, M. & Kussin, J. Experimental studies and modelling of four-way coupling in particle-laden horizontal channel flow. *Int. J. Heat Fluid Flow* **23**, 647–656 (2002).

12. Sommerfeld, M. & Kussin, J. Wall roughness effects on pneumatic conveying of spherical particles in a narrow horizontal channel. *Powder Technol.* **142**, 180–192 (2004).

13. Laín, S. & Sommerfeld, M. Euler/Lagrange computations of pneumatic conveying in a horizontal channel with different wall roughness. *Powder Technol.* **184**, 76–88 (2008).

14. Laín, S. & Sommerfeld, M. Numerical calculation of pneumatic conveying in horizontal channels and pipes: Detailed analysis of conveying behaviour. *Int. J. Multiph. Flow* **39**, 105–120 (2012).

15. Sommerfeld, M. & Lain, S. Parameters influencing dilute-phase pneumatic conveying through pipe systems: A computational study by the Euler/Lagrange approach. *Can. J. Chem. Eng.* **93**, 1–17 (2015).

16. Bitter, J. G. A. A Study of Erosion Phenomena Part I. *Wear* **6**, 5–21 (1963).

17. Meng, H. C. & Ludema, K. C. Wear models and predictive equations. *Wear* **181**–**183**, 443–457 (1995).

18. Parsi, M. *et al.* A comprehensive review of solid particle erosion modeling for oil and gas wells and pipelines applications. *J. Nat. Gas Sci. Eng.* **21**, 850–873 (2014).

19. Lyczkowski, R. W. & Bouillard, J. X. State-of-the-art review of erosion modeling in

fluid/solids systems. *Prog. Energy Combust. Sci.* **28**, 543–602 (2002).

20.   Finnie, I. Erosion of Surfaces by Solid Particles. *Wear* **3**, 87–103 (1960).

21.   Bitter, J. G. A. A study of erosion phenomena Part 2. *Wear* **6**, 169–190 (1963).

22.   Neilson, J. H. & Gilchrist, A. Erosion by a stream of solid particles. *Wear* **11**, 111–122 (1968).

23.   Hutchings, I. M. A model for the erosion of metals by spherical particles at normal incidence. , **70**, 269–281 (1981).

24.   Tilly, G. P. A two stage mechanism of ductile erosion. *Wear* **23**, 87–96 (1973).

25.   Sundararajan, G. A comprehensive model for the solid particle erosion of ductile materials. *Wear* **149**, 111–127 (1991).

26.   Sheldon, G. L. & Finnie, I. The mechanism of material removal in the erosive cutting of brittle materials. *J. Eng. Ind.* **88**, 393–399 (1966).

27.   Sundararajan, G. & Shewmon, P. G. A new model for the erosion of metals at normal incidence. *Wear* **84**, 237–258 (1983).

28.   Wiederhorn, S. M. & Hockey, B. J. Effect of material parameters on the erosion resistance of brittle materials. *J. Mater. Sci.* **18**, 766–780 (1983).

29.   Sheldon, G. L. & Kanhere, A. An investigation of impingement erosion using single particles. *Wear* **21**, 195–209 (1972).

30.   Oka, Y. I., Ohnogi, H., Hosokawa, T. & Matsumura, M. The impact angle dependence of erosion damage caused by solid particle impact. *Wear* **203**–**204**, 573–579 (1997).

31.   Oka, Y. I., Okamura, K. & Yoshida, T. Practical estimation of erosion damage caused by solid particle impact: Part 1: Effects of impact parameters on a predictive equation. *Wear* **259**, 95–101 (2005).

32.   Oka, Y. I. & Yoshida, T. Practical estimation of erosion damage caused by solid particle

impact: Part 2: Mechanical properties of materials directly associated with erosion damage. *Wear* **259**, 102–109 (2005).

33.   Lindsley, B. A. & Marder, A. R. The effect of velocity on the solid particle erosion rate of alloys. *Wear* **225**–**229**, 510–516 (1999).

34.   Humphrey, J. A. C. Fundamentals of fluid motion in erosion by solid particle impact. *Int. J. Heat Fluid Flow* **11**, 170–195 (1990).

35.   Finnie, I. Some observations on the erosion of ductile metals. *Wear* **19**, 81–90 (1971).

36.   Finnie, I. Some reflections on the past and future of erosion. *Wear* **186**–**187**, 1–10 (1995).

37.   Tilly, G. P. & Sage, W. The interaction of particle and material behaviour in erosion processes. *Wear* **16**, 447–465 (1970).

38.   Dundar, M. & Inal, O. T. Solid particle erosion of α-brass with 5 and 25 μm particles at normal incidence. *Wear* **224**, 226–235 (1999).

39.   Lynn, R. S., Wong, K. K. & Clark, H. M. I. On the particle size effect in slurry erosion. *Wear* **149**, 55–71 (1991).

40.   Desale, G. R., Gandhi, B. K. & Jain, S. C. Particle size effects on the slurry erosion of aluminium alloy (AA 6063). *Wear* **266**, 1066–1071 (2009).

41.   Elkholy, A. Prediction of abrasion wear for slurry pump materials. *Wear* **84**, 39–49 (1983).

42.   Clark, H. M. On the impact rate and impact energy of particles in a slurry pot erosion tester. *Wear* **146**, 165–183 (1991).

43.   Gandhi, B. K. & Borse, S. V. Effect of particle size and size distribution on estimating erosion wear of cast iron in sand-water slurries. *Indian J. Eng. Mater. Sci.* **9**, 480–486 (2002).

44.   Levy, A. V. & Chik, P. The effects of erodent composition and shape on the erosion of

steel. *Wear* **89**, 151–162 (1983).

45.   Levy, A. & Liebhard, M. The effect of erodent particle characteristics on the erosion of metals. *Wear* **151**, 381–390 (1991).

46.   Roy, M., Tirupataiah, Y. & Sundararajan, G. Effect of particle shape on the erosion of Cu and its alloys. *Mater. Sci. Eng. A* **165**, 51–63 (1993).

47.   Uuemŏis, H. & Kleis, I. A critical analysis of erosion problems which have been little studied. *Wear* **31**, 359–371 (1975).

48.   Andrews, D. R. & Horsfield, N. Particle collisions in the vicinity of an eroding surface. *J. Phys. D. Appl. Phys.* **16**, 525–538 (1983).

49.   Anand, K., Hovis, S. K., Conrad, H. & Scattergood, R. O. Flux effects in solid particle erosion. *Wear* **118**, 243–257 (1987).

50.   Turenne, S., Fiset, M. & Masounave, J. The effect of sand concentration on the erosion of materials by a slurry jet. *Wear* **133**, 95–106 (1989).

51.   Deng, T., Chaudhry, A. R., Patel, M., Hutchings, I. & Bradley, M. S. A. Effect of particle concentration on erosion rate of mild steel bends in a pneumatic conveyor. *Wear* **258**, 480–487 (2005).

52.   Wada, S. & Watanabe, N. Solid particle erosion of brittle materials (Part 3), the interaction with material properties of target and that of impingement on erosive wear mechanism. *Yogyo-Kyyokai-Shi* **95**, 573–578 (1987).

53.   Levy, A. & Hickey, G. Surface degradation of metals in simulated synthetic fuels plant environments. in *NACE Corrosion/82, International Corrosion Forum* 154 (1982).

54.   Hutchings, I. M., Winter, R. E. & Field, J. E. Solid particle erosion of metals: the removal of surface material by spherical projectiles. *Proc. R. Soc. Lond. A.* **348**, 379–392 (1976).

55.   Levy, A. V. The platelet mechanism of erosion of ductile metals. *Wear* **108**, 1–21

(1986).

56.   Islam, M. A. & Farhat, Z. N. Effect of impact angle and velocity on erosion of API X42 pipeline steel under high abrasive feed rate. *Wear* **311**, 180–190 (2014).

57.   Finnie, I. & Kabil, Y. H. On the formation of surface ripples during erosion. *Wear* **8**, 60–69 (1965).

58.   Carter, G., Nobes, M. J. & Arshak, K. I. The mechanism of ripple generation on sandblasted ductile solids. *Wear* **65**, 151–174 (1980).

59.   Griffin, M. J. & Macmillan, N. H. Longitudinal and transverse ripple formation during the solid particle erosion of lead. *Mater. Sci. Eng.* **80**, 1–4 (1986).

60.   Ballout, Y. A., Mathis, J. A. & Talia, J. E. Effect of particle tangential velocity on erosion ripple formation. *Wear* **184**, 17–21 (1995).

61.   Talia, J. E., Ballout, Y. A. & Scattergood, R. O. Erosion ripple formation mechanism in aluminum and aluminum alloys. *Wear* **196**, 285–294 (1996).

62.   Fang, Q., Sidky, P. S. & Hocking, M. G. Microripple formation and removal mechanism of ceramic materials by solid-liquid slurry erosion. *Wear* **223**, 93–101 (1998).

63.   Avcu, E., Yildiran, Y., Şahin, A. E., Fidan, S. & Sinmazçelik, T. Influences of particle impingement angle and velocity on surface roughness, erosion rate, and 3D surface morphology of solid particle eroded Ti6Al4V alloy. *Acta Phys. Pol. A* **125**, 541–543 (2014).

64.   Kazarinov, N. *et al.* Surface roughness investigation of ultrafine-grained aluminum alloy subjected to high speed erosion. *Procedia Struct. Integr.* **2**, 485–492 (2016).

65.   Atroshenko, S. A., Evsyifeev, A. D., Kazarinov, N. A., Petrov, Y. V. & Valiev, R. Z. Behavior of the grade 5 titanium alloy in different structural states in conditions of high-speed erosion. *Procedia Struct. Integr.* **6**, 190–195 (2017).

66.   Evstifeev, A., Kazarinov, N., Petrov, Y., Witek, L. & Bednarz, A. Experimental and

theoretical analysis of solid particle erosion of a steel compressor blade based on incubation time concept. *Eng. Fail. Anal.* **87**, 15–21 (2018).

67. Abedini, M. & Ghasemi, H. M. Erosion and erosion–corrosion of Al-brass alloy: Effects of jet velocity, sand concentration and impingement angle on surface roughness. *Trans. Nonferrous Met. Soc. China (English Ed.* **27**, 2371–2380 (2017).

68. Zhang, Y., Reuterfors, E. P., McLaury, B. S., Shirazi, S. A. & Rybicki, E. F. Comparison of computed and measured particle velocities and erosion in water and air flows. *Wear* **263**, 330–338 (2007).

69. Lee, B. E., Tu, J. Y. & Fletcher, C. A. J. On numerical modeling of particle-wall impaction in relation to erosion prediction: Eulerian versus Lagrangian method. *Wear* **252**, 179–188 (2002).

70. Fan, J., Yao, J., Zhang, X. & Cen, K. Experimental and numerical investigation of a new method for protecting bends from erosion in gas-particle flows. *Wear* **250**–**251**, 853–860 (2001).

71. Chen, X., McLaury, B. S. & Shirazi, S. A. Application and experimental validation of a computational fluid dynamics (CFD)-based erosion prediction model in elbows and plugged tees. *Comput. Fluids* **33**, 1251–1272 (2004).

72. Ahlert, K. Effects of Particle Impingement Angle and Surface Wetting on Solid Particle Erosion of AISI 1018 Steel. (University of Tulsa, USA, 1994).

73. McLaury, B. Predicting solid particle erosion resulting from turbulent fluctuations in oilfield geometries. (PhD Dissertation, The University of Tulsa, Tulsa, OK, 1996).

74. Grant, G. & Tabakoff, W. Erosion Prediction in Turbomachinery Resulting from Environmental Solid Particles. *J. Aircr.* **12**, 471–547 (1975).

75. Forder, A., Thew, M. & Harrison, D. Numerical investigation of solid particle erosion experienced within oilfield control valves. *Wear* **216**, 184–193 (1998).

76. Sommerfeld, M. Modelling of particle-wall collisions in confined gas-particle flows.

Int. J. Multiph. Flow **18**, 905–926 (1992).

77.   Finnie, I. & McFadden, D. H. On the velocity dependence of the erosion of ductile metals by solid particles at low angles of incidence. *Wear* **48**, 181–190 (1978).

78.   Mazumder, Q. H. Effect of Liquid and Gas Velocities on Magnitude and Location of Maximum Erosion in U-Bend. *Open J. Fluid Dyn.* **2**, 29–34 (2012).

79.   Edwards, J. K. Development, Validation, and Application of a Three Dimension, CFD-Based Erosion Prediction Procedure. (Ph.D. Thesis, The University of Tulsa, Tulsa, 2000).

80.   Njobuenwu, D. O. & Fairweather, M. Modelling of pipe bend erosion by dilute particle suspensions. *Comput. Chem. Eng.* **42**, 235–247 (2012).

81.   Grant, G. & Tabakoff, W. *An experimental investigation of the erosion characteristics of 2024 aluminum alloy*. (1973).

82.   Menguturk, M. & Sverdrup, E. F. Calculated tolerance of a large electric utility gas turbine to erosion damage by coal gas ash particles. in *Erosion: Prevention and Useful Applications* (ed. Adler, W. F.) 193–224 (American Society for Testing and Materials, ASTM-STP-664, 1979).

83.   Huang, C., Chiovelli, S., Minev, P., Luo, J. & Nandakumar, K. A comprehensive phenomenological model for erosion of materials in jet flow. *Powder Technol.* **187**, 273–279 (2008).

84.   Jun, Y. D. & Tabakoff, W. Numerical-simulation of a dilute particulate flow (laminar) over tube banks. *J. ofFluids Eng.* **116**, 770–777 (1994).

85.   Sommerfeld, M. & Huber, N. Experimental analysis and modelling of particle-wall collisions. **25**, 1457–1489 (1999).

86.   Wong, C. Y., Solnordal, C., Swallow, A. & Wu, J. Experimental and computational modelling of solid particle erosion in a pipe annular cavity. *Wear* **303**, 109–129 (2013).

87. Pereira, G. C., de Souza, F. J. & de Moro Martins, D. A. Numerical prediction of the erosion due to particles in elbows. *Powder Technol.* **261**, 105–117 (2014).

88. Kim, J. H., Joo, H. G. & Lee, K. Y. Simulation of solid particle erosion in WC-Ni coated wall using CFD. *J. Mater. Process. Technol.* **224**, 240–245 (2015).

89. Duarte, C. A. R., de Souza, F. J. & dos Santos, V. F. Numerical investigation of mass loading effects on elbow erosion. *Powder Technol.* **283**, 593–606 (2015).

90. Sommerfeld, M. Validation of a stochastic Lagrangian modelling approach for inter-particle collisions in homogeneous isotropic turbulence. *Int. J. Multiph. Flow* **27**, 1829–1858 (2001).

91. Duarte, C. A. R., de Souza, F. J., Salvo, R. de V. & dos Santos, V. F. The role of inter-particle collisions on elbow erosion. *Int. J. Multiph. Flow* **89**, 1–22 (2017).

92. Laín, S. & Sommerfeld, M. Numerical prediction of particle erosion of pipe bends. *Adv. Powder Technol.* **30**, 366–383 (2019).

93. Duarte, C. A. R., de Souza, F. J., Venturi, D. N. & Sommerfeld, M. A numerical assessment of two geometries for reducing elbow erosion. *Particuology* (2019) doi:10.1016/j.partic.2019.01.004.

94. Nečas, D. & Klapetek, P. Gwyddion: an open-source software for SPM data analysis. *Cent. Eur. J. Phys.* **10**, 181–188 (2012).

95. Gadelmawla, E. S., Koura, M. M., Maksoud, T. M. A., Elewa, I. M. & Soliman, H. H. Roughness parameters. *J. Mater. Process. Tecnol.* **123**, 133–145 (2002).

96. Schindelin, J., Arganda-Carreras, I. & Frise, E. Fiji: an open-source platform for biological-image analysis. *Nat. Methods* **9**, 676–682 (2012).

97. Rueden, C. T., Schindelin, J. & Hiner, M. C. ImageJ2: ImageJ for the next generation of scientific image data. *BMC Bioinformatics* **18**, (2017).

98. Bröder, D. Anwendung optischer Messtechniken zur Untersuchung disperser Gas-

Flüssigkeits-Strömungen. (Martin-Luther-University Halle-Wittenberg, Germany, 2003).

99.   Bröder, D. & Sommerfeld, M. Planar shadow image velocimetry for the analysis of the hydrodynamics in bubbly flows. *Meas. Sci. Technol.* **18**, 2513–2528 (2007).

100.   Marr, D. & Hildreth, E. Theory of edge detection. *Proc. R. Soc. London B* **207**, 187–217 (1980).

101.   Laín, S. & Sommerfeld, M. Characterisation of pneumatic conveying systems using the Euler/Lagrange approach. *Powder Technol.* **235**, 764–782 (2013).

102.   Issa, R. I. Solution of the implicitly discretised fluid flow equations by operator-splitting. *J. Comput. Phys.* **62**, 40–65 (1986).

103.   Patankar, S. V. & Spalding, D. B. A calculation procedure for heat, mass and momentum transfer in three-dimensional parabolic flows. *Int. J. Heat Mass Transf.* **15**, 1787–1806 (1972).

104.   Kalitzin, G., Medic, G., Iaccarino, G. & Durbin, P. Near-wall behavior of RANS turbulence models and implications for wall functions. *J. Comput. Phys.* **204**, 265–291 (2005).

105.   Schiller, L. & Naumann, A. A drag coefficient correlation. *Z. Ver. Dtsch. Ing* 233–241 (1935).

106.   Haider, A. & Levenspiel, O. Drag Coefficient and Terminal Velocity of Spherical and Nonspherical Particles. *Powder Technol.* **58**, 63–70 (1989).

107.   Saffman, P. G. The lift on a small sphere in a shear flow. *J. Fluid Mech.* **22**, 385–400 (1965).

108.   Mei, R. An approximate expression for the shear lift force on a spherical particle at finite Reynolds numberNo Title. *Int. J. Multiph. Flow* **18**, 145–147 (1992).

109.   Rubinow, S. I. & Keller, J. B. The transverse force on a spinning sphere moving in a

viscous liquid. *J. Fluid Mech.* **11**, 447–459 (1961).

110. Oesterlé, B. & Bui Dihn, T. Experiments on the lift of a spinning sphere in a range of intermediate Reynolds numbers. *Exp. Fluids* **25**, 16–22 (1998).

111. Dennis, S. C. R., Singh, S. N. & Ingham, D. B. The steady flow due to a rotating sphere at low and moderate Reynolds numbers. *J. Fluid Mech.* **101**, 257–279 (1980).

112. Sawatzki, O. Über den Einfluß der Rotation und der Wandstöße auf die Flugbahnen kugeliger Teilchen im Luftstrom. (Univ. Karlsruhe, 1961).

113. Sommerfeld, M., Kohnen, G. & Rüger, M. Some open questions and inconsistencies of lagrangian particle dispersion models. in *9th Symposium on Turbulent Shear Flows* 1–15 (1993).

114. von Karman, T. & Howarth, L. On the statistical theory of isotropic turbulence. *Stat. theory isotropic Turbul.* **164**, 192–215 (1938).

115. Sommerfeld, M. & Huber, N. A laser strobe technique combined with digital image analysis to study particle-wall collisions. in *Xu, Y., Wang, S. (Eds.), Modern Measuring Techniques for Multiphase Flows. Proceedings of the International Symposium on Measurement Techniques for Multiphase Flows* 428–440 (1995).

116. Tsuji, Y., Morikawa, Y., Tanaka, T., Nakatsukasa, N. & Nakatani, M. Numerical simulation of gas-solid two-phase fow in a two-dimensional horizontal channel. *Int. J. Multiph. Flow* **13**, 671–684 (1987).

117. Schuch, G. & Löffler, F. Über die Abscheidewahrscheinlichkeit von Feststoffpartikeln an Tropfen in einer Gasströmung durch Trägheitseffekte. *vt-Verfahrenstechnik* **12**, 302–306 (1978).

118. Göz, M. F., Laín, S. & Sommerfeld, M. Study of the numerical instabilities in Lagrangian tracking of bubbles and particles in two-phase flow. *Comput. Chem. Eng.* **28**, 2727–2733 (2004).

119. Lipowsky, J. & Sommerfeld, M. LES-Simulation of the formation of particle strands in

swirling flows using an unsteady Euler-Lagrange approach. in *6th International Conference on Multiphase Flow ICMF 2007* 1–10 (2007).

120. Sommerfeld, M. Analysis of collision effects for turbulent gas-particle flow in a horizontal channel: Part I. Particle transport. *Int. J. Multiph. Flow* **29**, 675–699 (2003).

121. Sommerfeld, M. & Kussin, J. Analysis of collision effects for turbulent gas-particle flow in a horizontal channel. Part II. Integral properties and validation. *Int. J. Multiph. Flow* **29**, 701–718 (2003).